

Development of Dielectric Spectroscopic Resonant Sensors for Biomedical and Industrial Applications

Richard Thomas Blakey

A thesis submitted in partial fulfilment of the
requirements of Liverpool John Moores University
for the degree of Doctor of Philosophy.

January 2014

Statement of Authorship

This thesis was completed as part of Postgraduate Research at Liverpool John Moores University. It is comprised of my own unaided work. Where the work of others has been used or drawn on then it has been fully attributed to the relevant source.

Signed: Richard Thomas Blakey

Date: 06/01/2014

Abstract

This research entailed the development of resonant dielectric sensors that utilising alternating electric fields at microwave frequencies. Characterisation and identification of biological samples is currently an expensive and time consuming procedure due to the extreme variation of seemingly similar biological systems. The work describes the development of resonant dielectric sensors for five distinct applications. The aim of the research was to develop non-invasive, affordable and compact dielectric spectroscopy sensors that may be used in-situ to characterise organic and biological systems. The suitability of using dielectric spectroscopy to a number of applications has been investigated. This is to address disadvantages of conventional laboratory analysis such as lengthy, costly and labour intensive assessment methods that require intermittent sampling and/or off site analysis. The research is structured into a series of progressive stages (work packages) that integrate and culminate into feasible inline analytical procedures that can quickly, safely and inexpensively assess a specified variable in organic and biological systems. Overall, a number of sensors using electromagnetic radiation at microwave frequencies were developed that have proven to be sensitive and extremely versatile to a number of detection and monitoring applications. Miniaturisation of microwave generation and analysis circuits will enable the sensors to be incorporated into feasible compact devices for in situ analysis of the analyte in question.

Acknowledgements

I would like to thank first and foremost my supervisor and friend Doctor Alex Mason. Without his help, advice and understanding this dissertation thesis would not have been possible. I would like to thank Professor Ahmed Al-Shamma'a for providing us with the opportunity and capabilities to conduct this research. I do not know of any other people who work harder while remaining passionate about what they do. I also thank other members of the BEST research group for their help and contributions to the research. Notably, Doctor Steve Wylie for his expertise and guidance in navigating electromagnetic theory, Doctor Jeff Cullen for bodging any problems that have been too much for one pair of hands, Doctor Montserrat Ortoneda Pedrola for her help and expertise in all matters biological and Doctor Eduardo Cordova Lopez for his humour and continuously contagious cheerful mood. Last but certainly not least I would like to thank Doctor Olga Korostynska for her patient ear and no nonsense advice. It has truly been a privilege to work as part of such a great team.

I would like to thank my mother, Denise Reader to whom I dedicate this thesis, for her devotion in raising me and her continual support which continues to this day. I would also like to thank my brother, Matthew Blakey for not talking about microwaves and reminding me that life is not all about studying and writing.

Lastly I would like to thank the countless other family members, friends and teachers who have contributed towards my personality and education, making me the person who I am today. I am truly a blessed and lucky individual.

A sincere thank you to you all.

Table of Contents

Abstract.....	3
Chapter 1. Introduction	22
1.1. Research Aim	22
1.2. Research objectives	25
1.3. Chapter overview.....	26
1.3.1. Chapter 2 - Dielectric relaxation and electromagnetic theory	26
1.3.2. Chapter 3 - Literature reviews	26
1.3.3. Chapter 4 - Equipment and software.....	26
1.3.4. Chapter 5 - Coplanar sensor development	26
1.3.5. Chapter 6 - Experimental Results.....	27
1.3.6. Chapter 7 - Conclusions and future work	28
Chapter 2. Dielectric relaxation and electromagnetic theory	29
2.1. Standing waves, resonance and radiation	31
2.2. Dielectric theory.....	34
2.3. Dielectric spectroscopy	39
2.4. Chapter 2 Summary	43
Chapter 3. Literature review.....	44
3.1. Quantification of neutral lipids in biological cells.....	45
3.1.1. Considerations of detecting neoplastic growth using dielectric spectroscopy.....	61
3.2. Differentiation of edible vegetable oils	71
3.2.1. Considerations of detecting adulterants in olive oil using dielectric spectroscopy.....	78

3.3. Detection of disease states in cattle by quantification of blood serum lactate	82
3.3.1. Considerations of detecting disease states in cattle utilising dielectric spectroscopy .	84
3.4. Quantification of Pseudomonas aeruginosa.....	89
3.4.1. Considerations of quantifying bacterial cells using dielectric spectroscopy	90
3.5. Quantification of lactate in cerebrospinal fluid	91
3.5.1. Considerations of quantifying lactate concentrations in cerebrospinal fluid using dielectric spectroscopy	92
3.6. Chapter 3 Summary	93
Chapter 4. Equipment and software.....	95
4.1. High frequency simulation software (HFSS)	95
4.2. Vector network analysers	95
4.2.1. Hewlett-Packard (Agilent) 8720 ET	96
4.3. Chapter 4 Summary	98
Chapter 5. Coplanar sensor development.....	99
5.1. Development of sensor SD-1	102
5.2. Development of sensor SD-2	105
5.3. Development of sensor SD-3	108
5.4. Development of sensor SD-4	111
5.5. Development of sensor SD-5	114
5.6. Chapter 5 Summary	116
Chapter 6. Experimental Results.....	117
6.1. Quantification of neutral lipids in biological cells.....	117

6.1.1.	Micelle quantification	117
6.1.2.	Lipid positive – lipid negative Lipomyces yeast culture differentiation.....	122
6.1.3.	Saline concentration quantification.....	125
6.1.4.	The finalised experimental fluidic apparatus.....	127
6.1.5.	Water absorption	130
6.1.6.	Temperature effects	132
6.1.7.	Lipomyces lipid droplet quantification	133
6.1.8.	Lipomyces cell quantification in a complex cell suspension	135
6.1.9.	Coplanar sensor substrate experimentation	137
6.2.	Differentiation of edible vegetable oils	139
6.2.1.	Dielectric characteristics of vegetable oils as calculated by the small perturbation technique	139
6.2.2.	Differentiation of olive oils using a capacitive coplanar resonant sensor	142
6.3.	Quantification of lactate in bovine blood	145
6.4.	Quantification of <i>Pseudomonas aeruginosa</i>	149
6.5.	Quantification of lactate in cerebrospinal fluid	152
6.6.	Chapter 6 Summary	156
Chapter 7.	Conclusions and future work	158
7.1.	Quantification of neutral lipids in biological cells.....	159
7.2.	Differentiation of edible vegetable oils	160
7.3.	Detection of disease states in cattle.....	160
7.4.	Quantification of <i>Pseudomonas aeruginosa</i>	161

7.5. Detection of lactate in cerebrospinal fluid	162
7.6. Research Overview	163
Chapter 8. References	165
Appendix 1. Publications resulting from the research.....	183
Journal publications	183
Conference Publications	184
Appendix 2. Technical Appendix.....	186
1.1 LabVIEW control software	186
1.2 PCB routing methodology	190
1.3 Statistical software.....	190

Table of Figures

Figure 2.1. The electromagnetic spectrum. Increasing frequency corresponding to an increase in energy potential [8].	31
Figure 2.5. Electric field (E) and magnetic field (B) [21]	33
Figure 2.6. A model linear two port system [25].	34
Figure 2.7. Net dipole moment of water and carbon dioxide.	35
Figure 2.8. Complex plane plots of Debye (a), Cole-Cole (b), Davidson-Cole (c) and Havriliak-Negami (d) relaxation types as calculated from the equations above [35].	37
Figure 2.9. Idealised dispersions of real permittivity associated with biological material [36].	37
Figure 2.10 a. Real permittivity and conductivity plotted against log. frequency. b. Imaginary permittivity plotted against log. frequency.	38
Figure 2.11. Experimental setup of a rectangular waveguide and VNA.	40
Figure 2.12. Schematic of a coaxial probe.	41
Figure 2.13. Agilent High Temperature Dielectric Probe.	42
Figure 3.1. The chemical structure of triacylglycerol and phospholipids.	46
Figure 3.2. Molecular mechanisms of cancer.	47
Figure 3.3. Schematic of proliferative and apoptosis signal transduction pathways.	48
Figure 3.4. Stages of metastasis, Reduction of adhesion to neighbouring cells (a), migration of the cells through the stroma layer (b) and into the vessel (intravasation) (c). Metastatic cells may bind to	

vascular receptors (d) or bind to platelets (e) protecting them from the immune system. Metastatic cells then extravasate from the bloodstream (f) before adhering to cells in the secondary site (g) [54]. 50

Figure 3.5. One year mortality rate (%) by detection route and age group. Breast cancer, England, 2007 [71]. 53

Figure 3.6. Pathways responsible for the formation of diacylglycerol. DAG: diacylglycerol; DHAP: dihydroxyacetone phosphate; FFA: free fatty acids; G3P; Glycerol-3-phosphate; lyso-PtdOH: lysophosphatidic acid; PL: phospholipid; X; alcohol molecule; Pi-X; alcohol phosphate [89, 90]. 55

Figure 3.7. Synthesis and degradation of triacylglycerols. Diacylglycerol is acylated with either Acy-CoA or a phospholipid yielding triacylglycerol. Degradation of TAG yields free fatty acids (FFA) and DAG. 55

Figure 3.8. The structure and molecular composition of lipid droplets. Left, Fluorescent staining of a cell with triacylglycerols (red) and lipid droplet associated proteins (green). Centre, triacylglycerol core encapsulated by phospholipids monolayer and lipid droplet associated proteins. Right, triacylglycerol molecule. 56

Figure 3.9. Budding model of lipid droplet formation [106]. Neutral lipid anabolic enzymes localise in the endoplasmic reticulum (ER) (A). TAGs and sterol esters accumulate between the phospholipid bilayer (B). This forms micro-droplets (C, D) which bud off when a critical mass is reached (E). 57

Figure 3.10. The configuration of a transmitter and receivers on the breast tissue. The patient is in the supine position [151]. 63

Figure 3.11. Risk probability maps generated using the SVM microwave approach. The actual tumour location is outlined with a white square [151]. 63

Figure 3.12. Experimental setup for monitoring 2D cell layers (A). Schematic drawing of direct electrode cell interaction (B) [153].	64
Figure 3.13. Resistance of differentiated (blues) and non-differentiated (red/orange) mesenchymal cells as a function of culture time. The differentiation to osteogenic cells is highlighted by the blue arrows [153].	64
Figure 3.14. Capillary based microfluidic cell for impedance measurement with integrated electrodes (A). Schematic drawing of capillary measurement setup [153].	65
Figure 3.15. Impedance spectra of osteogenic stem cells (blue), non-differentiated cells (red) and necrotic cells (yellow) with standard deviation error bars [153].	65
Figure 3.16. The spectra for MBA and MDCK cell suspensions. (a) Dielectric and conductivity of MBA and MBA-lectin suspensions. (b) Spectra of MDCK and MDCK-SEC13 suspensions. (c) High frequency spectra of MDCK and MDCK-SEC13 suspensions. (d) Loss spectra of MBA and MBA-lectin suspensions. (e) Loss spectra of MDCK and MDCK-SEC13 suspensions [154].	67
Figure 3.17. Two pole filter based EM biosensor configuration [41].	68
Figure 3.18. Electrical model of the sensor configuration [41].	68
Figure 3.19. The S-parameters (S_{11} and S_{21}) of the filter based EM sensor. Note the effect of capacitive loading (a) and resistive loading (b) on the sensitive mode (14.5 GHz) and the insensitive mode (S_{21}) [41].	68
Figure 3.20. Individual cells deposited in the interdigitated capacitor coupling region of the sensor. Simulation of the sensors indicates the region of uniform electric field [41].	69
Figure 3.21. Measured S-parameters spectra for unloaded and glial cell loaded sensor [41].	70
Figure 3.22. Measured S-parameters spectra for before and after fixed stem cell deposition [41].	70

Figure 3.23. Measured conductivity of sperm samples at 3 different frequencies in the MHz range [155].	71
Figure 3.24. A triacylglycerol molecule composed of a glycerol backbone esterified to three fatty acid chains.	73
Figure 3.25. NMR spectra of extra virgin olive oil (EVOO), hazelnut oil (HO), peanut oil (PO), sunflower oil (SuO) and soybean oil (SoO) at 900 MHz [174].	75
Figure 3.26. IR spectra of extra virgin olive oils and vegetable oils [192]	76
Figure 3.27. IR spectra of extra virgin olive oil samples with 0, 10, 20 and 40 % of high linoleic sunflower oil, canola oil, pomace olive oil and high oleic sunflower oil [21].	76
Figure 3.28. Fluorescence spectra of virgin olive oil (A), olive pomace oil (B), corn oil (C), sunflower oil (D), soybean oil (E), rapeseed oil (F) and walnut oil (G) [179].	77
Figure 3.29. Variable plate capacitor and instrumental setup of the olive oil water content methodology [211].	79
Figure 3.30. Correlation between capacitance and water content at 8 kHz [211].	79
Figure 3.31. Correlation between mono-unsaturated fatty acids and capacitance at 2 kHz [211].	80
Figure 3.32. Configuration of the coaxial probe and experimental setup [212].	81
Figure 3.33. Comparison between the reflected s-parameters of olive oil (left) and castor oil (right) [212].	81
Figure 3.34. Comparative results of averaged values for relaxation frequencies of vegetable oils with error bars (95 % confidence level) [212].	82

Figure 3.35. The prototype non-invasive blood glucose monitoring system with bracelet mounted electrode configuration [234].	85
Figure 3.36. The predicted results plotted against the actual blood glucose concentration for more than 100 subjects [234].	86
Figure 3.37. A ball and stick diagram of lactic acid.	86
Figure 3.38. Sensing structure (left) and completed contact lens (right) of lactate sensor. The arrows indicate the working electrode (WE), reference electrode (RE) and the counter electrode (CE) [236].	87
Figure 3.39. Measured sensor current as a function of lactate concentration of the tear film [236].	88
Figure 3.40. Linear relationship of between capacitance of the immuno-sensor (μF) and logarithmic concentrations of E. Coli. (CFU / ml) at a frequency of 1Hz [279].	91
Figure 4.1. Example of E-field and radiation plot generation.	95
Figure 4.3. Hewlett Packard (Agilent) 8720 ET.	97
Figure 4.4. A simple schematic of the HP 8720 ET VNA.	97
Figure 5.1. A number of coplanar PCB based resonant sensors.	100
Figure 5.2. Schematic of the 3D printed ABS sample well.	102
Figure 5.3. Schematic of sensor SD-1 in Eagle PCB software.	103
Figure 5.4. Electric field of sensor SD-1 at fundamental mode with a simulated frequency of 5.15 GHz and phase of 0 degrees.	103

Figure 5.5. Schematic of SD-1 with added slots along the feed line to match sensor impedance to source.....	104
Figure 5.6. S11 parameters of SD-1 with impedance matching slots of variable length (mm).	104
Figure 5.8. S11 resonant frequency (GHz) of SD-1 sensor interacting with yeast cell samples as a function of cell concentration (cells/ml).....	105
Figure 5.9. Schematic of sensor SD-2 in Eagle PCB software.....	106
Figure 5.10 Electric field of sensor SD-2 at fundamental mode with a simulated frequency of 2 GHz and phase of 0 degrees.....	106
Figure 5.11. Simulated S11 parameters of sensor SD-2 with the shorting post 0 mm (a), 1 mm (b) and 2 mm (c) from the boundary of the circular patch. The length of the slots are varied (mm) to match the impedance for each shorting post configuration.	107
Figure 5.13. S11 resonant frequency (GHz) of SD-2 sensor interacting with yeast cell samples as a function of cell concentration (cells/ml).....	108
Figure 5.14. Schematic of sensor SD-3 in Eagle PCB software.....	109
Figure 5.15. Electric field of sensor SD-3 at fundamental mode with a simulated frequency of 2.45 GHz and phase of 0 degrees.	109
Figure 5.16. Simulated S11 parameters of sensor SD-3 with varied coupling gap (mm).	110
Figure 5.18. S11 resonant frequency (GHz) of SD-3 sensor interacting with yeast cell samples as a function of cell concentration (cells/ml).....	111
Figure 5.19. Schematic of sensor SD-4 in Eagle PCB software.....	112

Figure 5.20. Electric field of sensor SD-4 at fundamental mode with a simulated frequency of 2.67 GHz and phase of 0 degrees.	112
Figure 5.21. Simulated S_{11} parameters of sensor SD-4 with varied coupling gap (mm).....	113
Figure 5.23. S_{11} resonant frequency (GHz) of SD-4 sensor interacting with yeast cell samples as a function of cell concentration (cells/ml).....	113
Figure 5.24. Schematic of sensor SD-5 in Eagle PCB software.....	114
Figure 5.25. Electric field of sensor SD-5 at fundamental mode with a simulated frequency of 0.9 GHz and phase of 0 degrees.....	114
Figure 5.26. Simulated S_{11} parameters of sensor SD-5 with varied capacitor coupling gap (mm).....	115
Figure 5.28. S_{11} resonant frequency (MHz) of SD-5 sensor interacting with yeast cell samples as a function of cell concentration (cells/ml).....	115
Figure 6.1. S_{21} parameters of olive oil in concentrations (v/v %) 100, 50, 10, 5, 1 and 0.5. S_{21} frequency ranges from 1.5 to 1.9 GHz.	118
Figure 6.2. Graph showing the effect of olive oil concentration against S_{21} parameter resonant frequency shift.	118
Figure 6.3. Graph showing a decrease in relative dielectric constant and dielectric loss as a function of olive oil concentration.	120
Figure 6.4. Plot of relative dielectric constant against dielectric loss to represent complex permittivity. Each data point indicates a concentration of olive oil suspension with oil concentration decreasing as the complex permittivity increases.....	120
Figure 6.5. Simulated surface current of the PCB based resonant structure.	122

Figure 6.6. Realised PCB based resonant structure.....	123
Figure 6.7. Microtitre plate mounted upon the platform. The resonant structure may be seen in place below wells A4 (A) and C6 (B).	123
Figure 6.8. S_{11} Parameters of the resonant PCB structure when exposed to an empty microtitre plate (air) and when <i>Lipomyces</i> cell cultures are in place.	124
Figure 6.9. Picture of the resonant structure used in this experiment consisting of 8 interdigitated finger pairs.	125
Figure 6.10. Experimental setup of the preliminary fluidic cell.	126
Figure 6.11. Resonant frequency (GHz) and quality factor (arbitrary) as a function of saline concentration (% w/v).	126
Figure 6.12. Fluidic cell configuration demonstrating the coplanar sensor (centre), taped threads and channels that lead to the measurement reservoir.	127
Figure 6.13. Photograph of the experimental setup, including quaternary pump, vector network analyser and sensor system.	128
Figure 6.14: Schematic of the fluidic cell sensor with (left) and without (right) ground plane (blue).	128
Figure 6.15. Simulation of fluidic cell coplanar sensor at a frequency of 0.....	129
Figure 6.16. Simulated electric field (magnitude) of the finalised sensor at a frequency of 0.65 GHz and phase angle of 0, 45, 90, 135 and 180 degrees (left to right). The radiation pattern of the electric field suggests the field is elliptically polarised.....	129

Figure 6.17. Simulated electric field (vector) of the finalised sensor at a frequency of 0.65 GHz and phase angle of 0, 45, 90, 135 and 180 degrees (left to right). The radiation pattern of the electric field suggests the field is elliptically polarised.....	130
Figure 6.18: Image of the fabricated fluidic cell EM sensor.....	130
Figure 6.19: Resonant frequency change over 85 hours, indicating resonant frequency stabilisation after 45 hours.....	131
Figure 6.20: Resonant frequency shift as a result of temperature change, indicating instability over 45°C.....	132
Figure 6.21: Resonant frequency of the sensor (MHz) as a result of accumulating lipid concentration in NLM cultures and lipid negative CLM cultures.	134
Figure 6.22. Resonant frequency of the sensor (MHz) as a result of cell concentration in defibrinised bovine blood.	136
Figure 6.23. Resonant frequency change over a period of 70 hours demonstrating the change in electrical characteristics of the substrate as water is pumped through the sensor.	138
Figure 6.24. Image and simulation of the cavity used to assess the dielectric characteristics. Simulation is shown with mode TM_{010} electric field.....	139
Figure 6.25. Image of the experimental set-up.	140
Figure 6.26. S_{11} parameters of olive oil, sunflower oil, grapeseed oil, groundnut oil and air for a frequency range of 1.65 to 1.75 GHz.	141
Figure 6.27. S_{21} parameters of olive oil, sunflower oil, grapeseed oil, groundnut oil and air for a frequency range of 1.65 to 1.75 GHz.	141

Figure 6.28. Interdigitated electrode with a fundamental frequency of 8.6 GHz.	143
Figure 6.29. Experimental setup of coplanar sensor for olive oil quality validation.	144
Figure 6.30. S ₁₁ parameters of the olive oil samples.	144
Figure 6.31. Fabricated resonant sensor applied to non-invasive lactate measurements.....	145
Figure 6.32. Silicone tubing in PE foam covered in cow hide to simulate jugular and supportive tissue.	146
Figure 6.33. The experimental apparatus consisting of a peristaltic pump, incubator, VNA and model cow (clockwise from bottom-left).	147
Figure 6.34. S ₁₁ parameters of bovine defibrinised blood with differing concentrations of lactate (mM).	147
Figure 6.35. Average resonant frequency of the sensor (GHz) as a function of logarithmic bovine blood lactate concentration (mM). Error bars represent standard deviation. Linearity was calculated at $r^2 = 0.941$	148
Figure 6.36. Overview of the experimental setup. Quaternary pump and vector network analyser (left). Fluidic cell embedded coplanar sensor system (right).....	149
Figure 6.37. SEM micrographs of <i>P. aeruginosa</i> biofilms grown on glass.	150
Figure 6.38. Plot of average resonant peak with changing <i>P. aeruginosa</i> optical density. Error bars indicate the standard deviation of the measurements. Linearity calculated at r^2 of 0.993.....	151
Figure 6.39. Plot of average Q-factor with changing <i>P. aeruginosa</i> optical density. Error bars indicate the standard deviation of the measurement. Linearity calculated at r^2 0.994.	151

Figure 6.40. Overview of the experimental setup, including quaternary pump, vector network analyser and sensor system.	154
Figure 6.41. Illustrating the shift in peak frequency at approx. 394 MHz for 0 and 20 mmol/ L concentrations of lactate.	155
Figure 6.42. The shift in peak frequency at approximately 394 MHz with different concentrations of lactic acid, with good correlation between results and the logarithmic best fit curve ($r^2 > 0.98$). Note that results have been normalised against a background sample of deionised water only.	155
Figure 4.5. LabVIEW Interface for configuring the HP 8720 ET VNA.	187
Figure 4.6. LabVIEW programming for above interface incorporating sub Vis.	187
Figure 4.7. LabView interface for setting up multiple frequency sweeps and recording the subsequent marker and sweep data.	188
Figure 4.8. Block diagram of the programming that enables multiple frequency sweeps, collection and amalgamation of data.	188
Figure 4.9. LabView interface for setting up multiple frequency sweeps at a variable time interval and recording the subsequent marker and sweep data.	189
Figure 4.10. Block diagram of the programming that enables multiple frequency sweeps at a variable time interval, collection and amalgamation of data. Note the conversion of LabVIEW time stamp to a Microsoft compatible time stamp in the left-centre of the diagram.	189
Figure 4.2. A typical PCB layout as seen in CadSoft EAGLE.	190

Table of Tables

Table 3.1. Fatty acid composition of vegetable oils as determined by Lee et al. [169].....	73
Table 2.1. Summary of the application, current methodologies, weaknesses of current methodologies	94
Table 6.1. The effect of Olive Oil Concentration on S_{21} Resonant Frequency.	119
Table 6.2. Calculated Dielectric Characteristics of TAG micelle samples	119
Table 6.3. Statistical analysis of resonant frequency of lipid positive and negative by one way anova.	124
Table 6.4. Statistical analysis of results Lipid cultures by two way ANOVA.....	134
Table 6.5. Statistical analysis of results Lipid cultures by two way ANOVA.....	136
Table 6.6. The Dielectric Characteristics of difference vegetable oils as calculated by the small perturbation technique at 1.75 GHz.	142
Table 6.7. The manufacturer, type and composition of olive oils assessed using impedance spectroscopy.	145
Table 6.8. One way ANOVA statistical analysis results.	148

Abbreviations

American joint committee on cancer	AJCC
Carbon limiting media	CLM
Cerebral spinal fluid	CSF
Colony forming units	CFU
Cystic fibrosis	CF
Dulbecco's modified essential media	DMEM
Electric substrate impedance sensing	ESIC
Electromagnetic	EM
Endoplasmic reticulum	ER
European Union	EU
Extra virgin olive oil	EVOO
Fatty acid methyl esters	FAMES
Fluidic cell	FC
Free fatty acids	FFA
General purpose interface bus	GPIB
Hazelnut oil	HO
High frequency simulation software	HFSS
High performance liquid chromatography	HPLC
Infra-red	IR
International union against cancer	UICC
Low density lipids	LDLs
Magnetic resonance	NMR
Material under test	MUT
Bone Marrow derived Pre-Osteoblastic	MBA
Madin-Darby canine kidney	MDCK
Nitrogen limiting media	NLM
Nutrient broth	NB
Parathyroid hormone-related protein	PTHrP
Peanut oil	PO
Phosphate buffered saline	PBS
Platelet activating factor	PAF
Poly(methyl methacrylate)	PMMA
Polymerase chain reaction	PCR
Polytetraflouroethylene	PTFE
Scattering parameters	S-parameters
Soybean oil	SoO
Sunflower oil	SuO
Time domain reflectometry	TDR
Tumour, lymph node and metastasis	TNM
Ultra-violet	UV
Vector network analyser	VNA
Very low density lipids	VLDLs
Virtual instrument software architecture	VISA

Chapter 1. Introduction

The research aims to address the issue of lengthy and sometimes unnecessary laboratory tests. On-site and/or online analyses of industrial processes and medical diagnostics could introduce a significant reduction in cost to industry and medical fields. Current analyses utilises lengthy procedure that often need to occur off site a specialised facilities requiring a lot of specialised staff, using highly specialised equipment. Although these procedures can be extremely precise there exists a niche for more economically viable alternatives that can rapidly determine the safety, quality or state of a sample. This may either serve as a conclusive result or an indicator for subsequent analysis which would result in less laboratory analysis.

1.1. Research Aim

The aim of the research was to develop non-invasive, affordable and compact dielectric spectroscopy sensors to characterise organic and biological systems. The suitability of using dielectric spectroscopy to a number of applications will be investigated. This is to address disadvantages of conventional laboratory analysis such as lengthy, costly and labour intensive assessment methods such as HPLC and bacterial culturing. The research is structured into a series of progressive stages (work packages) that integrate and culminate into feasible inline analytical procedures that can quickly, safely and inexpensively assess a specified variable in organic and biological systems. The sensors developed in this research are resonant structures designed to operate in the microwave frequencies of the electromagnetic spectrum differentiating sample based upon dielectric characteristics.

Dielectric spectroscopy has been found to be one of the most informative tools for defining the resistance and capacitance of biological material [1-6]. Coplanar sensor development and fabrication provided a means of reducing the physical size of the resonant structure while simultaneously significantly reducing production expenses. Incorporation of the sensor into a fluidic device

presented a means of increasing analyte-sensor interaction and measurement repeatability. A fluidic device also serves as a platform for the development of sample pre-treatment, handling and sorting. Notably, microwave radiation is non-ionising, utilising (at most) one-tenth the power required for transmission by a typical modern day mobile phone. Therefore, while the use of EM waves often raises safety concerns, there is a good argument to say that the method is safe, or at least no worse than what we are already subjected to on a daily basis.

The research comprises of applying the sensors to five distinct applications as follows.

The detection of neoplastic tumours (application 1) still represents a clinical challenge to the medical industry. The quantification of neutral lipids in biological cells may be used as a marker for the presence of neoplastic tumour development. This was achieved using yeast samples in which the lipid composition can be controlled and easily manipulated. Analysis of the lipid profile of biological cells is currently a lengthy procedure involving numerous extraction and analytical methodologies. The lipid profile of specific cells can yield important information of the health of the individual specifically to neoplasm and inflammation. The research proposes a novel minimally - invasive analytical technique that can quickly and effectively calculate the lipid content of biological cells based upon dielectric characteristics.

Olive oil adulteration is currently a significant problem faced by European food safety industry. Adding adulterants to olive oil constitutes fraud and having serious implications upon the economy of producing countries and public health. Analysis currently focuses upon the composition of the fatty acids that make up the oil. Gas and liquid chromatography is currently employed as a precise means of accomplishing this. However, the methodology requires specialist equipment that needs qualified professionals to operate with a lengthy turn around period. This research proposes a novel sensor that can rapidly detect small differences in the composition of the oil (application 2). This could be combined with miniaturised circuits to produce a handheld analysis device that can be used in the field to instantly test olive oils for adulterants which is currently unavailable to food standard

authorities. The experiments consisted of analysing vegetable oils from different sources to see if they could be differentiated.

Diseased livestock currently represent a significant cost to the agricultural industry. Disease epidemics can result in the loss of livelihoods and decimate a countries economy. Early detection of disease in livestock can significantly reduce the risk of a disease becoming endemic and reduce vaccination and treatment expenditure. This consequently reduces the impact and therefore cost of individual and epidemic disease. Currently there are no commercially available wearable sensors for livestock that are able to assess the health of the animal. A non-invasive sensor designed for the quantification of lactate in the blood of cows is developed (application 3). This sensor was applied to a model cow artery under the surface of the skin. The research develops a wearable sensor that can be incorporated into a collar mountable device to operate as part of a wireless sensor network when used in tandem with other collars.

Bacterial contamination of stored water represents a risk to health and wellbeing. This risk becomes significant when improper water treatment results in a build up of bacteria in the water delivery system. A sensor was designed that can be incorporated into water delivery systems to detect the presence of *Pseudomonas*, a water dwelling bacteria (application 4). The results show the presence of *Pseudomonas* can be detected using the experimental procedure. Water borne bacteria constitute a considerable risk in potable water when suitable storage procedures are not rigorously adhered to. Currently *Legionella* and *Pseudomonas* outbreaks are only detected upon a group of people becoming ill with the infection. There are no devices available that monitor the quality of water as it leaves storage tanks present in large buildings. This research proposes a device that can be incorporated into water supply pipes to monitor bacterial content of the water.

During cranial and spinal surgical procedures there is an inherent risk of hypoxia if pressure is exerted upon the cerebrospinal fluid. To reduce the risk of this occurring, a spinal tap is inserted to relieve any pressure that is applied. However, important information pertaining to the oxygen

saturation of the spinal cord can be obtained through analysis of the exuded CSF. Therefore a sensor was designed that can be incorporated in line with the spinal tap to analyse the lactate content which can be used as a marker of hypoxia in the spinal cord (application 5). Currently there are no analytical means of establishing the level of oxygenation in real time of the spinal cord. The development of a novel analytical procedure such as this would substantially reduce the risk of paraplegia occurrence. Synthetic cerebrospinal fluid was analysed to assess the lactate concentration at physiological ranges. The results indicate the experimental procedure is capable of detecting abnormal levels of lactate associated with hypoxia.

1.2. Research objectives

The aim of the research will be fulfilled by the research objectives:-

- Investigate current dielectric spectroscopy techniques used to differentiate organic and biological material.
- Design and evaluate the suitability of dielectric spectroscopy sensor configurations using computational simulation.
- Implement and evaluate the proposed analysis methodology of using resonant dielectric sensors to assess the characteristics of biological samples.
- Incorporate the dielectric spectroscopy sensor into a fluidic device (omitting applications 2 and 3) that allows online sensing of the intended analyte.
- Programme an interface to control parameters of the experimental equipment and subsequently acquire and analyse the resulting data.
- Documentation and statistical analysis of experimental results.

The novelty of the work will originate from the conformation of microwave dielectric spectroscopic sensors and their application in differentiating biological cells based upon neutral lipid content, the differentiation of vegetable oils extracted from different sources, the non-invasive detection of lactate levels in bovine blood, the quantification of pseudomonas in drinking water and the detection of abnormal concentrations of lactate in cerebrospinal fluid.

The research resulted in a number of journal, book chapter and conference publications as detailed in the appendix (Appendix 1. Publications resulting from the research).

1.3. Chapter overview

1.3.1. Chapter 2 - Dielectric relaxation and electromagnetic theory

The underlying theory and scope of the interaction of biological material and electromagnetic radiation in the microwave frequency range is discussed. The relevance of dielectric dispersions and how this is related to the chemical composition and structure of biological samples is also discussed. Different techniques and methodologies of established dielectric spectroscopy and their applicability are also explored.

1.3.2. Chapter 3 - Literature review

The requirement and background of sample analysis is outlined with the current methods of analysis. This chapter is divided into five distinct sections which individually assess the need for analysis and the problem it is detecting or quantifying. Strengths and deficiencies of current analytical methods are detailed followed by current research activities for the stated analytical purpose. A review of the literature related to the dielectric characteristics of the sample is also conducted.

1.3.3. Chapter 4 - Equipment and software

This chapter details the equipment used in the research as to avoid repetition. Methods for sensor simulation and fabrication techniques are included along with details pertaining to the signal generation and analysis equipment (vector network analyser). The customised software used to interact with the VNA is also detailed with the software used to conduct statistical analysis of the data.

1.3.4. Chapter 5 - Coplanar sensor development

This chapter documents the sensor development process in detail. Initially a simple patch antenna was designed that was improved so as to increase the electrical length of the sensor concurrently reducing the resonant frequency of the sensor while retaining the sensor dimensions. The sensor was validated using neutral lipid positive and negative cell cultures at a number of concentrations to determine which sensor was most sensitive to the analyte. This was verified using statistical analysis between the lipid positive and lipid negative samples.

1.3.5. Chapter 6 - Experimental Results

Chapter six is divided into sections that contain the experimental results relating to each application. Section one of chapter six details the results of experiments utilised to develop and verify the application of dielectric sensors to the quantification of neutral lipids within cells. Initially samples were analysed using a resonant cavity and the small perturbation technique. A number of developments to the coplanar sensor were then carried out to incorporate the sensor into a fluidic device which was characterised over time and temperature. The finalised experimental methodology was then used to assess the neutral lipid composition of cells. Section two of the chapter details the use of a resonant cavity and the small perturbation technique to assess the dielectric characteristics of different vegetable oils. An interdigitated capacitive coplanar sensor was then used to verify the quality of vegetable and olive oils. Section three demonstrates the applicability of dielectric coplanar sensors to non-invasively quantify the lactate composition of bovine blood in a major bovine blood vessel through a layer of epidermis and hair. This was done by pumping bovine blood containing physiological concentrations of lactate through a fabricated model of a cow blood vessel. This may be used as a marker pertaining to the overall health of the cow. Section four details the use of the fluidic cell to determine the concentration of *Pseudomonas* bacteria found in ill managed water storage systems. Section five presents the results of using the fluidic apparatus to determine the lactate concentration of cerebrospinal fluid which is exuded during cranial surgery and may be used as a marker to detect hypoxia of the brain during the procedure.

1.3.6. Chapter 7 - Conclusions and future work

Chapter seven summarises the results of the project. This chapter also explores the future potential of the work and possible developments to complement what has already been accomplished.

Chapter 2. Dielectric relaxation and electromagnetic theory

The electromagnetic (EM) spectrum has a frequency range from 0 to 10^{23} Hz. This starts at DC, a non-oscillating current and voltage; and goes through the radio, microwave, THz, infra-red, visible light, ultra-violet, X-ray and gamma frequencies. The differing characteristics of electromagnetism are due to how waves behave at different frequencies and how materials act in different ways to waves of different frequency. Consider a comparison between the properties of a conductive metal and borosilicate glass at low radio frequencies, visible light and X-ray. A metal will transmit low radio frequencies while reflecting and absorbing frequencies of visible light and X-rays. Conversely, glass will insulate low radio frequencies, while mostly transmitting visible light and X-rays. It is these differing properties of materials at differing frequencies that forms the fundamental of the sensor principle.

This vast difference in the behaviour of electromagnetism at differing frequencies has led to a number of methods being developed to analyse and quantify these properties at different frequencies. However, these methods are interlinked based upon time, power and wavelength. For any given frequency (time) of an oscillating field there is a wavelength (length), and energy level (power).

Amplitude refers to the magnitude of the wave and which can be voltage or current. At any specific point the amplitude is equal to the maximum amplitude multiplied by the sine of the corresponding angle. Therefore, at 0° and 180° , the amplitude is zero. At 90° and 270° the amplitude is at maxima and minima respectively. Frequency is the number of cycles; that is a full waveform per second. The units are Hertz (Hz) named after the German physicist Heinrich Hertz who empirically expanded Maxwell's equations.

The speed of light in a vacuum (299,792,458 m/s) is used as a standard from which length and time can be derived.

$$\lambda = \frac{c}{f} \quad \text{Equation 2.1}$$

where λ is wavelength of one full cycle, f is the frequency of cycles in one second and c is the speed of light [7]. Therefore, the time of one cycle is inversely proportional to frequency and proportional to wavelength. However, it is important to remember that the speed of light changes depending on the media through which it is propagating. Therefore, when reasoning theory it may be more suitable to represent a cycle time as degrees or 2π instead of a fixed frequency.

Energy is introduced based upon frequency and Planck's constant resulting in the minimum value of energy that can be transferred at this frequency.

$$E = h \times f \quad \text{Equation 2.2}$$

where, E is photon energy and h is Planck's constant (4.135667×10^{-15} electron Volts) [7]. Planck's constant specifies the amount of energy each waveform is capable of delivering as a function of frequency. The energy at a fixed point will be proportional to the frequency of the waveform propagating through that point. As frequency is inversely proportional to wavelength, increasing frequency will decrease wavelength resulting in more waveforms passing through the fixed point; increasing the energy density. At frequencies above approximately 3 PHz (UV) the energy is sufficient enough to liberate an electron from atoms and overcome covalent bonds to create ions leading to the term ionising radiation. At frequencies below 3 PHz the energy is insufficient to break bonds leading to the term non-ionising radiation. However, non-ionising radiation carries enough energy to attract and repulse ions, rotate molecules and excite electrons into higher energy states. Figure 2.1 shows the electromagnetic spectrum, associated frequencies and applications in the radio frequency and microwave frequency ranges.



Figure 2.1. The electromagnetic spectrum. Increasing frequency corresponding to an increase in energy potential [8].

However, electromagnetism consists of an electric component and a magnetic component each with separate but interrelated phenomena. Electric fields result from the magnitude of a charge while magnetic fields are generated by the movement of charge.

2.1. Standing waves, resonance and radiation

Calculating electromagnetic fields requires the use of lengthy computational simulations derived using software, such as High Frequency Simulation Software (HFSS, Ansys, USA), which has only become readily accessible in recent decades [9-13].

At frequencies where wavelength becomes a significant factor in the propagation of the wave in the circuit, the phase and subsequent reactance must be considered. The electrical length (EL) of a circuit is the physical length of a material as a function of wavelength as seen below (Equation 2.3) [14-16]. However, this equation is only applicable in a vacuum.

$$EL = \frac{L}{\lambda} \quad \text{Equation 2.3}$$

Generally, if electrical length is less than 0.05 it may be considered electrically short. Below this frequency, simple circuit theory is applicable but above this frequency where circuits are considered electrically long, an understanding of RF techniques and electromagnetic radiation is required. Basic circuit theory is not applicable due to waveforms reflecting at boundaries or irregularities of the transmission line causing standing waves inducing resonance [17-19]. At higher frequencies circuit component contain parasitic inductance and capacitance sometimes causing significant drops in voltage as a result of spurious radiation [20]. However, in the case of antennas these characteristics are precisely those that are required. Electrically long circuits result in antennas and the generation of electromagnetic radiation.

Radiation is the emission of energy in a wave form and is associated with an oscillating electrical and magnetic field that sustain each other and support propagation. Moving electrical currents produce an electric (**E**) and magnetic (**H**) field that oscillate perpendicular to the direction of wave propagation (transverse) and at right angles to each other (orthogonal) illustrated in Figure 2.2 [21].



*Figure 2.2. Electric field (**E**) and magnetic field (**B**) [21]*

Electromagnetic radiation increases the resistance of the transmission line. However, instead of the energy being converted into heat which is the case in ohmic resistance, energy is converted into electromagnetic radiation. Radiation from an AC source radiates energy in two characteristic spatial regimes, near-field and far field. Near field radiation, also known as the reactive field and storage field occurs in close proximity to the source. In the near field, absorption of the radiation may feedback affecting the impedance of the sensor. This is in contrast to far field radiation that cannot feedback and effect the impedance of the sensor.

Measurement of the near field radiation is inherently difficult as any instrument inserted into the field interacts with the source changing the resultant field. Near field radius may be calculated using the formula below.

$$R = \frac{A}{2\lambda} \quad \text{Equation 2.4}$$

where R is the radius of the field and A is the area of the antenna [7].

The sensors used in this study are designed to operate in the microwave region which comprises wavelengths 1 mm to 1 m corresponding to frequencies 300 MHz to 300 GHz [22-24]. At these frequencies high frequency theory may be used in addition to conventional circuit theory. Instead of lumped impedance and reactance being used to describe circuits, reflected and transmitted power become more applicable as elements appear to be distributed [25]. Reflected and transmitted power are presented as scattering parameters (s-parameters) plotted in the frequency domain or on a specialised polar plot called a smith chart which plots complex impedance. In a linear two port system port 1 reflection, port 2 reflection and port 1 to 2 transmission would be represented as S_{11} , S_{22} and S_{21} respectively (Figure 2.3.).

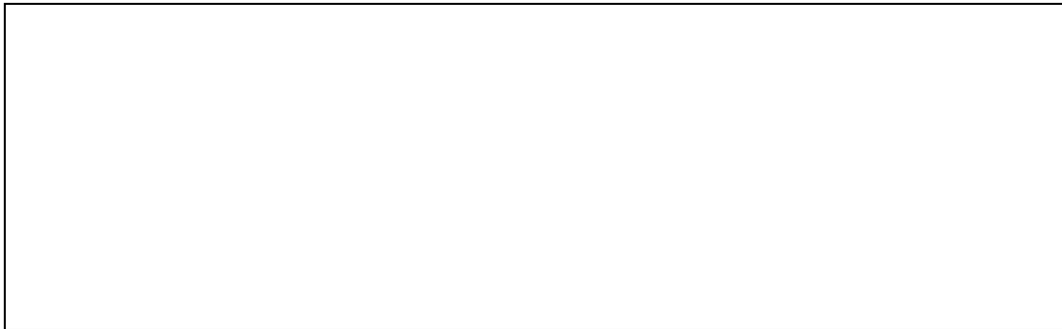


Figure 2.3. A model linear two port system [25].

A smith chart is a polar plot designed to aid in the impedance matching of transmission lines [26]. Smith charts are most commonly used to display the complex impedance of a transmission line plotted on the complex coefficient plane.

2.2. Dielectric theory

A material that can be polarised by an applied electric field is known as a dielectric. An external electric field applied to a material causes an amount of the electrical energy to be stored through an interaction with the molecular and structural properties of the material. The electric field subjects charged particles to a net electric force displacing them from average random orientation. Removing the external electric field allows the charged particles to return to their random orientation, in turn

releasing a charge. The ability of the material to store energy in this way is described as the permittivity (ϵ), usually expressed as a product of the permittivity of free space (ϵ_0) [27].

The permittivity of a material derives from its chemical state and structure; molecular composition and formation; and atomic valance. The permittivity is a measure of various polarisation phenomena that occur at different frequency ranges of oscillating electric fields. Dipolar polarisation is induced in molecules with an inherent dipole moment (orientation polarisation) [28]. An external electric field causes such molecules to rotate over a time period proportional to dipole moment and local viscosity. Dipole moment describes the separation of positive and negative charges on a molecule yielding the overall polarity. For example water has a dipole moment of 1.85 Debye length arising from the angle and valance of the covalent bond formed between oxygen and two hydrogen atoms [29]. This is in contrast to carbon dioxide which has a dipole moment of 0 D due to the molecule being centro-symmetric [30].



Figure 2.4. Net dipole moment of water and carbon dioxide.

Because there is a lag between the dipolar polarisation and the applied oscillating field, dispersions exist whereby the molecule does not have sufficient time to fully align to the oscillating electric field at higher frequencies. This process is known as dielectric relaxation and occurs in the microwave region of the electromagnetic spectrum. Oscillating electric fields exceeding this frequency no longer polarise the molecular polarity of the material.

Dielectric relaxation is often represented as permittivity as a function of frequency. A number of mathematical models have been developed by Debye, Cole and Cole [31], Cole and Davidson [32, 33]; and Havriliak and Negami [34] to explain relaxation phenomena of different materials. The simplest form of relaxation is described by Debye's equation (Equation 2.5) [35].

$$\varepsilon^* = \varepsilon_h + \frac{\Delta\varepsilon}{1 + j\omega\tau} \quad \text{Equation 2.5}$$

Debye relaxation is a dielectric response of an ideal, non-interacting population of dipoles when exposed to an alternating external electric field [35]. This model was introduced by the Dutch born physicist Peter Debye.

However, Debye relaxation does not explain all relaxation phenomena and as a result has been modified to suit a number of materials in different states. These include Cole-Cole, Cole-Davidson and Havriliak-Negami relaxation which will be described below.

Debye's original equation was improved by K.S. Cole and R.H. Cole by introducing an empirical parameter $0 < \alpha < 1$ (Equation 2.6). When $\alpha = 0$ the equation reduces to the Debye equation.

$$\varepsilon^* = \varepsilon_h + \frac{\Delta\varepsilon}{1 + (j\omega\tau)^{1-\alpha}} \quad \text{Equation 2.6}$$

The Cole-Cole equation above is valid for materials that exhibit a uniform, symmetrical distribution of relaxation times. However many relaxation phenomena have been discovered to not be symmetrical such as synthetic polymers. Cole and Davidson accounted for this non-uniform distribution by introducing an asymmetry parameter $0 < \beta < 1$ (Equation 2.7). Again when $\beta = 0$ the equation reverts to the Debye equation.

$$\varepsilon^* = \varepsilon_h + \frac{\Delta\varepsilon}{1 + (j\omega\tau)^\beta} \quad \text{Equation 2.7}$$

The next development of the equation came from Havriliak and Negami. They proposed combining the Cole-Cole and Cole-Davidson equation (Equation 2.8). Therefore in this equation when $\alpha = 0$ the formula reverts to the Cole-Davidson equation. Equally when $\beta = 0$ the equation reverts to the Cole-Cole equation.

$$\varepsilon^* = \varepsilon_h + \frac{\Delta\varepsilon}{1 + (j\omega\tau)^{(1-\alpha)\beta}} \quad \text{Equation 2.8}$$

The complex plane plots as calculated from the formulas above demonstrate the effect of the different parameters



Figure 2.5. Complex plane plots of Debye (a), Cole-Cole (b), Davidson-Cole (c) and Havriliak-Negami (d) relaxation types as calculated from the equations above [35].

Generally, the permittivity of a material decreases as a function of frequency but plateaus in a series of stages known as dispersions (Figure 2.6). Each step reflects the relaxation of different polarisation phenomena.

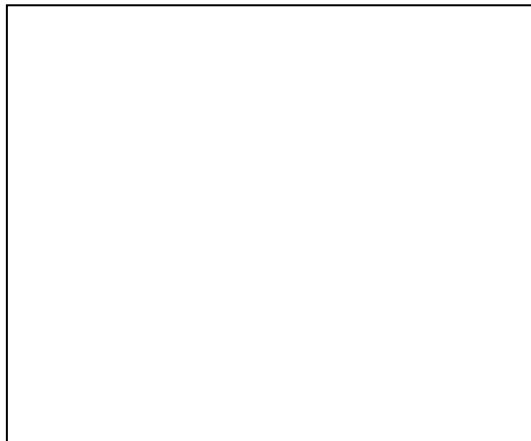


Figure 2.6. Idealised dispersions of real permittivity associated with biological material [36].

Dielectric spectroscopy quantifies permittivity of the material in the complex form. The complex permittivity is composed of the real and imaginary permittivity represented by the equation

$$\boldsymbol{\epsilon}^*(\omega) = \epsilon_r + \frac{\boldsymbol{\sigma}^*}{j\omega} \quad \text{Equation 2.9}$$

where $\boldsymbol{\epsilon}^*$ is the complex permittivity, ω is the angular frequency ($\omega = 2\pi f$), $\boldsymbol{\sigma}^*$ the conductivity and j represents the imaginary unit ($j = \sqrt{-1}$). Conductivity is sometimes represented as κ . The real and imaginary parts of the complex permittivity relate to the energy stored and lost respectively. In an ideal relaxation process, ϵ' will decrease as ϵ'' peaks. This phenomenon can be seen in Figure 2.7 [35].

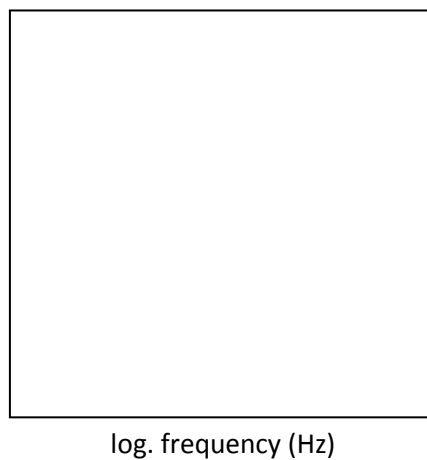


Figure 2.7 a. Real permittivity and conductivity plotted against log. frequency. b. Imaginary permittivity plotted against log. frequency.

The permittivity a material is more commonly quantified as the relative permittivity whereby the permittivity of the material is calculated relative to the permittivity of free space as below.

$$\epsilon_r^* = \frac{\boldsymbol{\epsilon}^*}{\epsilon_0} = \frac{\epsilon'(\omega) - j\epsilon''(\omega)}{\epsilon_0} = \epsilon'_r - j\epsilon''_r \quad \text{Equation 2.10}$$

Where ϵ_r^* is the relative permittivity, ϵ_0 is the permittivity of free space which is equal to $8.8541878 \times 10^{-12}$ F/m, ϵ'_r is the real part of the relative permittivity and ϵ''_r is the imaginary part of the relative permittivity.

2.3. Dielectric spectroscopy

Dielectric spectroscopy characterises the dielectric properties of a material under test (MUT) as a function of frequency. It is based upon the interaction of an externally applied electric field with the electric dipole relaxation moment of the MUT expressed in terms of real and imaginary permittivity. A wide variety of techniques have been developed that are based upon measuring the capacitance and conductance of the MUT as a function of frequency. The resulting dielectric spectra are interpreted to analyse and differentiate different MUT. The technique uses only a small amount of power in the microwave region (approx. 1 mW). It is therefore non-destructive and non-ionising.

One method utilises a rectangular waveguide with the MUT inserted into the enclosed space. The waveguide is connected to the reflection and transmission ports of a VNA (Figure 2.8). The VNA generates a frequency sweep which passes to the antenna present in the waveguide. This converts the electrical signal into a propagating electromagnetic wave. Some of the wave reflects back to the source while the remainder transmits through the MUT and waveguide. When the material dependent cut-off frequency is reached, the wave will propagate through the MUT where it is detected by the second antenna and is returned to the VNA through its transmission port. The VNA displays the amount of the signal which is reflected as S_{11} parameters and transmitted as S_{21} parameters which can be interpreted to calculate permittivity. The dielectric constant, dielectric loss and loss tangent of a MUT can be calculated using the following equations [11].

$$\epsilon' = \frac{V_c (f_c - f_s)}{2V_s f_s} + 1 \quad \text{Equation 2.11}$$

$$\epsilon'' = \frac{V_c}{4V_s} \left(\frac{1}{Q_s} - \frac{1}{Q_c} \right) \quad \text{Equation 2.12}$$

$$\tan \delta = \frac{\epsilon''}{\epsilon'} \quad \text{Equation 2.13}$$

where ϵ' and ϵ'' are the dielectric constant and dielectric loss respectively, f_c and f_s are the resonant frequencies of the empty cavity and loaded cavity respectively, V_s and V_c are the volumes of the sample and cavity respectively and Q_c and Q_s are the quality factors of the empty cavity and the loaded cavity respectively. Although this method is relatively straightforward, it also has limitations. When materials with high losses are being measured, it can become difficult to correctly assess the cut off frequency of the waveguide due to so much of the signal being attenuated. Also, the assessment of permittivity is limited to the physical dimensions of the waveguide and therefore limited to a number of frequencies.



Figure 2.8. Experimental setup of a rectangular waveguide and VNA.

Another method used for measuring the electrical permittivity of a material is utilisation of an open ended coaxial cable or probe. The probe consists of an inner conductor and an outer conductor separated by a dielectric (Figure 2.9).

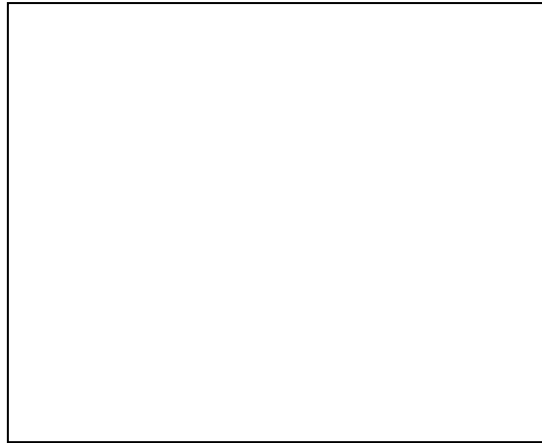


Figure 2.9. Schematic of a coaxial probe.

The dielectric is usually constructed of a stable material such as borosilicate glass so as to avoid damage when measuring the dielectric characteristics of caustic or high temperature substances. When a signal is passed down the probe, an electric field is generated between the inner and outer conductor which propagates to the terminus. Inserting the MUT into the electric field changes the reflection coefficient of the signal from which the dielectric characteristics can be calculated using the equation below.

$$Y_L(\omega, \varepsilon) = Y_0 \frac{1 - \Gamma(\omega, \varepsilon)}{1 + \Gamma(\omega, \varepsilon)} \quad \text{Equation 2.14}$$

where Y_0 is the characteristic admittance of the probe and Γ is the reflection coefficient. Permittivity may then be calculated from the equation

$$Y_L(\omega, \varepsilon) = j\omega C_1 + i\omega C_0\varepsilon + jA\omega^3\varepsilon^2 + B\omega^4\varepsilon^{2.5} \quad \text{Equation 2.15}$$

using a computational iterative procedure. It is important that the MUT is in full contact with the end of the probe so as no air gaps are present when a measurement is being performed. A number of commercially available kits are available to standardise this process such as the Agilent Dielectric Probe Kit (Agilent Technologies, USA) (Figure 2.10) [37-40].

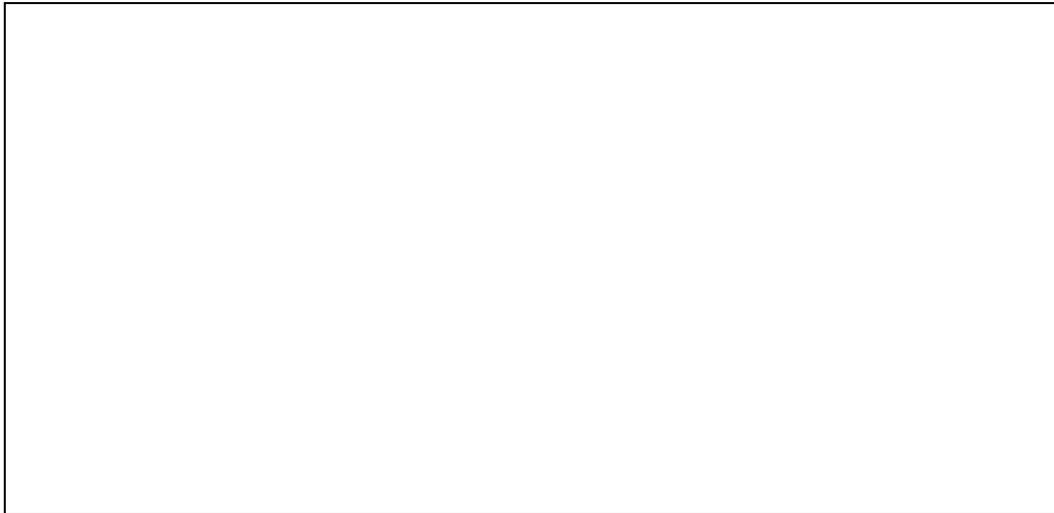


Figure 2.10. Agilent High Temperature Dielectric Probe.

Although less standardised than waveguides and probes, resonant sensors present an attractive method for measuring a material's dielectric characteristics. A resonant sensor is an antenna like structure whose impedance changes as the permittivity of the MUT changes. Some simple structures have mathematical models which determine the permittivity of an MUT at the resonant frequency. However, some resonant structures are too complex for a mathematical model to be formulated to calculate the permittivity of the MUT from the response of the resonant structure. In these cases, it is possible to estimate the permittivity from the sensor response using a calibration curve either utilising simulation software to identify a response which is associated with the permittivity of the MUT or similarly, use samples with known dielectric characteristics to compile the calibration curve. Although many configurations of resonant structures exist, a simple example of a resonant structure is a coplanar ring antenna. As the permittivity of the MUT increases, the resonant frequency of the ring decreases. With this simple configuration of sensor it is relatively simple to calculate the MUT permittivity from the response of the sensor using the formula below.

$$f = \frac{c}{2\pi r \sqrt{\epsilon_{eff}}} \quad \text{Equation 2.16}$$

where c is the speed of light, ϵ_{eff} is the effective permittivity, r is the ring's outer radius and f is the resonant frequency of the structure. However, using this technique the permittivity is only able to be

calculated at the primary resonant mode. The methods above only represent some of the available dielectric sensors. All have advantages and disadvantages such as stability, ease of design and physical size.

The microwave dielectric sensors developed in this research are electrically resonant. Resonant structures are very efficient at detecting tiny biological interactions [41, 42]. This is due to the inherent high quality factor yielding high resolution measurements [43].

2.4. Chapter 2 Summary

The underlying theory and scope of the interaction of biological material and electromagnetic radiation in the microwave frequency range is discussed. The relevance of dielectric dispersions and how this is related to the chemical composition and structure of biological samples is also discussed.

Chapter 3. Literature review

Sensors are devices that can measure a physical quantity and convert it into a form that can be interpreted by an observer or an instrument. This measurand may be converted into another physical property or into a signal that relates to the measured parameter. Sensors come in an enormous variety of forms. They appear in all manners and areas of life such as nature, domestic life, industrial applications and scientific research. Consider the eye which has evolved to gather electromagnetic radiation in the visible spectrum and convert it into an electrochemical signal in a nerve axon that directly relates to different frequencies of light. However, interpretations of brightness, temperature and humidity, for example, are subjective and can differ between individuals and so more precise methods of measuring were needed. Early sensing methods relied upon a physical change in a material relative to that of the property being measured were read out on an analogue scale. One example of this is the thermometer. Early methods in ancient Greece and later developed by Galileo Galilei linked the volume of air in an enclosed space acting upon a container of water to temperature [44]. This was improved into a device that linked the volume of mercury in an enclosed tube. One important development of sensors was the understanding that a scale linked to a standard was needed to compare independent measurements [45]. Two of the earliest temperature scales are Celsius and Fahrenheit which use the triple point of water and the freezing point of brine respectively as a standard on which to base the scale [46]. This allowed thermometer manufacturers and users to standardise temperature measurement allowing reproducibility, repeatability and standardisation to scientific and industrial processes worldwide; ultimately contributing to the progress of the industrial revolution.

There is also need for criteria by which sensors are described and judged. These are made up of an array of calculated characteristics that relate to the performance of the sensor. This allows different sensors to be compared against each other, quantifying the suitability of the sensor when measuring the intended measurand [47]. These criteria include:-

- Sensitivity – is a measurement of how the sensor response changes as a result of how much the measured quantity changes.
- Dynamic range - the maximum amount of analyte detectable minus the minimum amount of analyte detectable.
- Precision - the ability of the sensor to reproduce the output value when the analyte is unchanged.
- Resolution - the smallest change in analyte that causes a detectable change in output.
- Accuracy - the greatest difference between the actual value and the measured value in relation to a known reference standard.
- Linearity - measured as non-linearity is the deviation of the output response of the sensor across the range of measurable analyte concentrations. This deviation may change across the measurable range and can be quantified as a percentage of non-linearity.

As the research addresses multiple sensing applications the project will incorporate research, methodologies and principles from a range of scientific disciplines including food science, pathological biochemistry, microbiology, electrical engineering and theoretical physics.

3.1. Quantification of neutral lipids in biological cells

Lipid is a term that encompasses an array of hydrophobic or amphiphilic molecules that include sterols, glyceride based molecules, fatty acids, waxes and vitamins [48]. However as glycerol based molecules are of primary interest to this work, lipids will be used to define triacylglycerols and their derivatives. The main biological functions of lipids are biological membranes, energy storage and signalling. Triacylglycerols are formed from a glycerol back bone ester bound to three fatty acids (Figure 3.1) while diacylglycerides have two fatty acid chains. Phospholipids incorporate a phosphate group and a simple organic molecule (Figure 3.1). Biological membranes are formed by the unique polarity of phospholipids while triacylglycerols are used for energy storage due to high energy value.

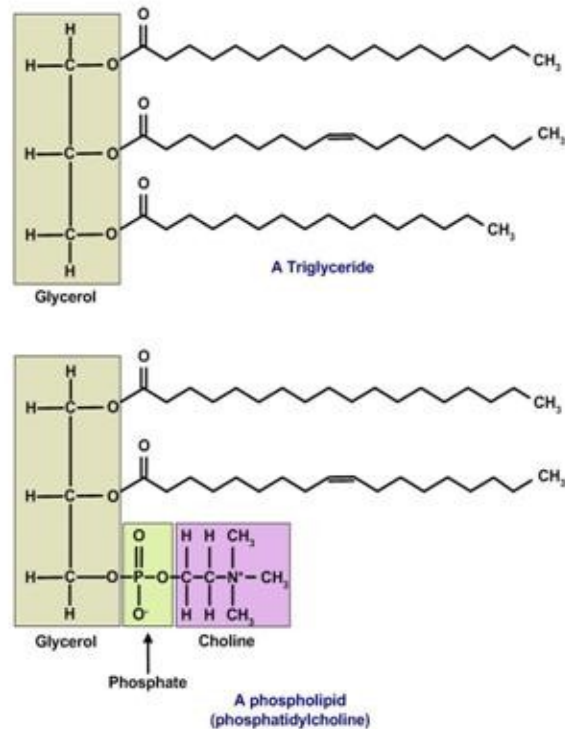


Figure 3.1. The chemical structure of triacylglycerol and phospholipids.

Neoplasia, translated as “new growth” from Greek, is defined as the abnormal proliferation of cells. Neoplasia often initiates as damage to DNA which can occur as a result of many different routes (e.g. radiation, chemical, thermal). This has the effect of changing the sequence, structure and quantity of proteins that are synthesised from the DNA. The result is a modified biochemical pathway which interacts in an abnormal way with its intended or indeed unintended target. However, due to the tight regulation of cell proliferation and apoptosis, it may take up to 50 separate gene mutations to result in neoplasia. Consequently, cellular developments that lead to uncontrolled cellular proliferation are extremely complex and vary for each individual occurrence.

DNA damage is considered to be the primary underlying cause of malignant neoplasms. DNA damage may arise naturally or through exposure to exogenous agents such as tobacco smoke, viral infections and UV radiation. This process may be compounded by deficient DNA repair genes which may be hereditary or damaged as above. When expression of DNA repair genes is diminished, damage accumulates in cells at an elevated rate than normal. This leads to an increase in cell

mutations which can affect potentially any signalling pathway altering cell phenotype, a number of which are shown in Figure 3.2.

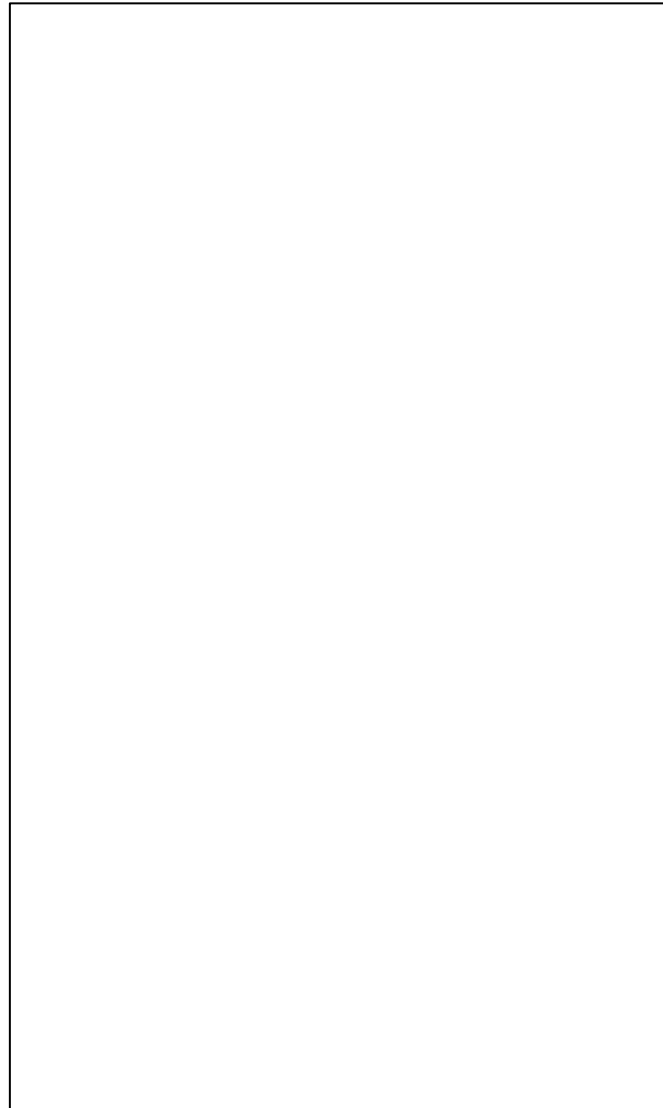


Figure 3.2. Molecular mechanisms of cancer.

Once enough DNA damage has occurred further mutations are also likely due to genome instability. These further mutations can include chromosome rearrangement, alteration of nucleic acid sequences and chromosome addition/deletion. Neoplasia may also result from epigenetic modifications. These are alterations to cell genome that do not involve DNA nucleotide resequencing such as deficient DNA transcription proteins.

Neoplasm usually initiates with a mutation that inactivates tumour suppressor genes or over activation of oncogenes. Tumour suppressor genes inhibit cell survival and proliferation. Conversely, oncogenes promote cell growth and proliferation (Figure 3.3).



Figure 3.3. Schematic of proliferative and apoptosis signal transduction pathways.

Notably, a protein called tumour protein 53 (p53) is crucial to the regulation of the cell cycle as a tumour suppressor and has even been called “the guardian of the genome” [49]. p53 has the ability to activate DNA repair proteins, suspend the cell cycle and initiate apoptosis should the damage be beyond repair. Should the p53 gene (*TP53*) be damaged, tumour suppression will be significantly diminished. Inheriting a dysfunctional *TP53* gene will likely result in the formation of neoplasia in early adulthood due to uncontrolled cell proliferation [50].

As genetic mutations accumulate the cells begin to behave in an abnormal manner having local and systematic effects. This is due to the competitive environment created by the uncontrolled proliferation of cells. As mutated cells compete for space and resources, any mutations that lead to a

competitive advantage over the other cells will become more prevalent as described in Darwinian evolution. This is called somatic evolution of cancer and leads to the development of “the hallmarks of cancer” [51]. These are:-

1. Self-generated growth signalling
2. Loss of sensitivity to anti-growth signalling
3. Inability to complete apoptosis
4. Limitless proliferation
5. Sustained angiogenesis, and
6. Tissue invasion and metastasis.

Localised symptoms arise due to the mass of the tumour and/or its ulceration. As the tumour enlarges it may put pressure on surrounding tissues and organs, disrupting normal function. Ulceration occurs when the tumour breaks through normal layers of tissue causing an open wound which may involve the production of blood and pus which can further disrupt normal function. The tumour may then go on to displacing normal functioning cells from which the tumour originated.

Systemic conditions originate either as abnormal signalling or metastasis. Abnormal signalling that has an effect that is not localised to the cancerous cells are called paraneoplastic syndromes. These are mediated by hormones or cytokines released by tumour cells or immune cells as a response to the tumour. The effects are extremely varied dependent upon the origin, site of gene mutation and level of metastasis. Hypercalcaemia is prevalent in lung, breast, renal and ovarian cancers due to the associated tumour excessively secreting parathyroid hormone-related protein (PTHrP) [52]. Polymyositis (inflammation of the muscle) occurs in non-Hodgkin lymphoma, lung and bladder cancers [53]. Polycythaemia (increased RBC blood volume proportion) develops in renal, cerebellar and hepatic cancers due to excessive production of the hormone erythropoietin [52].

Systematic effects also occur in the form of metastasis, the spread of cancer from one site to another (Figure 3.4). Metastasis develops in a number of consecutive stages which leads to a malignant phenotype. This allows cells to enter and exit the circulatory system, known as intravasation and extravasation respectively. This means that metastasis is marked by the presence of circulating tumour cells which provides a diagnostic marker for cancer staging. When malignant cells extravasate they continue proliferating causing a secondary tumour made up of the cell type from the origin. Metastatic tumours tend to seed particular organs of the body dependent on the origin due to the need for a location with similar characteristics. For example, colon cancer usually metastasises to liver while prostate has a tendency to metastasise to the bone. However, local lymph nodes are especially susceptible to secondary tumours.

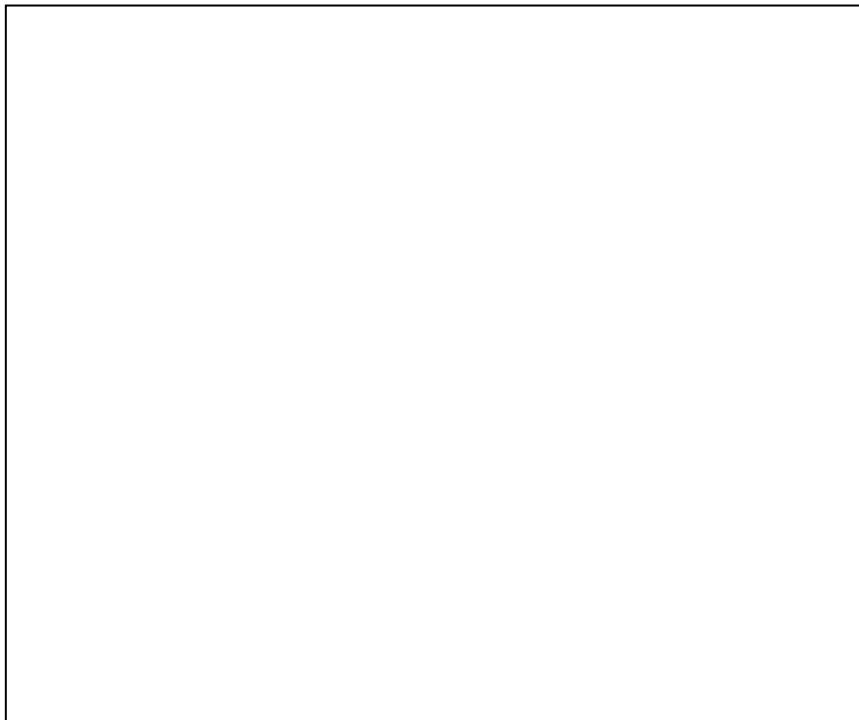


Figure 3.4. Stages of metastasis, Reduction of adhesion to neighbouring cells (a), migration of the cells through the stroma layer (b) and into the vessel (intravasation) (c). Metastatic cells may bind to vascular receptors (d) or bind to platelets (e) protecting them from the immune system. Metastatic cells then extravasate from the bloodstream (f) before adhering to cells in the secondary site (g) [54].

Metastasis is very common in the later stages of cancer development. Cancer staging is assessment method used to classify the phase and extent of cancer progression. The tumour, lymph node and metastasis (TNM) staging system is a widely used assessment method. It may be based upon the

pathologic or clinical information defined by a small “p” or “c” before the stage code. This method uses the following criteria to classify development into codes such as pT2N1M0 or cT4N2M1.

- T: mass and local invasion of the primary tumour
 - Tx – unable to evaluate tumour
 - Tis – tumour in situ
 - T0 – no signs of tumour
 - T1, T2, T3 and T4 – size and extension of primary tumour
- N: the extent of spread to local lymph nodes
 - Nx – unable to evaluate lymph nodes
 - N0 – no signs of tumour cells in lymph nodes
 - N1 – regional lymph node metastasis
 - N2 – tumour spread to some non-local lymph nodes
 - N3 – tumour spread to numerous and distant lymph nodes
- M: the presence of metastasis
 - M0 – no metastasis to distant sites observed
 - M1 – metastasis to distant organ beyond regional lymph nodes.

This method is used by medical professionals to plan treatment, indicate prognosis, evaluate treatment and to compare cancers from different individuals. The criteria and classification has varied over time and is subject to change as in light of recent discoveries. It is managed by the International union against cancer (UICC) and the American joint committee on cancer (AJCC) [55].

The incidence of malignant neoplasms or cancer has continued to rise for the past four decades and significantly contributes to population morbidity and mortality [56]. Neoplasms occur when cell proliferation exceeds cell apoptosis (naturally initiated cell death) which results in the formation of a tumour or increased blood cell volume depending on the origin of the cancerous cell [57]. Tumours can be difficult to identify in the early phase due to being asymptomatic with noticeable symptoms not arising until later development [58]. The earlier a neoplasm is identified the less invasive, simpler and cheaper treatments become resulting in increased patient comfort and prognosis [59-66]

Although the benefits of detecting neoplastic cells early are evident [64-70], current diagnostic processes can be expensive, invasive and may carry their own health risks. There are two main routes of cancer detection in the U.K. which comprise of health screening programmes (i.e. Breast, Cervical and Bowel) and referral by a health professional (e.g. General Practitioner, Dentist) [71].

Population screening has been extremely successful in lowering the incidence of late stage breast [72] and cervical [73] cancer but is restricted to detecting the specific type and site of cancer as well as requiring specialised facilities, laboratory, staff and transport.

Breast screening comprises of women aged between 50 and 70 years old being invited to attend appointments for a mammogram every three years. A mammogram utilises X-rays to detect the presence of cancer in the mammary tissue. However, some growths are not detected by this method, particularly those that are less than 1cm in diameter and those located in the upper outer quadrant. The patient is also exposed to ionising radiation every three years which research suggests may itself induce cancer [74].

Cervical screening entails women aged between 25 and 64 attending appointments every three years up to the age of 49 and every five years thereafter. The test used is called a cervical smear, otherwise known as a Pap test, where cells are collected from the endocervical canal and sent to clinical laboratories for histopathological assays. It is estimated that screening has reduced breast and cervical cancer mortality rates by 30-40% [72] and up to 80% [73] respectively .

Other than the established screening programmes, cancer detection can be an overdue procedure in that a patient will consult a GP about a condition that is already causing symptoms. The cancer may also be detected in the course of a patient being diagnosed or treated for an alternative clinical condition [71]. At this time the cancer may have progressed to a later stage cancer which in turn reduces quality of life and increased mortality for the patient, but also poses difficulties and added expense in treatment.

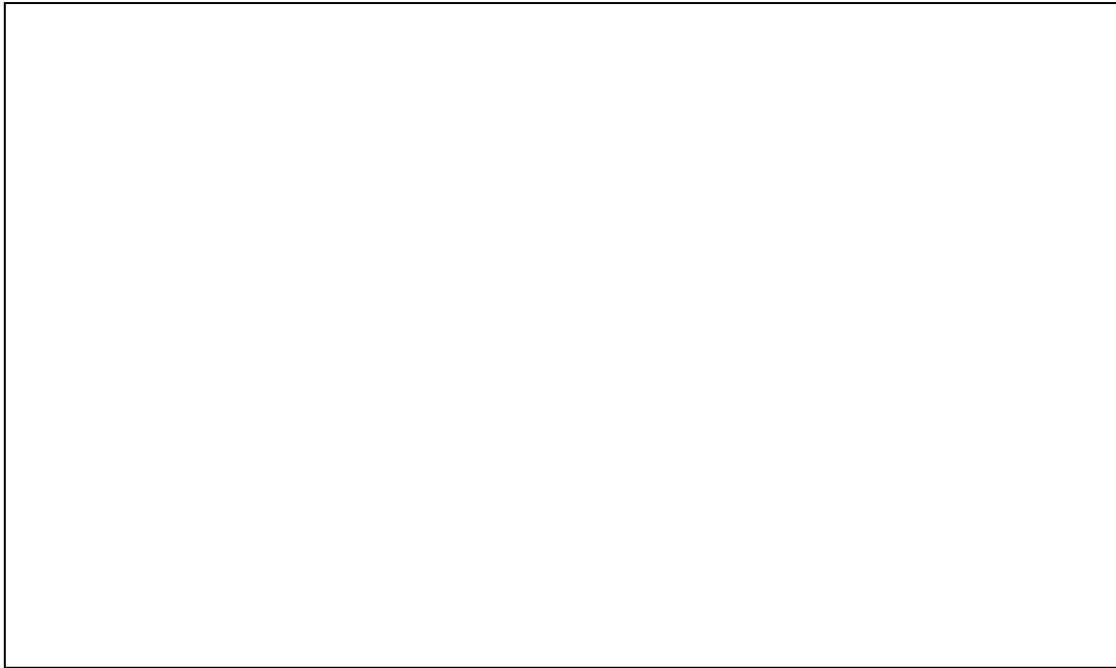


Figure 3.5. One year mortality rate (%) by detection route and age group. Breast cancer, England, 2007 [71].

This is demonstrated in Figure 3.5 which illustrates the one year survival rate of women diagnosed with breast cancer through a range of detection routes. As can be seen, the prognosis for breast cancer detected by screening is in stark contrast to those cancers diagnosed through emergency presentation. This is compounded by 23% of all cancers being detected through the emergency route, while only 3% are detected by screening programmes [71].

The proposed methodology will operate through the analysis of cellular lipid content, specifically neutral triacylglycerols stored within lipid droplets. Upregulated lipogenesis is a frequent phenotype of various neoplastic cells. Increased lipid droplet formation has been described in several types of cancer including but not exclusively cervical [75], brain [76], and colon [77]. Although some aspects of lipid droplet biogenesis and formation remain in question, upregulation and modification of lipogenic enzymes and signalling proteins have been associated with the accumulation of newly formed lipids and consequently lipid droplets [78, 79]. Proteins and pathways which have been thoroughly established as being involved in neoplastic development and progression localise in the membrane of lipid droplets indicating a role in intracellular signalling. Such signalling pathways include PI3K, ERK1, ERK2, p38, PKC and caveolin [80-82].

The current methods for assessing the lipid profile of a cell or sample are lengthy, require specialised facilities and are subject to calculation induced error caused by some lipids being bound to proteins. The assay consists of hydrolysing the fatty acids from the glycerol back bone employing lipase enzymes. The resulting glycerol is then quantified using colourimetric assays whereby an enzyme, usually glycerol kinase or glycerol triphosphate oxidase, reacts with the molecule producing hydrogen peroxide. This combined with a peroxidase results in a measurable colour change [83]. However, the drawbacks of this method are the inclusion of any free glycerol molecules already present in the blood and the patient having to fast for up to 12 hours before the test [84]. It is currently employed as a marker of cardiovascular risk and metabolic diseases. Low density lipids (LDLs) and very low density lipids (VLDLs) can be calculated as a result of this and other tests. This test is currently the “gold standard” used in laboratories around the world and therefore is the benchmark to which the product of this research will be compared.

Currently there are no point-of-care diagnostic assays that are commercially available to indicate neoplastic growth. This research proposes a novel diagnostic strategy that can detect a tumour in the body from any origin which will be detailed below.

The synthesis of neutral triacylglycerols can be formally divided into two phases. The first step involves the formation of diacylglycerols (Figure 3.6) while the second phase is an acylation reaction adding a fatty acid chain to DAG to form TAG (Figure 3.7).

Acetyl-CoA and its derivative acyl-CoA are important coenzyme involved in the metabolism of cells. It is produced by aerobic cellular respiration and is fed into the citric acid cycle [85-87]. However, when there is a surplus of energy acetyl-CoA and malonyl-CoA are used to produce fatty acids [88]. Therefore these molecules serve as the crossroads between glucose derived metabolism and lipogenic pathways, i.e. synthesising triacylglycerols from blood sugars.

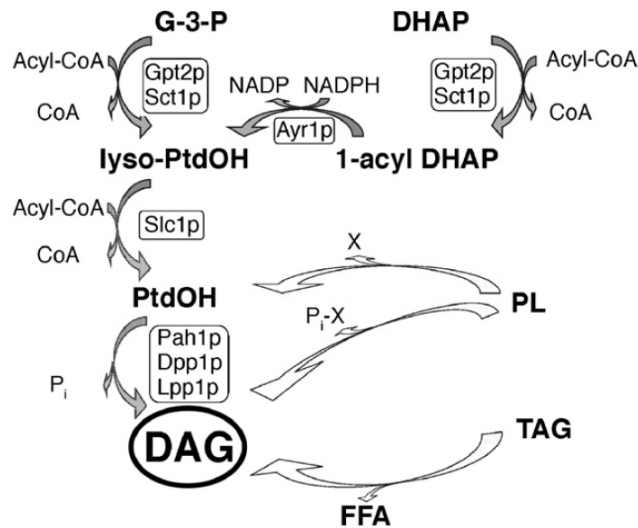


Figure 3.6. Pathways responsible for the formation of diacylglycerol. DAG: diacylglycerol; DHAP: dihydroxyacetone phosphate; FFA: free fatty acids; G3P: Glycerol-3-phosphate; lyso-PtdOH: lysophosphatidic acid; PL: phospholipid; X; alcohol molecule; Pi-X; alcohol phosphate [89, 90].

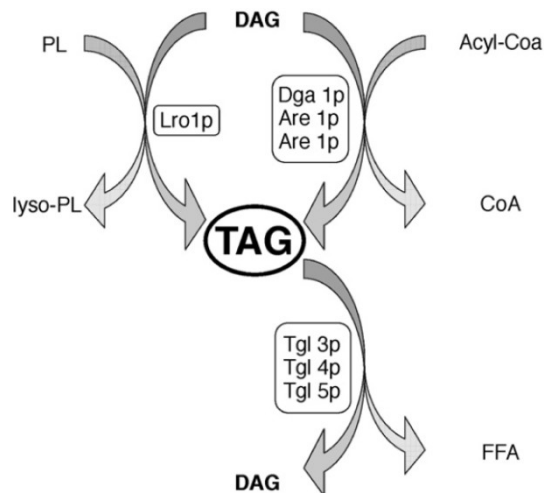


Figure 3.7. Synthesis and degradation of triacylglycerols. Diacylglycerol is acylated with either Acyl-CoA or a phospholipid yielding triacylglycerol. Degradation of TAG yields free fatty acids (FFA) and DAG.

Lipids contribute essential and varied functions in cells most obvious of which is energy storage and the principle constituent of cell membranes. It has been found that lipids play important roles in cell signalling. However, all of these roles are important to cells which undergo neoplastic transformation, progression and metastasis. Under normal circumstances, most cells store small amounts of TAGs in organelles called lipid droplets (lipid bodies, adiposomes). Lipid droplets are lipid rich cytoplasmic organelles formed by neutral triglyceride centre encapsulated by a monolayer of phospholipids (Figure 3.8) [91, 92]. Lipid droplets are the main organelle involved in neutral lipid storage in eukaryotic cells and although nearly absent in most non-adipocyte cells, increased volume

and numbers of lipid droplets are observed in cancer cells *in vitro* and *in vivo* [77]. Pathways that regulate lipid droplet formation and their interaction with tumour development are currently under close examination. It was once thought that lipid droplets were to do with storage and lipid trafficking, it is now well established that lipid droplets are highly regulated organelles involved in cell proliferation, metabolism and neoplastic processes.

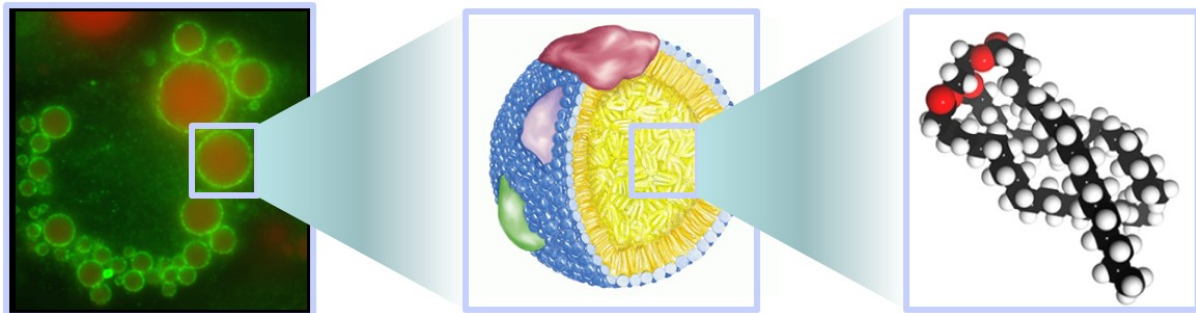


Figure 3.8. The structure and molecular composition of lipid droplets. Left, Fluorescent staining of a cell with triacylglycerols (red) and lipid droplet associated proteins (green). Centre, triacylglycerol core encapsulated by phospholipids monolayer and lipid droplet associated proteins. Right, triacylglycerol molecule.

The prevailing hypothesis of lipid droplet formation is that they are derived from the endoplasmic reticulum (ER) (Figure 3.9). The process involves accumulation of neutral lipids within the lipid bilayer membrane of the ER before budding off into the cytoplasm surrounded by a phospholipid monolayer derived from the ER membrane [92-94]. In this process the lipid droplets incorporate proteins from the ER that lack trans-membrane domains [95].

A number of well-regulated signalling pathways have been linked to lipid droplet formation in neoplastic cells. This is suggested by the induction of lipid droplets by *cis*-unsaturated but not triggered by saturated fatty acids indicative of formation involving more than incorporating exogenous lipids [96-98]. Moreover, stimulation with cytokines and hormones induces receptor mediated lipid droplet formation in the absence of exogenous lipids [99-103]. Inflammatory mediators such as platelet activating factor (PAF) acting via G-protein linked pathways are potent inducers of lipid formation [104, 105].



Figure 3.9. Budding model of lipid droplet formation [106]. Neutral lipid anabolic enzymes localise in the endoplasmic reticulum (ER) (A). TAGs and sterol esters accumulate between the phospholipid bilayer (B). This forms micro-droplets (C, D) which bud off when a critical mass is reached (E).

Due to cellular mutations and/or abnormal cell to cell signalling, the metabolism of the cell is altered resulting in TAGs being accumulated in lipid droplets [107-110]. Depending on the mutations that lead to neoplasm, a lipid droplet can constitute a significant sum of cell volume. Hence, the cell concentration of TAG is an excellent indicator or biomarker of cell metabolism and proliferative state. Lipid droplet accumulation also occurs in a range of cells that relate to specific conditions of infection, inflammation and metabolic diseases which increases the possible scope of the research in diagnostic applications [111].

Upregulated lipogenesis is a frequent phenotype of various neoplastic cells. Increased lipid droplet formation has been described in several types of cancer including but not exclusively cervical [75], brain [76], and colon [77]. Although some aspects of lipid droplet biogenesis and formation remain in question, upregulation and modification of lipogenic enzymes and signalling proteins have been associated with the accumulation of newly formed lipids and consequently lipid droplets [78, 79].

The specific function of lipid droplets in cancer is closely linked to the proliferation and metabolism of a cell. A number of signalling proteins have been found to collect within lipid droplets suggesting a clear role for this organelle as a site of intracellular signalling. Moreover, proteins and pathways which have been thoroughly established as being involved in neoplastic cell transformation, development, progression and metastasis localise in the membrane of lipid droplets indicating a role in intracellular signalling.

Such signalling pathways include PI3K, ERK1, ERK2, p38, PKC and caveolin [80-82, 112-114]. The MAP kinases ERK1, ERK2, and p38 are crucial enzymes in the activation of cPLA₂, the enzyme that exclusively hydrolyses arachidonic acid from glycerophospholipids. The close proximity of ERK1, ERK2 and cPLA₂ on lipid droplets may contribute to efficient phosphorylation in response to stimuli [115]. PI3K regulatory and catalytic subunits are also compartmentalised to lipid droplets in lymphoma cells and neutrophils [80]. Although more research is needed on the precise role of kinases present in lipid droplets, the available evidence indicate kinase mediated signalling on lipid droplets is active in neoplastic cells.

Lipid droplets have also been implicated as sites of ribosomal translation and protein synthesis involved in the regulation of neoplastic cells [116-118]. Ribosomes were found to be present within the neutral lipid core in human lymphoma, neutrophils and eosinophils [116]. Proteomic analysis of lipid droplets has also identified translation initiation factors in a hepatoma cell line [119].

Early insights into the role of lipid droplets in cell proliferation were provided by studies into yeast, suggestive of a direct link between cell cycle regulation and lipid droplet formation indicating cyclin-dependent phosphorylation of tgl4 mobilising lipid droplets to participate in membrane synthesis [120]. This research takes advantage of the lipid metabolism pathways of cancer cells and rapidly proliferating yeast cells being significantly comparable [121-124]. The six original hallmarks required for a normal cell to transform into a cancerous cell were discussed earlier in this section. In the latest revision of their work, the authors expanded the list of required modifications for cancer

development [125]. These are the ability to evade the immune system, chromosome abnormalities, inflammation and of significance to this research abnormal metabolic pathways.

In both yeast and mammalian cells glucose uptake is an important control step of glycolytic pathway [126]. In vivo, glucose is one of the main substrates consumed by tumours [127]. This is caused by the overexpression of glucose transporters within the lipid bilayer membrane. Accordingly, the genes coding for glucose transporters (GLUT1 and GLUT3) have been found to be overexpressed in tumour cells [128-130]. Yeast cells in their natural environment are subjected to fluctuations of glucose concentration. As a consequence they're glucose transporter expression profile must be highly adaptable in response to glucose availability [131]. In conditions of low availability only high affinity forms of glucose transporter are expressed, while low affinity forms are expressed as availability increases [132]. By controlling the glucose concentration in vitro, yeast cells can be manipulated to mimic tumour glycolytic pathways [133, 134]. Glycolysis provides the precursors for many pathways in yeast and tumour cells supporting proliferation including glycerol for triacylglyceride synthesis [135].

Pyruvate metabolism is a substrate in oxidative and fermentative pathways in eukaryotic cells. This intermediate can be reduced, oxidised, undergo carboxylation or decarboxylation. The inhibition of pyruvate oxidation in yeast cells may be used to explain glucose induced repression of oxidative metabolism [136] and model the Warburg effect in tumour cell [137].

The lipid content of cells can be used as a marker pertaining to cell and systematic pathology [111]. Accumulation of lipid droplets within specific cells of the body is repeatedly observed in non-adipocytic cells such as leukocytes (white blood cells), epithelial cells and hepatic cells in neoplastic (cancerous), infectious and inflammatory conditions.

A test apparatus that could rapidly quantify the lipid droplets in specific isolated cells and is cost effective might be used to reveal conditions that would previously have been missed by current

pathological examinations. In recent years, there has been a shifting priority toward early detection of neoplastic conditions through screening programs and public awareness of detectable signs and symptoms. There is a great deal of evidence which stresses the importance of early cancer detection or 'down-staging' in the eventual prognosis and survival rate of such conditions [58, 138-140]. In addition to the benefit to patient prognosis, the financial implications of early detection and treatment have also been found to be beneficial to the efficiency and cost of a nation's healthcare and healthcare insurance sectors [141-143].

The proposed system uses microwave dielectric spectroscopy at microwave frequencies to distinguish cells based upon the dielectric characteristics of cells which changes due to biochemical and structural variations which can be linked to specific cell phenotypes. The specific phenotype of interest in this research is that of lipogenic cells which has the effect of increasing cell size, lipid bilayer membrane surface area, neutral lipid concentration and lipogenic protein expression. These compositional and structural differences affect the amount of energy that can be temporarily stored, defined as capacitance, in the sample when a non-uniform electric field is applied.

This research project proposes a novel approach to differentiate biological cells based upon the total concentration of lipids held within organelles called lipid droplets. Lipid accumulation within cells is significant as it may serve as a marker pertaining to the metabolism and oncologic state of the cell and organism. This is accomplished through the use of sensors which emit electromagnetic radiation in the radio frequency and microwave frequency ranges. The electromagnetic fields interact with the biological cells yielding a measurable result. Experiments conducted so far have indicated that solutions of numerous different lipid suspensions at different concentrations can be differentiated based upon the dielectric characteristics of the sample. The research is currently progressing to miniaturise and incorporate the sensor into a test bed which allows cell samples in microtitre plates to be assessed. The capabilities of different sensors to differentiate cell samples can then be assessed and compared in a stable and repetitive method. Furthermore, a specific type of cell may

be isolated from samples using antibodies which are immobilised on the microtitre well internal surfaces. This progressively works towards the overall aim of producing a method that can isolate specific cells from blood samples which can then be assessed to serve as a detection tool for neoplasia. There is also scope for the technique in assessing numerous other cells that are associated with a disease state. Another aspect open to this research is a dielectric study of the specific cell types that are to be tested. This will aid in the design of the sensor, ensuring the frequencies the sensor is sensitive to is also selective to the cellular characteristic that is to be measured.

The aim of this research is to design, implement and incorporate a sensor capable of differentiating neoplastic and lipid accumulating cells from nominally functioning biological cells based upon the amount of lipid accumulated by biological cells. Lipid accumulation is significant in disease states as research has revealed some types of neoplasia to induce the expression of genes which increase the amount of lipids stored by cells [111, 144, 145]. This research proposes that lipid accumulation within cells may be used as a metabolic marker and therefore analytical tool for the detection of cancer. The methods used for detecting such characteristics are electromagnetic sensors within the microwave and radio frequencies range. This sensor will then be incorporated into a working methodology that may be easily tailored for point-of-care settings.

3.1.1. Considerations of detecting neoplastic growth using dielectric spectroscopy

Dielectric spectroscopy analysis of cellular material is dependent upon polarisation processes that occur across a frequency range of Hz up to the lower THz region (Figure 2.6). Biological cells exhibit a characteristic decrease in permittivity as a function of increasing frequency known as dispersions [36, 146-149], details of which are noted below.

- α dispersion is related to the adjacent flow of ions across the cell surface.
- β dispersion (also known as interfacial or Maxwell-Wagner interaction) is associated with the build-up of ions at the cell surface leading to polarisation across cell membranes.

- δ and γ dispersions are associated with molecular and sub-molecular rotations, predominantly bound and unbound water.

Dielectric spectroscopy techniques differentiate biological cells based upon dispersions occurring at shifted frequencies dependent on biological characteristics, such as cell morphology and composition. An increase in organelle size or numbers will result in increased membrane surface area, increasing the polarisable material susceptible to Maxwell-Wagner polarisation. In addition, compositional variations of ionic and water content of the cytoplasm will cause variation of relaxation frequencies. Many different dielectric spectroscopy techniques have been developed in an array of cancer diagnostic applications.

The appeal of dielectric spectroscopy as an analytical tool has resulted in a plethora of medical applications. The approach varies dependent on the site and type of cancer from characterising isolated individual cells to non-invasive *in-vivo* imaging techniques [150-152]. One of the most promising applications of dielectric spectroscopy the author has encountered presents a novel method for malignancy of the mamillary tissue or breast cancer [151]. The method generates 3D risk maps generated using a machine learning method. This approach uses a transmitter of 16 mm² located on the surface of the skin propagating a signal frequency of 6 GHz (Figure 3.10). A grid of 16 (4 x 4) receivers were arranged and located 3 mm above the skin which are used to gather the transmitted signal. Utilising a computational support vector machine classification technique a risk probability map is generated from the complex amplitude of the electric field intensity as demonstrated in Figure 3.11.

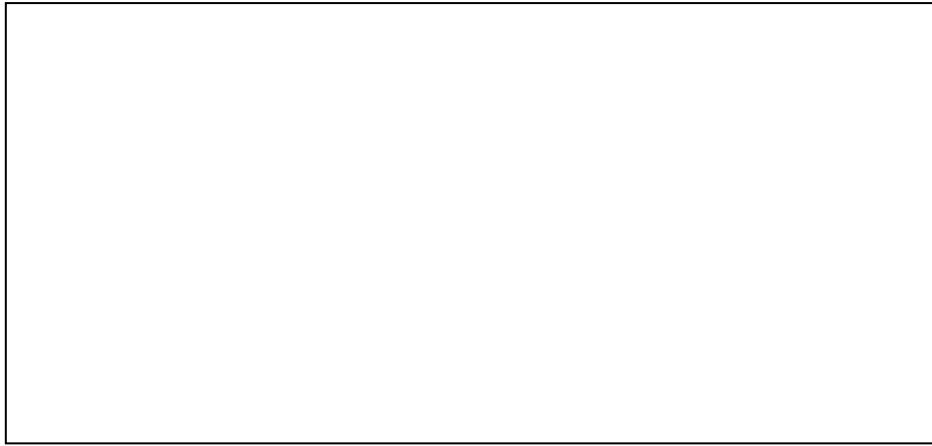


Figure 3.10. The configuration of a transmitter and receivers on the breast tissue. The patient is in the supine position [151].

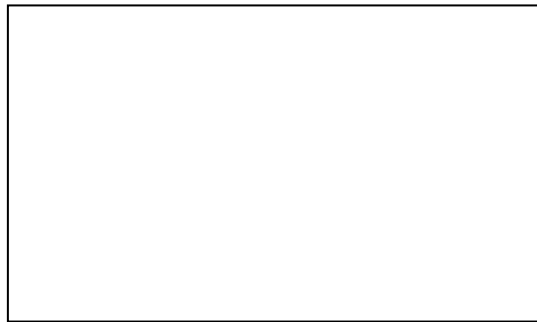


Figure 3.11. Risk probability maps generated using the SVM microwave approach. The actual tumour location is outlined with a white square [151].

Probability maps demonstrate that the region around the tumour location can be clearly differentiated from unaffected mammary tissue using this approach.

Techniques have been developed to detect, differentiate and determine the contents of cell samples based upon their electrical characteristics. Electric substrate impedance sensing (ESIC) is a method used to determine the phenotype of cells. In ESIC, cells adhere and spread across electrodes. This forms an insulating layer that inhibits the flow of current from the electrode to the suspending media. Confluent cell layers fully insulate the electrodes forcing the current to flow through the cells revealing information about the cell membrane and cytoplasm [2].

ECIS has been used to identify osteogenically differentiated mesenchymal stem cells in 2D and 3D cultures [153]. In the 2D cell culture methodology, stem cells are cultured directly upon electrodes

linked to an impedance analyser (Figure 3.12). The electrodes were pre treated with foetal bovine serum for 2 hours to improve cell adhesion. Cells were analysed between the frequency range 100 Hz to 1 MHz after 4 days of culturing.

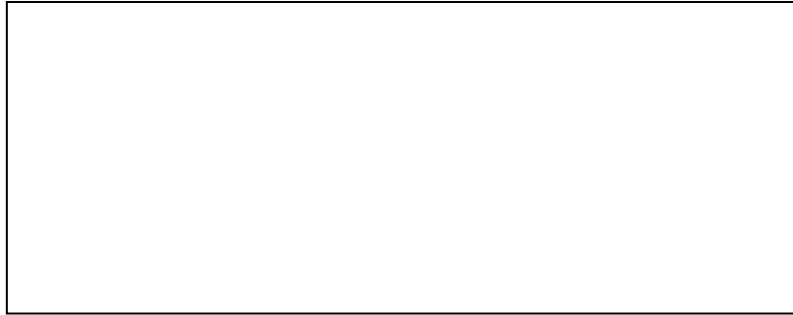


Figure 3.12. Experimental setup for monitoring 2D cell layers (A). Schematic drawing of direct electrode cell interaction (B) [153].

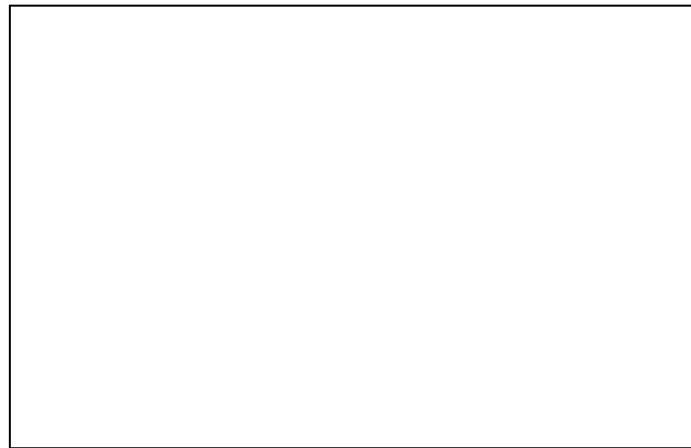


Figure 3.13. Resistance of differentiated (blues) and non-differentiated (red/orange) mesenchymal cells as a function of culture time. The differentiation to osteogenic cells is highlighted by the blue arrows [153].

The second approach formulated by Hildebrandt, C. et al involves analysing the cells in a 3D matrix contained within a fluidic cell as seen in Figure 3.14. The main part of this apparatus is a glass capillary tube (300 μm diameter) with integrated electrodes at each capillary end. 8 randomly selected cells for each condition (osteogenic, non-differentiating and necrotic) are precisely positioned within the capillary tube suspended in culture media using a cell tram pump. The electrodes are connected to an impedance analyser generating a signal in the frequency range from 100 Hz to 1 MHz.

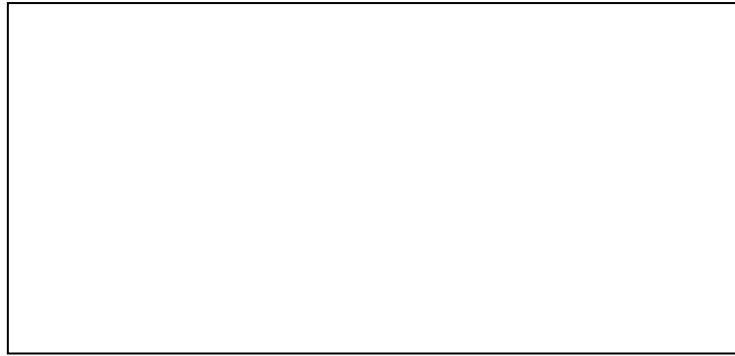


Figure 3.14. Capillary based microfluidic cell for impedance measurement with integrated electrodes (A). Schematic drawing of capillary measurement setup [153].

The impedance of osteogenic differentiated cells was significantly higher than that of non-differentiated and necrotic cells especially in the lower order frequencies. At frequencies around 100 kHz there is no significant difference between non-differentiated and necrotic cells (Figure 3.15).

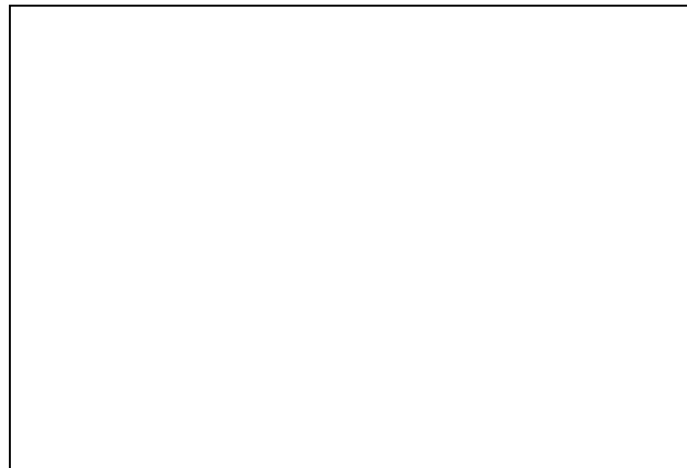


Figure 3.15. Impedance spectra of osteogenic stem cells (blue), non-differentiated cells (red) and necrotic cells (yellow) with standard deviation error bars [153].

This paper has shown that cells of different phenotype can be differentiated by their electrical characteristics. The experimental apparatus also demonstrates that dielectric spectroscopy is a suitable method for non-invasive continuous cell differentiation.

Ron, A. et al. utilised a Teflon substrate oblong parallel plate capacitor (15 x 10 mm) with a separation of 5mm which enclosed the cell samples [154]. A guard electrode charged with the same potential as the fed electrode was employed to cancel out the effects of stray capacitance between

the two measurement electrodes. Dielectric measurement between the electrodes was conducted using an impedance analyser over a frequency range of 100 Hz up to 100 MHz. This electrode arrangement was used to monitor the effect of cell membrane binding molecules lectin and SEC13 on MBA and MDCK cells. Cells were cultured in a Dulbecco's Modified Essential Media (DMEM) supplemented with serum and antibiotics at a temperature of 37 °C in 5 % CO₂.

Figure 3.16 show the dielectric spectra of MBA and MDCK cells treated with lectin and SEC13 respectively. SEC13 stimulates an increase in cytoplasmic protein while lectin binds to the surface of the cell membrane. This induces a change in the conductivity of the cell cytoplasm and the permittivity of the cell membrane respectively. This is evident in Figure 3.16 (a) where the dielectric constant for lectin treated cells is higher than that for non-treated cells which is concurrent with an increase in capacitance. Figure 3.16 (c) demonstrates a higher conductivity for cells treated with SEC13 than those which have not. Therefore this experiment has confirmed that both cell membrane permittivity and cytoplasmic constituents affect the dielectric characteristics of the sample which can be detected using dielectric spectroscopy.

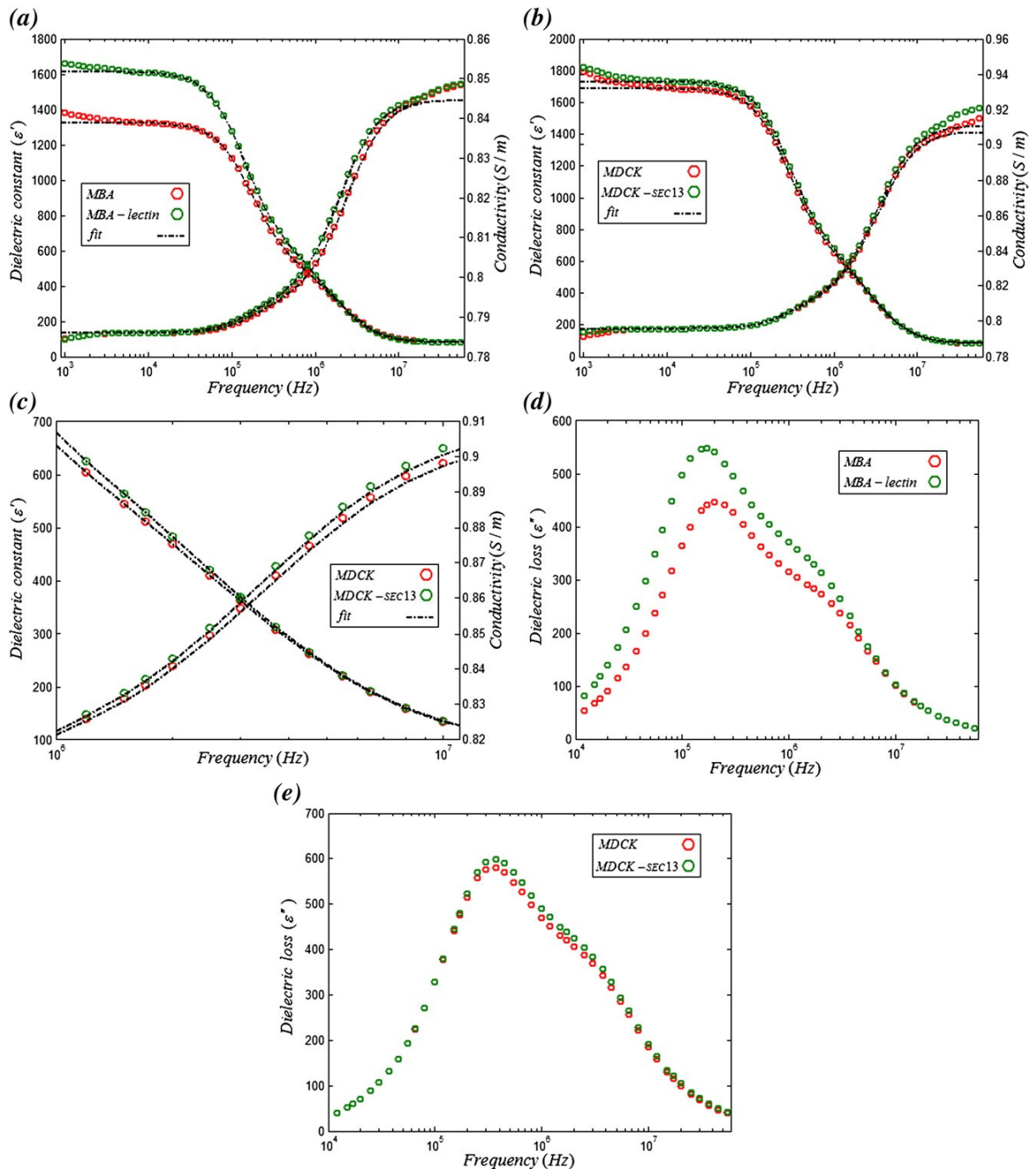


Figure 3.16. The spectra for MBA and MDCK cell suspensions. (a) Dielectric and conductivity of MBA and MBA-lectin suspensions. (b) Spectra of MDCK and MDCK-SEC13 suspensions. (c) High frequency spectra of MDCK and MDCK-SEC13 suspensions. (d) Loss spectra of MBA and MBA-lectin suspensions. (e) Loss spectra of MDCK and MDCK-SEC13 suspensions [154].

Dalmay, C et al. [41] use dielectric spectroscopy at microwave frequencies to distinguish between different cell types. Due to the resonant nature of the sensor, it is highly efficient at detecting tiny biological interactions. The experimental device is composed of a two half wavelength planar microstrip resonators coupled together through interdigitated comb capacitor (Figure 3.17) which may be electrically modelled as an RLC circuit (Figure 3.18).

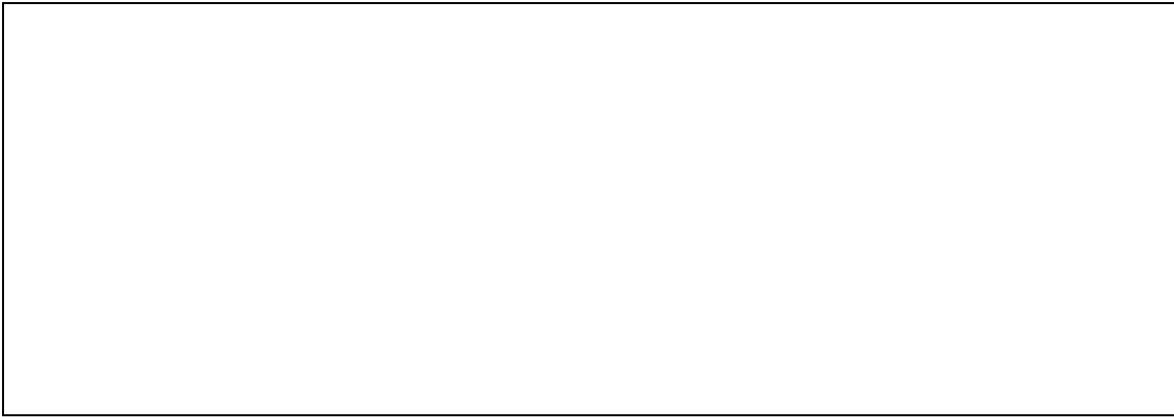


Figure 3.17. Two pole filter based EM biosensor configuration [41].

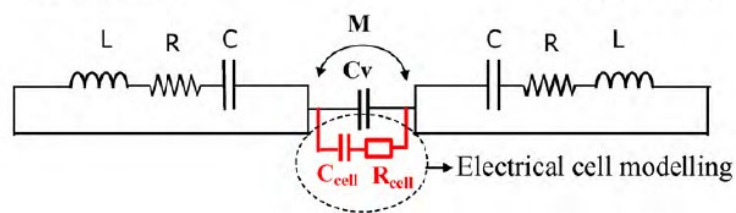


Figure 3.18. Electrical model of the sensor configuration [41].

This configuration is inspired by a two pole filter topology resulting in S-parameters that resemble that of a series RLC circuit filter (Figure 3.19). This configuration also results in the propagation of two semi quasi resonant modes. One which is sensitive to perturbations of cells within the coupling area (14.5 GHz) and the other which is insensitive that can be used as a reference mode (16.5 GHz).

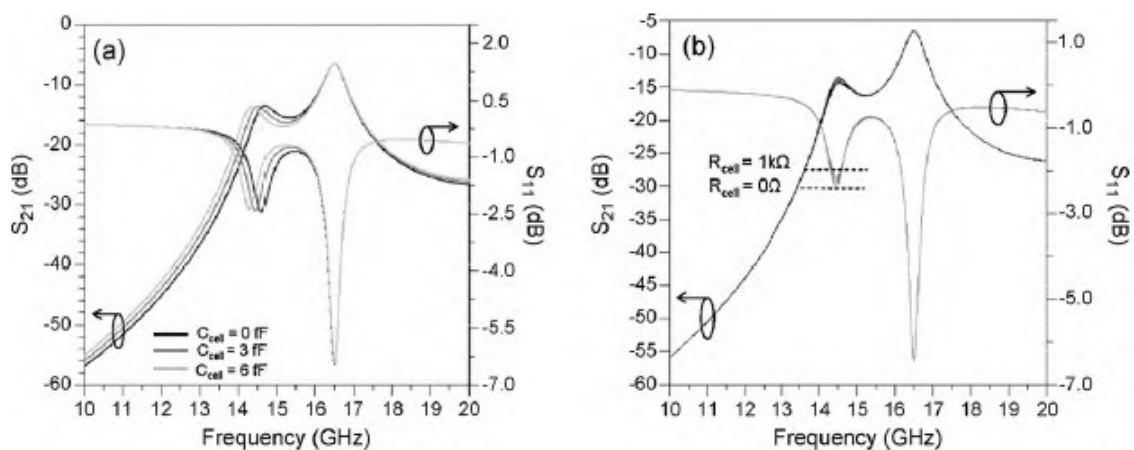


Figure 3.19. The S-parameters (S_{11} and S_{21}) of the filter based EM sensor. Note the effect of capacitive loading (a) and resistive loading (b) on the sensitive mode (14.5 GHz) and the insensitive mode (S_{21}) [41].

The frequencies of the two modes were calculated from Equation 3.1 and Equation 3.2 below. Due to the propagation of the two different modes, resonance occurs at slightly different frequencies.

The first mode mainly relies on electric coupling through the coupling region while the second couples through mutual inductance. It is this that makes the second mode insensitive due to biological samples having relatively low permeability.

$$f_m = \frac{1}{2\pi \sqrt{L(C + C_v)}} \quad \text{Equation 3.1}$$

$$f_e = \frac{1}{2\pi \sqrt{(L - M)C}} \quad \text{Equation 3.2}$$

where f_m is the magnetic coupling mode, f_e is the electrically coupling mode, C_v is coupler capacitance and M is mutual inductance.

The configuration was fabricated on a fused silica substrate for its low loss properties and transparency to visible light allowing optical observation of cell deposition. The electrodes were gold plated due to its biocompatibility and low loss performance in the GHz frequency region. The electrodes were patterned using a Cr/Au electroplating technique. Su8 photoresist is used to create a chamber on top of the interdigitated capacitor ensuring the cells only adhere in areas where the electric field is uniform (Figure 3.20).



Figure 3.20. Individual cells deposited in the interdigitated capacitor coupling region of the sensor. Simulation of the sensors indicates the region of uniform electric field [41].

The experimental apparatus was applied to distinguish adhering tumourous glial cells and non-adherent stem cells. This means that the glial cells will adhere and grow on the biosensor contrary to stem cells which require to be fixed to the coupling area. To avoid the high losses associated with a cell culture media, measurements were conducted with the media removed in open air. However ,

this presented difficulties in making time stable, reproducible measurements. To solve this cells were fixated a low concentration paraformaldehyde solution (4 %). This fixation step freezes the cells in a stable state for the measurement duration. Figure 3.21 demonstrates the effect of loading the sensor with a single glial cell with the reflected sensitive peak shifting 20 Mhz with 0.5 dB attenuation. Figure 3.22 show the result of fixating stem cells onto the sensor resulting in a 100 MHz shift and 0.5 dB attenuation.

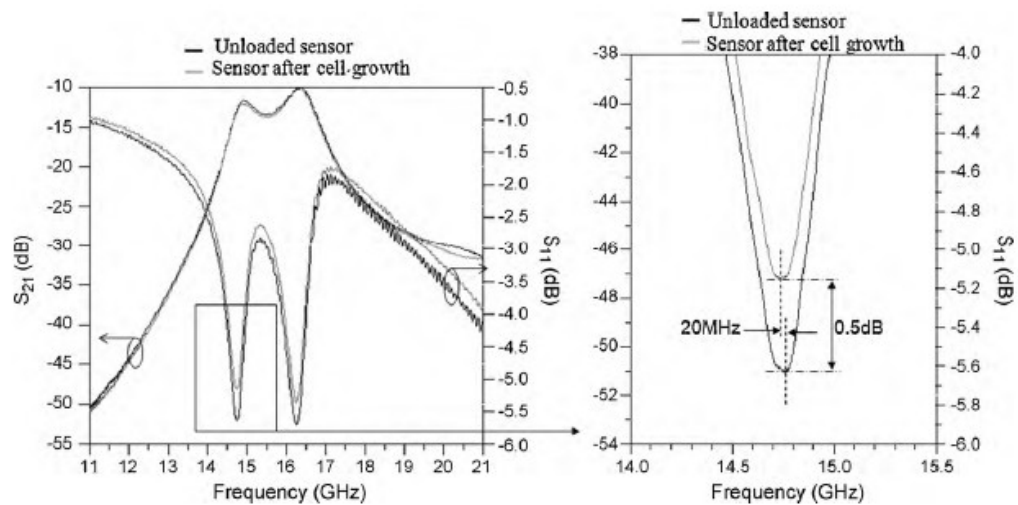


Figure 3.21. Measured S -parameters spectra for unloaded and glial cell loaded sensor [41].

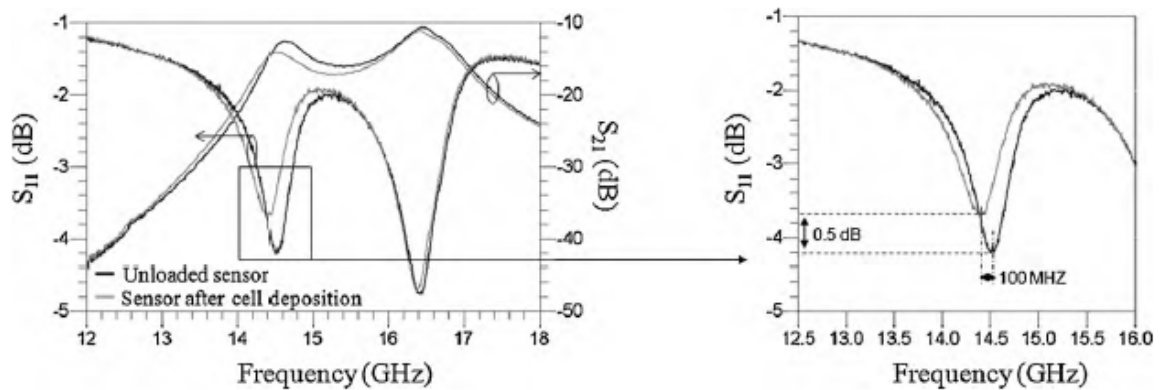


Figure 3.22. Measured S -parameters spectra for before and after fixed stem cell deposition [41].

Although the cell lines used in this experiment cannot be directly compared it nevertheless confirms that non-invasive dielectric spectroscopy is a viable method for distinguishing cells physiological state. This paper also shows that dielectric spectroscopy at microwave frequencies can be applied to differentiate biological samples. However, this paper interestingly suggests that RLC microwave resonant filters can be utilised as functional high sensitivity sensors.

One interesting application uses dielectric spectroscopy to analyse the quality, quantity and motility of sperm [155]. The authors utilise a rectangular cavity coupled with the small perturbation technique to analyse the dielectric characteristics of sperm samples at approximately 2.4 GHz. They found that the conductivity of semen increases as a function of frequency indicating the samples are lossy at higher frequencies (Figure 3.23). The conductivity is also greater for high motile samples of sperm and lower conductivity for dead sperm samples.

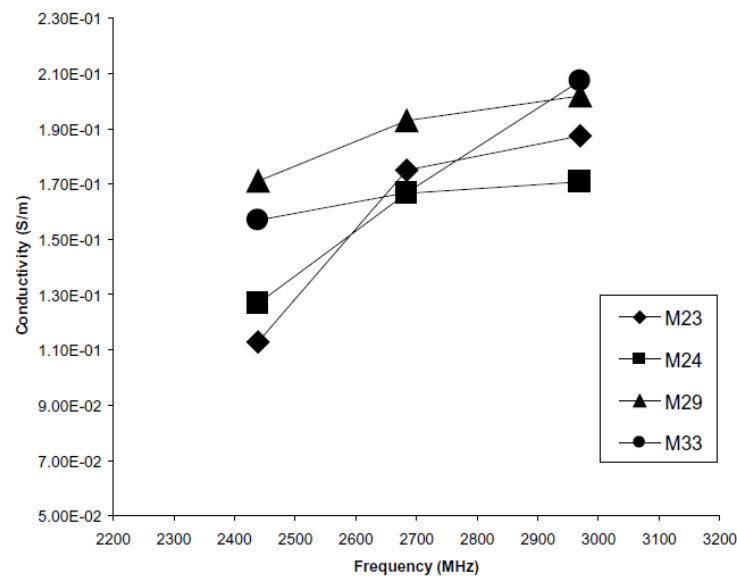


Figure 3.23. Measured conductivity of sperm samples at 3 different frequencies in the MHz range [155].

This paper effectively demonstrates that physical characteristics can be deduced from the dielectric characteristics of the sample.

3.2. Differentiation of edible vegetable oils

It was identified through journal and news articles that there is a need for a fast and cost effective method for olive oil quality verification in the food industry. Olive oil production has significant economic importance for Mediterranean and other olive oil producing countries. For example, in 2009 Greece produced 370,000 tons of olive oil worth an estimated 800 million Euros [156]. The International Olive Council has established quality standards to which olive oil must meet and in turn monitor occurrences of adulteration [157]. The European Union (EU) has also defined specific criteria for categorising olive oils and for assessing quality. Extra virgin olive oil must be extracted by

purely mechanical means without refinement and with a free acidity not exceeding 0.8 % v/v. Because of the high market value of extra virgin oil adulterants such as seed oils (corn, sunflower, rapeseed, soybean and walnut) and low quality olive pomace oils are added to increase yield [158-160]. The practice became so endemic in the late 1990s that a specialised task force was established by the EU anti-fraud office [161] with one EU official commenting that olive oil adulteration is “comparable to cocaine trafficking, with none of the risks” [162, 163]. At the 2012 meeting of the Agriculture Council of the EU, an action plan for the olive oil production and supply chain within the EU was agreed [164]. As part of this action plan, the implementation of strict anti-fraud controls that required specific tests to be conducted assessing the quality of olive oils was reinforced. The “global method for the detection of extraneous vegetable oils in olive oils” as specified by the International Olive Council [165] and sanctioned by the EU [164] is achieved using gas chromatography and liquid chromatography.

These expensive analytical techniques make extensive use of reagents; require specialised facilities such as laboratories and a number of trained personnel. Crucially, analysis cannot be carried out in-situ resulting in a delay in ascertaining the quality of the olive oil. The EU action plan for the olive oil sector addresses these issues by requiring the inclusion of research programmes which facilitate the detection of olive oil adulterants [164]. It is therefore evident that there is a demand for alternative measures of olive oil quality to supplement the established detection methodologies which can affordably be incorporated into the olive oil production and supply chain.

Olive oil and vegetable oil are predominantly composed of a category of lipids called triacylglycerols. Lipids are a broad group of naturally occurring hydrophobic and amphiphilic molecules. Triacylglycerols are formed from a glycerol backbone ester bound to three fatty acids (Figure 3.24). The glycerol backbone is a small polyol molecule having three hydroxyl groups (OH) which may react with the carboxyl groups (COOH) of three fatty acids to form triacylglycerols. Fatty acids are carboxyl acids with different lengths of long amphiphilic tails composed of an even number of carbon atoms

[166-168]. The covalent bonds between carbon molecules may either be saturated (single bond) or unsaturated (double bond). Additionally, there may be a single or multiple double bonds present in the amphiphilic chain called mono-unsaturated and poly-unsaturated respectively. This leads to a wide variation of possible fatty acids and an even wider range of triacylglycerols. An example of a saturated (stearic acid), mono-unsaturated (oleic acid) and poly-unsaturated (linoleic acid) are given in Figure 3.24.

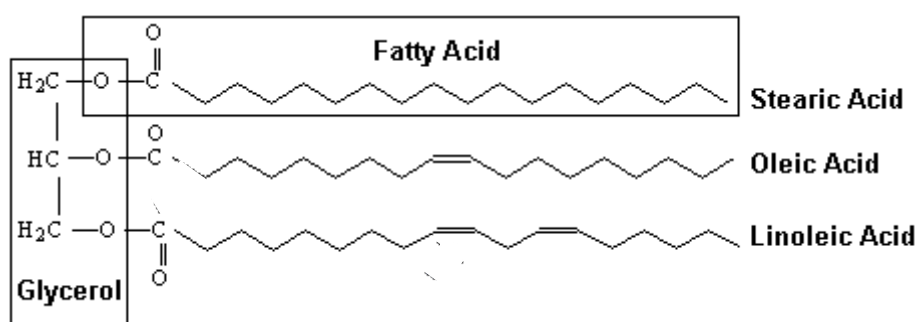


Figure 3.24. A triacylglycerol molecule composed of a glycerol backbone esterified to three fatty acid chains.

Triacylglycerols derived from different plants contain different varieties of fatty acids in different combinations and positions on the triacylglycerol molecule. Olive oils are predominantly composed of oleic and palmitic acids while sunflower oils are primarily composed of linoleic acids. A detailed list of vegetable oil composition may be seen below in Table 3.1 [169].

TABLE 3.1. FATTY ACID COMPOSITION OF VEGETABLE OILS AS DETERMINED BY LEE ET AL. [169]

Vegetable Oils	Fatty acid composition (%)				
	Palmitic C16:0	Stearic C18:0	Oleic C18:1	Linoleic C18:2	Linolenic C18:3
Olive Oil	10.60 - 12.84	2.98 - 3.66	73.60 - 74.86	10.12 - 10.21	0.46 - 0.67
Rapeseed Oil	3.98 - 4.78	2.02 - 2.50	60.43 - 61.24	20.63 - 23.27	9.50 - 11.65
Sesame Oil	8.72 - 11.67	4.69 - 5.23	36.00 - 39.12	45.80 - 47.77	0.32 - 1.51
Soybean Oil	7.00 - 10.15	1.86 - 4.07	25.47 - 58.91	22.80 - 52.35	8.83 - 9.43

HPLC and other chromatography techniques used in the EU to assess the quality of olive oil is able to detect the presence of high linoleic vegetable oils such as soybean, rapeseed and sunflower oil. Some high oleic oils such as hazelnut and olive pomace oil are also detectable using this method. The

detection range depends upon the type of olive oil and adulterant vegetable oil. However, the technique is unable to identify the adulterant oil only indicating if the olive oil is genuine [165].

The oil is first purified using solid phase extraction on silica gel cartridges. The composition of triacylglycerol is determined by reverse phase high performance liquid chromatography (HPLC) with propionitrile as the mobile phase. HPLC differentiates fatty acid species based upon the length and polarity of their amphiphilic chains. Fatty acids species are then detected using a refractive index detector. The second analytical technique firstly involves preparing fatty acid methyl esters (FAMES) by methylation by cold solution of potassium hydroxide in methanol. The esters are then analysed by capillary gas chromatography using high polar columns using the same principle as HPLC. The theoretical composition of the triacylglycerol is calculated from the fatty acid composition using a computer program. Several algorithms are generated from theoretical and empirical HPLC and LC triacylglycerol compositions which are then compared to a database of genuine olive oils.

Numerous novel analytical methods have emerged which supplement the detection of olive oil adulteration in the production and supply chain such as nuclear magnetic resonance (NMR) [170-174], infra-red (IR) [175-177], ultra-violet (UV) [178-182], Raman spectroscopy [183-186] and more recently genetic evaluation of the oil using polymerase chain reaction (PCR) analysis [187-191].

NMR spectroscopy has been used to detect and quantify adulterants of olive oil. Šmejkalová et al. apply NMR spectroscopy to measure the diffusion coefficient of various olive, sunflower, soybean, hazelnut and peanut oils (Figure 3.25). The minimum amount of hazelnut and peanut oil adulteration that could be detected was 30 % while adulteration by sunflower and soybean oil was detected as low as 30 % [174].

IR spectroscopy has also been applied to detect adulterants in olive oil. The differing chain length and positional patterns of fatty acids of triacylglycerol molecules are reflected in the absorbance of IR wavelengths of electromagnetic radiation [176]. Tay et al. describe the use of mid-infrared to

differentiate extra virgin olive oils from other vegetable oil (Figure 3.26) [192]. Furthermore, Maggio et al. utilise mid-infrared to quantify the concentration of vegetable oil adulterant in extra virgin olive oils (Figure 3.27) [176].

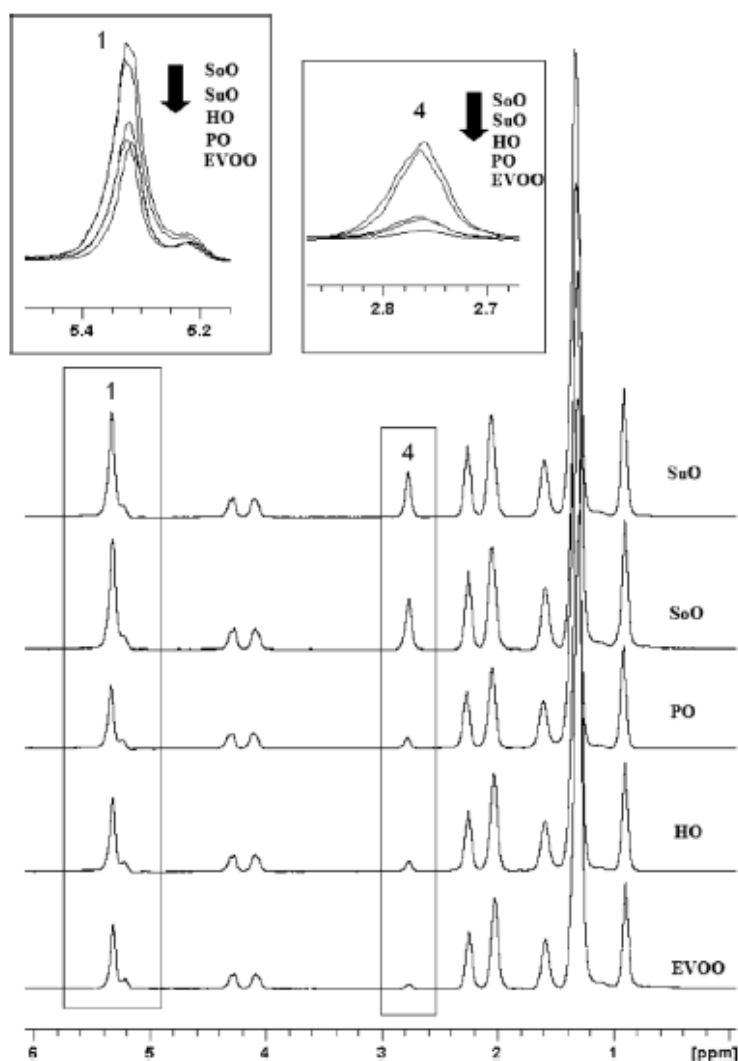


Figure 3.25. NMR spectra of extra virgin olive oil (EVOO), hazelnut oil (HO), peanut oil (PO), sunflower oil (SuO) and soybean oil (SoO) at 900 MHz [174].

Fluorescence spectroscopy has been used to differentiate virgin olive oil from other vegetable oils. This technique analyses the intensity of fluorescence of triacylglycerol molecules when excited by electromagnetic UV light [179, 193]. Plotting fluorescence intensity as a function of excitation frequency resulted in a characteristic spectrum for each vegetable oil (Figure 3.28.).

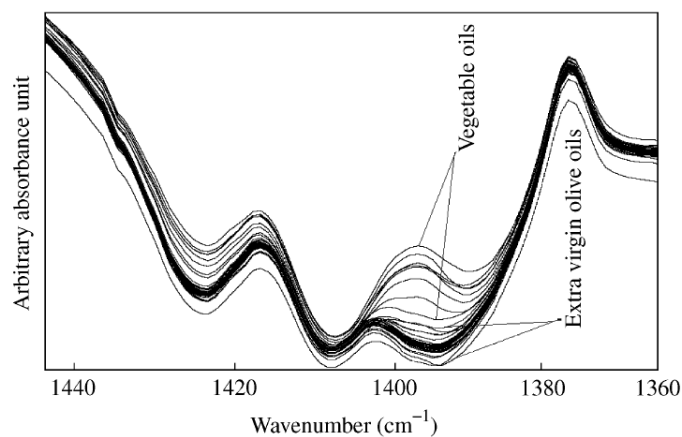


Figure 3.26. IR spectra of extra virgin olive oils and vegetable oils [192]

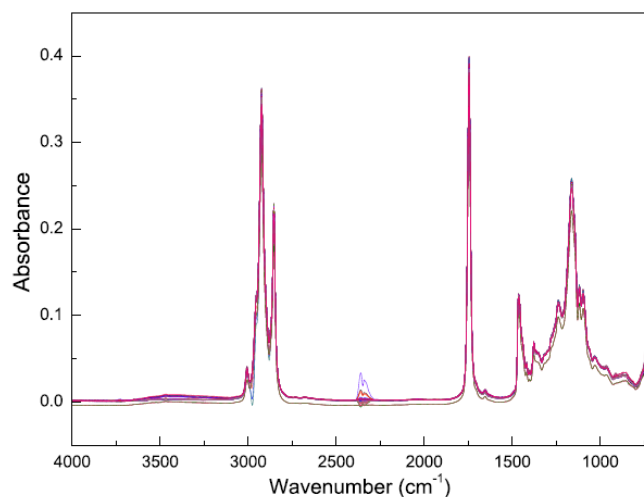


Figure 3.27. IR spectra of extra virgin olive oil samples with 0, 10, 20 and 40 % of high linoleic sunflower oil, canola oil, pomace olive oil and high oleic sunflower oil [21].

However, NMR spectroscopy is expensive, time consuming with the results needing a significant amount of interpretation. Despite IR spectroscopy being relatively cheap and easily adapted to different applications, it requires extensive sample preparation limiting the ability to be incorporated into online analysis. UV is ionising radiation which requires specialised UV light sources, UV transparent sample holders and cannot differentiate substances if they absorb similar wavelengths.

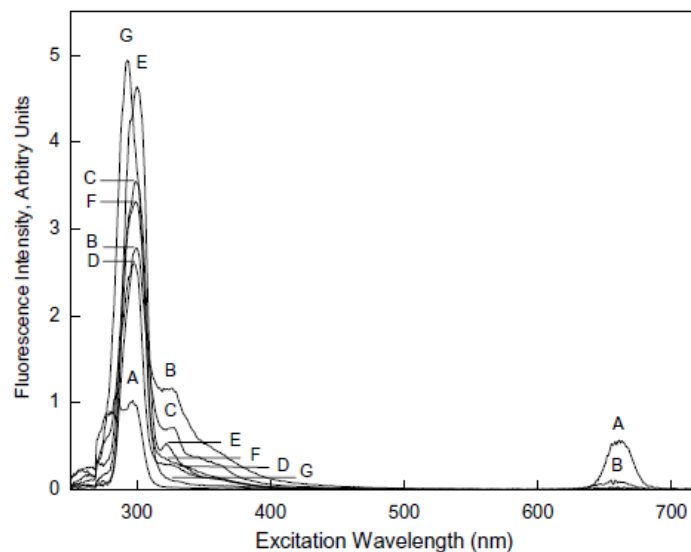


Figure 3.28. Fluorescence spectra of virgin olive oil (A), olive pomace oil (B), corn oil (C), sunflower oil (D), soybean oil (E), rapeseed oil (F) and walnut oil (G) [179].

Raman spectroscopy utilises laser light that interacts with the electron clouds of atoms present in the material which results in the detected energy of the laser light being shifted. When applied to olive oil adulteration detection, the technique is focused upon a band of 1441 cm^{-1} which is equivalent to that of the normalised vibration band of CH_2 . Raman spectroscopy is a promising technique as it is simple and does not require any sample processing [194].

Utilisation of PCR analysis detects variations in both coding and non-coding regions of DNA originating from both the nucleus and chloroplast. Several papers document how to fingerprint olive oil DNA, determining its origin [195-200]. The presence of adulterants was assessed by Wu et al. with an olive oils specific gene coding for the membrane intrinsic protein *PIP* [201]. Zhang et al. found that the gene *MT3-B* can differentiate olive oil from palm oil [202]. However, it was Spaniolas, Bazakos, Awad and Kalaitzis who identified a highly polymorphic region of chloroplast gene *trnL* intron that can differentiate eight of the ten oil-producing species [203]. This lab-on-a-chip system combined PCR analysis with a capillary electrophoresis technology enabling onsite detection of adulteration. Wu et al. uses a similar combination of PCR and capillary electrophoresis to differentiate DNA profiles of seven oil species [204]. Despite the technique being extremely sensitive, precise and specific, it requires sample preparation and expensive reagents.

Dielectric spectroscopy has emerged as a non-destructive, relatively cost effective, portable method of detecting vegetable adulterants in olive oil. The electronics and data handling hardware can easily be incorporated into a handheld device that can rapidly and effectively differentiate oils based upon their dielectric characteristics. This part of the research will focus on developing a sensor capable of detecting the standard of olive oils and differentiating different vegetable oils that could be incorporated into a handheld device.

3.2.1. Considerations of detecting adulterants in olive oil using dielectric spectroscopy

Dielectric spectroscopy provides a rapid non-destructive analytical technique based upon the dielectric response of the material to electromagnetic fields. The convenience of the method in this regard has lead to its application in evaluating food quality, notably quantifying food moisture content [205-207]. Several methods relating the dielectric properties of a food to compositional variations in the molecular structure have been developed [208-210].

Ragni et al. (2012) describe a capacitive instrument consisting of a variable capacitor used as a probe to determine the water content of olive oils [211]. The capacitive probe is a modified variable plate capacitor consisting of 22 interacting plates which can be manually rotated as to modify the total plate surface area of the capacitor (Figure 3.29). Measurement of the capacitance of the oil was carried out at 500 Hz, 2 kHz, 8 kHz, 32 kHz, 128 kHz and 512 kHz. The capacitance was then calculated using **Error! Reference source not found..**

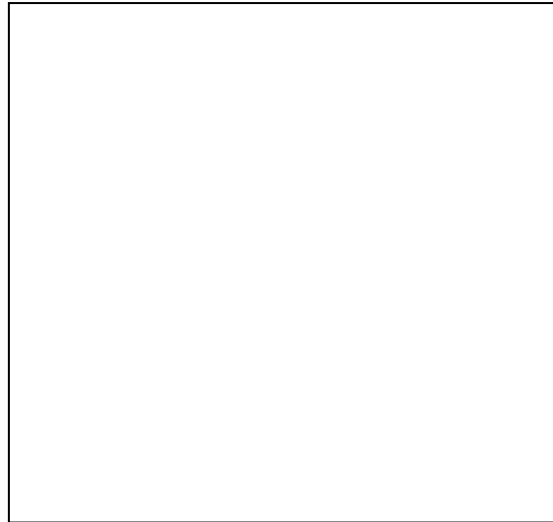


Figure 3.29. Variable plate capacitor and instrumental setup of the olive oil water content methodology [211].

Figure 3.30 shows the linear relationship between water content and capacitance of the olive oils. R^2 values representing linearity was calculated at 0.818. Figure 3.31 details the correlation between monounsaturates of the oil and calculated capacitance with a R^2 value of 0.627.

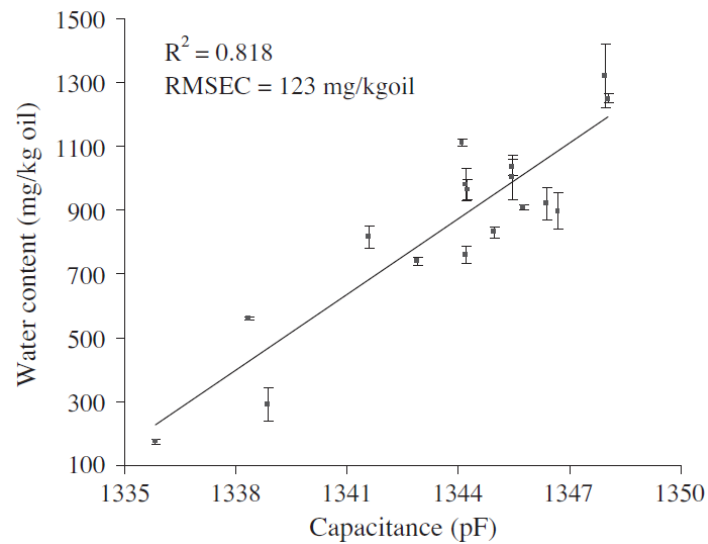


Figure 3.30. Correlation between capacitance and water content at 8 kHz [211].

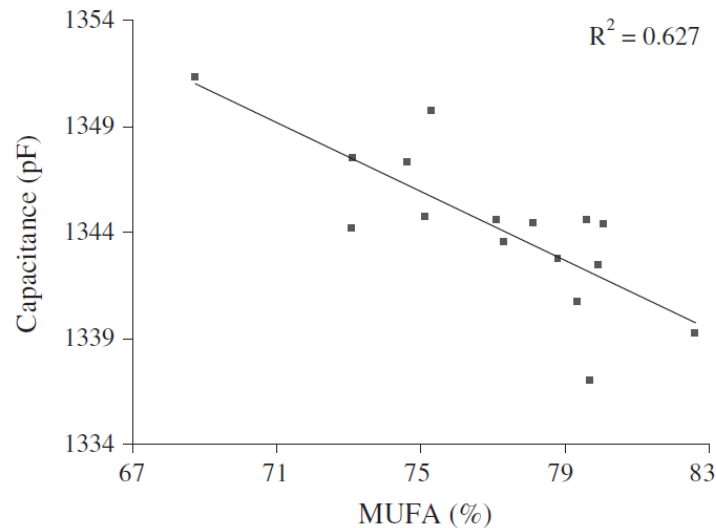


Figure 3.31. Correlation between mono-unsaturated fatty acids and capacitance at 2 kHz [211].

The paper demonstrates that capacitive techniques are capable of calculating extremely low moisture content of olive oils (0.03 – 0.13 %) and the monounsaturated fatty acid composition at frequencies in the low kHz region (2 and 8 kHz). This could potentially be used as a method for olive oil adulteration detection.

Cataldo et al. (2010) detail a probe which mimics a coaxial cable that is filled with oil as the dielectric material that operates a frequency of 1 GHz [212]. The probe is fabricated out of brass with dimensions chosen resulting in a characteristic impedance of 50Ω so as to minimise impedance mismatch (Figure 3.32). Measurements are performed using time domain reflectometry (TDR). In this way, reflected power resulting from impedance mismatch is recorded as a function of time instead of frequency. The authors suggest that this reduces the cost and size of the measurement and analysis circuitry.

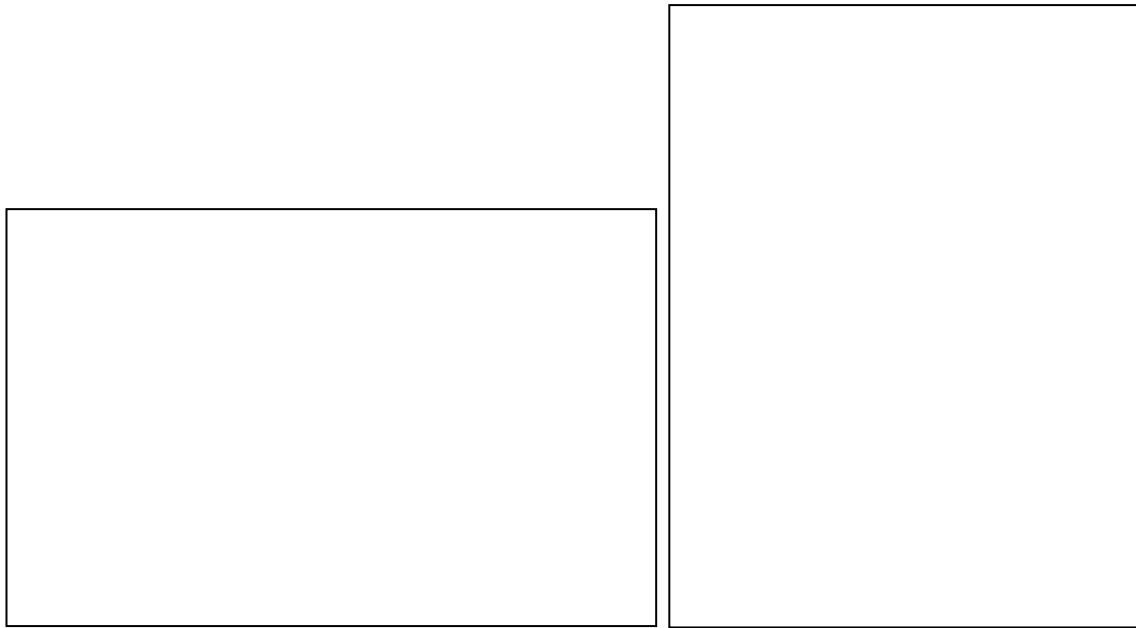


Figure 3.32. Configuration of the coaxial probe and experimental setup [212].

Figure 3.33 shows the S_{11} parameters of olive and castor oils. The relaxation frequency was calculated for each oil which is presented in Figure 3.34.

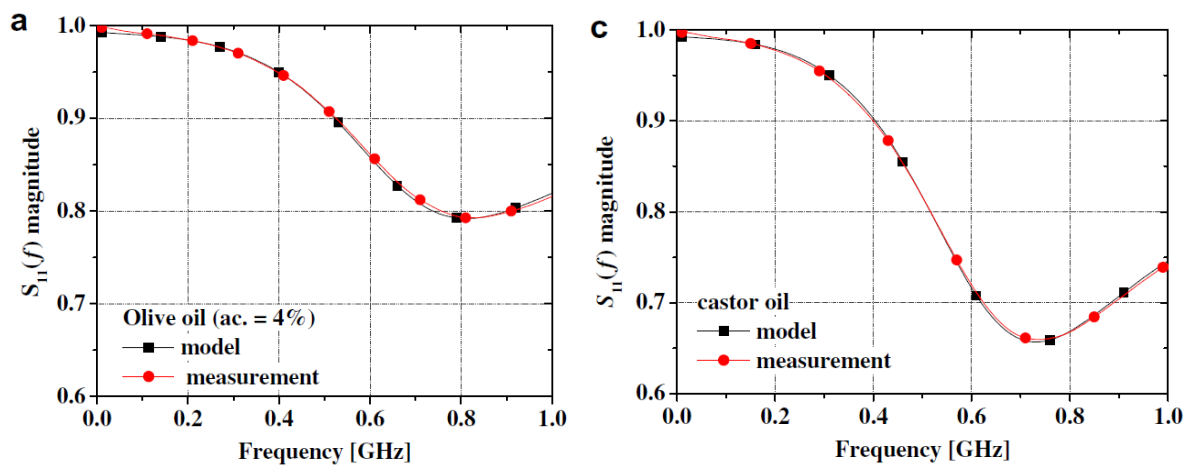


Figure 3.33. Comparison between the reflected s -parameters of olive oil (left) and castor oil (right) [212].

The authors attribute the dielectric response of the oils to the acidity and therefore quality of the oil. In this way adulterants of olive oil may be identified. However, the probe construction represents a significant cost due to being made of copper and the system in its current state cannot be incorporated into an inline monitoring system.

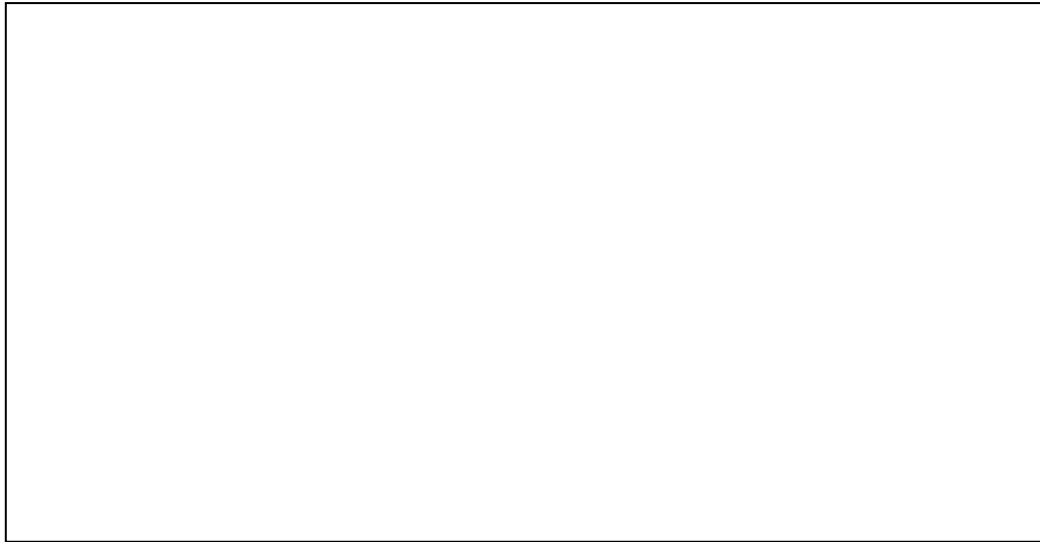


Figure 3.34. Comparative results of averaged values for relaxation frequencies of vegetable oils with error bars (95 % confidence level) [212].

3.3. Detection of disease states in cattle by quantification of blood serum lactate

Domesticated cattle or *Bos primigenius* are bred and reared as livestock for dairy products, meat and traditionally as draft animals. Beef and dairy exports can constitute a significant amount of GDP for countries with a climate that can sustain pasture for cattle grazing. For example, New Zealand exported dairy products to the value of 8.38 billion New Zealand dollars from approximately 4.2 million dairy cows in the year ending June 2007 [213]. There were a further 4.39 million beef cattle in the same year. The profitability of this agricultural economy is heavily dependent on maintaining healthy and disease free animals. For example, in the 2001 foot and mouth outbreak in the United Kingdom, over 4.2 million cattle were slaughtered for disease control purposes causing a 60 % fall in revenue for the UK agricultural sector [214]. Real time monitoring of cattle health could reduce the impact of such epidemics in the future by providing an early warning of ill health in cattle herds.

Interest in real-time wearable wireless health monitoring systems has increased in recent years as wireless technologies, such as Wi-Fi and Bluetooth circuits have become sufficiently miniaturised and economically viable. Sardini and Serpelloni (2010) have developed a wearable belt for the monitoring of electrocardiogram derived heart rate, body temperature, respiratory rate and three axis position and movement in convalescing patients. Data is collated on the belt before being

wirelessly transmitted to a base station connected to the internet for remote health monitoring [215].

Wearable health monitoring sensors can be integrated into wireless sensor networks providing an appealing non-invasive real time monitoring system able to operate over wide, open spaces. Therefore the prospect of applying wireless sensor networks for the monitoring of cattle herd location, behaviour and health is extremely promising. Huircán et al. present a ZigBee-based wireless sensor network for monitoring the location of grazing cattle using the programming protocol to estimate distances between nodes and the base stations [216]. Hiroaki and Takaaki incorporated GPS into collars for accurate cattle location to monitor grazing habits [217]. However, power constraints of sensor nodes limit the number of functions that may be incorporated into a remote health monitoring device. Therefore there is a need for small, non-invasive low power sensors that are capable of measuring an appropriate analyte that is an informative gauge of cattle health.

A number of sensors have been developed to non-invasively assess various physiological analytes of the blood. Due to the sensor signal needing to penetrate the skin without causing any damage low power, non-ionising radiation must be used. The sensor must also be miniaturised as to be wearable, inconspicuous and be integrated into a collar or similar assembly in a way that does not stress or limit the movement of the cattle. Saptari and Youcef-Toumi describe a near-infrared device for sensing blood glucose concentrations by measuring the absorption of glucose at a wavelength of 2257 nm [218, 219]. Solanki et al. similarly describe an optical reflectometry device for blood glucose monitoring [220]. However, these sensors require relatively high amounts of power to operate, limiting the operability period. There are also security concerns over passing such data over a non-encrypted wireless data network.

Blood glucose concentration is also prone to periodic variations as food is consumed, metabolised to glucose which is stored in the liver. This natural physiological variation reduces the applicability of blood glucose concentration as a marker for disease states. Lactate, as a major metabolite of

glycolytic activity, may be used as a marker for the assessment of metabolic, cardiovascular and respiratory stress induced by excessive exercise [221-223], infectious disease [224-226], dehydration [227, 228] and pregnancy [229] in mammals. Bovine serum lactate concentrations vary from 0.06 – 2.2 mmol/ L (5.0 – 20.0 mg/dL) [230].

Dielectric spectroscopy presents an attractive sensing method due to low power and high penetration characteristics associated with millimetre wavelengths [35, 231]. Dielectric spectroscopy coplanar sensors provide an unobtrusive solution as the sensors are small and can be constructed on thin flexible substrates that flex with movements of the cows skin.

This part of the research aims to assess the effectiveness of coplanar resonant structures applied to dielectric spectroscopy to non-invasively detect physiologically high concentrations of lactate in bovine blood. The sensor therefore needs to be capable of differentiating small changes in the permittivity of blood due to lactate concentration. Blood is made up of a suspension of different cells, proteins, saccharides, hormones and other dissolved molecules in water the permittivity of which is a result of these constituents. However, microwave sensors are able to measure one specific parameter in an environment in which several parameters may change [232]. Microwave circuits are also small, relatively inexpensive and low power.

3.3.1. Considerations of detecting disease states in cattle utilising dielectric spectroscopy

Semenov et al. (2012) demonstrate the feasibility of dielectric spectroscopy at microwave frequencies for assessing tissue oxygenation however, this requires the sensor be in direct contact with the brachial artery while the animal is under anaesthesia [233]. Malinin (2012) developed a proof of concept prototype for non-invasive monitoring of blood glucose in diabetic patients using impedance measurements at kHz and MHz frequencies. The device is incorporated into a wrist bracelet mounted electrodes [234]. The system however relies upon feedback from the subject regarding eating and insulin injections to compute blood glucose concentrations from impedance

measurements so as to learn a typical response. However, this potentially introduces error regarding the patient forgetting to enter an event or entering the wrong event into the system.

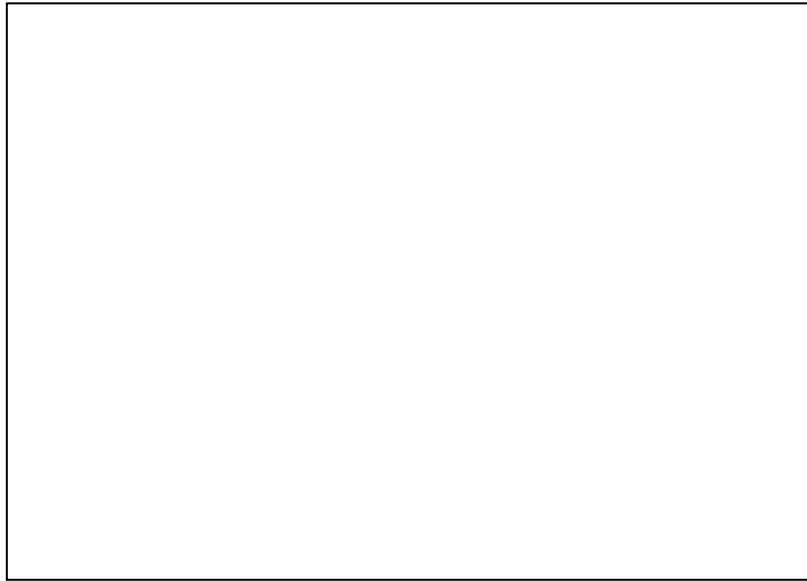


Figure 3.35. The prototype non-invasive blood glucose monitoring system with bracelet mounted electrode configuration [234].

Although the prototype system that could monitor blood glucose concentrations (Figure 3.36) average error was in the range of 15 – 20 % which the authors attributed to inconsistent contact between the sensor and the surface of the skin due to subject movement. The system also had to incorporate temperature reading in the calculations, compensating for temperature dependent impedance changes.

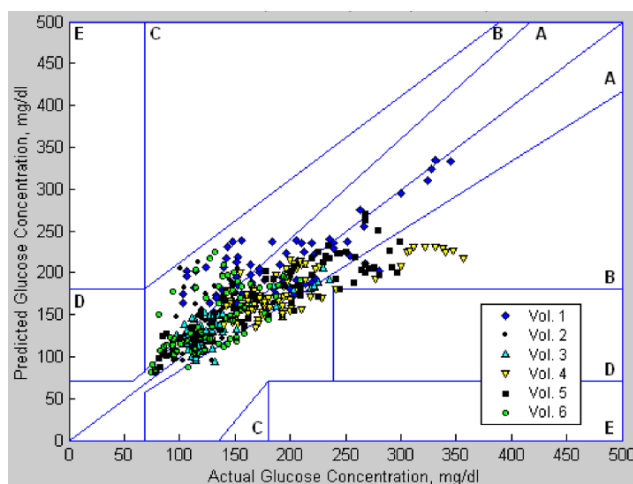


Figure 3.36. The predicted results plotted against the actual blood glucose concentration for more than 100 subjects [234].

However, blood glucose concentration is prone to periodic variations as food is consumed, metabolised to glucose which is stored in the liver. This natural physiological variation reduces the applicability of blood glucose concentration as a marker for disease states. Lactate, as a major metabolite of glycolytic activity, may be used as a marker for the assessment of metabolic, cardiovascular and respiratory stress.

Lactate is a conjugate base of lactic acid (Figure 3.37) and is an alpha hydroxide acid that plays a role in a number of biochemical processes. When in solution a proton may be lost from the carboxyl group generating a lactate ion with a molecular charge on the carboxyl group. It is this charge that allows the measurement of lactate in solution by dielectric spectroscopy. Lactate concentration will have affect upon the conductivity and permittivity of the solution [235].

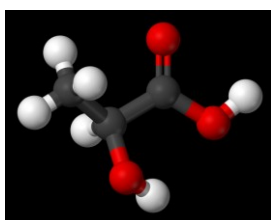


Figure 3.37. A ball and stick diagram of lactic acid.

Thomas et al. (2012) have developed an enzymatic lactate sensor fabricated on a polymer substrate moulded into a contact lens for non-intrusive healthcare monitoring [236]. The sensor relies upon

the selective enzyme lactate oxidase which converts lactate to pyruvate in the presence of oxygen yielding hydrogen peroxide. A sufficient applied potential applied to a platinum electrode (working electrode) will result in oxidation of hydrogen peroxide yielding electrons which yields electrons which complete the circuit to a second electrode (reference electrode). The current is directly proportional to the amount of lactate oxidised by the enzyme. A counter electrode is included as a current drain to the working electrode. This configuration allows for a stable reference voltage between the working and reference electrode (Figure 3.38).

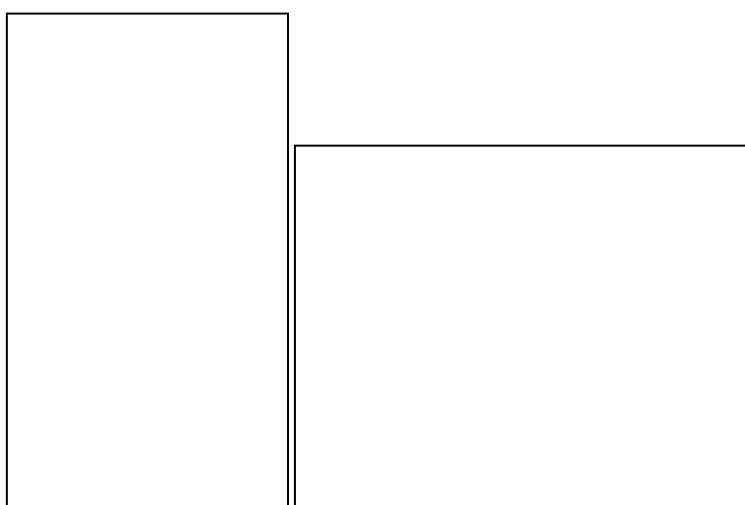


Figure 3.38. Sensing structure (left) and completed contact lens (right) of lactate sensor. The arrows indicate the working electrode (WE), reference electrode (RE) and the counter electrode (CE) [236].

Artificial tear solutions were prepared from phosphate buffer solution and lactic acid with measurements conducted at room temperature. The sensor was introduced into a beaker of the solution while measurements were conducted. Figure 3.39 details the results which show a correlation between current and lactate concentration of the solutions.

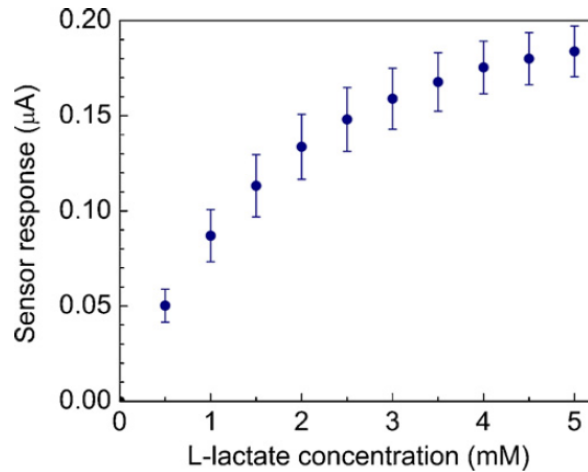


Figure 3.39. Measured sensor current as a function of lactate concentration of the tear film [236].

The sensors have a quick response time (35 s) with sufficient resolution within the physiological range of lactate concentrations. The sensors are functional at temperatures comparable to the surface of the eye and have a stable response over 24 hours. The enzyme element of the sensor gives the sensor specificity which is an important feature of this sensor.

3.4. Quantification of *Pseudomonas aeruginosa*

The opportunity arose to assess the use of the apparatus as a method to rapidly analyse biological samples for infection of bacteria. *Pseudomonas aeruginosa* PA01 (ATCC 15692) was used for this experiment. This bacterium is gram-negative, motile, rod-shaped, and it is recognised as an emerging opportunist pathogen of significant clinical interest [237-241]. During infection, it enters the host's bloodstream and competes for iron. *P. aeruginosa* produces siderophores, low molecular weight compounds that allow the organism to sequester the host's iron with high affinity [242, 243]. Siderophore isolation has recently been characterised [244-246]. Siderophore production is directly linked to the organism's virulence. Also regulation of exotoxin A is iron dependent [247-249]. Upon infection, *P. aeruginosa* colonises the lungs of patients suffering from cystic fibrosis (CF), producing an extracellular polysaccharide that attaches to bronchial mucus and thus causing obstruction of the respiratory system. Although more infant and children with CF survive to adult life, *P. aeruginosa* is the primary cause of morbidity and mortality in such cases [239, 250, 251]. It can also infect critical organs and the results can be fatal. *P. aeruginosa* is notoriously resistant to antibiotic treatments and it is difficult to eradicate [252-255]. Due to the nature of *P. aeruginosa*, it is important that rapid and early biomedical diagnostic techniques are developed in order to detect it early in its development, therefore enhancing the chance and rate of patient recovery. For example, it is one of the main species of pathogenic bacteria commonly found in burn wound infections [255-258]. It is also found in human skin flora and associated with virulence factors for the suspected lysis of healthy eukaryotic cells and tissue matrices upon infection.

Transmission of *Pseudomonas* can occur through many routes [259-262]. However, a frequent transmission vector is the contamination of drinking water that has been stored in a holding tank [263-268]. *Pseudomonas* can thrive in relatively nutrient poor environments at a range of different temperatures [269]. *Pseudomonas* is one species of bacteria that contributes to the formation of bio-films that adhere to surfaces containing most bacteria [270, 271]. However, disruption of the

film can result in sections of the bio-film to become dislodged resulting in bacterial contamination of the water supply [272]. Contaminated water can transmit *Pseudomonas* to people and food through the following ways.

- Direct contact with the contaminated water through:
 - Ingestion (drinking and washing food with contaminated water)
 - Bathing
 - Contact with an open wound
- Inhalation of micro-droplets produced by some taps
- Washing surgical equipment or cooking utensils with contaminated water
- Indirect contact arising from physical contact with professionals and workers who have washed their hands with contaminated water.

It is generally accepted that contamination only results from a failure in the recommended control measures (temperature control and water treatment regimes) [273-275]. In contrast, the original source of *Pseudomonas* is less well understood. Given the variety of possible origins, facility managers are may carry out risk assessment of their particular practices in reducing contamination risk and minimising microbial inoculation of the transmission vectors noted above [276, 277].

Detection of *Pseudomonas* strains is conventionally carried out using selective culture and staining methodologies. These techniques are still the cornerstone of bacteriological differentiation in healthcare and food industries [278].

To this end, this experiment aims to evaluate the performance of coplanar sensors excited at microwave frequencies to detect significant presence *P. aeruginosa*.

3.4.1. Considerations of quantifying bacterial cells using dielectric spectroscopy

Li *et al.* (2011) describe capacitive immuno-sensor for in-situ sensitive detection of *E.coli* [279]. The methodology takes advantage of high affinity anti-*E. coli* antibodies immobilised onto the surface of a quartz crystal substrate gold plated electrode. Dielectric measurements were taken over 1 Hz to 100 kHz. Capacitance, real and imaginary impedance were recorded by the experimental setup. As

E.coli culture is passed over the sensor, the antibodies selectively capture the cells adding capacitance to the sensor circuit as demonstrated in Figure 3.40.

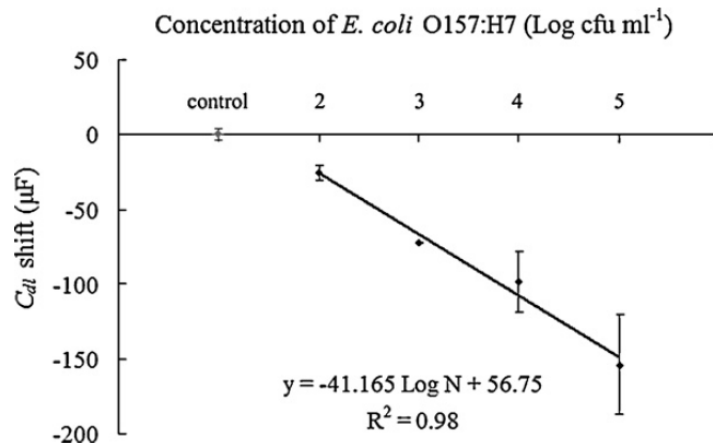


Figure 3.40. Linear relationship of between capacitance of the immuno-sensor (μF) and logarithmic concentrations of *E. Coli*. (CFU / ml) at a frequency of 1Hz [279].

3.5. Quantification of lactate in cerebrospinal fluid

The opportunity arose to assess the lactate content of cerebral spinal fluid (CSF) as a marker of hypoxia in surgical patients. Routine analytical tests performed on CSF include those for protein, glucose, differential cell counts and differential microbiological culture. The most common clinical test of CSF is microscopic staining for the detection of meningitis causing bacteria which inflame the meninges. Other analytical procedures may be performed on CSF to exclude other infectious [280], inflammatory [281] or neoplastic diseases [282, 283] affecting the central nervous system. Other conditions which may be differentially diagnosed using CSF include subarachnoid haemorrhage [284, 285], hydrocephalus [286, 287] and intracranial hypertension [288].

Patients who undergo cerebrospinal surgeries have an inherent risk of paraplegia. This is caused by an increase in cerebrospinal fluid pressure in turn applying pressure upon the arteries that supply blood to the spinal cord. To reduce the risk of this occurring, a lumbar puncture is performed and a pressure valve fitted which enables CSF to be expelled should the pressure rise above a determined threshold. At the moment any CSF expelled would normally be discarded as biological waste, but this bodily fluid contains specific markers that may be used to identify the onset of paraplegia in

patients. This notion that CSF might harbour such important information is supported by Williams *et al.* [289], who observed that lactate concentration in CSF increased with the risk of patient paraplegia. As noted in chapter 3.3, lactate concentration is closely correlated to glycolytic activity and oxygen availability. One would normally expect to see physiological levels of lactate in blood around 1 mmol/L; in pathology this may rise to 10-15 mmol/L, or higher in the case of exercise [289]. In this case, previous work has demonstrated that EM wave techniques are sensitive to changes in lactate concentration in the order of 0-20 mmol/L, which adds weight to support the use of the electromagnetic sensing technique proposed in this work for point-of-care diagnostics. It is thought that the use of EM sensors for the purpose of monitoring lactate concentrations in CSF will provide an affordable and rapid diagnostics tool to aid in the treatment of patients by surgeons therefore improving the prognosis of such surgery.

CSF is composed of proteins, cells and electrolytes similar to that of blood serum which occupies the subarachnoid space between the arachnoid mater and the pia mater [290]. It is primarily produced in the choroid plexus of the brain with the remainder being exuded from blood vesicles and ventricular walls. The CSF serves four main functions of buoyancy, cushioning, homeostasis and regulation of intracranial pressure.

3.5.1. Considerations of quantifying lactate concentrations in cerebrospinal fluid using dielectric spectroscopy

Cerebrospinal fluid is mainly composed of water (94 - 96 %) with the inclusion of proteins, some cells and electrolytes [290]. The concentration of lactate will have an effect on the conductivity and permittivity of the CSF as noted in chapter 3.3.1.

It has been found that normal and pathologically anomalous CSF samples exhibit distinct dielectric properties [291]. However, there are a very limited number of publications that pertain to the effect of lactate concentration in CSF. Nevertheless, the interest of this work is a change of CSF lactate concentration from basal levels at the start of the surgical procedure. Therefore a variation from

initial measurements as the surgery commences is sufficient to detect an increase in lactate concentration.

Lonnappan, A. *et al.* (2006) present data on the dielectric characteristics of CSF samples using the cavity perturbation technique [291]. The study uses a cavity operating at 2.68 GHz. At these frequencies the overwhelming factor influencing the dielectric properties of the sample are that of bound water which relax in the δ dispersion discussed in Chapter 2.3 . The journal article reports that abnormal CSF has a higher dielectric constant and lower conductivity than normal CSF. This is attributed to higher glucose and protein concentrations in abnormal CSF. The article concludes with acknowledgment that microwave dielectric spectroscopy has the potential to be used for the clinical analysis of CSF based upon the permittivity and conductivity of the sample.

3.6. Chapter 3 Summary

The requirement and background of sample analysis is outlined with the current methods of analysis. This chapter is divided into five distinct sections which individually assess the need for analysis and the problem it is detecting or quantifying. Strengths and deficiencies of current analytical methods are detailed followed by current research activities for the stated analytical purpose which is summarised in Table 2.1. A review of the literature related to the dielectric characteristics of the sample is also conducted.

TABLE 2.1. SUMMARY OF THE APPLICATION, CURRENT METHODOLOGIES, WEAKNESSES OF CURRENT METHODOLOGIES

Application	Current Methodologies	Weaknesses of current methodology	How weaknesses will be addressed
Quantification of neutral lipids in biological cells.	Laboratory analysis using enzyme linked spectrophotometry.	Lengthy analysis requiring multiple solvents and expensive enzymes. Specialised facilities consisting of laboratory and qualified staff are also required.	Non-invasive analysis not requiring any solvents or substrates or specialised facilities.
Differentiation of vegetable oils	Laboratory analysis using chromatography methodologies.	Lengthy analysis required using expensive chromatography equipment resulting in intermittent sample analysis of olive oil.	In-situ analysis of oil samples not requiring any solvents or specialised facilities consequently yielding an instant result of olive oil quality.
Detection of disease states in cattle.	Physical examination and laboratory investigation upon identifying an illness.	Physical symptoms need to occur before illness is identified which need to be verified by a qualified veterinarian.	In-situ real time analysis of cattle health pre-empting illness in cattle herds.
Quantification of <i>Pseudomonas aeruginosa</i> .	Laboratory analysis using selective culture medias.	Widespread illness needed in population before the transmission vector is investigated and identified.	In-situ real time detection of bacterial contamination of drinking water. Can be incorporated into a device that stops water flow if contamination is detected.
Quantification of lactate in cerebrospinal fluid.	No current methodology for analysis of lactate in cerebrospinal fluid.		Real time feedback to surgeons who can take corrective action should hypoxia occur reducing the risk of paraplegia.

Chapter 4. Equipment and software

4.1. High frequency simulation software (HFSS)

Due to the nature of electromagnetic propagation, for some resonant structures it is extremely time consuming to estimate resonant characteristics from equations and difficult to account for complex conformations of sensor geometry. It is therefore necessary to employ specialised computer software which uses Maxwells' equations to simulate the EM characteristics of materials and structures. High frequency simulation software (Ansys, USA) is software designed for simulation at microwave frequencies that uses a finite element method combined with an automatic adaptive measuring technique. This provides a mesh that is conformal with the 3-D model and the nature of the electromagnetic characteristics. This type of software enables circuit, component and antenna design functions such as modelling, simulation, analysis and optimisation. This may be displayed as scattering parameters (S, impedance and admittance), visualises 3-D electromagnetic fields as well as generating near and far field radiation plots (Figure 4.1).

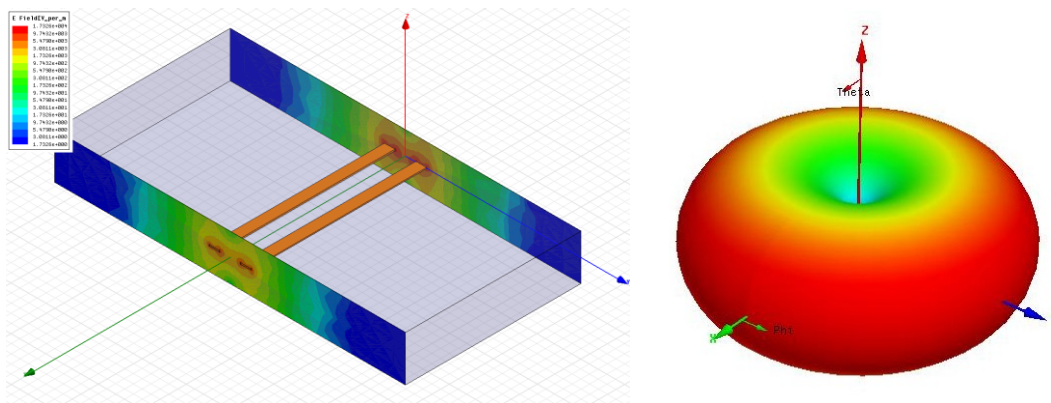


Figure 4.1. Example of E-field and radiation plot generation.

This software was exclusively used in this research to simulate coplanar sensor configurations and specific details of simulations will be provided where appropriate.

4.2. Vector network analysers

A vector network analyser is a piece of electrical equipment that can measure electrical characteristics of electrical networks. A VNA test system consists of a source, a signal separation

device, a receiver and a display. In a two port system, the analyser applies a signal that is then transmitted through or reflected off the test device to the transmission and reflected ports respectively. The signals are then applied to receivers for measurement comparing them with the generated signal generated by the source.

Instead of oscilloscopes that measure the power response of circuits over a frequency range, a vector network analyser also measures the voltage and current phase. The two main methods of displaying this information are s-parameters which display magnitude in the frequency domain and polar smith charts which display complex reflected coefficient and complex impedance.

4.2.1. Hewlett-Packard (Agilent) 8720 ET

The VNA primarily used in this research is a Hewlett Packard (Agilent Technologies, USA) Vector Network Analyser 8720ET and is used unless otherwise stated (Figure 4.2). This model has two ports and is capable of generating a high resolution swept or continuous RF signal from 50 MHz to 20 GHz while analysing the reflected and transmitted parameters of the circuit between the two ports with a resolution of 1 Hz. The VNA is able to measure and display signal magnitude, phase and delay of the reflected and transmitted power. A block diagram of the network analyser is show in Figure 4.3.

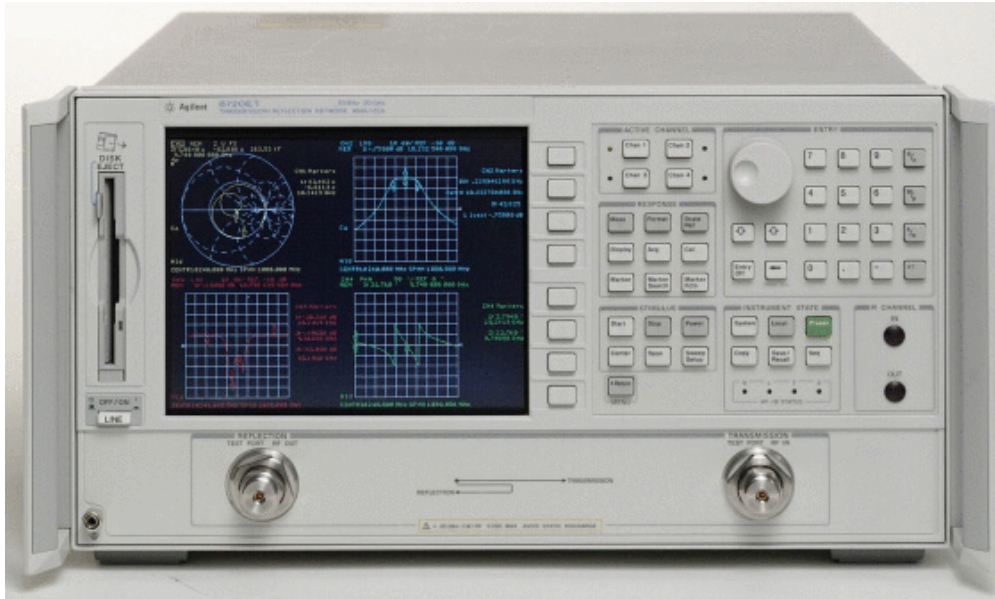


Figure 4.2. Hewlett Packard (Agilent) 8720 ET.

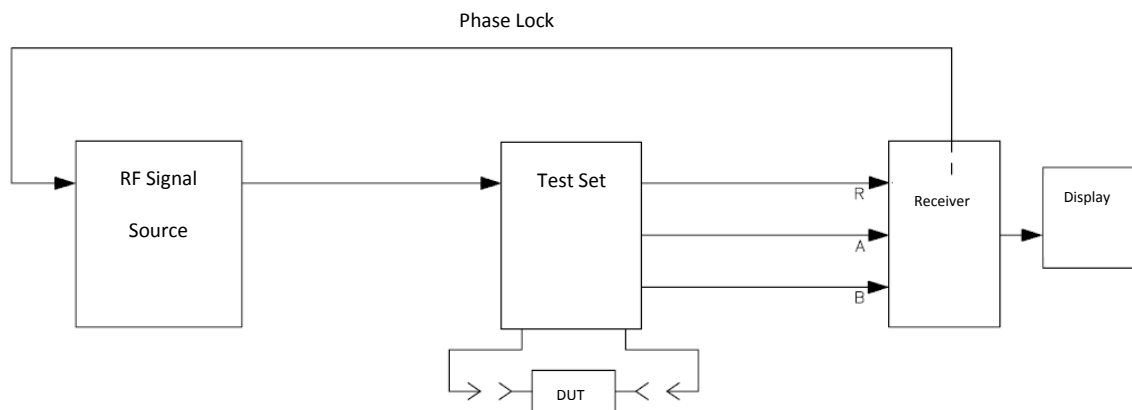


Figure 4.3. A simple schematic of the HP 8720 ET VNA.

Frequency accuracy and phase measuring capability is achieved by phase locking to a highly stable crystal oscillator. The test set provides signal-separation and the test ports which connect to the device under test. Some of the transmitted signal is routed through input R where it is sampled by a phase detection loop and fed back to the source. The reflected signal is routed from port 1 to the A input of the receiver and the transmitted power to the B input of the receiver.

The receiver contains three sampler mixers for R, A and B inputs which feed the signals into the analogue-to-digital converter where they are converted into a digital signal where amplitude and phase are measured simultaneously. The microprocessor performs all additional functions such as error correction, averaging, scaling, formatting, and marker functions. The microprocessor also

allows the VNA to be controlled by the front panel or via the general purpose interface bus (GPIB) interface. The formatted data is displayed on the monitor or acquired by GPIB interface. The VNA is also capable of converting the measured s-parameter data into the equivalent complex impedance (Z), admittance (Y) or inverted s-parameters (1/S).

The VNA was remotely controlled by PC via GPIB using custom programs written in LabVIEW (Appendix 1.1).

4.3. Chapter 4 Summary

This chapter details the equipment used in the research as to avoid repetition. Methods for sensor simulation and fabrication techniques are included along with details pertaining to the signal generation and analysis equipment (vector network analyser). The customised software used to interact with the VNA is also detailed with the software used to conduct statistical analysis of the data.

Chapter 5. Coplanar sensor development

Due to the physical size and subsequent use of resources of cavity resonators (i.e. large hollowed out metal blocks), a smaller and cheaper method of assessing the dielectric characteristics of samples was pursued. A number of methods were reviewed but coplanar sensors were chosen due to their low profile, ease of fabrication, straightforward to feed with a microwave signal, narrow bandwidth, can be incorporated with other circuit elements and have acceptable radiation properties. Coplanar sensors were also chosen due to the structure only interacting with samples very close (< 1 mm) to the patterned surface as determined by simulation [292, 293]. However, coplanar sensors have disadvantages such as less well understood characteristics, interference from external radiation sources and difficulty in deriving standardised results for permittivity. The design process was iterative, where each design was studied for pros and cons with the next design prototype designed accordingly.

The resonant frequency of a patch antenna may be estimated by the equation

$$f_0 \cong \frac{c}{\sqrt{\epsilon_r}} \left(\frac{1}{2L} \right) \quad \text{Equation 5.1}$$

where f_0 is the primary resonant frequency of the structure, c is the speed of light, ϵ_r is the relative permittivity of the substrate and L is length of the transmission path. From this it can be deduced that a substrate with a high permittivity allows for smaller antenna design at a fixed resonant frequency. However, coplanar resonant structures have fringing fields due to the open end nature of the patch. To account for this the fringing length must be incorporated into the equation so as to yield the effective length of the structure [294, 295].

$$f_0 \cong \frac{c}{2\sqrt{\epsilon_r}} \left(\frac{1}{L_e} \right) \quad \text{Equation 5.2}$$

where L_e is the effective length. The bandwidth of the resonant structure is directly proportional to substrate thickness and indirectly proportional to the permittivity of the substrate where thinner and high permittivity substrates decrease bandwidth.

The use of a shorting wall or pin is a well-known method for reducing the physical size of microwave resonant structures. Adding a shorting post makes a micro-strip antenna act like a quarter wavelength structure reducing physical size by half.

Meandering the length of the patch is also an effective method of reducing the physical size of resonant structures. In the case of a rectangular patch, several narrow slits may be inserted into non-radiating edges having the effect of lengthening the current path.

A number of coplanar sensors were researched in the literature to find a suitable conformation with desirable characteristics of narrow bandwidth and low electrical length to physical size ratio. Initially work focused upon understanding the effects on electrical length and attenuation of different micro strip structures such as rings, interdigitated fingers, loops and coupling gaps. Below are a number of designs that were investigated to understand the effect of different coplanar configurations (Figure 5.1).



Figure 5.1. A number of coplanar PCB based resonant sensors.

Following this, a more rigorous development pathway was established to identify the effects of interdigitated fingers and loops. The initial design chosen was a circular patch which was fed by a strip connected to the SMA connector, sometimes known as a lollipop patch due to the resulting pattern.

Although the radiation characteristics of this resonant structure were well defined, the resonant frequency was too high to interact with the target β -dispersion (MHz range). In an effort to reduce the resonant frequency, the patch sensor was shorted to the earth as previously described in the literature [296, 297]. The next step involved splitting the patch into two segments and incorporating capacitive fingers to increased interaction with the material under test. Parallel to this, a ring was incorporated into the design in place of shorting the patch through the substrate to increase fabrication reliability. These two concepts were then combined to form a sensor with capacitance and inductance which reduced the resonant frequency of the sensor to the lower end of the microwave frequency range.

SMA connectors were used to connect the resonant structures to the VNA via coaxial cable. SMA is a very common, popular and readily available connector, which is used to connect micro-strips. The connector used is a 50 Ω probe with a central conductor extended to connect to the micro-strip element. Depending on the size of the pattern or substrate, the connector dimensions may be different [49]. Molex 50 Ω edge mount connectors (RS, U.K.) were used in this work, as they are designed to excite a printed circuit horizontally thus minimising discontinuities and therefore source/load mismatch.

At each stage of development the overall dimensions remained constant as did the micro-strip feed width and patch diameter. Each was designed to be affixed to 3D printed wells with a diameter of that of the patch which would hold the sample above the sensor (Figure 5.2). These were fabricated from ABS plastic and had a floor thickness of 0.5 mm.

The suitability of each sensor was assessed by measuring the difference in resonant frequency for lipid positive and lipid negative yeast cell samples within the well. A “good” sensor was one whose resonant frequency shifted significantly with the change in lipid positive and negative yeast cell samples i.e. high sensitivity.

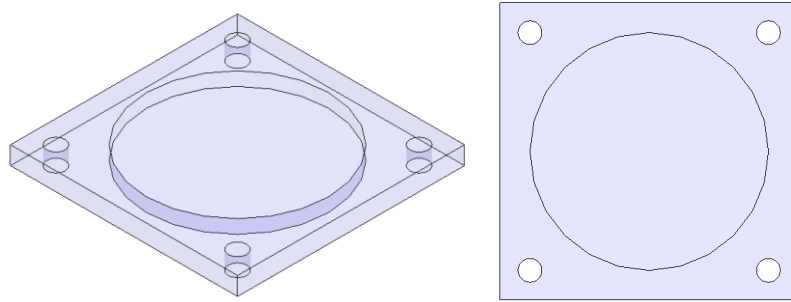


Figure 5.2. Schematic of the 3D printed ABS sample well.

5.1. Development of sensor SD-1

The initial design was a coplanar circular monopole half-wave antenna comprising of a circular disc fed by a micro-strip waveguide backed by a ground plane (Figure 5.3). This design was chosen due to its predictable nature and ease of design (i.e. symmetrical). The size of the sensor was dictated by the size of wells on 6 x 4 microtitre plates. The coplanar structure is routed from copper laminate on a substrate ($\epsilon_r = 4.35$) of 1.4 mm thickness. The total dimensions of the substrate are 25 mm (width) by 35 mm (length). Using Equation 5.1 and Equation 5.2 the effective resonant frequency of the circular patch was designed to be approximately 5 GHz. The coplanar structure was characterised using Ansoft HFSS.

Figure 5.4 shows the electric field magnitude of SD-1 at its fundamental mode. It can be seen that the propagated field results from fringe fields as a result of the circular patch acting as a vertically enclosed cavity with boundaries formed by the copper laminate. The vertical boundaries around the circumference of the circular patch are loosely alike to that of a fully enclosed cavity. But because of the undefined boundary the field extends the outer periphery to some degree.

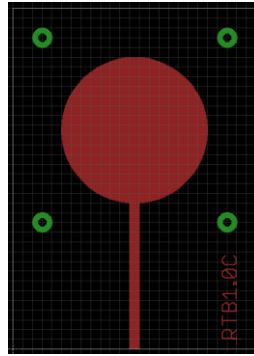


Figure 5.3. Schematic of sensor SD-1 in Eagle PCB software.

Figure 5.4 demonstrates the concept of a partially enclosed cavity with electric field minimum and maximum at the centre and periphery respectively. It may be noted that there is significant field intensity at the patch feed by the micro-strip waveguide as a result of impedance mismatching.

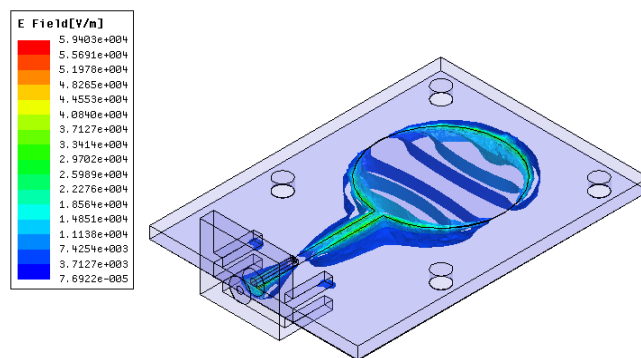


Figure 5.4. Electric field of sensor SD-1 at fundamental mode with a simulated frequency of 5.15 GHz and phase of 0 degrees.

Slots were introduced into the patch along the feed axis as a method of impedance matching (Figure 5.5) and were investigated using Ansoft HFSS software.

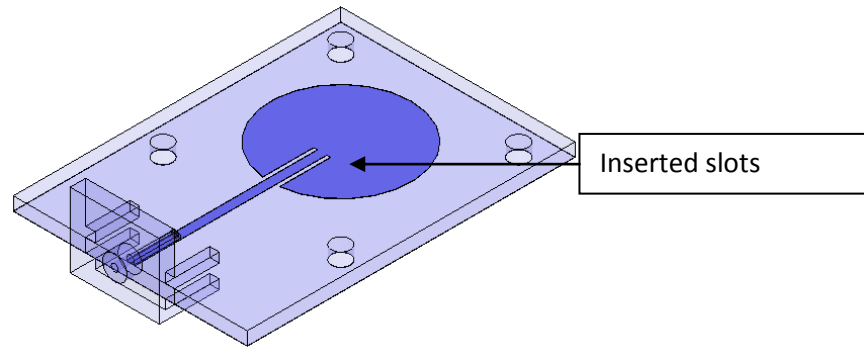


Figure 5.5. Schematic of SD-1 with added slots along the feed line to match sensor impedance to source.

The length of the slots into the circular patch greatly affects the impedance of the sensor. This allows the sensor to be easily tuned to match the impedance of the source [298] This was demonstrated in HFSS simulation software (Figure 5.6).

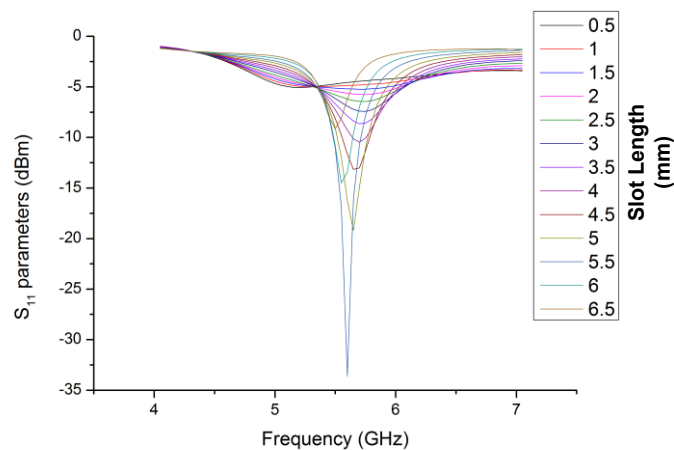


Figure 5.6. S₁₁ parameters of SD-1 with impedance matching slots of variable length (mm).

The HFSS simulations suggest that slots of 5.5 mm closely match the sensor impedance to that of the source.

The implemented sensor was then tested using lipid accumulating and non-accumulating yeast cultures. Yeast cells of the genus *Lipomyces Starkeyi* were cultured under different conditions to alter the cell phenotype. When cultured in carbon rich / nitrogen limiting media, the cells accumulate neutral triacylglycerols due to the abundance of carbon. In contrast, when cultured in nitrogen rich / carbon limiting media the cells use up any neutral triacylglycerols present as a carbon

source. Cells were cultured over 5 days at 30 °C in specified media in an rotary incubation chamber at 150 rpm. Error bars represent the range of measured results.

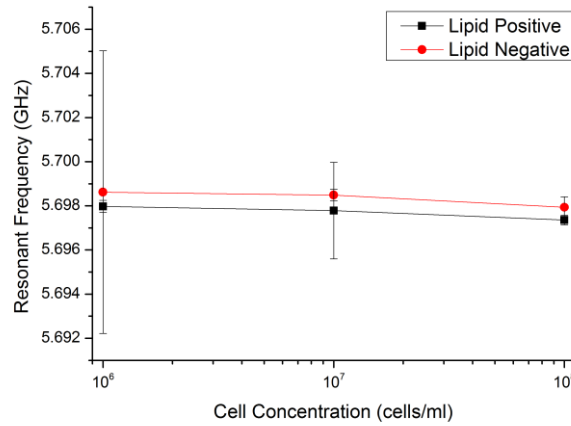


Figure 5.7. *S11 resonant frequency (GHz) of SD-1 sensor interacting with yeast cell samples as a function of cell concentration (cells/ml).*

Introducing the samples into the well shifts the resonant frequency of the sensor to approximately 5.7 GHz. From Figure 5.7 it may be seen that there is very little difference in the sensor resonant frequency between the lipid positive and lipid negative yeast culture samples. This was due to the electric field intensity being greatest at the periphery of the patch and not interacting with the sample. However, lipid positive samples induced the structure to resonate at a lower frequency than lipid negative cultures.

5.2. Development of sensor SD-2

In an effort to reduce the resonant frequency of the sensor, a shorting post of 1 mm diameter was added to the circular patch (Figure 5.8). This modified the half-wave coplanar antenna into a quarter-wave coplanar antenna theoretically reducing resonant frequency. This also has the effect of only having one radiating edge as fringe fields caused by coupling are eliminated. This is demonstrated in Figure 5.9.

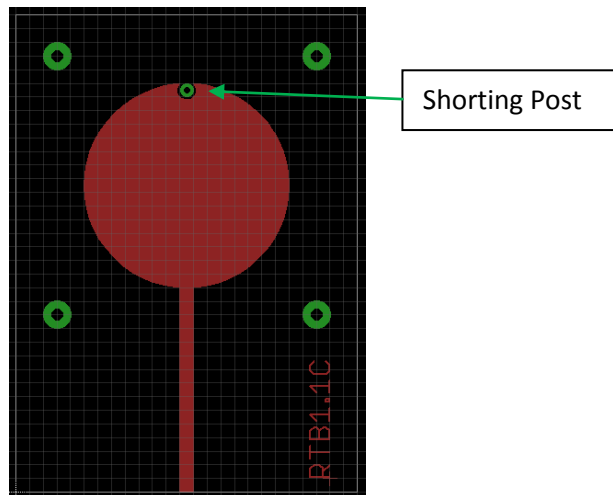


Figure 5.8. Schematic of sensor SD-2 in Eagle PCB software.

However, the position of the shorting post plays an important role in the characteristics of the structure and so was investigated using Ansoft HFSS software. For each position of the shorting post it is also necessary to carry out impedance matching using the slot method as with SD-1 (Figure 5.10).

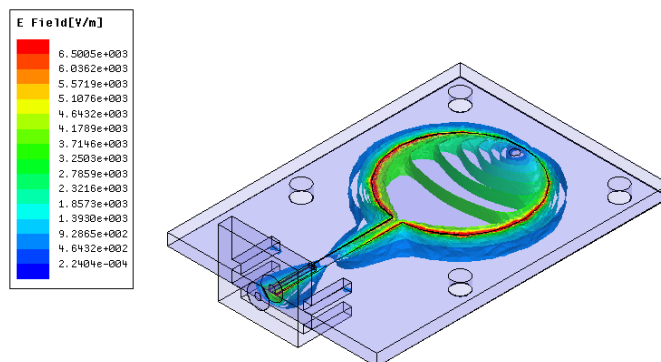


Figure 5.9 Electric field of sensor SD-2 at fundamental mode with a simulated frequency of 2 GHz and phase of 0 degrees.

From the data produced by the simulations the optimum combination of shorting post configuration and impedance matching slots is 2 mm and 13.5 mm respectively.

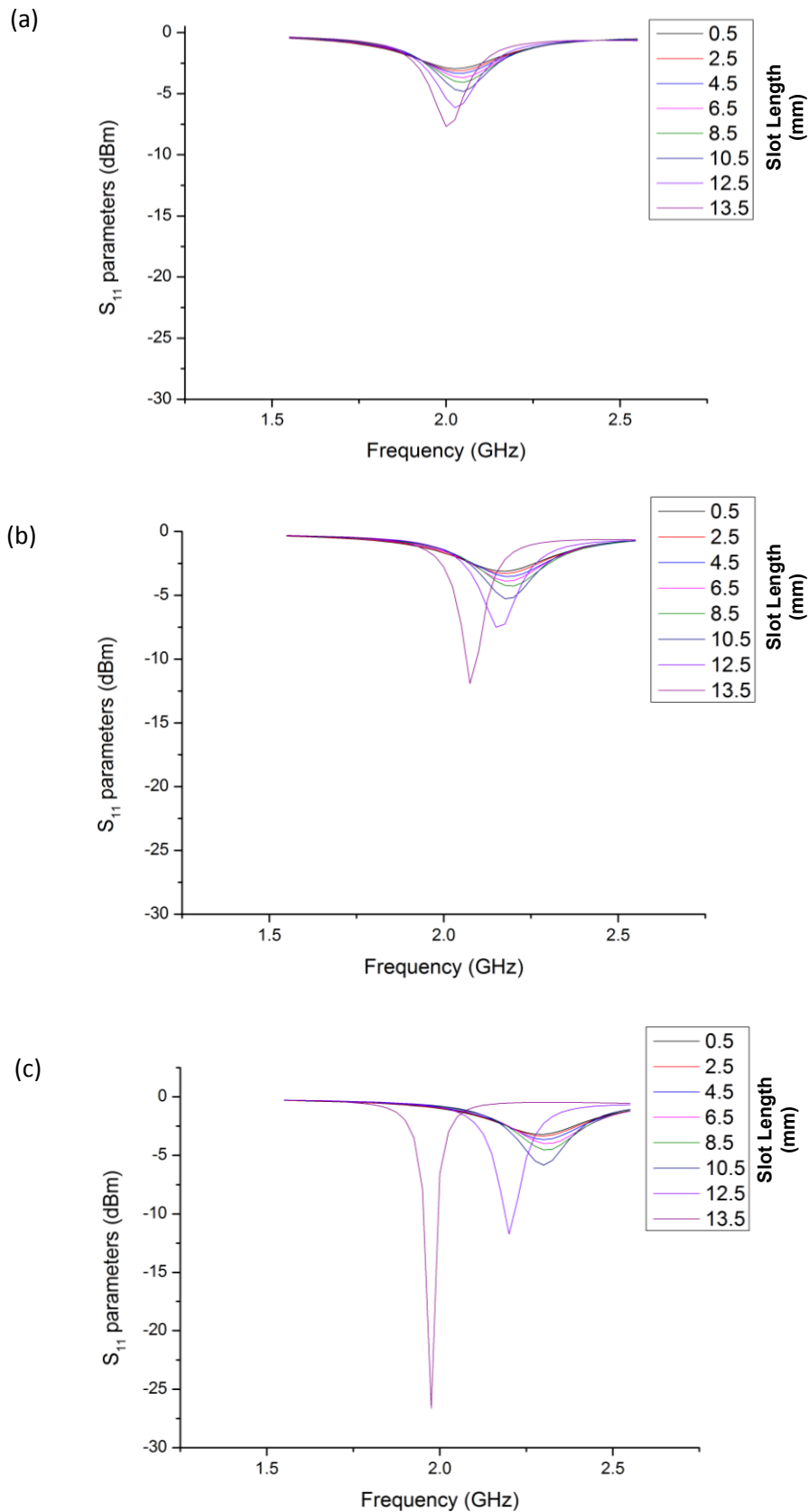


Figure 5.10. Simulated S_{11} parameters of sensor SD-2 with the shorting post 0 mm (a), 1 mm (b) and 2 mm (c) from the boundary of the circular patch. The length of the slots are varied (mm) to match the impedance for each shorting post configuration.

The implemented sensor was then assessed using lipid accumulating and non-accumulating lipids as described in section 5.1.

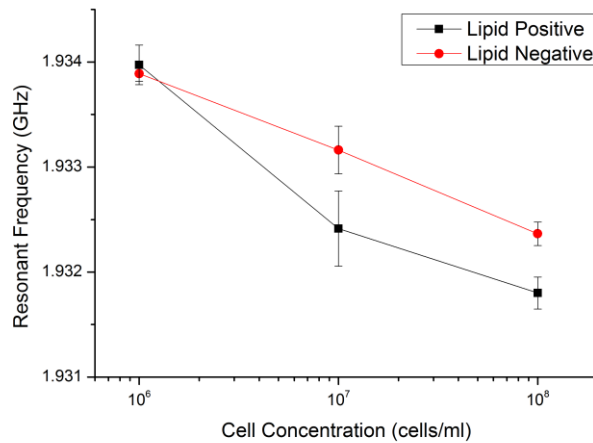


Figure 5.11. S11 resonant frequency (GHz) of SD-2 sensor interacting with yeast cell samples as a function of cell concentration (cells/ml).

Shorting the patch has the effect of reducing the resonant frequency of the structure to approximately 1.93 GHz when the samples are situated in the well. As may be seen in Figure 5.11, SD-2 also performs much better at differentiating the lipid positive and lipid negative yeast samples than SD-1 with a difference of 0.7 MHz in resonant frequency between the two samples at a cell concentration of 1×10^7 , above the range of error. This is due to the electric field radiating around the circumference of the patch. Increasing cell concentration results in lowering the resonant frequency indicating an increase in capacitance. The presence of lipid droplets in the yeast cells further increases the capacitance of the sample additionally reducing the resonant frequency. The greatest shift of resonant frequency between the two culture conditions was seen at a cell concentration of 10×10^7 .

5.3. Development of sensor SD-3

For SD-3, interdigitated capacitive fingers were introduced into the design with the structure shortened as in SD-2 (Figure 5.12). Capacitive sensors have been utilised in many sensing applications in recent years [299-303]. Introducing interdigitated fingers into the structure creates

an interaction zone in the centre of the patch where electric field is at a maximum caused by the coupling between the two halves of the patch.

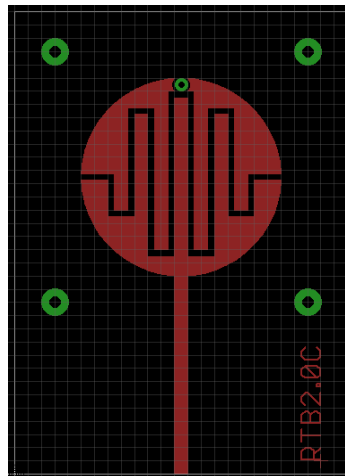


Figure 5.12. Schematic of sensor SD-3 in Eagle PCB software.

Figure 5.13 demonstrates the electric field propagated by the structure and within the fr4 substrate. It may be seen that coupling fields between the interdigitated fingers creates an electric field with which the sample may interact. However, the dimensions of the distance of separation of the two interdigitated halves influence the characteristics of the sensor and so were investigated using Ansoft HFSS software.

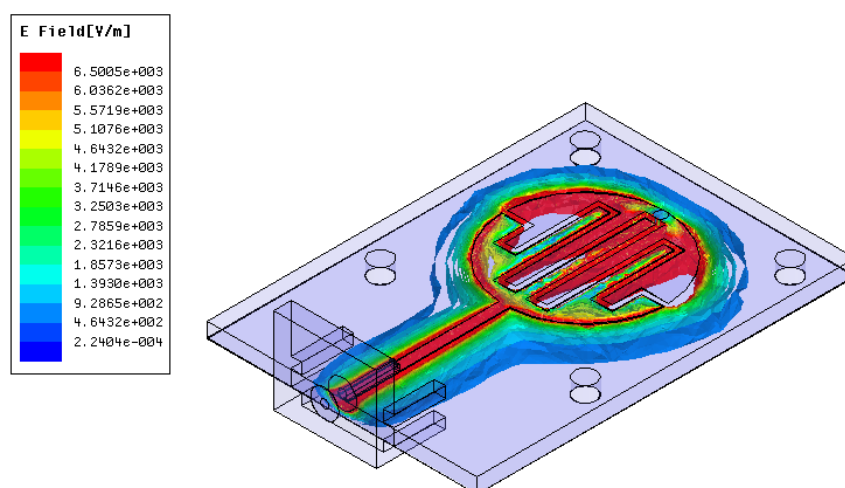


Figure 5.13. Electric field of sensor SD-3 at fundamental mode with a simulated frequency of 2.45 GHz and phase of 0 degrees.

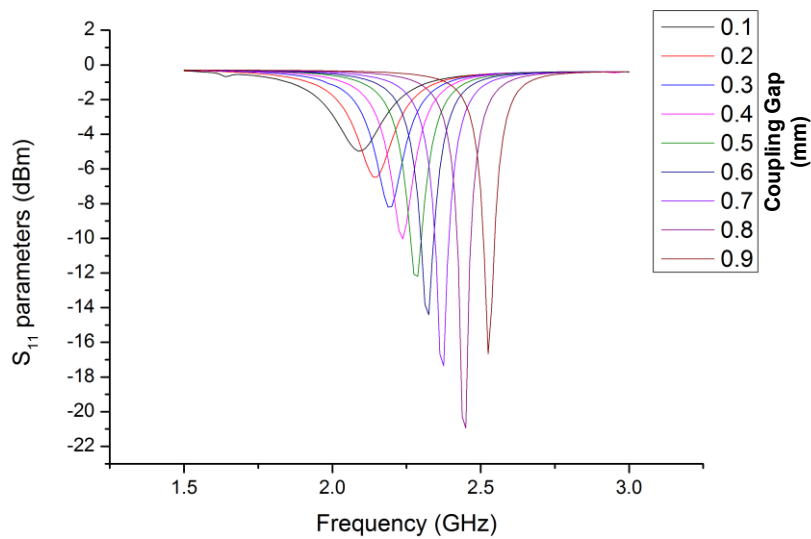


Figure 5.14. Simulated S_{11} parameters of sensor SD-3 with varied coupling gap (mm).

Figure 5.14 demonstrates the characteristic of the sensor when the coupling distance between the two halves of the capacitor is varied. Simulation of the S_{11} parameters and the smith chart indicate that the best performing SD-3 sensor to be one that is separated by 0.8 mm. The coupling distance of a capacitor is highly correlated to the amount of energy that may be stored which is demonstrated by **Error! Reference source not found.**. Increasing the distance between the capacitor electrodes decreases the capacitance stored. Therefore, it may be construed that at lower separation distances, there is too much capacitance to achieve impedance matching and above 0.8 mm there is too little as correlated in **Error! Reference source not found.**.

The implemented sensor was then assessed using lipid accumulating and non-accumulating lipids as described in section 5.1.

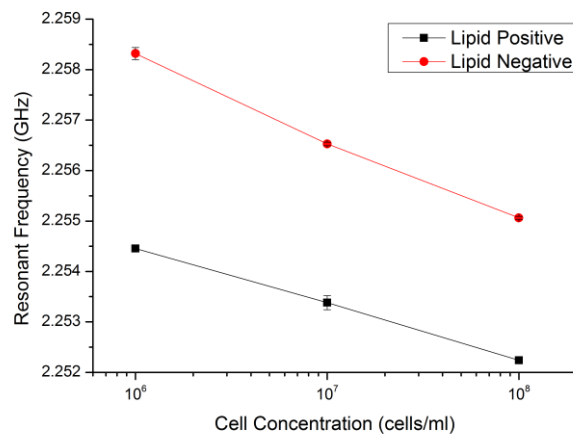


Figure 5.15. *S11 resonant frequency (GHz) of SD-3 sensor interacting with yeast cell samples as a function of cell concentration (cells/ml).*

As may be seen in Figure 5.15, the interdigitated fingers of SD-3 increase the sensitivity of the sensor to differentiate lipid positive and lipid negative samples. Increasing cell numbers results in increased capacitance caused by the presence of cells, lowering the resonant frequency of the structure. This equates to a sensitivity of 22.3 and 32.9 kHz/cell $\times 10^6$ for lipid positive and negative cells respectively. Again, lipid positive samples result in shifting the resonant peak to lower frequencies than that for lipid negative samples indicating increased capacitance. However, introducing the sample shifts the resonant frequency of the structure to between 2.25 and 2.26 GHz, higher than that of SD-2 and above that of the target frequency of the β dispersion. The greatest shift of resonant frequency between the two culture conditions was seen at a cell concentration of 10×10^6 .

5.4. Development of sensor SD-4

In order to reduce the resonant frequency of the sensor the capacitance introduced in SD-3 would be balanced by induction produced by a ring encircling the patch. To achieve this, the short post was replaced by shorting the patch with a micro-strip ring routed to the earth terminals of the SMA connector (Figure 5.16). In this manner, inconsistencies caused by soldering of the shorting post during prototype fabrication seen in SD-2 and SD-3 were also removed.

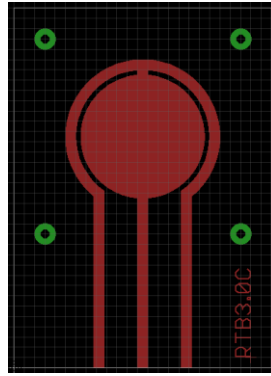


Figure 5.16. Schematic of sensor SD-4 in Eagle PCB software

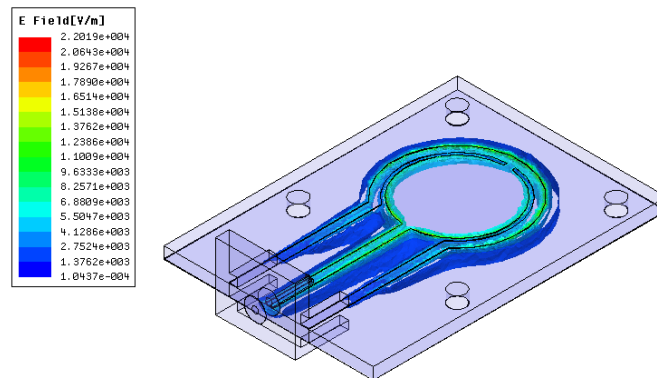


Figure 5.17. Electric field of sensor SD-4 at fundamental mode with a simulated frequency of 2.67 GHz and phase of 0 degrees.

Figure 5.17 shows the electric field at the fundamental mode of SD-4. With this configuration the electric field is closely associated with the coupling gap between patch and ring elements. The size of the coupling gap between the ring and patch influences the characteristics of the sensor. This variable was investigated using Ansoft HFSS.

Figure 5.18 demonstrates the simulated characteristics of the sensor when the coupling distance between the ring and central circular patch is varied. Simulation of the S_{11} parameters and the smith chart indicate that the best performing SD-4 sensor to be one that is separated by 0.2 mm. Interpretation of the simulation data suggests that smaller separation distances improve the quality factor of the sensor. Introducing an inductive element into the design shifts the resonant frequency of the sensor to approximately 2.3 GHz when the sample is present, not too dissimilar a frequency to that of SD-3.

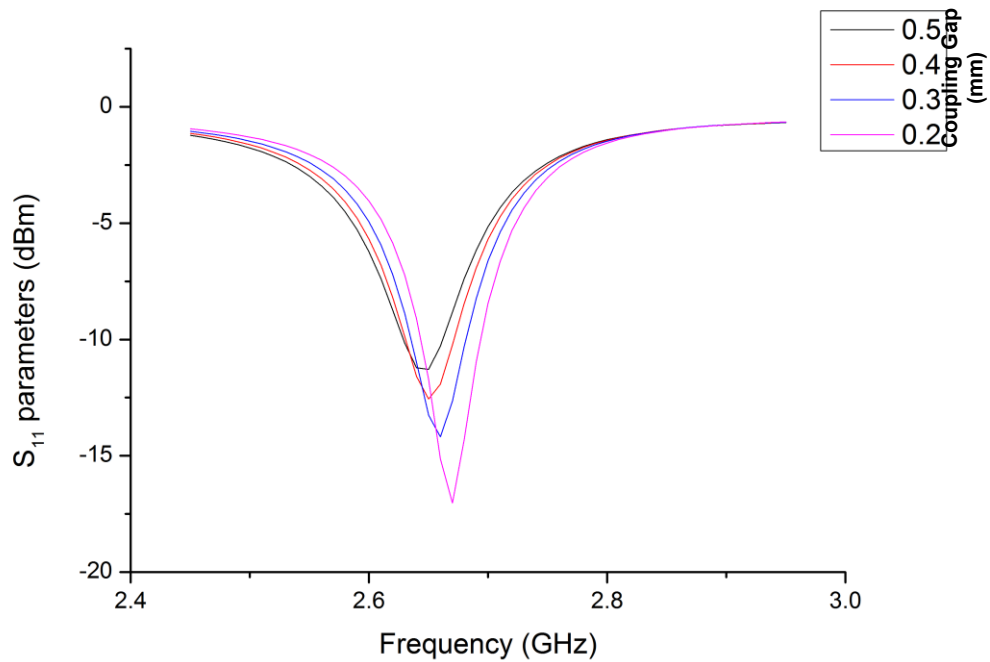


Figure 5.18. Simulated S_{11} parameters of sensor SD-4 with varied coupling gap (mm).

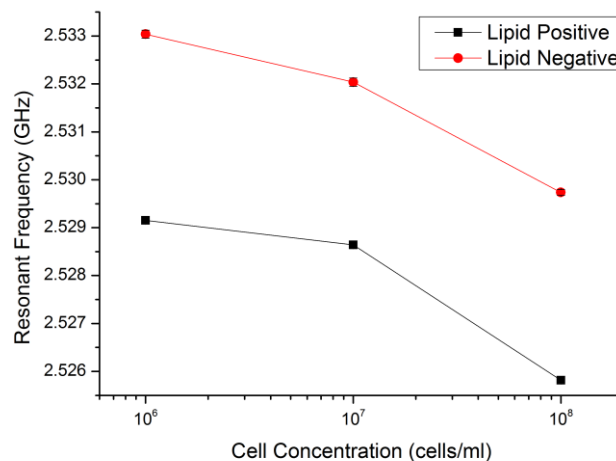


Figure 5.19. S_{11} resonant frequency (GHz) of SD-4 sensor interacting with yeast cell samples as a function of cell concentration (cells/ml).

Figure 5.19 demonstrates lipid positive and lipid negative yeast cultures being differentiated at log concentration of cells. Again, it can be seen that increasing cell concentration decreases the resonant frequency of the sensor with lipid positive cultures further reducing the frequency. Sensitivity was calculated at 33.7 and 33.3 kHz / cells $\times 10^6$ for lipid positive and negative cultures respectively. The greatest shift of resonant frequency between the two culture conditions was seen at a cell concentration of 10×10^6 .

5.5. Development of sensor SD-5

Sensor 5 incorporated elements from the above sensors into a single resonant structure (Figure 5.20) by splitting the patch of SD-4 with the interdigitated design of SD-3.

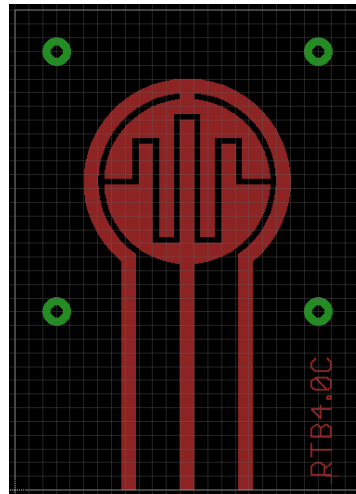


Figure 5.20. Schematic of sensor SD-5 in Eagle PCB software.

Figure 5.21 demonstrate the electric field propagated by the structure and within the fr4 substrate. It may be seen in Figure 5.21 that coupling fields between the interdigitated fingers and between the patch and shorting ring creates an electric field with which the sample may interact.

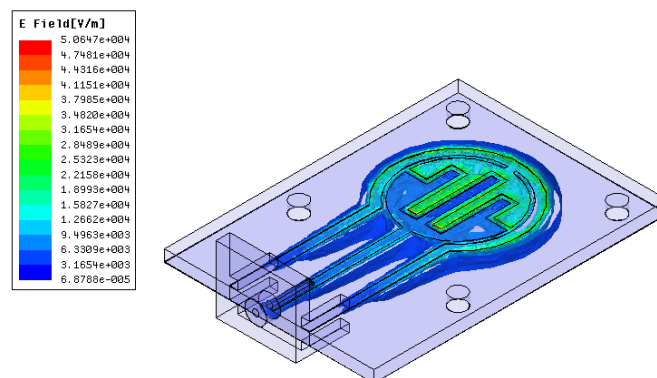


Figure 5.21. Electric field of sensor SD-5 at fundamental mode with a simulated frequency of 0.9 GHz and phase of 0 degrees.

However the coupling gaps of the element play a major role in the determination of its characteristics therefore these were investigated using Ansoft HFSS. Figure 5.22 demonstrates the simulated characteristics of the sensor when the coupling distance between the capacitor fingers is varied. Simulation of the S_{11} parameters and the smith chart indicate that the best performing SD-5

sensor to be one that is separated by 0.5 mm. It was found that the coupling distance between the central patch and the inductive ring in this design had no effect upon the simulated impedance of the sensor. Introducing an capacitive fingers into the design of SD-4 shifts the resonant frequency of the sensor to approximately 0.795 GHz when the sample is present. This is due to the matching of reactive elements (i.e. capacitance and inductance) of the sensor as stated in Equation 5.1.

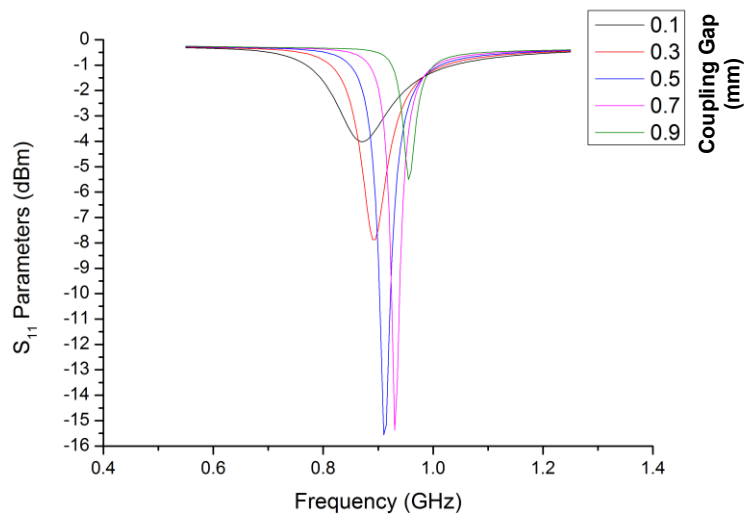


Figure 5.22. Simulated S_{11} parameters of sensor SD-5 with varied capacitor coupling gap (mm).

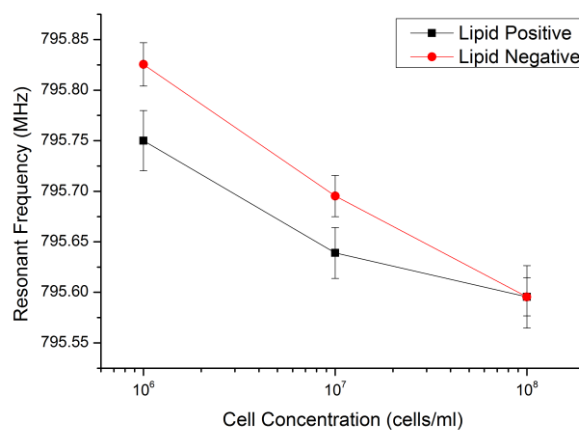


Figure 5.23. S_{11} resonant frequency (MHz) of SD-5 sensor interacting with yeast cell samples as a function of cell concentration (cells/ml).

Figure 5.23 shows the resonant frequency of the structure for each of the samples. Again, increased cell concentration and increased lipid concentration results in a lower resonant frequency than that for lower cell concentrations and lipid negative cell samples. Sensitivity to cell numbers was

calculated at 1.555 and 2.323 MHz / cell x 10^6 for lipid positive and lipid negative cultures respectively. Although SD-5 proved less adept at differentiating between lipid positive and lipid negative cell samples, the desired frequency for the sensor was attained. The greatest shift of resonant frequency between the two culture conditions was seen at a cell concentration of 10×10^7 .

5.6. Chapter 5 Summary

This chapter documents the sensor development process in detail. Initially a simple patch antenna was designed that was improved so as to increase the electrical length of the sensor concurrently reducing the resonant frequency of the sensor while retaining the sensor dimensions. The sensor was validated using neutral lipid positive and negative cell cultures at a number of concentrations to determine which sensor was most sensitive to the analyte. This was verified using statistical analysis between the lipid positive and lipid negative samples.

Chapter 6. Experimental Results

6.1. Quantification of neutral lipids in biological cells

Initially a resonant cavity and the small perturbation technique were utilised to calculate the dielectric characteristics of TAG micelles suspended in an ionic media. Resonant coplanar sensors were then developed and analysed upon the ability to differentiate TAG droplet positive and TAG droplet negative yeast cells. Concurrently, fabrication processes for fluidic cells were investigated and implemented to assess applicability and suitability. The final stages combined the developed coplanar sensor with the fluidic device. The resonant coplanar structure was optimised to allow the analyte to flow through the sensor. The final system was then characterised for suitability to quantifying lipid composition in yeast cells suspended in an ionic media and subsequently in defibrinised blood.

6.1.1. Micelle quantification

A logarithmic suspension of TAG was carried out in YEPD media. Olive oil was chosen due to the fatty acid composition while YEPD media was chosen to model a biological ionic media. YEPD was prepared to the following protocol: 10 g/ L of yeast extract, 20 g/ L of bacto-peptone and 20 g/ L of dextrose diluted in distilled water. Log suspensions were prepared in the following concentrations: 100, 10, 1 and 0.1 (v/v %) ready for impedance measurement.

Before measurement, the tube to be sampled would be vortex a number of times until an adequately homologous suspension was achieved. The VNA would scan the frequency range in 1 second sweeps, carrying out and averaging 10 sweeps.

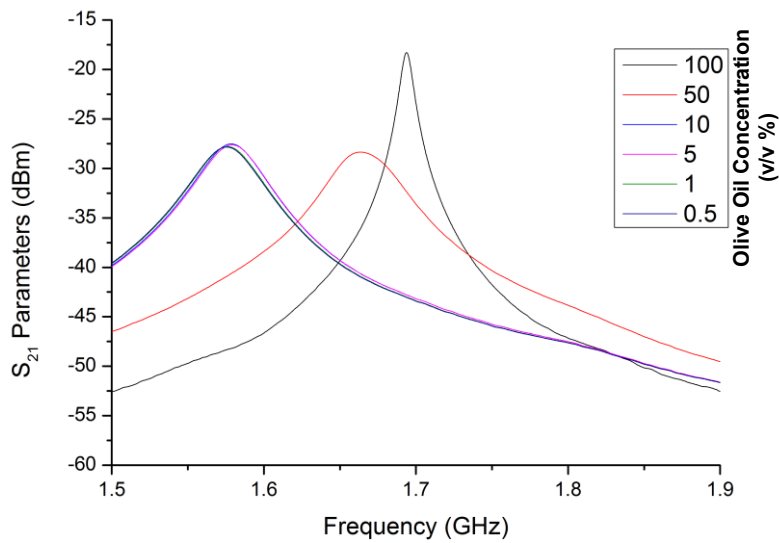


Figure 6.1. S_{21} parameters of olive oil in concentrations (v/v %) 100, 50, 10, 5, 1 and 0.5. S_{21} frequency ranges from 1.5 to 1.9 GHz.

Figure 6.1 shows the S_{21} parameters of select differing concentrations of Olive Oil suspended in YEPD (Table 6.1). It can be seen that as the concentration of olive oil increases, the resonant frequency of the sample increases or shifts to the right. The total frequency shift between 100% media and 100% oil is 0.62 MHz in the S_{11} parameters and 12.31 MHz for the S_{21} parameters. It can be seen that as the concentration of YEPD media decreases, the shift becomes less prominent resulting in the concentration curve seen in Figure 6.2. The intensity of the detected parameters, reflected and transmitted, varies by 9 dBm and 8 dBm respectively. Sensitivity of the resonant cavity to the olive oil was calculated at 0.12 MHz per percent of olive oil.

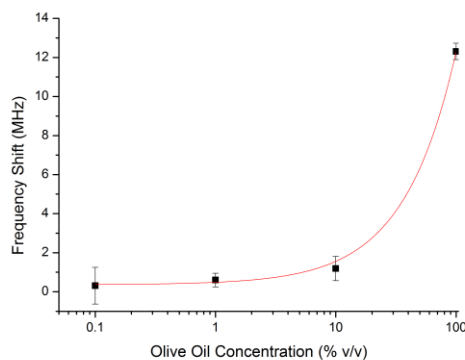


Figure 6.2. Graph showing the effect of olive oil concentration against S_{21} parameter resonant frequency shift.

TABLE 6.1. THE EFFECT OF OLIVE OIL CONCENTRATION ON S_{21} RESONANT FREQUENCY.

Olive oil concentration (% v/v)	Average frequency shift (MHz)	Standard deviation
0.1	0.31	0.94
1	0.6	0.35
10	1.19	0.62
100	12.31	0.42

TABLE 6.2. CALCULATED DIELECTRIC CHARACTERISTICS OF TAG MICELLE SAMPLES

TAG (% v/v)	ϵ' (ω)	ϵ'' (ω)	$\tan \delta$
100	3.004	0.063	0.021
50	10.106	0.612	0.059
40	17.658	1.423	0.080
35	18.215	1.635	0.090
32.5	19.423	1.650	0.085
30	20.078	1.714	0.085
27.5	21.138	1.844	0.087
25	22.992	2.066	0.090
22.5	23.434	2.110	0.090
20	24.585	2.190	0.089
17.5	25.336	2.206	0.087
15	25.489	2.247	0.088
12.5	25.118	2.217	0.088
10	26.028	2.345	0.090
5	26.269	2.480	0.094
2.5	26.256	2.441	0.093
1	26.588	2.441	0.093
0.75	26.504	2.453	0.093
0.5	27.024	2.549	0.094

Figure 6.3 shows the relative dielectric constant and dielectric loss of olive oil suspensions (Table 6.2). As the concentration of TAG increases within the suspension, both the dielectric constant and dielectric loss decrease with TAG concentration.

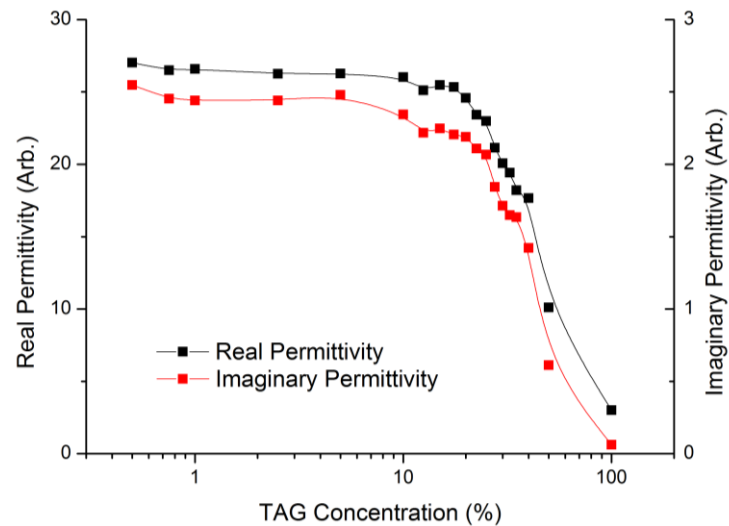


Figure 6.3. Graph showing a decrease in relative dielectric constant and dielectric loss as a function of olive oil concentration.

In Figure 6.4 the dielectric loss was plotted against the relative dielectric constant representing the complex permittivity. As the concentration of lipid droplet increases and the YEPD media inversely decreases, the permittivity of the sample decreases. Detailed results may be seen in Table 6.2.

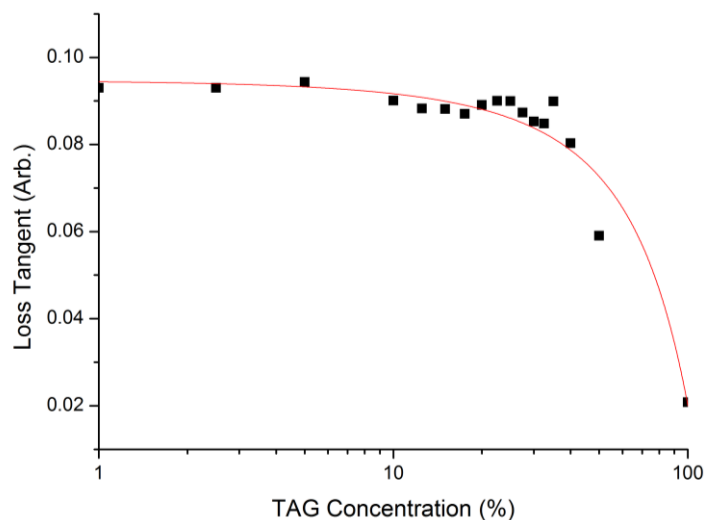


Figure 6.4. Plot of relative dielectric constant against dielectric loss to represent complex permittivity. Each data point indicates a concentration of olive oil suspension with oil concentration decreasing as the complex permittivity increases.

When the oil mixtures are agitated, the oil does not dissolve into the YEPD media. Instead the hydrophobic oil converges into lipid droplets resulting in a colloidal sample. At lower frequencies (\sim MHz region) charge builds up at the interface of the separate phases known as the Maxwell-Wagner effect and is responsible for the β -dispersion [8]. At the frequency of this experiment however it is likely that the major influence to relative complex permittivity is attributable to the organic and ionic content of the YEPD media. The media contains a combination of molecules necessary for yeast culture namely carbohydrates (sugars), amino acids (protein) and minerals (salt). Such molecules are well known to interact in aqueous solution, lowering the relaxation frequency of the water molecules into roughly the lower GHz frequency range [15]. This loss of polarisation is known as the δ dispersion attributable to the rotation of molecular side chains and bound water (Figure 2.6). Increasing the proportion of media increases the amount of material that can be polarised increasing the amount of energy that can be stored by the sample.

The instability of the samples under test is currently the largest source of error. After agitation, as the sample is introduced to the cavity the lipid droplets begin to converge into larger droplets until the lipid begins to separate into a different phase resting on the YEPD media. This results in the lipid droplet surface area being lower than the newly agitated suspension. As this process occurred, a decrease in the frequency perturbation was noted signifying a decrease in permittivity. Therefore, it is possible that a change to the β dispersion, due to the decreasing lipid droplet surface area, may contribute to the complex permittivity of the sample at this frequency. Acquiring data periodically from agitation to phase separation could be carried out to investigate the consequence of a changing droplet surface area. Stabilisation of the lipid droplets using phospholipids would improve the homogeneity of the suspensions also improving measurement repeatability. The use of phospholipids would also result in droplets that further resemble intracellular lipid droplets. Volume calculation of the sample and cavity also contributes to calculation error [11]. Precise measurement and documentation of the frequency shift and Q-factor by the VNA and data handling software reduced measurement error.

6.1.2. Lipid positive – lipid negative Lipomyces yeast culture differentiation

A sensor was designed to initially assess the suitability of using coplanar resonant structures to assess the lipid quantity of cells. The final sensor design was not used for this experiment as it was carried out during the sensor development phase. Therefore, an early variation of the finalised sensor design (SD-5) was used.

Yeast cells of the genus *Lipomyces* were cultured in Carbon rich and Nitrogen rich medias as described by A. Anschau, *et al.* [304]. Following culture and cell concentration normalisation, 2ml samples (n=10) were dispensed into 24 well microtitre plates ready for dielectric measurement. A water bath was employed to maintain the samples at 25 °C.

Measurements were made through a custom PCB based inter-digitated resonant structure designated RB04 (Figure 6.5 and Figure 6.6). The VNA was set to generate a signal between 3.2 and 3.5 GHz over 1601 data points for 10 linear frequency sweeps and calculate the S_{11} (reflection) parameters.

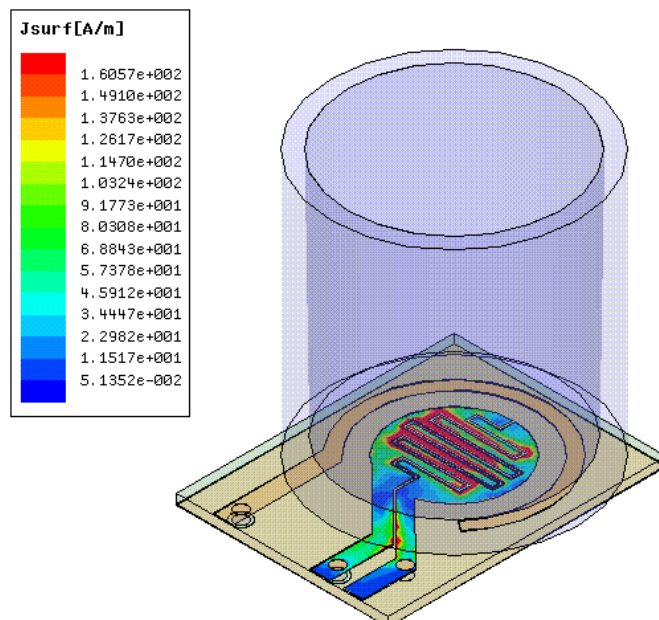


Figure 6.5. Simulated surface current of the PCB based resonant structure.



Figure 6.6. Realised PCB based resonant structure.

The resonant structure was mounted into a platform which would hold one well of the microtitre plate above the resonant structure. The plate could then be adjusted to position any of the other wells over the sensing area (Figure 6.7). In this way the electromagnetic field of the resonant structure could consistently interact with the sample under test.



Figure 6.7. Microtitre plate mounted upon the platform. The resonant structure may be seen in place below wells A4 (A) and C6 (B).

The calculated S-parameters for lipid positive and lipid negative cell cultures are presented in Figure 6.8. The molecular and structural composition of cells, interactions between molecules, interfaces between substrates and the frequency employed must be considered as to the contribution to the dielectric qualities of the samples under test.

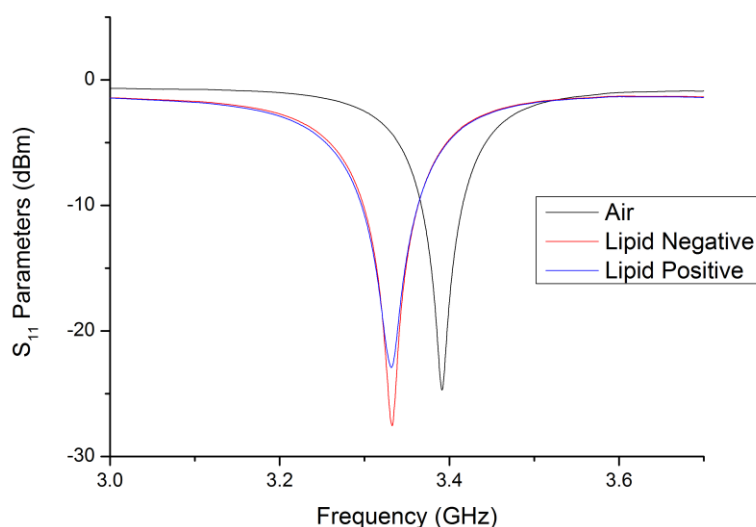


Figure 6.8. S_{11} Parameters of the resonant PCB structure when exposed to an empty microtitre plate (air) and when *Lipomyces* cell cultures are in place.

It may be seen that lipid negative cultures has the effect of shifting the resonant frequency of the structure 1.07 MHz more than the lipid positive cultures. It may also be seen that signal loss is greater in the lipid positive culture than the lipid negative culture.

TABLE 6.3. STATISTICAL ANALYSIS OF RESONANT FREQUENCY OF LIPID POSITIVE AND NEGATIVE BY ONE WAY ANOVA.

	DF	Sum of Squares	Mean Square	F Value	Prob>F
Model	1	2.05E+12	2.05E+12	2.91381	0.1099
Error	14	9.85E+12	7.04E+11		
Total	15	1.19E+13			

Statistical analysis of the resonant frequency by one way ANOVA found the shift in frequency between lipid positive and lipid negative cells not to be significant ($p > 0.05$).

This experiment has shown that lipid positive and lipid negative yeast cell cultures can be distinguished based on the electromagnetic properties of the samples using the coplanar resonant structure RTB04. The presence of lipid droplets causes a frequency shift indicating a change in dielectric constant and loss of the samples at this frequency range.

6.1.3. Saline concentration quantification

To test the bonding properties and suitability of the fluidic cell the system was employed to differentiate saline concentration in water. Saline was used as it is an easily differentiated sample using dielectric spectroscopy due to the ionic content of the saline drastically changing the conductivity of the sample. The use of PMMA was utilised due to its ability to be chemically bonded, easily handled and easily routed. A capacitive interdigitated resonant structure consisting of 8 interdigitated electrode pairs with a resonant frequency of approximately 1.14 GHz was used for this experiment (Figure 6.9).

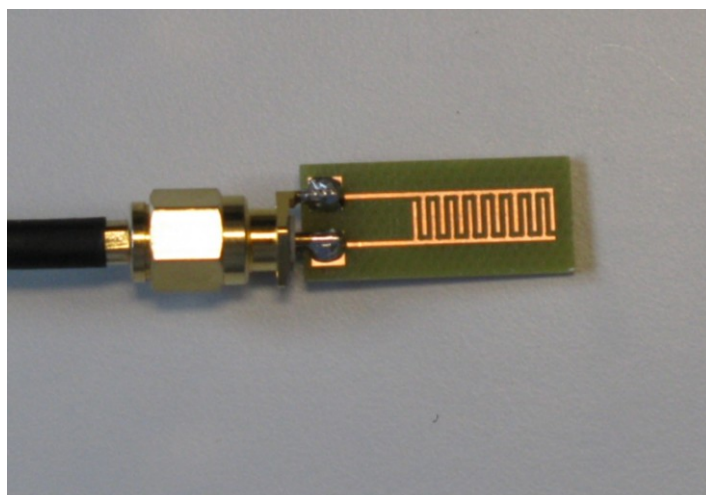


Figure 6.9. Picture of the resonant structure used in this experiment consisting of 8 interdigitated finger pairs.

The VNA was set to generate a frequency range of 1 to 1.3 GHz over 1601 data points. The saline solutions were mixed and pumped through the fluidic cell using the Perkin-Elmer HPLC pump. The experimental setup may be seen below (Figure 6.10.).

Figure 6.11 shows the resonant frequency and quality factor of the sensor as a function of saline concentration. It may be observed that the resonant frequency of the sensor decreases proportionally with the saline concentration. Sensitivity of the experimental setup was calculated at 0.23 MHz per percent of sodium chloride composition.

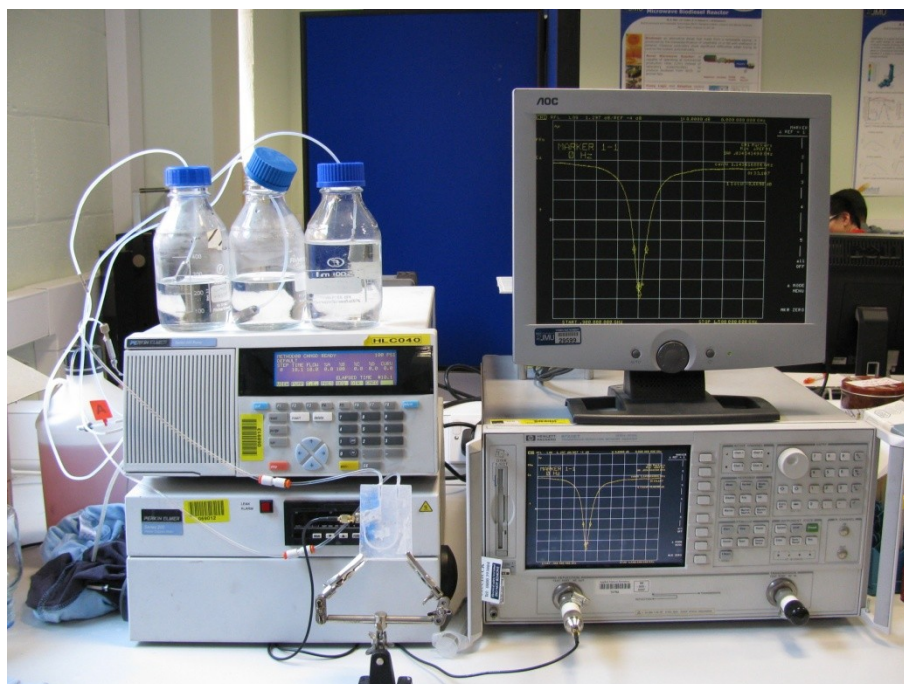


Figure 6.10. Experimental setup of the preliminary fluidic cell.

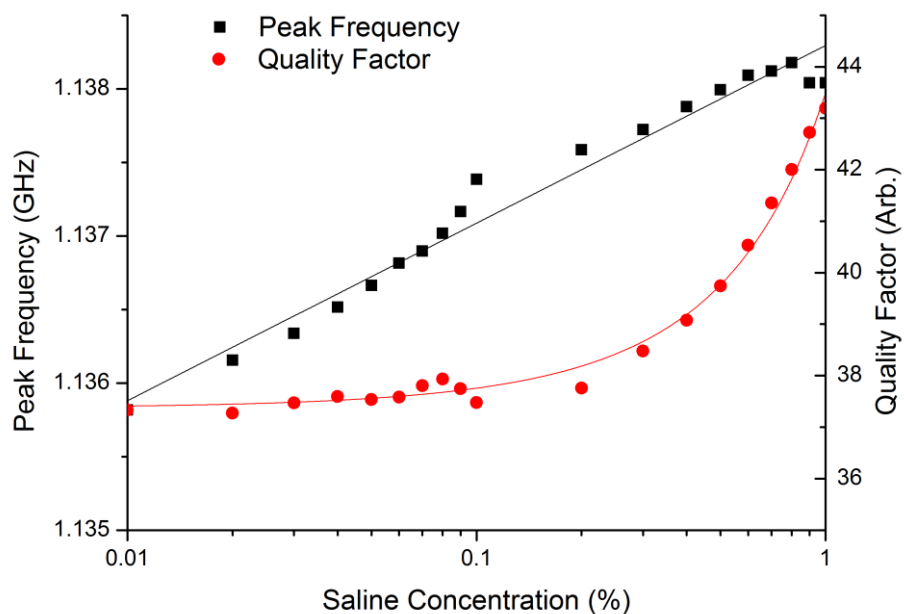


Figure 6.11. Resonant frequency (GHz) and quality factor (arbitrary) as a function of saline concentration (% w/v).

This experiment has shown that saline concentration can be distinguished using this methodology. However, several issues were identified from previous elements of the study such as limited analyte/radiation interaction, issues with fluidic cell bonding reproducibility and the frequency of the

sensor. The final configuration of fluidic cell and microwave coplanar resonant sensor were designed with these considerations in mind.

6.1.4. *The finalised experimental fluidic apparatus*

The finalised fluidic cell (FC) was fabricated from Poly(methyl methacrylate) (PMMA) rectangular rods. Two symmetrical halves were prepared by taping threads for the attachment of inlet and outlet nuts and ferrules. The coplanar sensor would then be positioned between the two halves (Figure 6.12). To increase the sensor interaction with the sample, the coplanar resonant structure was designed so the sample flows through the substrate.

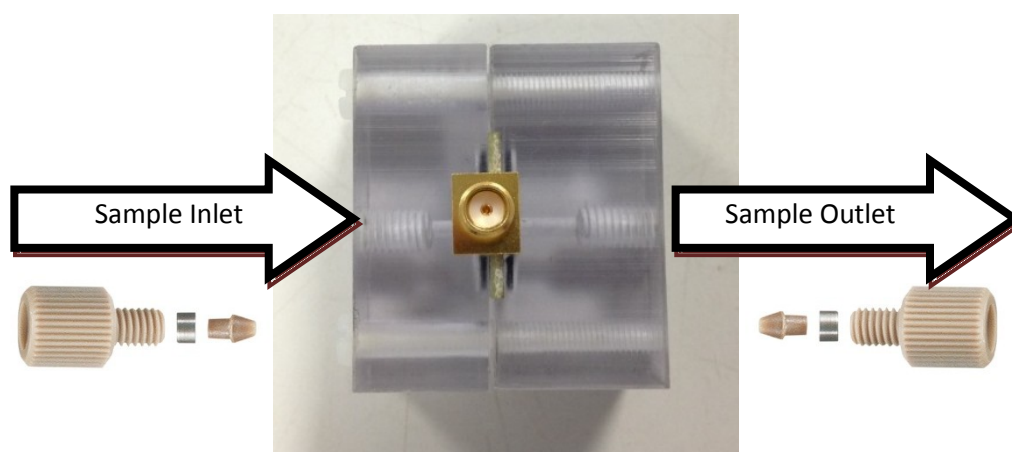


Figure 6.12. Fluidic cell configuration demonstrating the coplanar sensor (centre), taped threads and channels that lead to the measurement reservoir.

Incisions were milled through the substrate and ground plane at positions of highest electric field as indicated by simulation. The sensor was held in place by rubber o-rings ensuring a water tight seal around the measurement reservoir. The fluidic cell would then be connected to a quaternary pump (Perkin Elmer, Series 200) (Figure 6.13).

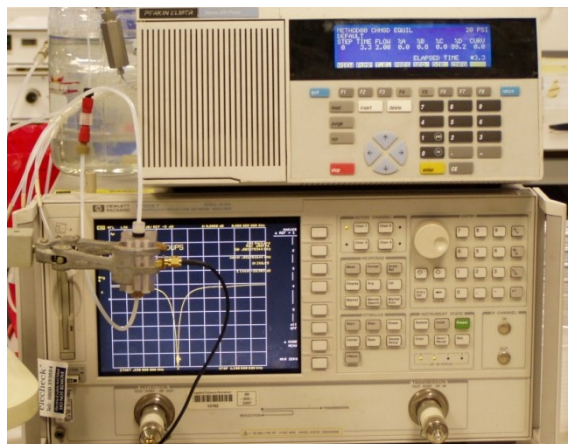


Figure 6.13. Photograph of the experimental setup, including quaternary pump, vector network analyser and sensor system.

The coplanar sensor comprises of tin plated copper laminated fr4 PCB which is patterned as seen in Figure 6.14. The fr4 substrate is milled so the solution flows through the capacitive fingers and inductive loop which are the areas of highest electric field, increasing the interaction of the EM field and the analyte sample. As seen in sensor development, the coupling gaps between the capacitive fingers influences the characteristics of the sensor. However, milling the substrate in the final sensor design proved to be troublesome and severely reduced the integrity of the capacitive interdigitated fingers. This constrained the width of the capacitive fingers to 1 mm. Therefore, the variables of the sensor needed careful consideration and was investigated using HFSS resulting in the finalised sensor design.

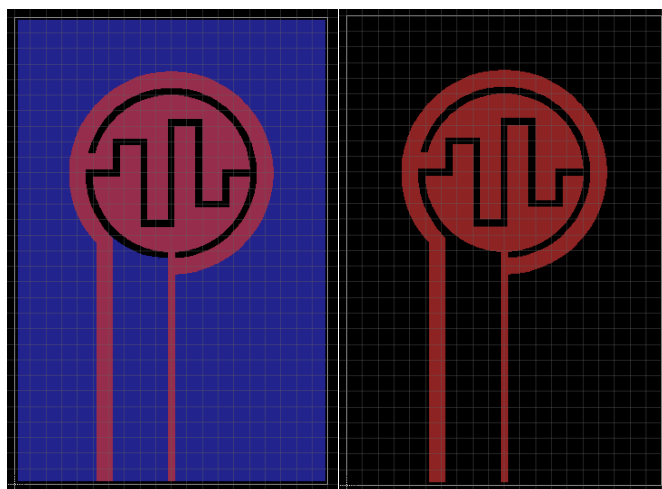


Figure 6.14: Schematic of the fluidic cell sensor with (left) and without (right) ground plane (blue).

This design was chosen in order to minimise losses and interferences which might occur from external sources, and also due to the fact that they can be made suitably small in order to be embedded within fluidic cell structures. Co-planar devices are well known for exhibiting this vital property, and therefore in this application offer a great deal of control in relation to how the sensor responds to analyte materials. In particular, the sensor is constructed to ensure that only a small area is sensitive to dielectric change, which enhances significantly its robustness for the aforementioned use. In addition, and as demonstrated in Figure 6.15, the electric field created by the sensor is dissipated significantly within 2 mm of its surface.

The sensor is constructed in-house using an end mill process. An FR4 epoxy substrate is used which is coated on both sides with a 35 μm copper layer. After the milling process, the copper is tin plated, and a side mount SMA connector is attached to provide connectivity to a VNA.

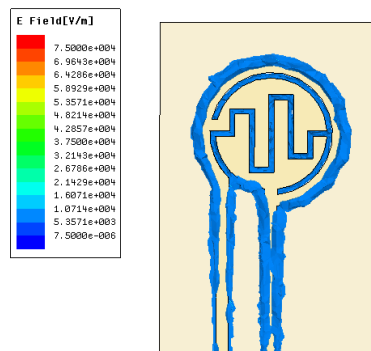


Figure 6.15. Simulation of fluidic cell coplanar sensor at a frequency of 0

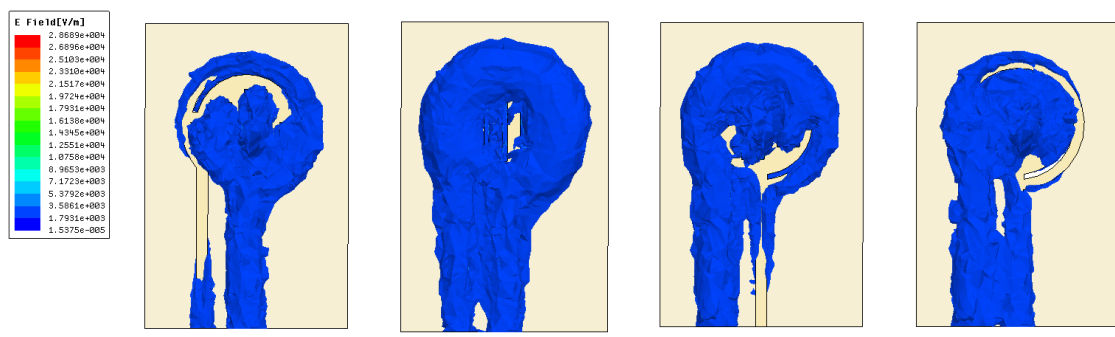


Figure 6.16. Simulated electric field (magnitude) of the finalised sensor at a frequency of 0.65 GHz and phase angle of 0, 45, 90, 135 and 180 degrees (left to right). The radiation pattern of the electric field suggests the field is elliptically polarised.

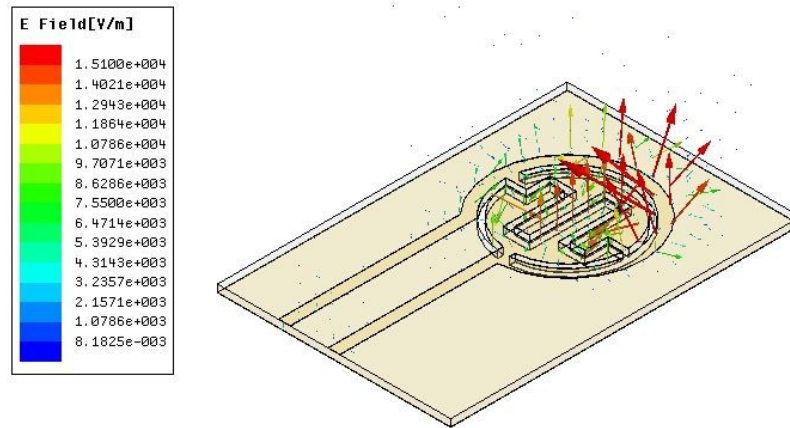


Figure 6.17. Simulated electric field (vector) of the finalised sensor at a frequency of 0.65 GHz and phase angle of 0, 45, 90, 135 and 180 degrees (left to right). The radiation pattern of the electric field suggests the field is elliptically polarised.

The optimal configuration as suggested during simulation of the sensor was then fabricated (Figure 6.18).



Figure 6.18: Image of the fabricated fluidic cell EM sensor.

6.1.5. Water absorption

One feature of note with the sensor, namely with the substrate material chosen, was the effect of water absorption. Over a period of time, the sensor substrate could be observed to absorb water, which was evident as drift in the sensor output signal. Fr4 is fibreglass reinforced epoxy laminate and is well known for absorbing liquids [305-308]. This was easily compensated however by allowing a significant pre-experimental period where the sensing system was exposed continuously to deionised water for a period > 40 hours.

The experimental setup and distilled water were encased in an incubator and allowed to stabilise at 30 °C. After temperature stabilisation a quaternary pump was activated pumping the distilled water from a reservoir through the fluidic cell and back to the reservoir until the resonant peak had sufficiently stabilised. The pump rate was fixed at a rate of 2ml / min. The sensor was connected to the VNA and set to generate a frequency sweep of 0.05 to 1 GHz over 1601 data points. Ten sweeps were performed and averaged for each measurement. A custom LabVIEW programme was utilised to initiate the sweeps at a set time interval of 60 seconds and gather the S_{11} parameters and the peak frequency data.

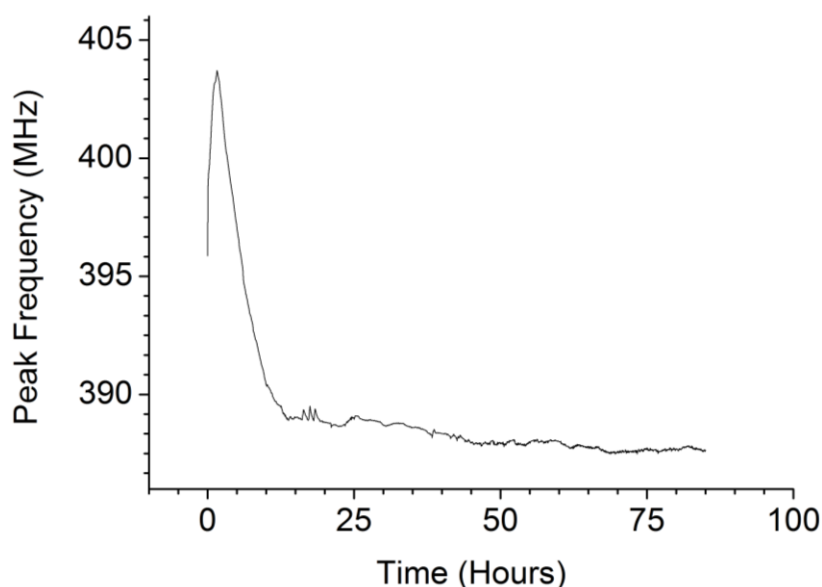


Figure 6.19: Resonant frequency change over 85 hours, indicating resonant frequency stabilisation after 45 hours.

After this time, the change in sensor output as a result of drift during a single experiment (i.e. maximum change is 6.17×10^4 Hz). This drift could be compensated during manufacture, and would not be a feature of any sensor used for *in-situ* measurements. This could also be resolved with the use of water resistant substrates namely PTFE. Figure 6.19 shows the variation of sensor output over time, with the largest change in resonant frequency apparent within the first 20 hours of operation. After this time the sensor output stabilises significantly, with small variations being accounted for by small changes (± 2 °C) in the laboratory temperature as a result of the thermostat controlled heating and ventilation system.

6.1.6. Temperature effects

An experiment was designed to investigate the effect of temperature on the resonant frequency of the system. A temperature range of 15 °C to 65 °C was investigated. The fluidic cell was contained together with a sample of circulating distilled water within a temperature controlled incubator. The distilled water was pumped from the reservoir through the fluidic cell using a quaternary pump and recycled back into the reservoir for a continuous period of 40 hours. At the beginning of the experiment the apparatus and sample were all at ambient temperature. The incubator was then set at 65 °C for a period of 20 hours before being deactivated and left to cool for a further 20 hours. The sensor was connected to the VNA and set to generate a frequency sweep of 0.05 to 1 GHz over 1601 data points. Ten sweeps were performed and averaged for each measurement. A custom LabVIEW programme was utilised to initiate the sweeps at a set time interval of 60 seconds and gather the S_{11} parameters and the peak frequency data.

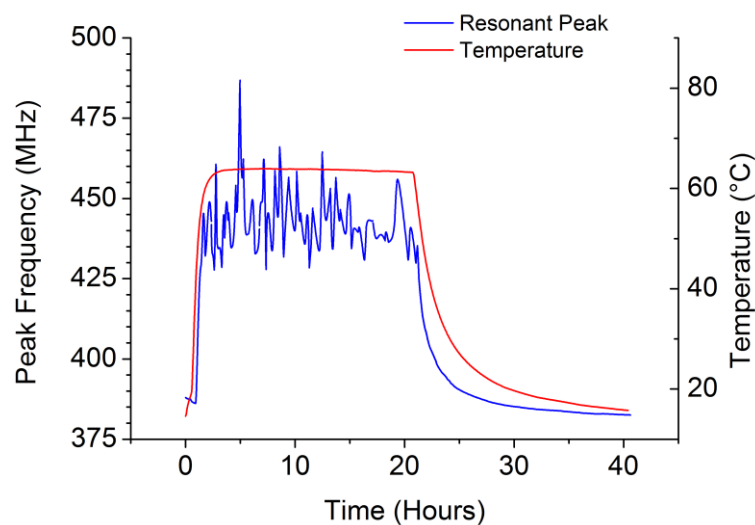


Figure 6.20: Resonant frequency shift as a result of temperature change, indicating instability over 45°C.

Figure 6.20 details the rise in frequency over the temperature range 15°C to 65°C. It may be noted that the resonant frequency shifts consistently with temperature up to approximately 60 °C. Above this temperature the resonant frequency becomes highly unstable. The frequency returns to a stable profile below this temperature and steadily returns to the initial frequency in close correlation with the decreasing temperature.

This experiment demonstrates the impact of temperature on resonant frequency. The effect was calculated between the temperatures of 20 °C and 60 °C to be an average of 1.83 MHz per 1 °C. This reiterates the need to carefully control the temperature of experiments including the analyte sample and apparatus. This also suggests that if the temperature is unable to be sufficiently controlled the ambient temperature could be monitored and be included into the analysis process as the result is highly correlated to this factor.

6.1.7. *Lipomyces lipid droplet quantification*

The experimental setup was assessed for its ability to distinguish the lipid content of biological cells. Two *Lipomyces* cell cultures were prepared in nitrogen limiting media (NLM) and carbon limiting media (CLM) as described in section 5.1. On days 4, 5 and 6 samples of the cultures were prepared ready for measurement (n = 10). Samples were centrifuged at 600 G and 10 °C for 5 minutes. Cell numbers and supporting media were normalised for each culture and day at 4×10^9 cell density and re-suspended in phosphate buffer solution (85 % w/v).

The analyte was pumped through the FC using a Perkin Elmer series 200 quaternary pump at a flow rate of 0.1 ml/min and pressure of <20 PSI. The sensor used in this study was bedded in using distilled water and later with phosphate buffer solution (85 % w/v). The analyte solutions and FC were housed in an incubation chamber and maintained at temperature of 25 °C. The sensor was connected to the VNA and set to generate a frequency sweep of 0.05 to 1 GHz over 1601 data points. Ten sweeps were performed and averaged for each measurement. A custom LabVIEW programme (as described in section 0) was utilised to initiate the sweeps and acquire the S_{11} parameters and the peak frequency data.

Figure 6.21 shows the resonant frequency of the sensor when interacting with lipid accumulating and non-accumulating *Lipomyces* cell suspensions on day 3, 4 and 5 of culture. The resonant frequency of the structure increases by 6.1 MHz over the measurement period from 320.7 MHz on day 3 to 226.8 MHz on day 6. Conversely, the resonant frequency for non-accumulating cultures

decreases from 318.8 MHz on day 3 to 318.0 MHz on day 6 and varies by 0.8 MHz. On day 6 the total difference in resonant frequency between the two culture conditions was 8.8 Mhz. Table 6.4 details the results of statistical analysis by means of two way ANOVA of the experimental results. The results indicate the resonant frequency of lipid accumulating and lipid non-accumulating is significantly different to a significance of 95 %.

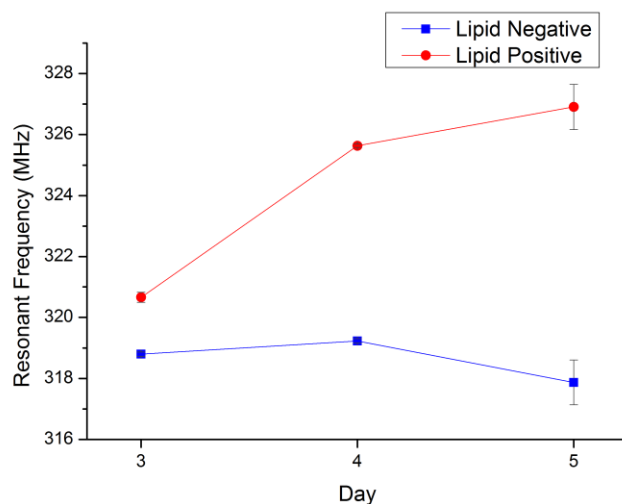


Figure 6.21: Resonant frequency of the sensor (MHz) as a result of accumulating lipid concentration in NLM cultures and lipid negative CLM cultures.

TABLE 6.4. STATISTICAL ANALYSIS OF RESULTS LIPID CULTURES BY TWO WAY ANOVA

	DF	Sum of Squares	Mean Square	F Value	P Value
Day	2.0000E+00	5.90E+16	2.95E+16	4.14505	0.02738
Culture Condition	1.0000E+00	3.61E+16	3.61E+16	5.06653	0.03307
Error	2.6000E+01	1.85E+17	7.12E+15	--	--
Corrected Total	29	3.22E+14	--	--	--

It may be seen in lipid accumulating cultures the resonant frequency increases as neutral TAGs are accumulated within the cells while the resonant frequency decreases over the experiment period. These frequency shifts in lipid accumulating cultures may be associated with increasing lipid concentration which is accumulated between days 3 and 5 of culture [309, 310]. Between measurement on days 3 and 4 the resonant frequency increases sharply which is linked to the exponential accumulation phase of the cultures. The transition into the stationary phase is demonstrated by a relatively small increase in frequency between days 4 and 5 in lipid accumulating

cell cultures. Conversely in non-accumulating cultures the resonant frequency increases slightly between days 3 and 4 which could be because of a small amount of lipid accumulation. However, on the 6th day the resonant frequency drops which is due to the *Lipomyces* cells metabolising the stored carbon after depleting that found in the growth media.

This experiment has shown that the experimental apparatus can distinguish cells based upon the concentration of neutral TAG found within the cells in lipid droplets as modelled by *Lipomyces* cultures.

6.1.8. *Lipomyces* cell quantification in a complex cell suspension

The experimental setup was assessed for its ability to distinguish differing numbers of biological cells in a complex media. *Lipomyces* cell cultures were prepared in CLM and NLM media as described in section 5.1. On days 5 samples of the cultures were prepared ready for measurement (n = 10). Samples were centrifuged at 600 G and 10 °C for 5 minutes. Cell numbers and supporting media were normalised at 1×10^6 , 1×10^7 and 1×10^8 cell density and re-suspended in defibrinised bovine blood.

The analyte was pumped through the FC using a Perkin Elmer series 200 quaternary pump at a flow rate of 0.1 ml/min and pressure of <20 PSI. The sensor used in this study was bedded in using distilled water and later with phosphate buffer solution (85 % w/v). The analyte solutions and FC were housed in an incubation chamber and maintained at temperature of 25 °C. The sensor was connected to the VNA and set to generate a frequency sweep of 0.05 to 1 GHz over 1601 data points. Ten sweeps were performed and averaged for each measurement. A custom LabVIEW programme was utilised to initiate the sweeps and acquire the S_{11} parameters and the peak frequency data.

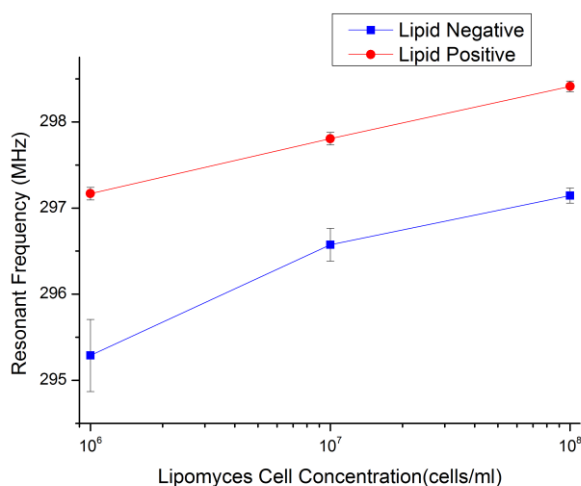


Figure 6.22. Resonant frequency of the sensor (MHz) as a result of cell concentration in defibrinised bovine blood.

Figure 6.22 shows the resonant frequency of the sensor when interacting with lipid accumulating and non-accumulating *Lipomyces* cell suspensions at differing concentrations. The resonant frequency of the structure increases by 1.2 MHz from 297.2 MHz when cell concentration is at 1×10^6 to 298.4 MHz at 1×10^8 in lipid accumulating cells. The resonant frequency for non-accumulating cultures increases from 295.3 MHz when cell concentration is at 1×10^6 to 297.0 MHz when cell concentration is at 1×10^8 and varies by 1.7 MHz. Table 6.5 details the results of statistical analysis by means of two way ANOVA of the experimental results. The results indicate the resonant frequency of the sensor is significantly different to a significance of 95 % between cell concentrations for both lipid accumulating and non-accumulating cells.

TABLE 6.5. STATISTICAL ANALYSIS OF RESULTS LIPID CULTURES BY TWO WAY ANOVA

	DF	Sum of Squares	Mean Square	F Value	P Value
Cell Concentration	2	1.23E+13	6.13E+12	99.77429	6.35E-13
Culture Condition	1	1.60E+13	1.60E+13	259.6961	4.77E-15
Error	26	1.60E+12	6.15E+10	--	--
Corrected Total	29	2.98E+13	--	--	--

It may be seen in lipid accumulating cultures that the resonant frequency increases as cell concentration increases which is mirrored by increasing resonant shift in non-accumulating cultures. These frequency shifts in both cultures are associated with increasing cell concentrations. This experiment has shown that the experimental apparatus can distinguish cell numbers in a complex

media based upon the increase in biological membranes meaning more energy may be stored within the sample.

6.1.9. Coplanar sensor substrate experimentation

The suitability of an alternative substrate for the sensor construction was investigated. Polytetrafluoroethylene (PTFE) was selected due to its water absorption characteristics. PTFE is non-reactive and is therefore widely used as a non-stick coating in a number of applications. PTFE is also highly hydrophobic as a result of the high electronegativity of the fluorine. Therefore PTFE is unable to absorb water or water containing substances making it an ideal material for this application which requires direct exposure of the substrate to the analyte sample. Using PTFE as a substrate increased the resonant frequency of the sensor to 469 MHz when dry as a result of PTFE having a relative dielectric permittivity of 2.1, lower than that of Fr4. The stability of the sensor was then investigated by pumping deionised water through the sensor for a period until which the sensor resonant frequency fully stabilised.

The experimental setup and distilled water were encased in an incubator and allowed to stabilise at 30 °C. After temperature stabilisation a quaternary pump was activated pumping the distilled water from a reservoir through the fluidic cell and back to the reservoir until the resonant peak had sufficiently stabilised. The pump rate was fixed at a rate of 2ml / min. The sensor was connected to the VNA and set to generate a frequency sweep of 0.05 to 1 GHz over 1601 data points. Ten sweeps were performed and averaged for each measurement. A custom LabVIEW programme was utilised to initiate the sweeps at a set time interval of 60 seconds and gather the S_{11} parameters and the peak frequency data.

After this time, the change in sensor output as a result of drift during the experiment was 60 MHz. This drift could be compensated during manufacture, and would not be a feature of any sensor used for *in-situ* measurements. Figure 6.23 shows the variation of sensor output over time, with the largest change in resonant frequency apparent within the first 24 hours of operation. After this time

the sensor output stabilises significantly, with small variations being accounted for by small changes (± 2 °C) in the laboratory temperature as a result of the thermostat controlled heating and ventilation system.

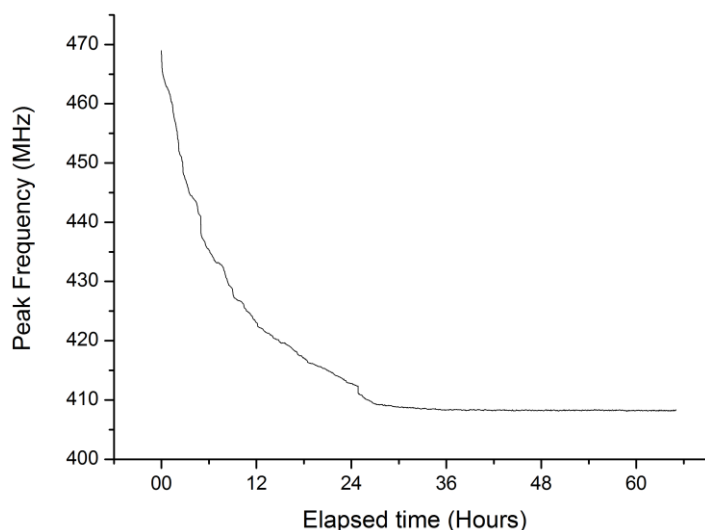


Figure 6.23. Resonant frequency change over a period of 70 hours demonstrating the change in electrical characteristics of the substrate as water is pumped through the sensor.

Despite the hydrophobic characteristics of PTFE a significant change in the resonant frequency of the sensor occurred over a period of 24 hours of water being pumped through the sensor. This suggests that there are other elements affecting the performance of the sensor. As small variations in temperature of the experimental setup were present throughout the experiment, this effect may be ruled out. Therefore, variations in the composition of the water analyte used for this experiment are likely to be responsible for the shift observed. Water oxygenation as a result of the pumping apparatus is a possible factor that could influence the characteristics of the sensor. Another possibility is the slow incorporation of residues present within the pumping apparatus accumulating in the deionised water. Although every precaution is taken to thoroughly decontaminate the pump after every use, it is possible that small amounts of salts and other hydrophilic compounds remain in the mechanism of the pump.

However the experiment proved that PTFE is a suitable substrate for future experiments and sensors, providing a non-reactive hydrophobic material for sensor fabrication. The dielectric characteristics of PTFE can easily be accounted for in the design of future sensors.

6.2. Differentiation of edible vegetable oils

6.2.1. Dielectric characteristics of vegetable oils as calculated by the small perturbation technique

Initially, different vegetable oils were differentiated using a resonant cavity and the dielectric characteristics calculated using the small perturbation technique. Commercially available nut, seed and fruit oils were used to see if they could be differentiated using resonant dielectric spectroscopy. Oils extracted from several types of plants were selected due to their triacylglycerol content. The oils selected were extracted from groundnut, olive, rapeseed and sunflower seed.

Measurements were made through a custom fabricated aluminium cylindrical resonating cavity, designed and constructed in house (Figure 6.25). The cavity has a diameter of 130 mm and a height of 20 mm with resonant mode TM_{010} at ~ 1.75 GHz (Figure 6.24).

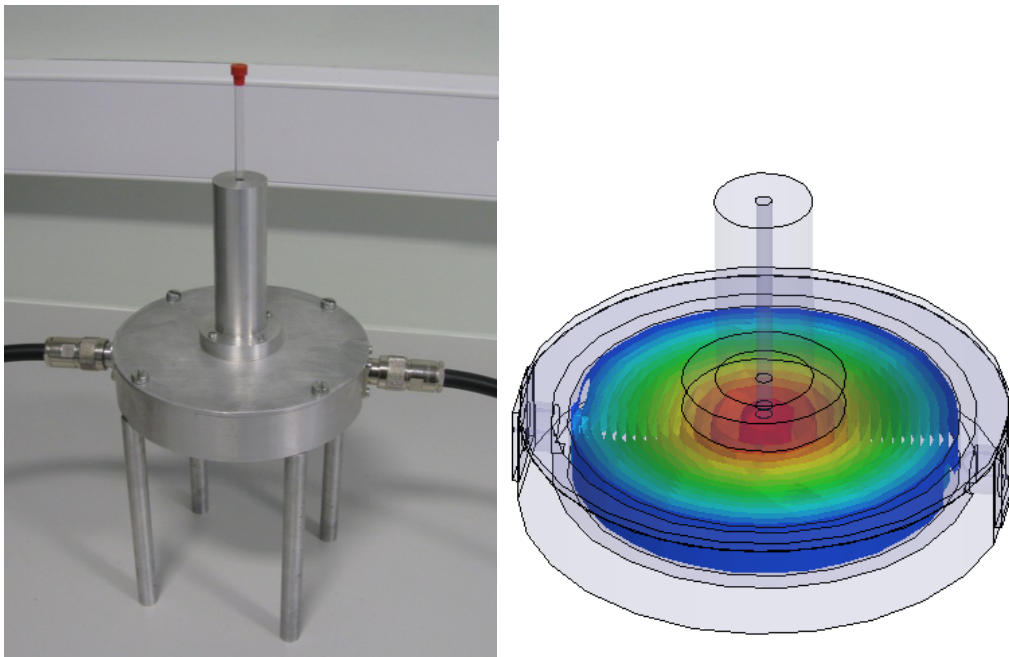


Figure 6.24. Image and simulation of the cavity used to assess the dielectric characteristics. Simulation is shown with mode TM_{010} electric field.

After purchase, oils were stored in a cool dry location out of direct sunlight to reduce the rate of degradation [311-313]. For each type of vegetable oil, 4 ml of oil was measured into NMR tubes (Wilmad NMR tubes 5mm) sourced from Sigma Aldrich, UK ready for impedance measurements. Five samples of each oil were prepared and measured. The NMR tubes were then introduced to the geometric centre of the cavity where the electric field is at maximum intensity. The VNA was set to generate a signal between 1.5-1.8 GHz over 1601 data points and calculate S_{11} (reflection) and S_{21} (transmission) parameters. The VNA conducted 10 sweeps per measurement averaging the attenuation at each frequency step. The experimental setup may be seen in Figure 6.25. The S-parameters were gathered on a PC using custom LabVIEW programmes detailed in section 0.



Figure 6.25. Image of the experimental set-up.

Figure 6.26 and Figure 6.27 shows the S_{11} and S_{21} parameters respectively of vegetable oils as a function of frequency. Introducing oil samples into the cavity reduced the resonant frequency of the principal mode by approximately 16.5 MHz for both the reflected and transmission s-parameters. The resonant peak seen in the reflected and transmission s-parameters of the oils show little variation in frequency shift or change in attenuation.

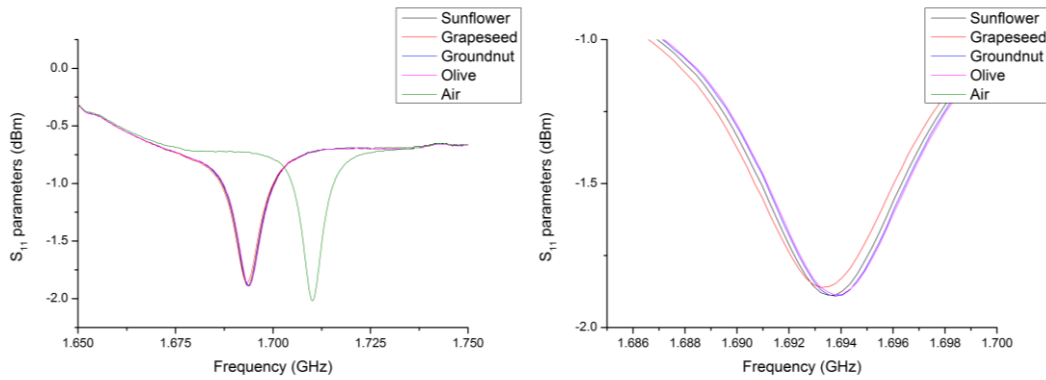


Figure 6.26. S_{11} parameters of olive oil, sunflower oil, grapeseed oil, groundnut oil and air for a frequency range of 1.65 to 1.75 GHz.

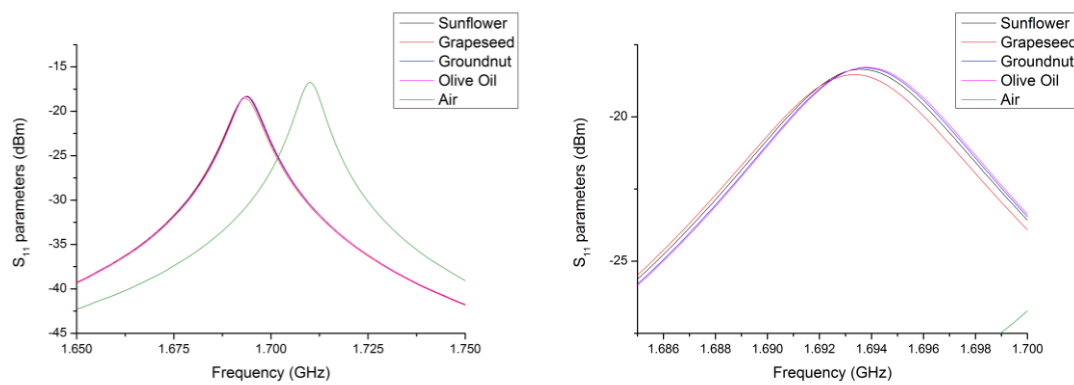


Figure 6.27. S_{21} parameters of olive oil, sunflower oil, grapeseed oil, groundnut oil and air for a frequency range of 1.65 to 1.75 GHz.

The small perturbation technique, as described in Chapter 2.3 using Equation 2.11, Equation 2.12 and Equation 2.16, was used to determine the dielectric characteristics of the sample. The calculated results may be seen below (Table 6.6).

TABLE 6.6. THE DIELECTRIC CHARACTERISTICS OF DIFFERENCE VEGETABLE OILS AS CALCULATED BY THE SMALL PERTURBATION TECHNIQUE AT 1.75 GHZ.

Vegetable Oil	$\epsilon' (\omega)$	$\epsilon'' (\omega)$	$\tan \delta$
Grapeseed	3.014	0.073	0.024
Groundnut	2.991	0.066	0.022
Olive	3.004	0.063	0.021
Sunflower	3.005	0.069	0.023

Groundnut oil, which is relatively low in mono-unsaturates (16%), has a relative dielectric constant of 2.991 while grapeseed oil with comparatively higher concentrations of mono-unsaturates (53%) has a dielectric constant of 3.014. This is in agreement with literature that reports an increase in dielectric constant as the proportion of mono-unsaturated TAG increases [13].

This experiment proved that differing conformations of TAG can be distinguished based on the electromagnetic properties of the samples which are apparent in the frequency shift and therefore dielectric constant and losses of the samples at this frequency range. Yet the molecular and structural composition, interactions between molecules, interfaces between substrates and the frequency employed must be considered as to the contribution to the dielectric qualities of the samples under test.

6.2.2. Differentiation of olive oils using a capacitive coplanar resonant sensor

Because of this, a number of olive oils of differing quality were compared using coplanar resonant structure. A coplanar sensor would reduce the physical size and resources needed for the olive oil adulteration sensor. For this experiment, a number of commercially available olive oils of differing quality were the used. High quality extra virgin olive oil (Fillipo Berio Gusto Fruttato) is mechanically extracted from mature ripened olives resulting in increased chlorophyll and carotenoid content [314]. Regular extra virgin olive oil (Fillipo Berio extra virgin olive oil) is mechanically extracted from freshly ripened olives resulting in a lower concentration of chlorophyll. Lower quality olive (Don Mario olive oil) consists of a combination of mechanically and refined olive oils resulting even lower

concentrations of chlorophyll. Lastly refined olive oil extracted from olive fruit by chemical methods is used which contains no chlorophyll.

The sensor used in this experiment was of an interdigitated finger capacitor arrangement as seen in Figure 6.28. The sensor is small and consists of 3 pairs of interdigitated electrodes of 0.4 mm width and a length of 3.6 mm.

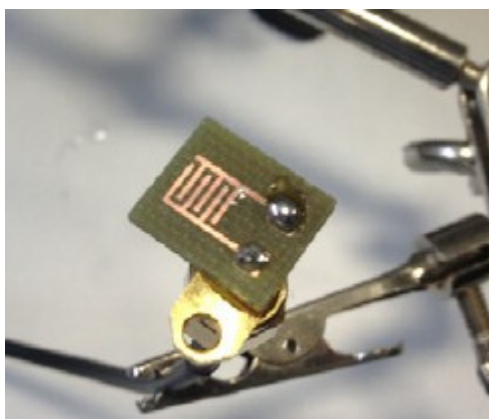


Figure 6.28. Interdigitated electrode with a fundamental frequency of 8.6 GHz.

20 μ l of oil was placed directly upon the electrode surface. 5 samples of each oil were measured. After each measurement the oil was removed and the sensor surface cleaned with an ethanol/water 90/10 % (v/v) mixture. The VNA was set to generate a signal between 6 – 7.5 GHz over 1601 data points and calculate S_{11} (reflection) parameters. The VNA conducted 10 sweeps per measurement averaging the attenuation at each frequency step. The experimental setup may be seen in Figure 6.29. The S-parameters were gathered on a PC using custom LabVIEW programmes detailed in section 0.

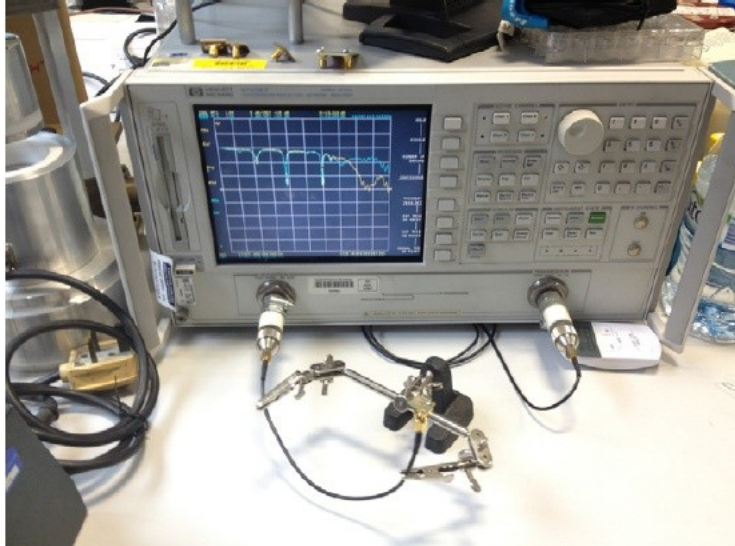


Figure 6.29. Experimental setup of coplanar sensor for olive oil quality validation.

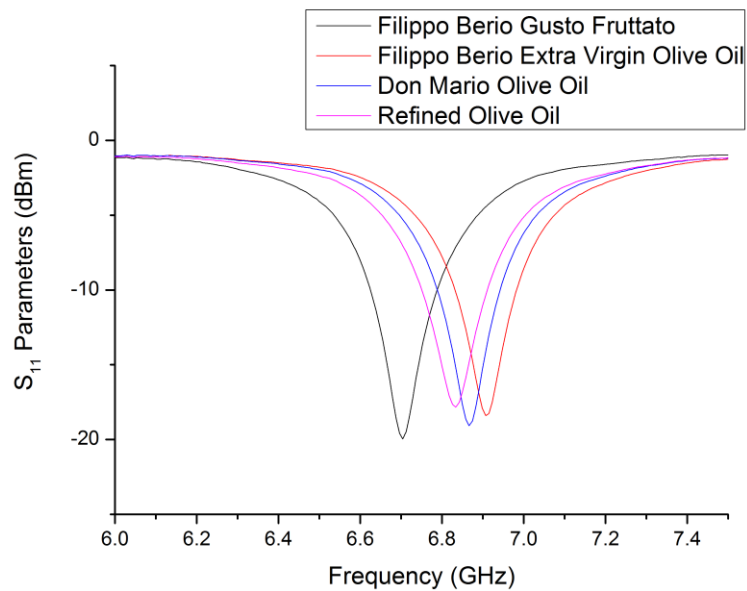


Figure 6.30. S_{11} parameters of the olive oil samples.

It can be seen in Figure 6.30. that the resonant frequency of the sensor changes when interacting with different types of olive oil with a total variance of 205 MHz. This is due to the differences in the chemical composition of the olive oil. The fatty acid composition as stated by the manufacturers is stated below.

TABLE 6.7. THE MANUFACTURER, TYPE AND COMPOSITION OF OLIVE OILS ASSESSED USING IMPEDANCE SPECTROSCOPY.

Manufacturer/type	Lipid (g/ml)	Saturated (g/ml)	Monounsaturates (g/ml)	Polyunsaturated (g/ml)
Filippo Berio Gusto Fruttato	91.3	15.5	66.1	9.7
Filippo Berio Extra Virgin	91.3	15.1	66.2	10.0
Don Mario Olive Oil	91.4	13.2	66.7	8.5
ASDA Refined Olive Oil	91.4	13.1	66.9	9.2

However, one parameter that is not listed in the manufacturers' nutritional values is the moisture, chlorophyll, carotenoid and polyphenol content of the oil. These constituents are thought to play a major role in the permittivity of lipids [212].

The experiment shows that olive oils of differing quality have characteristic spectra providing a clear identification methodology. Using a database of previously measured olive oil standards, the quality of the measured oil could be determined.

6.3. Quantification of lactate in bovine blood

This section of the research is concerned with designing a non-invasive sensor for the detection of lactate in bovine blood. Defibrinised bovine blood was used spiked with differing concentrations of lactic acid (Sigma Aldrich, U.K.). An experimental apparatus was fabricated to model an artery under the surface of a cow's epidermis. In this fashion the sensor would have to penetrate the skin and artery to interact with the bovine blood.



Figure 6.31. Fabricated resonant sensor applied to non-invasive lactate measurements.

The sensor used, designated RTB04, was a previously used in Section 6.1.2. It consists of two interdigitated semi-circular patch electrodes which are encircled by an earthed ring (Figure 6.31).

The cow artery was modelled using silicone tubing fed through polyethylene foam over which 15 cm² of cow hide with a thickness of approximately 8 mm sourced from a local butcher was affixed (Figure 6.32).



Figure 6.32. Silicone tubing in PE foam covered in cow hide to simulate jugular and supportive tissue.

Using a peristaltic pump, defibrinised bovine blood was pumped from a reservoir through the apparatus and back to the reservoir which was contained within an incubator set at 55°C to ensure the temperature of the blood running through the apparatus was approximately the bovine basal temperature of 38°C (Figure 6.33). A number of bovine blood solutions were prepared using lactic acid to the concentrations 64, 32, 16, 8, 4, 2, 0.5 and 0 mM. Each concentration of lactate was measured a total of 7 times. Measurements were carried out from low to high lactate concentration with the blood was pumped out of the apparatus after each measurement.

The coplanar resonant structure RTB04 was held in place above the simulated vein and connected to the VNA. The VNA was set to generate a signal between 1.5 – 2.5 GHz over 1601 data points and calculate S_{11} (reflection) parameters. The VNA conducted 10 sweeps per measurement averaging the attenuation at each frequency step. The S-parameters were gathered on a PC using custom LabVIEW programmes detailed in section 0.

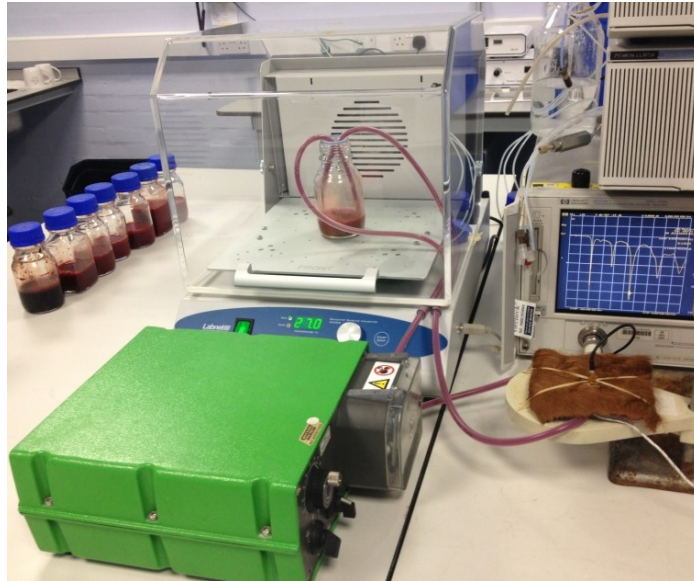


Figure 6.33. The experimental apparatus consisting of a peristaltic pump, incubator, VNA and model cow (clockwise from bottom-left).

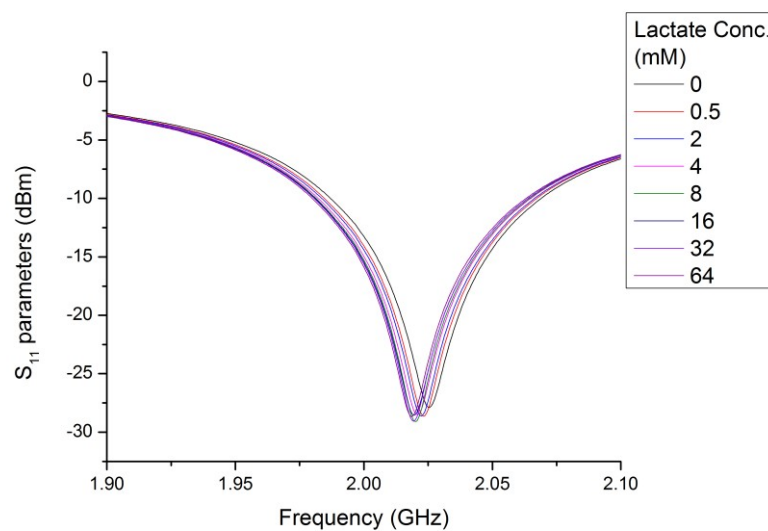


Figure 6.34. S_{11} parameters of bovine defibrinised blood with differing concentrations of lactate (mM).

Figure 6.34 shows the S_{11} parameters of bovine blood spiked with differing concentrations of lactate. It may be seen that as lactate concentration increases the resonant frequency of the sensor decreases and the attenuation increases. This is more clearly demonstrated in Figure 6.35 which plots the peak frequency of the sensor against lactate concentration.

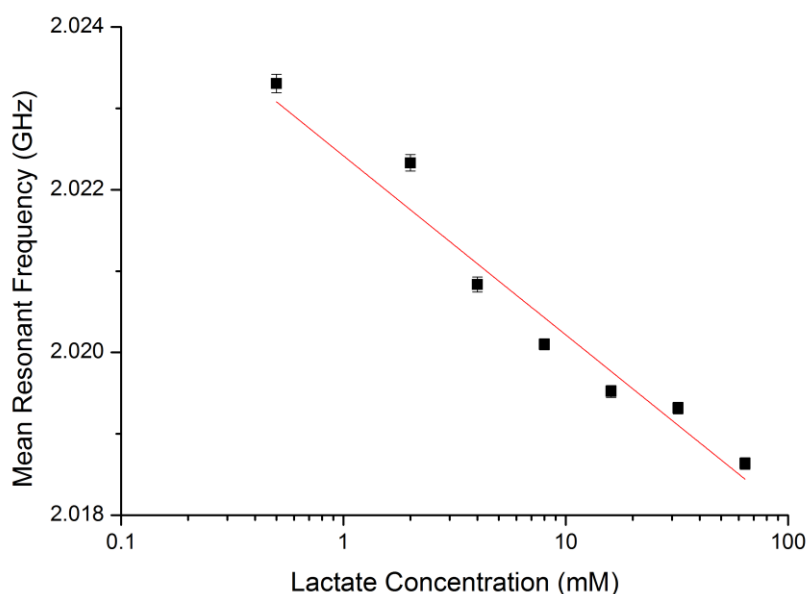


Figure 6.35. Average resonant frequency of the sensor (GHz) as a function of logarithmic bovine blood lactate concentration (mM). Error bars represent standard deviation. Linearity was calculated at $r^2 = 0.941$.

From these graphs it may be seen that the maximum shift and attenuation between lactate concentration of 0 and 64 mM was 5 MHz with a linearity r^2 of 0.941. Sensitivity of the sensor was calculated at 0.571 MHz / 0.1 mM of lactate. The resonant frequency associated with lactate concentration were found to be significantly different upon one way ANOVA statistical analysis ($p = 0$) (Table 6.8).

TABLE 6.8. ONE WAY ANOVA STATISTICAL ANALYSIS RESULTS.

	DF	Sum of Squares	Mean Square	F Value	Prob>F
Model	7	1.89E+14	2.70E+13	931.8111	0
Error	32	9.26E+11	2.89E+10		
Total	39	1.90E+14			

This experiment has shown that differing concentrations of lactate in bovine blood may be remotely and non-invasively differentiated using microwave spectroscopy. The physical size of the sensor will allow it to be easily incorporated into a collar to fit cattle. Consistent interaction of the sensor with the area of skin over the artery is essential to reproducibility of the measurement.

6.4. Quantification of *Pseudomonas aeruginosa*

This part of the research demonstrates the novelty in the application of coplanar resonant sensors, excited at microwave frequencies, to the detection of *P. aeruginosa*. The experimental setup used was that previously developed in section 6.1.4 (Figure 6.36).



Figure 6.36. Overview of the experimental setup. Quaternary pump and vector network analyser (left). Fluidic cell embedded coplanar sensor system (right).

The culture method of *P. aeruginosa* is that stated in the journal paper resulting from this experiment [315]. *P. aeruginosa* was inoculated into 50 ml of sterile nutrient broth (NB) and incubated for 24 hours at 37 °C in an orbital culture chamber at 250 rpm. Following incubation, the optical density (OD) was measured as 550 nm (OD_{550}). The arbitrary spectrophotometry measurement at OD_{550} of the culture was 1.74. For the purposes of experiment, this culture sample was diluted to an OD_{550} of 1.0 to ensure there was sufficient quantity of bacteria for measurement, and also to prevent clogging of the fluidic system since *P. aeruginosa* is particularly known for its adherent properties. For the purposes of comparison with other techniques, a 1.0 OD_{550} reading was found, via a filtration method, to be equivalent to 0.583 g/L. In other works where the units CFU·m/L are used, 0.6 OD_{550} is typically approximated to 1×10^8 CFU·m/L. Using this approximation, the original sample here contained 16.7×10^8 CFU·m/L.

In order to verify growth of the bacteria, it was grown on glass at 30 °C for 48h. A sample of *P. aeruginosa* biofilm was treated with 1% glutaraldehyde, washed twice with distilled water and left in

air to dehydrate for 24h. The sample was then coated using a gold sputter coater (Emitech K550X) at 25 mA for 2.5 min, giving a thickness of 12 nm. It was then examined under a scanning electron microscope (FEI Quanta 200 ESEM) with the result shown in Figure 6.37.

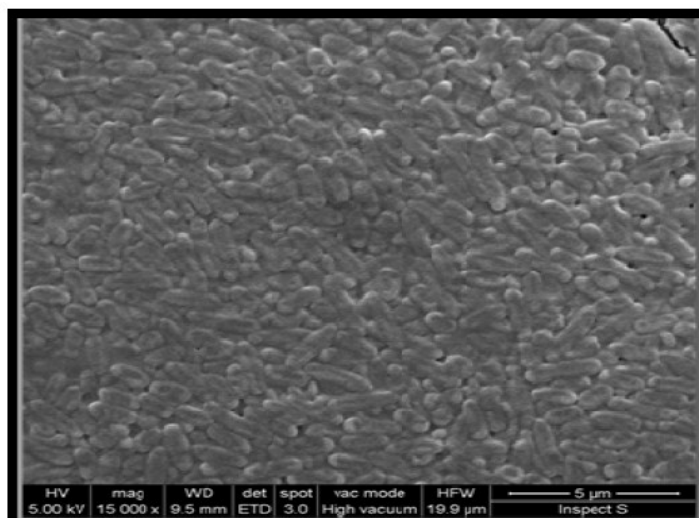


Figure 6.37. SEM micrographs of *P. aeruginosa* biofilms grown on glass.

The bacterial culture and a sterile nutrient broth were fed to a quaternary pump (Perkin Elmer), which was used to introduce samples to the fluidic cell. The cell OD_{550} ranged from 0.025 to 1.0, in the following dilutions: 0.025, 0.1, 0.25, 0.5, 0.75 and 1.0. The nutrient broth acted as a diluting media. The experimental work was repeated 6 times alternating between high-low and low-high concentrations. Between each repetition the fluidic cell was cleaned with deionised water in order to eliminate possible contamination, and to remove any cell build up or clogging. Each individual measurement took approximately 3 minutes. 1 minute was allowed for the system to be flooded with the analyte and a further 2 minutes stabilisation time. A low pumping speed (2 ml/min) was selected to minimise the build-up of air in the fluidic cell resulting from turbulent analyte flow, particularly in the area of the sensor. The resonant coplanar sensor was connected via a SMA connector and coaxial lead to an Agilent Technologies (Hewlett Packard) 8720 ET VNA to allow measurements to be taken. The instrument was set to generate a signal between 100 MHz and 1 GHz over 1601 data points for 10 linear frequency sweeps and calculate the S_{11} (reflected signal) parameters. The sensor had a fundamental resonance at approx. 292 MHz when the fluidic cell was

loaded with nutrient broth. Data (peak frequency and Q-factor) was collected at this frequency using bespoke LabView software detailed in section 0 for later analysis.

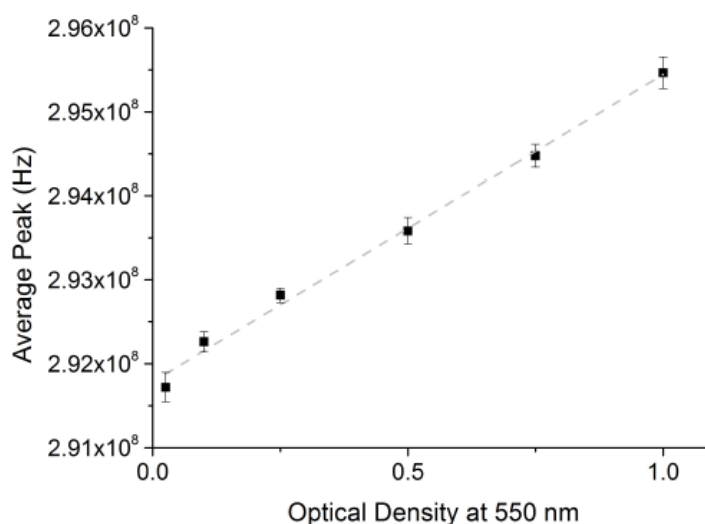


Figure 6.38. Plot of average resonant peak with changing *P. aeruginosa* optical density. Error bars indicate the standard deviation of the measurements. Linearity calculated at r^2 of 0.993.

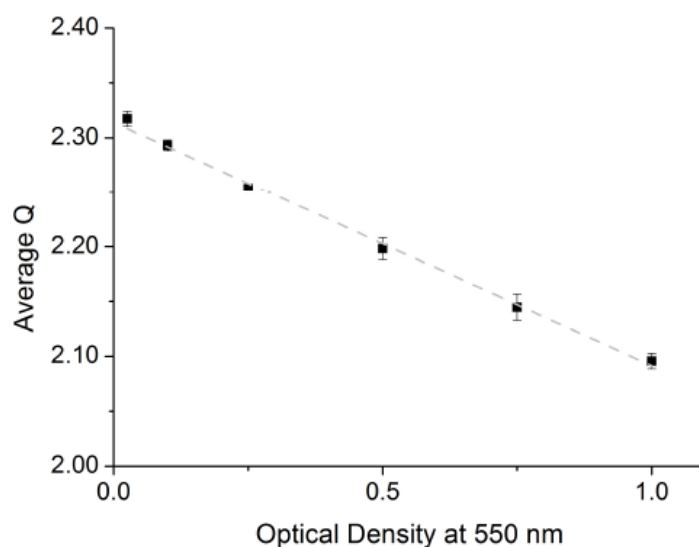


Figure 6.39. Plot of average Q-factor with changing *P. aeruginosa* optical density. Error bars indicate the standard deviation of the measurement. Linearity calculated at r^2 0.994.

Results from the data collected at the sensor resonant peak of approximately 292 MHz are shown in Figure 6.38 and Figure 6.39 for peak and Q-factor shift respectively. Results from all 6 concentration repetitions, low-high and high-low, were averaged and error bars show the range of readings at each concentration. As evidenced in Figure 6.38 and Figure 6.39, there is a clear relationship between sensor response and OD₅₅₀ and therefore concentration of *P. aeruginosa*. Even more encouraging is

the near linear relationship demonstrated with both sets of results. In Figure 6.38, the linear best fit line has an r^2 value of 0.993, while in Figure 6.39 r^2 is 0.994. Sensor resonant frequency was calculated to have a sensitivity of 0.4 MHz/0.1 OD at a wavelength of 550 nm. Furthermore, the sensor has been demonstrated to have a good level of repeatability. In the range over which the sensor was tested (OD₅₅₀ 0.025-1.0), the resonant peak shifted by 3.8 MHz and the Q-factor changed by 0.222. Therefore, the maximum percentage error, over the tested range can be calculated to be 20.4% (peak) and 18.5% (Q-factor).

By way of comparison with previous works, where information is available, the sensor has demonstrated a linear operating range of OD₅₅₀ 0.025-1.0. In addition, the resolution of the sensor has been demonstrated to be at least OD₅₅₀ 0.075. Importantly, the proposed technique gives a real-time response and has the ability of instantaneous diagnostics of presence and concentration of *P. aeruginosa*. The repeatability of measurements and reusable nature of the sensor makes this technique a welcome cost effective tool for clinical use. The proposed solution would not require specialist medical training and therefore could be carried out by non-experts such as technicians, nurses, etc. In addition, the system could potentially be made portable for use by emergency service providers, when combined with hardware to replace the VNA used in this work, as demonstrated by the authors in previous work [316]. This would be possible by selecting a particular frequency of interest at which *P. aeruginosa* show a response, and therefore allows its concentration to be determined. Importantly, other types of bacteria may be more sensitive to other frequencies. Based on this the proposed EM sensor technique has the unique capability of not only determining the type of the bacteria present in the analyte, but also provides tool for real-time quantitative assessment which is vital for early medical diagnostics.

6.5. Quantification of lactate in cerebrospinal fluid

The sensor is embedded in a bespoke fluidic cell constructed of PMMA, which has a HPLC compatible inlet and outlet ports in order to allow fluid to pass through the cell and come into contact with the

sensor device itself. Although this setup represents a laboratory environment system, it is feasible that a fluidic cell such as this could be placed in-line with a spinal tap, or similar depending on the application, and thus the CSF analyte could easily be introduced to the sensor during a surgical procedure.

In order to test the capability of this sensor system, the work involves the use of a synthetic CSF, comprising deionised water combined, in varying quantities, with L-(+)-Lactic acid solution (Sigma-Aldrich, 27714). In particular, the following concentrations (mmol/ L) were measured: 0, 0.2, 0.4, 1, 1.6, 2, 4, 10 and 20. The experimental work was repeated 6 times and an average of the results taken. Between each repetition the fluidic cell was cleaned with deionised water in order to eliminate possible contamination. The sensor response, after cleaning, returned to its original baseline output when flooded with deionised water which is promising in terms reliability and robustness for long term use. A quaternary pump (Perkin Elmer) was used to introduce samples to the fluidic cell, and this was used to mix the lactic acid and deionised water to the concentrations previously detailed. The deionised water and lactate solutions were stored in an incubator at 30 °C, and feed tubes between the solutions and fluidic cell were kept short to minimise temperature loss. Each measurement took 3 minutes; 1 minute was allowed for the system to be flooded with the analyte and a further 2 minutes settling time was allowed. A low (2 ml/min) pumping speed was selected to minimise the build-up of air in the fluidic cell resulting from turbulence, particularly in the area contacted by the sensor. In the real world, this speed could easily be emulated *in-situ* although the speed of pumping itself has been found to have little direct effect on the response of the sensor beyond issues with air build-up.

Dielectric measurements were performed using an Agilent Technologies (Hewlett Packard) 8720 ET VNA. The instrument was set to generate a signal between 100 MHz and 1 GHz over 1601 data points for 10 linear frequency sweeps and calculate the S_{11} (reflected signal) parameters. Data was

collected using bespoke LabView software (section 0) and later analysed. The complete experimental setup is shown in Figure 6.40.

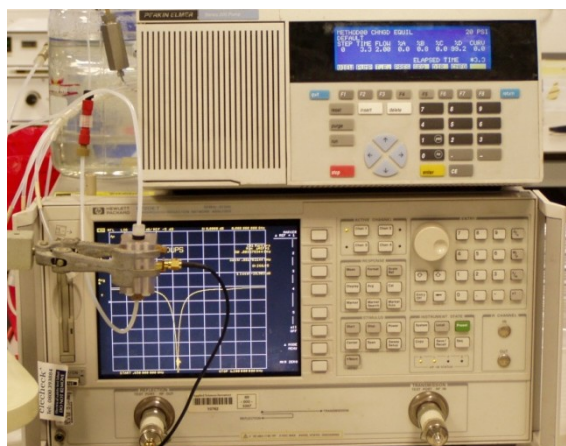


Figure 6.40. Overview of the experimental setup, including quaternary pump, vector network analyser and sensor system.

The S_{11} measurements taken during the experimental work were used in order to identify change which occurred due to the varying concentration of lactic acid. Two resonant peaks were noted as responding to the change in lactate concentration. When water was present in the cell, these peaks were at approximately 394 MHz and 573 MHz; the latter however was found to give more pronounced response to lactate and so results for the fundamental resonance only are presented in this paper.

In Figure 6.41, the response of the sensor is shown as captured from the VNA, with the shift in reflected S_{11} parameters clearly demonstrated. In Figure 6.42, the sensor response is shown in the form of a calibration curve over the full range of concentrations tested. Deionised water is used as a background reading against which all other readings are normalised; thus the results emphasise the change in response of the sensor at the indicated frequency. The sensor shows a logarithmic response, with the greatest sensitivity shown up to concentration levels of 2 mmol/ L. From Figure 6.42 it is clear that there is a good correlation ($r^2 = 0.98$) between the sensor response and the lactate concentration. Sensor sensitivity to lactate was calculated at 0.5425 MHz per mmol/L.

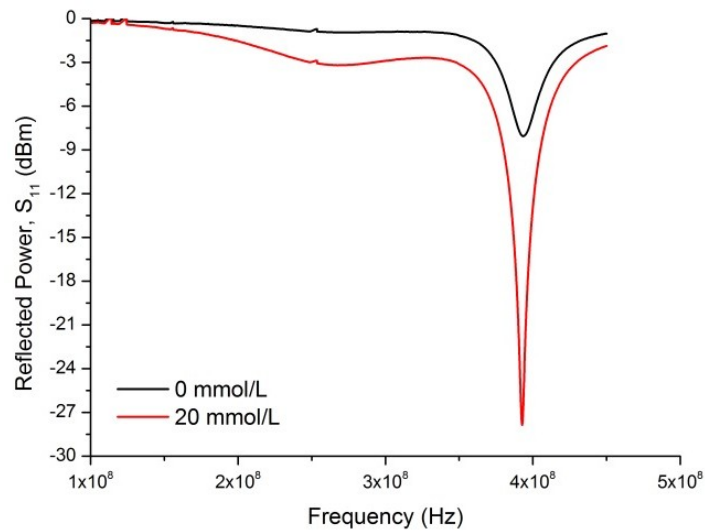


Figure 6.41. Illustrating the shift in peak frequency at approx. 394 MHz for 0 and 20 mmol/L concentrations of lactate.

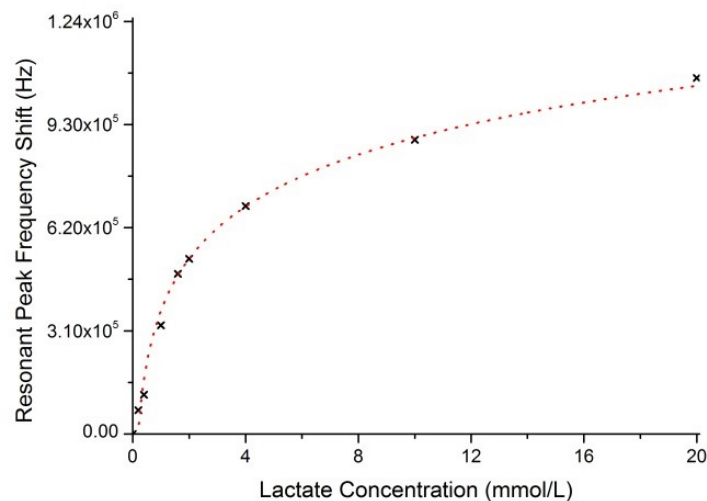


Figure 6.42. The shift in peak frequency at approximately 394 MHz with different concentrations of lactic acid, with good correlation between results and the logarithmic best fit curve ($r^2 > 0.98$). Note that results have been normalised against a background sample of deionised water only.

This methodology and results are an important step forward for this work, which has for a number of years been under development for real-time CSF analysis. The method would be simple to implement and not require any significant change to current surgical procedure. While previous work has shown the potential for electromagnetic wave techniques (e.g. cavities and planar structures), this shows a technique which could be applied in-line to current spinal tap procedures.

Longevity may not be a pressing concern in the healthcare field, as it is likely the sensor system would be single use due to potential biohazard risks. However, in other applications long term use of the sensor would certainly be preferable, and the authors are looking to apply this technique in other areas including water quality monitoring, industrial process monitoring and for biomedical screening.

This experiment suggests that the apparatus is versatile and so the response of the sensor to other analyte solution types and concentrations is being explored and a database of these microwave signature spectra being compiled, which can later be used for online process control in a broad range of industrial applications in the wastewater industry, chemical and pharmaceutical production lines.

The system demonstrates an improvement over previous work by the research group [317, 318], and is a step toward achieving the goal of a truly online system for the indication of lactate level in a patient under-going a procedure such as surgical or endovascular aneurysm repair. The paper demonstrated sensitivity of the sensor system to varying levels of lactic acid, in the range 0 to 20 mmol/ L in a deionised water solution. The measured results (i.e. resonant peak shift) at 394 MHz from the electromagnetic wave sensor show an excellent correlation with the varying concentration. Further work in this area will consider other background media (e.g. blood), in addition to other potential applications in the biomedical, process and water industries where real-time monitoring of various fluidic analyte materials is becoming ever more necessary.

6.6. Chapter 6 Summary

Chapter six is divided into sections that contain the experimental results relating to each application. Section one of chapter six details the results of experiments utilised to develop and verify the application of dielectric sensors to the quantification of neutral lipids within cells. Initially samples were analysed using a resonant cavity and the small perturbation technique. A number of

developments to the coplanar sensor were then carried out to incorporate the sensor into a fluidic device which was characterised over time and temperature. The finalised experimental methodology was then used to assess the neutral lipid composition of cells. Section two of the chapter details the use of a resonant cavity and the small perturbation technique to assess the dielectric characteristics of different vegetable oils. An interdigitated capacitive coplanar sensor was then used to verify the quality of vegetable and olive oils. Section three demonstrates the applicability of dielectric coplanar sensors to non-invasively quantify the lactate composition of bovine blood in a major bovine blood vessel through a layer of epidermis and hair. This was done by pumping bovine blood containing physiological concentrations of lactate through a fabricated model of a cow blood vessel. This may be used as a marker pertaining to the overall health of the cow. Section four details the use of the fluidic cell to determine the concentration of *Pseudomonas* bacteria found in ill managed water storage systems. Section five presents the results of using the fluidic apparatus to determine the lactate concentration of cerebrospinal fluid which is exuded during cranial surgery and may be used as a marker to detect hypoxia of the brain during the procedure.

Chapter 7. Conclusions and future work

The project aimed to develop resonant microwave dielectric sensors for biomedical and industrial applications. The research objectives, which are re-stated below for clarity, will be discussed below with specific chapters for each of the application areas. The research aims were:

- **Investigate current dielectric spectroscopy techniques used to differentiate organic and biological material.** Chapter 2 and 3 discuss the theory surrounding dielectric spectroscopy, different dielectric spectroscopy techniques and their application in each of the application areas. It was found that a number of resonant structures may be utilised for these applications however development of coplanar sensors was chosen due to their physical size, economical cost and electrical characteristics which made them the most suitable for the applications covered by the research.
- **Design and evaluate the suitability of dielectric spectroscopy sensor configurations using computational simulation.** Chapter 5 documents the development of the resonant dielectric sensors used in the project. Each development stage improves the sensors desired characteristics (frequency, quality factor) to yield a resonant microwave frequency sensor that is sensitive to biological analytes.
- **Implement and evaluate the proposed analysis methodology of using resonant dielectric sensors to assess the characteristics of biological samples.** Chapter 6 documents the experimental procedure used to verify the application of the sensors designed in chapter 5. The developed sensors were shown to be sensitive to their target analyte which was demonstrated through experimentation and statistical analysis of the results.
- **Incorporate the dielectric spectroscopy sensor into a fluidic device (omitting applications 2 and 3) that allows online sensing of the intended analyte.** A number of materials were investigated as to their suitability for fluidic cells. PMMA was chosen as a material and a fluidic cell devised that can incorporate the designed sensor which is documented in Chapter 6. The fluidic cell allowed the direct in-line measurement of analytes in a cost effective manner while increasing sensor-analyte interaction.
- **Programme an interface to control parameters of the experimental equipment and subsequently acquire and analyse the resulting data.** A LabVIEW programme was designed and implemented that permitted quick configuration and facilitated the acquisition of data from the VNA. This is documented in Appendix 2.

7.1. Quantification of neutral lipids in biological cells

The suitability of microwave dielectric spectroscopy to assess the neutral lipid content of biological cells was investigated. Primarily, suspensions of vegetable oils were assessed to investigate the effect of varying neutral lipid concentration using the small cavity perturbation technique. The technique proved successful in non-invasively differentiating cell samples with differing compositions of neutral lipid.

Following this, development started on a resonant patch to replace the large and expensive resonant cavity. A number of progressive modifications were made to a simple circular patch with the sensor performance analysed for cell differentiation suitability after each modification step. The footprint of the resonant structure was successfully reduced to 3.4 % of the resonant cavity and 0.15 % of the total volume using this technique while also propagating a primary resonant mode of a lower frequency than that of the resonant cavity to interact with Maxwell-Wagner polarisation phenomena. Reducing the frequency of the resonant mode was achieved by introducing reactive impedance elements into the structure in the form of capacitive interdigitated fingers and an inductive ring.

The final resonant structure was used to quantify the neutral lipid content of yeast cell cultures. The final sensor design incorporated into the fluidic apparatus proved successful in differentiating lipid positive and lipid negative cell cultures. The total difference in measured resonant frequency between the two culture conditions on day 6 was 8.8 MHz. This would be sufficient enough for a circuit embedded power meter to differentiate the sensor response as a result of the differing conditions. The sensor also proved successful at detecting different concentrations of yeast cells in blood with a total average difference in resonant frequency of 1.42 MHz. This fulfils the objective of proving the applicability of dielectric spectroscopy to differentiate cell samples based upon the neutral lipid composition of biological cells using coplanar sensors of novel conformation. This element of the research resulted in a number of publications as detailed in the appendix.

Future work regarding this project would involve the use of leukocytes as the analyte for the sensor. Optimisation steps would be needed to ensure the sensor is sensitive to the new cell type. Cells could be captured from a complex media such as blood in the sensing area of the sensor using a monoclonal immunoglobulin serotype sensitive to the target cell line immobilised to the sensor surface. Although this would mean the sensors would be single use, the cost of such sensors would be inexpensive enough to justify such a methodology. Broadband analysis of the cells immobilised using immunoglobulin would be required to investigate the effects of immobilisation and the sensors redesigned to a frequency sensitive to cell binding.

7.2. Differentiation of edible vegetable oils

The dielectric characteristics of different vegetables were determined using the cavity perturbation technique. It was found that different oils had different dielectric characteristics due to the concentration of mono-unsaturated fatty acids present in the different oils. Following this a coplanar interdigitated capacitive sensor was designed and used to differentiate the different oils. The sensor proved successful in differentiating the vegetable oils of differing quality as a result of the mono-unsaturated composition. This reveals that dielectric spectroscopy can be used as an affordable technique for in-situ analysis of olive oil quality removing the need for laboratory analysis using expensive chromatography techniques. This element of the research resulted in a number of publications as detailed in the appendix. The sensor used in this experiment could easily be incorporated into a small mobile hand-held device for the in-situ determination of olive oil quality. Future work would focus upon designing a compact battery powered circuit capable of generating and analysing electromagnetic radiation in the microwave frequencies using a voltage controlled oscillator. The circuit would also incorporate a user interface and display to read out the result.

7.3. Detection of disease states in cattle

A coplanar resonant sensor was used to non-invasively determine the lactic acid content of sub-dermal intravenous blood. The developed sensor proved successful in determining lactic acid

concentration at physiological levels which could be used as an indicator of ill health in cattle. The sensor had a sensitivity of 0.571 MHz / 0.1 mM of lactate concentration and linearity (r^2) of 0.941. The experiments conducted indicate that dielectric spectroscopy is effective in non-invasively monitoring the health of cattle using lactate as a marker. Due to the small size of the novel coplanar sensor, it could easily be incorporated into a collar with the analytical circuitry needed to interpret the sensor data and transmit the result as part of a wireless sensor network that would monitor the health of individual cows and the overall herd. Additionally GPS circuitry could be incorporated into the collar providing additional data to better understand herd habits and grazing characteristics. Future work would focus upon this element of the system.

7.4. Quantification of *Pseudomonas aeruginosa*

A novel resonant electromagnetic patch sensor system for the real-time detection and quantification of *Pseudomonas aeruginosa* was developed. It employs a bespoke planar sensor embedded within a microfluidic cell structure which allows instantaneous assessment of bacteria concentration in the range of OD₅₅₀ 25×10^{-3} - 1.0, which is comparable with other currently reported techniques. Sensitivity was calculated at 0.4 MHz / 0.1 OD at a wavelength of 550 nm with linearity (r^2) of 0.994. However, the proposed system is reusable, cost efficient and has the potential to be developed into a novel cost effective device for installation into a water supply network.

This work has successfully proven the concept that novel electromagnetic sensor embedded into a fluidic cell is an attractive technique capable of providing real-time information on the composition of the CSF. In previous work [318] a microwave cavity technique was used to perform offline measurements of lactate suspended in a phosphate buffered saline (PBS) solution, since this is considered more representative of blood than deionised water. Due to the added conductivity of the media, it is proposed that this is a far more challenging environment for the sensor to operate in. Therefore further work with this sensor will consider the use of both PBS and blood background media spiked with similar concentrations of lactate as demonstrated in this paper in order to

determine a more realistic idea on the sensitivity of this sensor for the intended application. An important aspect however is that the purpose of this sensor is not for precise quantification of lactate in blood, but rather to determine if the level is too high. This alone would indicate if there is some underlying issue with the patient; a precise value would not be necessary to a surgeon in theatre. If the sensor indicates the elevated lactate level, its exact value could later be determined using standard laboratory procedures.

This element of the research resulted in a number of publications as detailed in the appendix. This novel device would stop the flow of water if bacterial contamination was detected. As the cost of the sensor and support analytical circuitry is relatively low, installation of such devices could easily be justified in large installations such as hospitals and food processing plants as a failsafe to water management procedures. Future work would focus upon developing such a device that can be incorporated into the outlet of a water storage tank similar to that found in such installations.

7.5. Detection of lactate in cerebrospinal fluid

The suitability of the fluidic device embedded resonant coplanar sensor to the lactate concentration of cerebrospinal fluid was analysed. Currently no device or methodology exists that can measure this in real time. Such a device would provide an extremely useful real-time analytical technique for the monitoring of cerebral oxygenation during cranial surgery. The coplanar sensor of novel conformation proved to be successful in significantly quantifying physiological concentrations of lactate in cerebrospinal fluid to a sensitivity of 0.5425 MHz per mmol/L of lactate and linearity (r^2) of 0.98. This element of the research resulted in a number of publications as detailed in the appendix. Future work would focus upon incorporating the sensor with the support circuitry and a GUI so the information could be read by surgeons and support staff in real time. In all the methodology is a novel approach to a problem that faces surgeons daily when carrying out cranial operations.

7.6. Future work

A number of opportunities and research pathways are available to further explore the sensing capabilities of the methodology developed as part of this project. The coplanar sensors used as part of this project rely upon the perturbation of the principle resonant frequency. Due to the size of the coplanar sensors, it would be possible to combine a number of coplanar sensors into a fluidic device that target different dispersions of a samples dielectric relaxation profile allowing further characterisation of the sample. Alternatively, the coplanar sensor could be configured so as the resonant modes of the sensor target the different dispersions of the sample.

There also exist a number of applications that dielectric spectroscopy is well suited to. These include the characterisation of dairy products and the characterisation of meat products. The characteristics detected could be the water content of milk, cheese, raw meats and cooked meats. The water content of such products is closely linked to quality and shelf life of the products. Characteristics which are closely linked to water content, such as bacteria and fat composition could also be monitored using dielectric spectroscopy. Pollutants in waste water which alter the relaxation frequency of water molecules could also be detected using this technique allowing continuous measurement of waste water flows and alerting water companies when a pollutant is detected. This would ensure the rapid action from the water companies and stop the pollutant entering the water system.

7.7. Research Overview

In the process of this research, a number of important sensing applications have been developed to address issues in a number of healthcare and industrial sectors. The research shows that dielectric spectroscopy can be used effectively in a wide range of fields and purposes to differentiate samples based upon a target analyte. Additionally, a number of novel coplanar sensors have been designed, developed and modified to fit each purpose showing the proficiency and versatility of the technique.

Interestingly, future work may focus upon any of the above applications to develop a novel final product that could be used for the intended purpose.

Chapter 8. References

1. Hollingsworth, A.D., *Remarks on the determination of low-frequency measurements of the dielectric response of colloidal suspensions*. Current Opinion in Colloid & Interface Science, 2013. **18**(2): p. 157-159.
2. Heileman, K., J. Daoud, and M. Tabrizian, *Dielectric spectroscopy as a viable biosensing tool for cell and tissue characterization and analysis*. Biosensors and Bioelectronics, 2013. **49**(0): p. 348-359.
3. Zidi, N., A. Chaouchi, S. d'Astorg, M. Rguiti, and C. Courtois, *Dielectric and impedance spectroscopy characterizations of CuO added (Na_{0.5}Bi_{0.5})_{0.94}Ba_{0.06}TiO₃ lead-free piezoelectric ceramics*. Journal of Alloys and Compounds, 2014. **590**(0): p. 557-564.
4. Justice, C., A. Brix, D. Freimark, M. Kraume, P. Pfromm, B. Eichenmueller, and P. Czermak, *Process control in cell culture technology using dielectric spectroscopy*. Biotechnology Advances, 2011. **29**(4): p. 391-401.
5. Floudas, G., 2.32 - *Dielectric Spectroscopy*, in *Polymer Science: A Comprehensive Reference*, K. Matyjaszewski and M. Möller, Editors. 2012, Elsevier: Amsterdam. p. 825-845.
6. Bonincontro, A. and G. Risuleo, *Dielectric spectroscopy as a probe for the investigation of conformational properties of proteins*. Spectrochimica Acta Part A: Molecular and Biomolecular Spectroscopy, 2003. **59**(12): p. 2677-2684.
7. 1 - *Principles of Nonionizing Radiation*, in *Industrial Hygiene Engineering (Second Edition)*, T.T. John and P.E. P.E.A2 - John T. Talty, Editors. 1998, William Andrew Publishing: Park Ridge, NJ. p. 564-597.
8. Mehdizadeh, M., *Chapter 1 - The Impact of Fields on Materials at RF/Microwave Frequencies*, in *Microwave/RF Applicators and Probes for Material Heating, Sensing, and Plasma Generation*. 2010, William Andrew Publishing: Boston. p. 1-34.
9. Nanni, E.A., A.B. Barnes, Y. Matsuki, P.P. Woskov, B. Corzilius, R.G. Griffin, and R.J. Temkin, *Microwave field distribution in a magic angle spinning dynamic nuclear polarization NMR probe*. Journal of Magnetic Resonance, 2011. **210**(1): p. 16-23.
10. Gamet, E., J.P. Chatelon, T. Rouiller, B. Bayard, G. Noyel, and J.J. Rousseau, *Simulation of the contribution of magnetic films on planar inductors characteristics*. Journal of Magnetism and Magnetic Materials, 2005. **288**(0): p. 121-129.
11. Al-Kizwini, M.A., S.R. Wylie, D.A. Al-Khafaji, and A.I. Al-Shamma'a, *The monitoring of the two phase flow-annular flow type regime using microwave sensor technique*. Measurement, 2013. **46**(1): p. 45-51.
12. Al-Kizwini, M.A., D.A. Al-Khafaji, S.R. Wylie, and A.I. Al-Shamma'a, *The use of an EM mixing approach for the verification of an EM wave sensor for a two phase (oil-water) dispersed flow*. Flow Measurement and Instrumentation, 2013. **32**(0): p. 35-40.
13. Aghdam, K.M.P., R. Faraji-Dana, and J. Rashed-Mohassel, *The sinuous antenna-A dual polarized feed for reflector-based searching systems*. AEU - International Journal of Electronics and Communications, 2005. **59**(7): p. 392-400.
14. Wynn-Williams, C.G., *Accurate measurement of the electrical length of long coaxial radio-frequency cables*. Proceedings of the Institution of Electrical Engineers, 1972. **119**(2): p. 113-4.
15. Saito, Y., S. Furuya, S. Kato, H. Sugawara, and Y. Asano, *Coaxial line with highest electrical length stability*. Sumitomo Electric Technical Review, 1983(22): p. 91-101.
16. Biryukov, V.N., *Application of different electrical length cable sections for measuring the SWR of coaxial connectors*. Measurement Techniques, 1980. **23**(6): p. 547-50.
17. Naishadham, K., 4 - *Transmission Lines*, in *The Electrical Engineering Handbook*. 2005, Academic Press: Burlington. p. 525-537.

18. Miano, G. and A. Maffucci, *Chapter 1 - Transmission Line Equations and Properties*, in *Transmission Lines and Lumped Circuits*. 2001, Academic Press: San Diego. p. 15-48.
19. *8 - Transmission Lines*, in *Electromagnetics Explained*, S. Ron, Editor. 2002, Newnes: Burlington. p. 153-179.
20. Bräunig, D. and F. Wulf, *Chapter 10 Radiation effects in electronic components*, in *Instabilities in Silicon Devices*, B. Gérard and V. André, Editors. 1999, North-Holland. p. 639-722.
21. Ibbotson, L., *3 - Electromagnetic waves*, in *The Fundamentals of Signal Transmission*. 1999, Butterworth-Heinemann: London. p. 36-45.
22. Thostenson, E.T. and T.W. Chou, *Microwave processing: fundamentals and applications*. Composites Part A: Applied Science and Manufacturing, 1999. **30**(9): p. 1055-1071.
23. Kitchen, R., *1 - Introduction to RF and microwave radiation*, in *RF and Microwave Radiation Safety (Second Edition)*. 2001, Newnes: Oxford. p. 1-20.
24. Carr, J.J., *Chapter 1 - Introduction to Microwaves*, in *Microwave & Wireless Communications Technology*. 1996, Newnes: Newton. p. 1-12.
25. Hollister, A., *Wideband Amplifier Design*. 2007: Institution of Engineering and Technology.
26. Smith, P.H., *Electronic applications of the Smith Chart: in waveguide, circuit, and component analysis*. 1995: Noble.
27. Barthel, J. and R. Buchner, *Permittivity of Liquids*, in *Encyclopedia of Physical Science and Technology (Third Edition)*, A.M. Editor-in-Chief: Robert, Editor. 2003, Academic Press: New York. p. 697-706.
28. Grimnes, S. and Ø.G. Martinsen, *Chapter 3 - DIELECTRICS*, in *Bioimpedance and Bioelectricity Basics (Second Edition)*. 2008, Academic Press: New York. p. 57-92.
29. Yaws, C.L. and M.A. Satyro, *Chapter 20 - Dipole moment—Inorganic compounds*, in *Thermophysical Properties of Chemicals and Hydrocarbons*, L.Y. Carl, Editor. 2009, William Andrew Publishing: Norwich, NY. p. 683-685.
30. Suzuki, I., *Dipole moment functions of carbon dioxide and nitrous oxide*. *Journal of Molecular Spectroscopy*, 1980. **80**(1): p. 12-22.
31. Cole, K.S. and R.H. Cole, *Dispersion and Absorption in Dielectrics I. Alternating Current Characteristics*. *The Journal of Chemical Physics*, 1941. **9**(4): p. 341-351.
32. Davidson, D.W. and R.H. Cole, *Dielectric Relaxation in Glycerol, Propylene Glycol, and n-Propanol*. *The Journal of Chemical Physics*, 1951. **19**(12): p. 1484-1490.
33. Davidson, D.W. and R.H. Cole, *Dielectric Relaxation in Glycerine*. *The Journal of Chemical Physics*, 1950. **18**(10): p. 1417-1417.
34. Havriliak, S. and S. Negami, *A complex plane representation of dielectric and mechanical relaxation processes in some polymers*. *Polymer*, 1967. **8**(0): p. 161-210.
35. Asami, K., *Characterization of heterogeneous systems by dielectric spectroscopy*. *Progress in Polymer Science*, 2002. **27**(8): p. 1617-1659.
36. Markx, G.H. and C.L. Davey, *The dielectric properties of biological cells at radiofrequencies: applications in biotechnology*. *Enzyme and Microbial Technology*, 1999. **25**(3-5): p. 161-171.
37. Ragni, L., A. Al-Shami, G. Mikhaylenko, and J. Tang, *Dielectric characterization of hen eggs during storage*. *Journal of Food Engineering*, 2007. **82**(4): p. 450-459.
38. Castro-Giráldez, M., P.J. Fito, and P. Fito, *Application of microwaves dielectric spectroscopy for controlling pork meat (Longissimus dorsi) salting process*. *Journal of Food Engineering*, 2010. **97**(4): p. 484-490.
39. Castro-Giráldez, M., M.C. Aristoy, F. Toldrá, and P. Fito, *Microwave dielectric spectroscopy for the determination of pork meat quality*. *Food Research International*, 2010. **43**(10): p. 2369-2377.
40. McKeown, M.S., S. Trabelsi, E.W. Tollner, and S.O. Nelson, *Dielectric spectroscopy measurements for moisture prediction in Vidalia onions*. *Journal of Food Engineering*, 2012. **111**(3): p. 505-510.

41. Dalmay, C., M. Cheray, A. Pothier, F. Lalloué, M.O. Jauberteau, and P. Blondy, *Ultra sensitive biosensor based on impedance spectroscopy at microwave frequencies for cell scale analysis*. *Sensors and Actuators A: Physical*, 2010. **162**(2): p. 189-197.
42. Mason, A., O. Korostynska, M. Ortoneda-Pedrola, A. Shaw, and A. Al-Shamma'a, *A resonant co-planar sensor at microwave frequencies for biomedical applications*. *Sensors and Actuators A: Physical*, (0).
43. Ghavanini, F.A., H. Rodjégard, and P. Enoksson, *An easy-to-implement method for evaluation of capacitive resonant sensors*. *Journal of Micromechanics and Microengineering*, 2006. **16**(6): p. 156-60.
44. Sherry, D., *Thermoscopes, thermometers, and the foundations of measurement*. *Studies in History and Philosophy of Science Part A*, 2011. **42**(4): p. 509-524.
45. Dunn, P.F., *Fundamentals of Sensors for Engineering and Science*. 2011: Taylor & Francis.
46. Baura, G.D., *Chapter 12 - Thermometers*, in *Medical Device Technologies*. 2012, Academic Press: Oxford. p. 257-274.
47. Fraden, J., *Handbook of Modern Sensors: Physics, Designs, and Applications*. 2010: Springer.
48. Imura, T., S. Yokoyama, and M. Abe, *Chapter 6: Molecular Interactions between Lipid and Its Related Substances in Bilayer Membranes*, in *Advances in Planar Lipid Bilayers and Liposomes*, A.L. Liu, Editor. 2006, Academic Press. p. 191-227.
49. Strachan, T. and A.P. Read, *Human Molecular Genetics*. 2010/12/07 ed. 1999.
50. Varley, J.M., *Germline TP53 mutations and Li-Fraumeni syndrome*. *Hum Mutat*, 2003. **21**(3): p. 313-20.
51. Hanahan, D. and R.A. Weinberg, *The hallmarks of cancer*. *Cell*, 2000. **100**(1): p. 57-70.
52. Kumar, V., A.K. Abbas, and J.C. Aster, *Robbins Basic Pathology*. 2012: Elsevier/Saunders.
53. Hill, C.L., Y. Zhang, B. Sigurgeirsson, E. Pukkala, L. Mellemkjaer, A. Airio, S.R. Evans, and D.T. Felson, *Frequency of specific cancer types in dermatomyositis and polymyositis: a population-based study*. *Lancet*, 2001. **357**(9250): p. 96-100.
54. Schroeder, A., D.A. Heller, M.M. Winslow, J.E. Dahlman, G.W. Pratt, R. Langer, T. Jacks, and D.G. Anderson, *Treating metastatic cancer with nanotechnology*. *Nat Rev Cancer*, 2012. **12**(1): p. 39-50.
55. Paleri, V., H. Mehanna, and R.G. Wight, *EDITORIAL: TNM classification of malignant tumours 7th edition: what's new for head and neck?* *Clinical Otolaryngology*, 2010. **35**(4): p. 270-272.
56. Alan, K.W., S.T. Catherine, F. David, and M. Siegfried, *Men's Health and the Excess Burden of Cancer in Men*. *European Urology*, 2010. **9**(3): p. 467-470.
57. Dow, J., G. Lindsay, and J. Morrison, *Biochemistry: molecules, cells and the body*. 1996: Addison-Wesley.
58. Ott, J.J., A. Ullrich, and A.B. Miller, *The importance of early symptom recognition in the context of early detection and cancer survival*. *European Journal of Cancer*, 2009. **45**(16): p. 2743-2748.
59. Richards, M.A., *The size of the prize for earlier diagnosis of cancer in England*. *Br J Cancer*, 2009. **101**(S2): p. S125-S129.
60. Sant, M., C. Allemani, R. Capocaccia, T. Hakulinen, T. Aareleid, J.W. Coebergh, M.P. Coleman, P. Grosclaude, C. Martinez, J. Bell, J. Youngson, F. Berrino, and E.W.G. the, *Stage at diagnosis is a key explanation of differences in breast cancer survival across Europe*. *International Journal of Cancer*, 2003. **106**(3): p. 416-422.
61. Horn, L.C., U. Fischer, G. Raptis, K. Bilek, and B. Hentschel, *Tumor size is of prognostic value in surgically treated FIGO stage II cervical cancer*. *Gynecologic Oncology*, 2007. **107**(2): p. 310-315.
62. Vis, A.N., S. Roemeling, A.M.J. Reedijk, S.J. Otto, and F.H. Schröder, *Overall Survival in the Intervention Arm of a Randomized Controlled Screening Trial for Prostate Cancer Compared with a Clinically Diagnosed Cohort*. *European Urology*, 2008. **53**(1): p. 91-98.

63. Wang, J.-H., C.-S. Changchien, T.-H. Hu, C.-M. Lee, K.-M. Kee, C.-Y. Lin, C.-L. Chen, T.-Y. Chen, Y.-J. Huang, and S.-N. Lu, *The efficacy of treatment schedules according to Barcelona Clinic Liver Cancer staging for hepatocellular carcinoma – Survival analysis of 3892 patients*. European journal of cancer (Oxford, England : 1990), 2008. **44**(7): p. 1000-1006.
64. Mhaskar, A.R., G. Quinn, S. Vadaparampil, B. Djulbegovic, C.K. Gwede, and A. Kumar, *Timing of first-line cancer treatments – Early versus late – A systematic review of phase III randomized trials*. Cancer Treatment Reviews, 2010. **36**(8): p. 621-628.
65. J.L. H., *Life expectancy as a measurement of the benefit shown by clinical trials of treatment for early breast cancer*. Clinical Oncology, 1998. **10**(2): p. 92-94.
66. de Gramont, A., A. de Gramont, B. Chibaudel, A.K. Larsen, C. Tournigand, and T. André, *The Evolution of Adjuvant Therapy in the Treatment of Early-Stage Colon Cancer*. Clinical Colorectal Cancer, 2011. **10**(4): p. 218-226.
67. Schwarzer, R., A. Luszczynska, S. Boehmer, S. Taubert, and N. Knoll, *Changes in finding benefit after cancer surgery and the prediction of well-being one year later*. Social Science & Medicine, 2006. **63**(6): p. 1614-1624.
68. Rustin, G.J.S., M.E.L. van der Burg, C.L. Griffin, D. Guthrie, A. Lamont, G.C. Jayson, G. Kristensen, C. Mediola, C. Coens, W. Qian, M.K.B. Parmar, and A.M. Swart, *Early versus delayed treatment of relapsed ovarian cancer (MRC OV05/EORTC 55955): a randomised trial*. The Lancet, 2010. **376**(9747): p. 1155-1163.
69. Kitagawa, Y., H. Takeuchi, Y. Saikawa, and M. Kitajima, *Surgical treatment of esophageal cancer: benefit and limitation of endoscopic surgery*. The American Journal of Surgery, 2007. **194**(4, Supplement): p. S158-S161.
70. Blinman, P., V. Duric, A.K. Nowak, P. Beale, S. Clarke, K. Briscoe, A. Boyce, D. Goldstein, M. Hudson, and M. Stockler, *Adjuvant chemotherapy for early colon cancer: What survival benefits make it worthwhile?* European Journal of Cancer, 2010. **46**(10): p. 1800-1807.
71. National Cancer Intelligence, N., *Routes to Diagnosis -- NCIN Data Briefing*. 2010.
72. Wyld, L. and C.E. Ingram, *Screening of the population for breast cancer*. 2007. **25**(6): p. 254-256.
73. Peto, J., C. Gilham, O. Fletcher, and F.E. Matthews, *The cervical cancer epidemic that screening has prevented in the UK*. The Lancet, 2004. **364**(9430): p. 249-256.
74. Stephen A, F., *Screening Benefits Versus Radiation Risks from Mammography for Women Age 40–49 Years: How Wide Is Our Margin of Safety?* Breast Diseases: A Year Book Quarterly, 2006. **17**(3): p. 213-214.
75. Than, N.G., B. Sumegi, S. Bellyei, T. Berki, G. Szekeres, T. Janaky, A. Szigeti, H. Bohn, and G.N. Than, *Lipid droplet and milk lipid globule membrane associated placental protein 17b (PP17b) is involved in apoptotic and differentiation processes of human epithelial cervical carcinoma cells*. European Journal of Biochemistry, 2003. **270**(6): p. 1176-1188.
76. Opstad, K.S., B.A. Bell, J.R. Griffiths, and F.A. Howe, *An investigation of human brain tumour lipids by high-resolution magic angle spinning 1H MRS and histological analysis*. NMR in Biomedicine, 2008. **21**(7): p. 677-685.
77. Accioly, M.T., P. Pacheco, C.M. Maya-Monteiro, N. Carrossini, B.K. Robbs, S.S. Oliveira, C. Kaufmann, J.A. Morgado-Diaz, P.T. Bozza, and J.P.B. Viola, *Lipid Bodies Are Reservoirs of Cyclooxygenase-2 and Sites of Prostaglandin-E2 Synthesis in Colon Cancer Cells*. Cancer Research, 2008. **68**(6): p. 1732-1740.
78. Swinnen, J.V., K. Brusselmans, and G. Verhoeven, *Increased lipogenesis in cancer cells: new players, novel targets*. Current Opinion in Clinical Nutrition & Metabolic Care, 2006. **9**(4): p. 358-365 10.1097/01.mco.0000232894.28674.30.
79. Kuhajda, F.P., *Fatty Acid Synthase and Cancer: New Application of an Old Pathway*. Cancer Research, 2006. **66**(12): p. 5977-5980.

80. Yu, W., J. Cassara, and P.F. Weller, *Phosphatidylinositide 3-kinase localizes to cytoplasmic lipid bodies in human polymorphonuclear leukocytes and other myeloid-derived cells*. *Blood*, 2000. **95**(3): p. 1078-1085.
81. Martin, S. and R.G. Parton, *Caveolin, cholesterol, and lipid bodies*. *Seminars in Cell & Developmental Biology*, 2005. **16**(2): p. 163-174.
82. Chen, J.-S., A.S. Greenberg, and S.-M. Wang, *Oleic acid-induced PKC isozyme translocation in RAW 264.7 macrophages*. *Journal of Cellular Biochemistry*, 2002. **86**(4): p. 784-791.
83. Warnick, G.R. and K. Nakajima, *Fasting versus Nonfasting Triglycerides: Implications for Laboratory Measurements*. *Clinical Chemistry*, 2008. **54**(1): p. 14-16.
84. Hokanson, J.E. and M.A. Austin, *Plasma triglyceride level is a risk factor for cardiovascular disease independent of high-density lipoprotein cholesterol level: a meta-analysis of population-based prospective studies*. *J Cardiovasc Risk*, 1996. **3**(2): p. 213-9.
85. Garbay, B., S. Bauxis-Lagrave, F. Boiron-Sargueil, G. Elson, and C. Cassagne, *Acetyl-CoA carboxylase gene expression in the developing mouse brain. Comparison with other genes involved in lipid biosynthesis*. *Developmental Brain Research*, 1997. **98**(2): p. 197-203.
86. Kim, K.W., H. Yamane, J. Zondlo, J. Busby, and M. Wang, *Expression, purification, and characterization of human acetyl-CoA carboxylase 2*. *Protein Expression and Purification*, 2007. **53**(1): p. 16-23.
87. Wang, C., C. Xu, M. Sun, D. Luo, D.-f. Liao, and D. Cao, *Acetyl-CoA carboxylase- α inhibitor TOFA induces human cancer cell apoptosis*. *Biochemical and Biophysical Research Communications*, 2009. **385**(3): p. 302-306.
88. Takamura, Y., Y. Kitayama, A. Arakawa, S. Yamanaka, M. Tosaki, and Y. Ogawa, *Malonyl-CoA: acetyl-CoA cycling. A new micromethod for determination of acyl-CoAs with malonate decarboxylase*. *Biochimica et Biophysica Acta (BBA) - Lipids and Lipid Metabolism*, 1985. **834**(1): p. 1-7.
89. Athenstaedt, K. and G. Daum, *Phosphatidic acid, a key intermediate in lipid metabolism*. *European Journal of Biochemistry*, 1999. **266**(1): p. 1-16.
90. McDermott, M., M.J.O. Wakelam, and A.J. Morris, *Phospholipase D*. *Biochemistry and Cell Biology*, 2004. **82**(1): p. 225-253.
91. Bozza, P.T., K.G. Magalhães, and P.F. Weller, *Leukocyte lipid bodies - Biogenesis and functions in inflammation*. *Biochimica et Biophysica Acta - Molecular and Cell Biology of Lipids*, 2009. **1791**(6): p. 540-551.
92. Martin, S. and R.G. Parton, *Lipid droplets: A unified view of a dynamic organelle*. *Nature Reviews Molecular Cell Biology*, 2006. **7**(5): p. 373-378.
93. Murphy, D.J., *The biogenesis and functions of lipid bodies in animals, plants and microorganisms*. *Progress in Lipid Research*, 2001. **40**(5): p. 325-438.
94. Robenek, M.J., N.J. Severs, K. Schlattmann, G. Plenz, K.P. Zimmer, D. Troyer, and H. Robenek, *Lipids partition caveolin-1 from ER membranes into lipid droplets: updating the model of lipid droplet biogenesis*. *The FASEB journal : official publication of the Federation of American Societies for Experimental Biology*, 2004. **18**(7): p. 866-868.
95. Brown, D.A., *Lipid droplets: Proteins floating on a pool of fat*. *Current Biology*, 2001. **11**(11): p. R446-R449.
96. Bozza, P.T., J.L. Payne, J.L. Goulet, and P.F. Weller, *Mechanisms of platelet-activating factor-induced lipid body formation: requisite roles for 5-lipoxygenase and de novo protein synthesis in the compartmentalization of neutrophil lipids*. *J Exp Med*, 1996. **183**(4): p. 1515-25.
97. Weller, P.F., S.W. Ryeom, S.T. Picard, S.J. Ackerman, and A.M. Dvorak, *Cytoplasmic lipid bodies of neutrophils: formation induced by cis-unsaturated fatty acids and mediated by protein kinase C*. *Journal of Cell Biology*, 1991. **113**(1): p. 137-146.
98. Moreira, L.S., B. Piva, L.B. Gentile, F.P. Mesquita-Santos, H. D'Avila, C.M. Maya-Monteiro, P.T. Bozza, C. Bandeira-Melo, and B.L. Diaz, *Cytosolic phospholipase A2-driven PGE2*

- synthesis within unsaturated fatty acids-induced lipid bodies of epithelial cells*. Biochimica et Biophysica Acta - Molecular and Cell Biology of Lipids, 2009. **1791**(3): p. 156-165.
99. Bozza, P.T., W. Yu, J. Cassara, and P.F. Weller, *Pathways for eosinophil lipid body induction: Differing signal transduction in cells from normal and hypereosinophilic subjects*. Journal of Leukocyte Biology, 1998. **64**(4): p. 563-569.
100. Bandeira-Melo, C., M. Phoofolo, and P.F. Weller, *Extranuclear Lipid Bodies, Elicited by CCR3-mediated Signaling Pathways, Are the Sites of Chemokine-enhanced Leukotriene C4 Production in Eosinophils and Basophils*. Journal of Biological Chemistry, 2001. **276**(25): p. 22779-22787.
101. Maya-Monteiro, C.M., P.E. Almeida, H. D'Ávila, A.S. Martins, A.P. Rezende, H. Castro-Faria-Neto, and P.T. Bozza, *Leptin induces macrophage lipid body formation by a phosphatidylinositol 3-kinase- and mammalian target of rapamycin-dependent mechanism*. Journal of Biological Chemistry, 2008. **283**(4): p. 2203-2210.
102. Vieira-De-Abreu, A., E.F. Assis, G.S. Gomes, H.C. Castro-Faria-Neto, P.F. Weller, C. Bandeira-Melo, and P.T. Bozza, *Allergic challenge-elicited lipid bodies compartmentalize in vivo leukotriene C4 synthesis within eosinophils*. American Journal of Respiratory Cell and Molecular Biology, 2005. **33**(3): p. 254-261.
103. Pacheco, P., A. Vieira-De-Abreu, R.N. Gomes, G. Barbosa-Lima, L.B. Wermelinger, C.M. Maya-Monteiro, A.R. Silva, M.T. Bozza, H.C. Castro-Faria-Neto, C. Bandeira-Melo, and P.T. Bozza, *Monocyte chemoattractant protein-1/CC chemokine ligand 2 controls microtubule-driven biogenesis and leukotriene B4-synthesizing function of macrophage lipid bodies elicited by innate immune response*. Journal of Immunology, 2007. **179**(12): p. 8500-8508.
104. De Assis, E.F., A.R. Silva, L.F.C. Caiado, G.K. Marathe, G.A. Zimmerman, S.M. Prescott, T.M. McIntyre, P.T. Bozza, and H.C. De Castro-Faria-Neto, *Synergism between platelet-activating factor-like phospholipids and peroxisome proliferator-activated receptor γ agonists generated during low density lipoprotein oxidation that induces lipid body formation in leukocytes*. Journal of Immunology, 2003. **171**(4): p. 2090-2098.
105. Bozza, P.T., W. Yu, J.F. Penrose, E.S. Morgan, A.M. Dvorak, and P.F. Weller, *Eosinophil lipid bodies: Specific, inducible intracellular sites for enhanced eicosanoid formation*. Journal of Experimental Medicine, 1997. **186**(6): p. 909-920.
106. Czabany, T., K. Athenstaedt, and G. Daum, *Synthesis, storage and degradation of neutral lipids in yeast*. Biochimica et Biophysica Acta (BBA) - Molecular and Cell Biology of Lipids, 2007. **1771**(3): p. 299-309.
107. Lin, H.J., W.L. Ng, L. Tung-Ma, and C.L.H. Lee, *Absence of the ether lipid tumour marker in diethylnitrosamine-induced rat liver cell cancer*. Cancer Letters, 1981. **11**(3): p. 231-237.
108. Sinha Roy, S., S. Mukhopadhyay, S. Mukherjee, and S.K. Das, *Breast cancer is associated with an increase in the activity and expression of cholinephosphotransferase in rats*. Life Sciences, 2008. **83**(19-20): p. 661-665.
109. Swinnen, J.V. and G. Verhoeven, *Androgens and the control of lipid metabolism in human prostate cancer cells*. The Journal of Steroid Biochemistry and Molecular Biology, 1998. **65**(1-6): p. 191-198.
110. Torday, J., J. Hua, and R. Slavin, *Metabolism and fate of neutral lipids of fetal lung fibroblast origin*. Biochimica et Biophysica Acta (BBA) - Lipids and Lipid Metabolism, 1995. **1254**(2): p. 198-206.
111. Bozza, P.T. and J.P.B. Viola, *Lipid droplets in inflammation and cancer*. Prostaglandins, Leukotrienes and Essential Fatty Acids, 2010. **82**(4-6): p. 243-250.
112. Pol, A., R. Luetterforst, M. Lindsay, S. Heino, E. Ikonen, and R.G. Parton, *A caveolin dominant negative mutant associates with lipid bodies and induces intracellular cholesterol imbalance*. Journal of Cell Biology, 2001. **152**(5): p. 1057-1070.

113. Fujimoto, T., H. Kogo, K. Ishiguro, K. Tauchi, and R. Nomura, *Caveolin-2 is targeted to lipid droplets, a new "membrane domain" in the cell*. Journal of Cell Biology, 2001. **152**(5): p. 1079-1085.
114. Cohen, A.W., B. Razani, W. Schubert, T.M. Williams, X.B. Wang, P. Iyengar, D.L. Brasaemle, P.E. Scherer, and M.P. Lisanti, *Role of Caveolin-1 in the Modulation of Lipolysis and Lipid Droplet Formation*. Diabetes, 2004. **53**(5): p. 1261-1270.
115. Khatchadourian, A., S.D. Bourque, V.R. Richard, V.I. Titorenko, and D. Maysinger, *Dynamics and regulation of lipid droplet formation in lipopolysaccharide (LPS)-stimulated microglia*. Biochimica et Biophysica Acta (BBA) - Molecular and Cell Biology of Lipids, 2012. **1821**(4): p. 607-617.
116. Wan, H.C., R.C.N. Melo, Z. Jin, A.M. Dvorak, and P.F. Weller, *Roles and origins of leukocyte lipid bodies: Proteomic and ultrastructural studies*. FASEB Journal, 2007. **21**(1): p. 167-178.
117. Dvorak, A.M., *Mast cell secretory granules and lipid bodies contain the necessary machinery important for the in situ synthesis of proteins*. Chemical immunology and allergy, 2005. **85**: p. 252-315.
118. Dvorak, A.M., E.S. Morgan, and P.F. Weller, *RNA is closely associated with human mast cell lipid bodies*. Histology and Histopathology, 2003. **18**(3): p. 943-968.
119. Sato, S., M. Fukasawa, Y. Yamakawa, T. Natsume, T. Suzuki, I. Shoji, H. Aizaki, T. Miyamura, and M. Nishijima, *Proteomic profiling of lipid droplet proteins in hepatoma cell lines expressing hepatitis C virus core protein*. Journal of Biochemistry, 2006. **139**(5): p. 921-930.
120. Kurat, C.F., H. Wolinski, J. Petschnigg, S. Kaluarachchi, B. Andrews, K. Natter, and S.D. Kohlwein, *Cdk1/Cdc28-Dependent Activation of the Major Triacylglycerol Lipase Tgl4 in Yeast Links Lipolysis to Cell-Cycle Progression*. Molecular Cell, 2009. **33**(1): p. 53-63.
121. Natter, K. and S.D. Kohlwein, *Yeast and cancer cells – common principles in lipid metabolism*. Biochimica et Biophysica Acta (BBA) - Molecular and Cell Biology of Lipids, 2013. **1831**(2): p. 314-326.
122. Diaz-Ruiz, R., S. Uribe-Carvajal, A. Devin, and M. Rigoulet, *Tumor cell energy metabolism and its common features with yeast metabolism*. Biochimica et Biophysica Acta (BBA) - Reviews on Cancer, 2009. **1796**(2): p. 252-265.
123. Diaz-Ruiz, R., M. Rigoulet, and A. Devin, *The Warburg and Crabtree effects: On the origin of cancer cell energy metabolism and of yeast glucose repression*. Biochimica et Biophysica Acta (BBA) - Bioenergetics, 2011. **1807**(6): p. 568-576.
124. Čáp, M., L. Štěpánek, K. Harant, L. Váchová, and Z. Palková, *Cell Differentiation within a Yeast Colony: Metabolic and Regulatory Parallels with a Tumor-Affected Organism*. Molecular Cell, 2012. **46**(4): p. 436-448.
125. Hanahan, D. and R.A. Weinberg, *Hallmarks of cancer: the next generation*. Cell, 2011. **144**(5): p. 646-74.
126. Reijenga, K.A., J.L. Snoep, J.A. Diderich, H.W. Van Verseveld, H.V. Westerhoff, and B. Teusink, *Control of glycolytic dynamics by hexose transport in Saccharomyces cerevisiae*. Biophysical Journal, 2001. **80**(2): p. 626-634.
127. Sauer, L.A., J.W. Stayman III, and R.T. Dauchy, *Aminoacid, glucose, and lactic acid utilization in vivo by rat tumors*. Cancer Research, 1983. **42**: p. 4090-4097.
128. Rastogi, S., S. Banerjee, S. Chellappan, and G.R. Simon, *Glut-1 antibodies induce growth arrest and apoptosis in human cancer cell lines*. Cancer Letters, 2007. **257**(2): p. 244-251.
129. Au, K.K., E. Liong, J.Y. Li, P.S. Li, C.C. Liew, T.T. Kwok, Y.M. Choy, C.Y. Lee, and K.P. Fung, *Increases in mRNA levels of glucose transporters types 1 and 3 in Ehrlich ascites tumor cells during tumor development*. Journal of Cellular Biochemistry, 1997. **67**(1): p. 131-135.
130. Suzuki, T., A. Iwazaki, H. Katagiri, Y. Oka, J.L. Redpath, E.J. Stanbridge, and T. Kitagawa, *Enhanced expression of glucose transporter GLUT3 in tumorigenic HeLa cell hybrids associated with tumor suppressor dysfunction*. European Journal of Biochemistry, 1999. **262**(2): p. 534-540.

131. Özcan, S. and M. Johnston, *Function and regulation of yeast hexose transporters*. Microbiology and Molecular Biology Reviews, 1999. **63**(3): p. 554-569.
132. Reifengerger, E., K. Freidel, and M. Ciriacy, *Identification of novel HXT genes in Saccharomyces cerevisiae reveals the impact of individual hexose transporters on glycolytic flux*. Mol Microbiol, 1995. **16**(1): p. 157-67.
133. Reifengerger, E., E. Boles, and M. Ciriacy, *Kinetic characterization of individual hexose transporters of Saccharomyces cerevisiae and their relation to the triggering mechanisms of glucose repression*. European Journal of Biochemistry, 1997. **245**(2): p. 324-333.
134. Boles, E. and C.P. Hollenberg, *The molecular genetics of hexose transport in yeasts*. FEMS Microbiology Reviews, 1997. **21**(1): p. 85-111.
135. Dell' Antone, P., *Energy metabolism in cancer cells: How to explain the Warburg and Crabtree effects?* Medical Hypotheses, 2012. **79**(3): p. 388-392.
136. Pronk, J.T., H.Y. Steensma, and J.P. Van Dijken, *Pyruvate metabolism in Saccharomyces cerevisiae*. Yeast, 1996. **12**(16): p. 1607-1633.
137. Baggetto, L.G., *Deviant energetic metabolism of glycolytic cancer cells*. Biochimie, 1992. **74**(11): p. 959-974.
138. Louwman, W.J., M.L.G. Janssen-Heijnen, S. Houterman, A.C. Voogd, M.J.C. van der Sangen, G.A.P. Nieuwenhuijzen, and J.W.W. Coebergh, *Less extensive treatment and inferior prognosis for breast cancer patient with comorbidity: A population-based study*. European Journal of Cancer, 2005. **41**(5): p. 779-785.
139. Gobbi, P.G., M. Bergonzi, M. Comelli, L. Villano, D. Pozzoli, A. Vanoli, and P. Dionigi, *The prognostic role of time to diagnosis and presenting symptoms in patients with pancreatic cancer*. Cancer Epidemiology, 2013. **37**(2): p. 186-190.
140. Aloia, T.A. and J.E. Gershenwald, *Management of Early-Stage Cutaneous Melanoma*. Current Problems in Surgery, 2005. **42**(7): p. 468-534.
141. Martin-Moreno, J.M., A. Anttila, L. von Karsa, J.L. Alfonso-Sanchez, and L. Gorgojo, *Cancer screening and health system resilience: Keys to protecting and bolstering preventive services during a financial crisis*. European Journal of Cancer, 2012. **48**(14): p. 2212-2218.
142. Martin-Moreno, J.M., J.L. Alfonso-Sanchez, M. Harris, and B.G. Lopez-Valcarcel, *The effects of the financial crisis on primary prevention of cancer*. European Journal of Cancer, 2010. **46**(14): p. 2525-2533.
143. Hillner, B.E., *S2 Optimal allocation of cancer directed financial resources – tensions between primary prevention, early detection, and treatment*. European Journal of Cancer Supplements, 2010. **8**(2): p. 1.
144. Casamassima, F., S. Pacini, A. Dragotto, M. Anichini, V. Chiarugi, and M. Ruggiero, *Intracellular diacylglycerol: a mitogenic second messenger proposable as marker of transformation in squamous cell carcinoma of the lung*. Lung Cancer, 1996. **15**(2): p. 161-170.
145. Fernandis, A.Z. and M.R. Wenk, *Lipid-based biomarkers for cancer*. Journal of Chromatography B, 2009. **877**(26): p. 2830-2835.
146. Grant, E.H., V.E.R. McClean, N.R.V. Nightingale, R.J. Sheppard, and M.J. Chapman, *Dielectric behavior of water in biological solutions: Studies on myoglobin, human low-density lipoprotein, and polyvinylpyrrolidone*. Bioelectromagnetics, 1986. **7**(2): p. 151-162.
147. Grosse, C. and A.V. Delgado, *Dielectric dispersion in aqueous colloidal systems*. Current Opinion in Colloid & Interface Science, 2010. **15**(3): p. 145-159.
148. Ron, A., N. Fishelson, N. Croitoriu, D. Benayahu, and Y. Shacham-Diamand, *Theoretical examination of aggregation effect on the dielectric characteristics of spherical cellular suspension*. Biophysical Chemistry, 2009. **140**(1-3): p. 39-50.
149. Sheen, J., Z.-W. Hong, W. Liu, W.-L. Mao, and C.-A. Chen, *Study of dielectric constants of binary composites at microwave frequency by mixture laws derived from three basic particle shapes*. European Polymer Journal, 2009. **45**(4): p. 1316-1321.

-
150. Sun, T.-P., C.T.-S. Ching, C.-S. Cheng, S.-H. Huang, Y.-J. Chen, C.-S. Hsiao, C.-H. Chang, S.-Y. Huang, H.-L. Shieh, W.-H. Liu, C.-M. Liu, and C.-Y. Chen, *The use of bioimpedance in the detection/screening of tongue cancer*. *Cancer Epidemiology*, 2010. **34**(2): p. 207-211.
151. Kerhet, A., M. Raffetto, A. Boni, and A. Massa, *A SVM-based approach to microwave breast cancer detection*. *Engineering Applications of Artificial Intelligence*, 2006. **19**(7): p. 807-818.
152. Bellorofonte, C., C. Vedruccio, P. Tombolini, M. Ruoppolo, and A. Tubaro, *Non-Invasive Detection of Prostate Cancer by Electromagnetic Interaction*. *European Urology*, 2005. **47**(1): p. 29-37.
153. Hildebrandt, C., H. Büth, S. Cho, Impidjati, and H. Thielecke, *Detection of the osteogenic differentiation of mesenchymal stem cells in 2D and 3D cultures by electrochemical impedance spectroscopy*. *Journal of Biotechnology*, 2010. **148**(1): p. 83-90.
154. Ron, A., R.R. Singh, N. Fishelson, I. Shur, R. Socher, D. Benayahu, and Y. Shacham-Diamand, *Cell-based screening for membranal and cytoplasmatic markers using dielectric spectroscopy*. *Biophysical Chemistry*, 2008. **135**(1-3): p. 59-68.
155. Lonappan, A., G.N. Bindu, V. Thomas, and K.T. Mathew, *Analysis of Human Semen using Microwaves*. *Progress in Electromagnetics Research*, 2006. **57**: p. 277-284.
156. *Greek olive oil production statistics* - <http://www.eleones.gr/>. 2012 [cited 2013].
157. *International Olive Oil Council*. 17/07/2013]; Available from: <http://www.internationaloliveoil.org/>.
158. Mildner-Szkudlarz, S. and H.H. Jeleń, *The potential of different techniques for volatile compounds analysis coupled with PCA for the detection of the adulteration of olive oil with hazelnut oil*. *Food Chemistry*, 2008. **110**(3): p. 751-761.
159. Garcia, R., N. Martins, and M.J. Cabrita, *Putative markers of adulteration of extra virgin olive oil with refined olive oil: Prospects and limitations*. *Food Research International*, 2013(0).
160. Al-Ismael, K.M., A.K. Alsaed, R. Ahmad, and M. Al-Dabbas, *Detection of olive oil adulteration with some plant oils by GLC analysis of sterols using polar column*. *Food Chemistry*, 2010. **121**(4): p. 1255-1259.
161. Errico, S. *Olive Oil's Dark Side* - <http://www.newyorker.com/online/blogs/books/2012/02/the-exchange-tom-mueller.html>. 2012 [cited 2013].
162. Renton, A. *Extra Virginity: The Sublime and Scandalous World of Olive Oil by Tom Mueller – review*. 2012 [cited 2013].
163. Mueller, T., *Extra Virginity: The Sublime and Scandalous World of Olive Oil*. 2011: W. W. Norton.
164. *An "action plan" for the olive oil sector*, in *Agriculture Council Meeting 2012*. 2012: Luxembourg.
165. *Global method for the detection of extraneous oils in olive oil*. 2012, International Olive Council: Madrid, Spain.
166. Vance, J.E. and K. Adeli, *Chapter 18 - Assembly and secretion of triacylglycerol-rich lipoproteins*, in *Biochemistry of Lipids, Lipoproteins and Membranes (Fifth Edition)*, E.V. Dennis and E.V. Jean, Editors. 2008, Elsevier: San Diego. p. 507-XII.
167. Frayn, K.N. and D. Langin, *Triacylglycerol metabolism in adipose tissue*, in *Advances in Molecular and Cell Biology*, V. van der, Editor. 2003, Elsevier. p. 337-356.
168. Bell, R.M. and R.A. Coleman, *3 Enzymes of Triacylglycerol Formation in Mammals*, in *The Enzymes*, D.B. Paul, Editor. 1983, Academic Press. p. 87-111.
169. Lee, D.-S., B.-S. Noh, S.-Y. Bae, and K. Kim, *Characterization of fatty acids composition in vegetable oils by gas chromatography and chemometrics*. *Analytica Chimica Acta*, 1998. **358**(2): p. 163-175.
170. Shaw, A.D., A. di Camillo, G. Vlahov, A. Jones, G. Bianchi, J. Rowland, and D.B. Kell, *Discrimination of the variety and region of origin of extra virgin olive oils using ¹³C NMR and*
-

- multivariate calibration with variable reduction*. *Analytica Chimica Acta*, 1997. **348**(1–3): p. 357-374.
171. Fang, G., J.Y. Goh, M. Tay, H.F. Lau, and S.F.Y. Li, *Characterization of oils and fats by 1H NMR and GC/MS fingerprinting: Classification, prediction and detection of adulteration*. *Food Chemistry*, 2013. **138**(2–3): p. 1461-1469.
172. Alonso-Salces, R.M., K. Héberger, M.V. Holland, J.M. Moreno-Rojas, C. Mariani, G. Bellan, F. Reniero, and C. Guillou, *Multivariate analysis of NMR fingerprint of the unsaponifiable fraction of virgin olive oils for authentication purposes*. *Food Chemistry*, 2010. **118**(4): p. 956-965.
173. Agiomyrgianaki, A., P.V. Petrakis, and P. Dais, *Detection of refined olive oil adulteration with refined hazelnut oil by employing NMR spectroscopy and multivariate statistical analysis*. *Talanta*, 2010. **80**(5): p. 2165-2171.
174. Šmejkalová, D. and A. Piccolo, *High-power gradient diffusion NMR spectroscopy for the rapid assessment of extra-virgin olive oil adulteration*. *Food Chemistry*, 2010. **118**(1): p. 153-158.
175. Rohman, A. and Y.B. Che Man, *The use of Fourier transform mid infrared (FT-MIR) spectroscopy for detection and quantification of adulteration in virgin coconut oil*. *Food Chemistry*, 2011. **129**(2): p. 583-588.
176. Maggio, R.M., L. Cerretani, E. Chiavaro, T.S. Kaufman, and A. Bendini, *A novel chemometric strategy for the estimation of extra virgin olive oil adulteration with edible oils*. *Food Control*, 2010. **21**(6): p. 890-895.
177. Gurdeniz, G. and B. Ozen, *Detection of adulteration of extra-virgin olive oil by chemometric analysis of mid-infrared spectral data*. *Food Chemistry*, 2009. **116**(2): p. 519-525.
178. Poulli, K.I., G.A. Mousdis, and C.A. Georgiou, *Monitoring olive oil oxidation under thermal and UV stress through synchronous fluorescence spectroscopy and classical assays*. *Food Chemistry*, 2009. **117**(3): p. 499-503.
179. Poulli, K.I., G.A. Mousdis, and C.A. Georgiou, *Rapid synchronous fluorescence method for virgin olive oil adulteration assessment*. *Food Chemistry*, 2007. **105**(1): p. 369-375.
180. Öztürk, B., A. Ankan, and D. Özdemir, *Chapter 50 - Olive Oil Adulteration with Sunflower and Corn Oil Using Molecular Fluorescence Spectroscopy*, in *Olives and Olive Oil in Health and Disease Prevention*, R.P. Victor and W. Ronald Ross, Editors. 2010, Academic Press: San Diego. p. 451-461.
181. Guimet, F., J. Ferré, and R. Boqué, *Rapid detection of olive–pomace oil adulteration in extra virgin olive oils from the protected denomination of origin “Siurana” using excitation–emission fluorescence spectroscopy and three-way methods of analysis*. *Analytica Chimica Acta*, 2005. **544**(1–2): p. 143-152.
182. Guimet, F., R. Boqué, and J. Ferré, *Application of non-negative matrix factorization combined with Fisher's linear discriminant analysis for classification of olive oil excitation–emission fluorescence spectra*. *Chemometrics and Intelligent Laboratory Systems*, 2006. **81**(1): p. 94-106.
183. Kim, M., S. Lee, K. Chang, H. Chung, and Y.M. Jung, *Use of temperature dependent Raman spectra to improve accuracy for analysis of complex oil-based samples: Lube base oils and adulterated olive oils*. *Analytica Chimica Acta*, 2012. **748**(0): p. 58-66.
184. Guzmán, E., V. Baeten, J.A.F. Pierna, and J.A. García-Mesa, *A portable Raman sensor for the rapid discrimination of olives according to fruit quality*. *Talanta*, 2012. **93**(0): p. 94-98.
185. Guzmán, E., V. Baeten, J.A. Fernández Pierna, and J.A. García-Mesa, *Application of low-resolution Raman spectroscopy for the analysis of oxidized olive oil*. *Food Control*, 2011. **22**(12): p. 2036-2040.
186. Graham, S.F., S.A. Haughey, R.M. Ervin, E. Cancouët, S. Bell, and C.T. Elliott, *The application of near-infrared (NIR) and Raman spectroscopy to detect adulteration of oil used in animal feed production*. *Food Chemistry*, 2012. **132**(3): p. 1614-1619.

187. Zhang, H., Y. Wu, Y. Li, B. Wang, J. Han, X. Ju, and Y. Chen, *PCR-CE-SSCP used to authenticate edible oils*. Food Control, 2012. **27**(2): p. 322-329.
188. Vietina, M., C. Agrimonti, and N. Marmiroli, *Detection of plant oil DNA using high resolution melting (HRM) post PCR analysis: A tool for disclosure of olive oil adulteration*. Food Chemistry, 2013. **141**(4): p. 3820-3826.
189. Kumar, S., T. Kahlon, and S. Chaudhary, *A rapid screening for adulterants in olive oil using DNA barcodes*. Food Chemistry, 2011. **127**(3): p. 1335-1341.
190. Giménez, M.J., F. Pistón, A. Martín, and S.G. Atienza, *Application of real-time PCR on the development of molecular markers and to evaluate critical aspects for olive oil authentication*. Food Chemistry, 2010. **118**(2): p. 482-487.
191. Bazakos, C., A.O. Dulger, A.T. Uncu, S. Spaniolas, T. Spano, and P. Kalaitzis, *A SNP-based PCR-RFLP capillary electrophoresis analysis for the identification of the varietal origin of olive oils*. Food Chemistry, 2012. **134**(4): p. 2411-2418.
192. Tay, A., R.K. Singh, S.S. Krishnan, and J.P. Gore, *Authentication of Olive Oil Adulterated with Vegetable Oils Using Fourier Transform Infrared Spectroscopy*. LWT - Food Science and Technology, 2002. **35**(1): p. 99-103.
193. Sauer, M., J. Hofkens, and J. Enderlein, *Basic Principles of Fluorescence Spectroscopy*, in *Handbook of Fluorescence Spectroscopy and Imaging*. 2011, Wiley-VCH Verlag GmbH & Co. KGaA. p. 1-30.
194. Zhang, X.-F., M.-Q. Zou, X.-H. Qi, F. Liu, C. Zhang, and F. Yin, *Quantitative detection of adulterated olive oil by Raman spectroscopy and chemometrics*. Journal of Raman Spectroscopy, 2011. **42**(9): p. 1784-1788.
195. Pafundo, S., C. Agrimonti, E. Maestri, and N. Marmiroli, *Applicability of SCAR markers to food genomics: olive oil traceability*. J Agric Food Chem, 2007. **55**(15): p. 6052-9.
196. Consolandi, C., L. Palmieri, M. Severgnini, E. Maestri, N. Marmiroli, C. Agrimonti, L. Baldoni, P. Donini, G. Bellis, and B. Castiglioni, *A procedure for olive oil traceability and authenticity: DNA extraction, multiplex PCR and LDR-universal array analysis*. European Food Research and Technology, 2008. **227**(5): p. 1429-1438.
197. Pafundo, S., C. Agrimonti, E. Maestri, and N. Marmiroli, *Applicability of SCAR Markers to Food Genomics: Olive Oil Traceability*. Journal of Agricultural and Food Chemistry, 2007. **55**(15): p. 6052-6059.
198. *DNA Extraction from Olive Oil and PCR Amplification of Microsatellite Markers*. 2012; Available from: <http://www.ift.org/Knowledge%20Center/Read%20IFT%20Publications/Journal%20of%20Food%20Science/JFS%20Abstracts%20Search/JFS%20Abstract%20Search%20Details.aspx?id=7321&title=DNA%20Extraction%20from%20Olive%20Oil%20and%20PCR%20Amplification%20of%20Microsatellite%20Markers&doi=10.1111/j.1365-2621.2005.tb09011.x>.
199. Agrimonti, C., M. Vietina, S. Pafundo, and N. Marmiroli, *The use of food genomics to ensure the traceability of olive oil*. Trends in Food Science & Technology, 2011. **22**(5): p. 237-244.
200. Vietina, M., C. Agrimonti, M. Marmiroli, U. Bonas, and N. Marmiroli, *Applicability of SSR markers to the traceability of monovarietal olive oils*. Journal of the Science of Food and Agriculture, 2011. **91**(8): p. 1381-1391.
201. Wu, Y., Y. Chen, Y. Ge, J. Wang, B. Xu, W. Huang, and F. Yuan, *Detection of olive oil using the Evagreen real-time PCR method*. European Food Research and Technology, 2008. **227**(4): p. 1117-1124.
202. Zhang, L., G. Wu, Y. Wu, Y. Cao, L. Xiao, and C. Lu, *The Gene MT3-B Can Differentiate Palm Oil from Other Oil Samples*. Journal of Agricultural and Food Chemistry, 2009. **57**(16): p. 7227-7232.
203. Spaniolas, S., C. Bazakos, M. Awad, and P. Kalaitzis, *Exploitation of the Chloroplast trnL (UAA) Intron Polymorphisms for the Authentication of Plant Oils by Means of a Lab-on-a-Chip*

- Capillary Electrophoresis System*. Journal of Agricultural and Food Chemistry, 2008. **56**(16): p. 6886-6891.
204. Wu, Y., H. Zhang, J. Han, B. wang, W. Wang, X. Ju, and Y. Chen, *PCR-CE-SSCP applied to detect cheap oil blended in olive oil*. European Food Research and Technology, 2011. **233**(2): p. 313-324.
205. Trabelsi, S. and S.O. Nelson, *Nondestructive sensing of bulk density and moisture content in shelled peanuts from microwave permittivity measurements*. Food Control, 2006. **17**(4): p. 304-311.
206. Bouraoui, M., P. Richard, and J. Fichtali, *A review of moisture content determination in foods using microwave oven drying*. Food Research International, 1993. **26**(1): p. 49-57.
207. Al-Muhtaseb, A.a.H., M.A. Hararah, E.K. Megahey, W.A.M. McMinn, and T.R.A. Magee, *Dielectric properties of microwave-baked cake and its constituents over a frequency range of 0.915–2.450 GHz*. Journal of Food Engineering, 2010. **98**(1): p. 84-92.
208. Willert-Porada, M., *Advances in Microwave and Radio Frequency Processing: Report from the 8th International Conference on Microwave and High-Frequency Heating held in Bayreuth, Germany, September 3-7, 2001*. 2007: Springer.
209. Ryyänänen, S., *The electromagnetic properties of food materials: A review of the basic principles*. Journal of Food Engineering, 1995. **26**(4): p. 409-429.
210. Sakai, N., W. Mao, Y. Koshima, and M. Watanabe, *A method for developing model food system in microwave heating studies*. Journal of Food Engineering, 2005. **66**(4): p. 525-531.
211. Ragni, L., E. Iaccheri, C. Cevoli, A. Berardinelli, A. Bendini, and T.G. Toschi, *A capacitive technique to assess water content in extra virgin olive oils*. Journal of Food Engineering, 2013. **116**(1): p. 246-252.
212. Cataldo, A., E. Piuze, G. Cannazza, E. De Benedetto, and L. Tarricone, *Quality and anti-adulteration control of vegetable oils through microwave dielectric spectroscopy*. Measurement, 2010. **43**(8): p. 1031-1039.
213. *New Zealand Official Yearbook*. 2008.
214. Franks, J., P. Lowe, J. Phillipson, and C. Scott, *The impact of foot and mouth disease on farm businesses in Cumbria*. Land Use Policy, 2003. **20**(2): p. 159-168.
215. Sardini, E. and M. Serpelloni, *Instrumented wearable belt for wireless health monitoring*. Procedia Engineering, 2010. **5**(0): p. 580-583.
216. Huircán, J.I., C. Muñoz, H. Young, L. Von Dossow, J. Bustos, G. Vivallo, and M. Toneatti, *ZigBee-based wireless sensor network localization for cattle monitoring in grazing fields*. Computers and Electronics in Agriculture, 2010. **74**(2): p. 258-264.
217. Hiroaki, M. and N. Takaaki, *Grazing behavior of cows measured by handheld GPS and bite counter collar: a case of Fazenda Baia Bonita in South Pantanal, Brazil*. Japanese Journal of Human Geography, 2007. **59**(1): p. 30-42.
218. Saptari, V.A. and K. Youcef-Toumi. *Sensitivity analysis of near-infrared glucose absorption signals: toward noninvasive blood glucose sensing*. 2000.
219. Saptari, V.A. and K. Youcef-Toumi. *Sensitivity analysis of near infrared glucose absorption signals: Toward noninvasive blood glucose sensing*. in *Optical Techniques and Instrumentation for the Measurement of Blood Composition, Structure, and Dynamics, July 7, 2000 - July 8, 2000*. 2000. Amsterdam, Neth: Society of Photo-Optical Instrumentation Engineers.
220. Solanki, J., O.P. Choudhary, P. Sen, and J.T. Andrews, *Polarization sensitive optical low-coherence reflectometry for blood glucose monitoring in human subjects*. Review of Scientific Instruments, 2013. **84**(7).
221. Lipponen, J.A., V.F. Gladwell, H. Kinnunen, P.A. Karjalainen, and M.P. Tarvainen, *The correlation of vectorcardiographic changes to blood lactate concentration during an exercise test*. Biomedical Signal Processing and Control, 2013. **8**(6): p. 491-499.

222. Gavin, J.P., M.E.T. Willems, and S.D. Myers, *Reproducibility of lactate markers during 4 and 8 min stage incremental running: A pilot study*. Journal of Science and Medicine in Sport, (0).
223. Campbell, E.H., *Lactate-driven equine conditioning programmes*. The Veterinary Journal, 2011. **190**(2): p. 199-207.
224. Zanaty, O.M., M. Megahed, H. Demerdash, and R. Swelem, *Delta neutrophil index versus lactate clearance: Early markers for outcome prediction in septic shock patients*. Alexandria Journal of Medicine, 2012. **48**(4): p. 327-333.
225. Shapiro, N.I., C. Fisher, M. Donnino, L. Cataldo, A. Tang, S. Trzeciak, G. Horowitz, and R.E. Wolfe, *The Feasibility and Accuracy of Point-of-Care Lactate Measurement in Emergency Department Patients with Suspected Infection*. The Journal of Emergency Medicine, 2010. **39**(1): p. 89-94.
226. Murphy, G., D. Markeson, R. Choa, and A. Armstrong, *Raised serum lactate: A marker of necrotizing fasciitis?* Journal of Plastic, Reconstructive & Aesthetic Surgery, (0).
227. von Duvillard, S.P., W.A. Braun, M. Markofski, R. Beneke, and R. Leithäuser, *Fluids and hydration in prolonged endurance performance*. Nutrition, 2004. **20**(7–8): p. 651-656.
228. Carter Iii, R., S.N. Chevront, D.W. Wray, M.A. Kolka, L.A. Stephenson, and M.N. Sawka, *The influence of hydration status on heart rate variability after exercise heat stress*. Journal of Thermal Biology, 2005. **30**(7): p. 495-502.
229. Castagnetti, C., A. Pirrone, J. Mariella, and G. Mari, *Venous blood lactate evaluation in equine neonatal intensive care*. Theriogenology, 2010. **73**(3): p. 343-357.
230. *Appendix 3: Laboratory Reference Values: Biochemistry*, in *Clinical Examination of Farm Animals*. 2007, Blackwell Science Ltd. p. 303-305.
231. Peng, J., J. Tang, Y. Jiao, S.G. Bohnet, and D.M. Barrett, *Dielectric properties of tomatoes assisting in the development of microwave pasteurization and sterilization processes*. LWT - Food Science and Technology, 2013. **54**(2): p. 367-376.
232. Jean, B., *Guided Microwave Spectrometry for In-line Analysis of Flowable Materials*, in *Sensor Update*. 2000, Wiley-VCH, Weinheim
233. Semenov, S., J. Kellam, T. Williams, M. Quinn, B. Nicholson, and S. Thirunavukkarasu. *Microwave tomographic spectroscopy for an assessment tissue oxygenation*. in *2012 6th European Conference on Antennas and Propagation (EuCAP), 26-30 March 2012*. 2012. Piscataway, NJ, USA: IEEE.
234. Malinin, L., *Development of a non-invasive blood glucose monitor based on impedance measurements*. International Journal of Biomedical Engineering and Technology, 2012. **8**(1): p. 60-81.
235. Aparicio, S., S. Halajian, R. Alcalde, B. García, and J.M. Leal, *Liquid structure of ethyl lactate, pure and water mixed, as seen by dielectric spectroscopy, solvatochromic and thermophysical studies*. Chemical Physics Letters, 2008. **454**(1–3): p. 49-55.
236. Thomas, N., I. Lahdesmaki, and B.A. Parviz, *A contact lens with an integrated lactate sensor*. Sensors and Actuators B (Chemical), 2012. **162**(1): p. 128-34.
237. Orsi, G.B., A. Mansi, P. Tomao, F. Chiarini, and P. Visca, *Lack of association between clinical and environmental isolates of Pseudomonas aeruginosa in hospital wards*. Journal of Hospital Infection, 1994. **27**(1): p. 49-60.
238. Komor, U., P. Bielecki, H. Loessner, M. Rohde, K. Wolf, K. Westphal, S. Weiss, and S. Häussler, *Biofilm formation by Pseudomonas aeruginosa in solid murine tumors – a novel model system*. Microbes and Infection, 2012. **14**(11): p. 951-958.
239. Kerr, K.G. and A.M. Snelling, *Pseudomonas aeruginosa: a formidable and ever-present adversary*. Journal of Hospital Infection, 2009. **73**(4): p. 338-344.
240. Iversen, B.G., A.B. Brantsæter, and P. Aavitsland, *Nationwide study of invasive Pseudomonas aeruginosa infection in Norway: Importance of underlying disease*. Journal of Infection, 2008. **57**(2): p. 139-146.

241. Gellen-Dautremer, J., F. Bert, X. Panhard, B. Fantin, and A. Lefort, *Physicians fail to consider Pseudomonas aeruginosa as a potential pathogen in medicine patients with bacteremia*. Journal of Infection, 2011. **63**(1): p. 99-101.
242. Royt, P.W., R.V. Honeychuck, R.R. Pant, M.L. Rogers, L.V. Asher, J.R. Lloyd, W.E. Carlos, H.E. Belkin, and S. Patwardhan, *Iron- and 4-hydroxy-2-alkylquinoline-containing periplasmic inclusion bodies of Pseudomonas aeruginosa: A chemical analysis*. Bioorganic Chemistry, 2007. **35**(2): p. 175-188.
243. Screen, J., E. Moya, I.S. Blagbrough, and A.W. Smith, *Iron uptake in Pseudomonas aeruginosa mediated by N-(2,3-dihydroxybenzoyl)-L-serine and 2,3-dihydroxybenzoic acid*. FEMS Microbiology Letters, 1995. **127**(1–2): p. 145-149.
244. Stintzi, A., K. Evans, J.-m. Meyer, and K. Poole, *Quorum-sensing and siderophore biosynthesis in Pseudomonas aeruginosa: lasR/lasI mutants exhibit reduced pyoverdine biosynthesis*. FEMS Microbiology Letters, 1998. **166**(2): p. 341-345.
245. Rivault, F., V. Schons, C. Liébert, A. Burger, E. Sakr, M.A. Abdallah, I.J. Schalk, and G.L.A. Mislin, *Synthesis of functionalized analogs of pyochelin, a siderophore of Pseudomonas aeruginosa and Burkholderia cepacia*. Tetrahedron, 2006. **62**(10): p. 2247-2254.
246. Hannauer, M., M. Schäfer, F. Hoegy, P. Gizzi, P. Wehrung, G.L.A. Mislin, H. Budzikiewicz, and I.J. Schalk, *Biosynthesis of the pyoverdine siderophore of Pseudomonas aeruginosa involves precursors with a myristic or a myristoleic acid chain*. FEBS Letters, 2012. **586**(1): p. 96-101.
247. Zheng, P., J. Sun, R. Geffers, and A.-P. Zeng, *Functional characterization of the gene PA2384 in large-scale gene regulation in response to iron starvation in Pseudomonas aeruginosa*. Journal of Biotechnology, 2007. **132**(4): p. 342-352.
248. Wedekind, J.E., C.B. Trame, M. Dorywalska, P. Koehl, T.M. Raschke, M. McKee, D. FitzGerald, R.J. Collier, and D.B. McKay, *Refined crystallographic structure of Pseudomonas aeruginosa exotoxin A and its implications for the molecular mechanism of toxicity*. Journal of Molecular Biology, 2001. **314**(4): p. 823-837.
249. Walker, S.L., L.S. Hiremath, D.J. Wozniak, and D.R. Galloway, *ToxR (RegA)-mediated in vitro transcription of Pseudomonas aeruginosa toxA*. Gene, 1994. **150**(1): p. 87-92.
250. Fang, L.-C., C.-C. Peng, H. Chi, K.-S. Lee, and N.-C. Chiu, *Pseudomonas aeruginosa sepsis with ecthyma gangrenosum and pseudomembranous pharyngolaryngitis in a 5-month-old boy*. Journal of Microbiology, Immunology and Infection, (0).
251. Cordero, L., M. Sananes, B. Coley, M. Hogan, M. Gelman, and L.W. Ayers, *Ventilator-associated pneumonia in very low-birth-weight infants at the time of nosocomial bloodstream infection and during airway colonization with Pseudomonas aeruginosa*. American Journal of Infection Control, 2000. **28**(5): p. 333-339.
252. Mesaros, N., P. Nordmann, P. Plésiat, M. Roussel-Delvallez, J. Van Eldere, Y. Glupczynski, Y. Van Laethem, F. Jacobs, P. Lebecque, A. Malfroot, P.M. Tulkens, and F. Van Bambeke, *Pseudomonas aeruginosa : résistance et options thérapeutiques à l'aube du deuxième millénaire*. Antibiotiques, 2007. **9**(3): p. 189-198.
253. Master, R.N., R.B. Clark, J.A. Karlowisky, J. Ramirez, and J.M. Bordon, *Analysis of resistance, cross-resistance and antimicrobial combinations for Pseudomonas aeruginosa isolates from 1997 to 2009*. International Journal of Antimicrobial Agents, 2011. **38**(4): p. 291-295.
254. Kataoka, H., T. Ida, Y. Ishii, K. Tateda, T. Oguri, A. Yoshida, K. Okuzumi, T. Oishi, M. Tsukahara, S.-i. Mori, A. Yoneyama, H. Araoka, T. Mitsuda, M. Sumitomo, K. Moriya, M. Goto, Y. Nakamori, A. Shibayama, N. Ohmagari, T. Sato, and K. Yamaguchi, *Analysis of the influence of drug resistance factors on the efficacy of combinations of antibiotics for multidrug-resistant Pseudomonas aeruginosa isolated from hospitals located in the suburbs of Kanto area, Japan*. Journal of Global Antimicrobial Resistance, 2013. **1**(2): p. 91-96.
255. Douglas, M.W., K. Mulholland, V. Denyer, and T. Gottlieb, *Multi-drug resistant Pseudomonas aeruginosa outbreak in a burns unit — an infection control study*. Burns, 2001. **27**(2): p. 131-135.

256. Mirsalehian, A., M. Feizabadi, F.A. Nakhjavani, F. Jabalameli, H. Goli, and N. Kalantari, *Detection of VEB-1, OXA-10 and PER-1 genotypes in extended-spectrum β -lactamase-producing Pseudomonas aeruginosa strains isolated from burn patients*. Burns, 2010. **36**(1): p. 70-74.
257. Estahbanati, H.K., P.P. Kashani, and F. Ghanaatpisheh, *Frequency of Pseudomonas aeruginosa serotypes in burn wound infections and their resistance to antibiotics*. Burns, 2002. **28**(4): p. 340-348.
258. Jabalameli, F., A. Mirsalehian, B. Khoramian, M. Aligholi, S.S. Khoramrooz, P. Asadollahi, M. Taherikalani, and M. Emameini, *Evaluation of biofilm production and characterization of genes encoding type III secretion system among Pseudomonas aeruginosa isolated from burn patients*. Burns, 2012. **38**(8): p. 1192-1197.
259. Pankhurst, C.L. and J. Philpott-Howard, *The environmental risk factors associated with medical and dental equipment in the transmission of Burkholderia (Pseudomonas) cepacia in cystic fibrosis patients*. Journal of Hospital Infection, 1996. **32**(4): p. 249-255.
260. Brimicombe, R.W., L. Dijkshoorn, T.J.K. van der Reijden, I. Kardoes, T.L. Pitt, P.J. van den Broek, and H.G.M. Heijerman, *Transmission of Pseudomonas aeruginosa in children with cystic fibrosis attending summer camps in The Netherlands*. Journal of Cystic Fibrosis, 2008. **7**(1): p. 30-36.
261. Bertrand, X., C. Slekovec, P. Cholley, and D. Talon, *Épidémiologie des infections à Pseudomonas aeruginosa*. Revue Francophone des Laboratoires, 2011. **2011**(435): p. 35-40.
262. Bajolet, O., D. Ciocan, C. Vallet, C. de Champs, V. Vernet-Garnier, T. Guillard, L. Brasme, G. Thieffin, G. Cadiot, and F. Bureau-Chalot, *Gastroscopy-associated transmission of extended-spectrum beta-lactamase-producing Pseudomonas aeruginosa*. Journal of Hospital Infection, 2013. **83**(4): p. 341-343.
263. Trautmann, M., C. Bauer, C. Schumann, P. Hahn, M. Höher, M. Haller, and P.M. Lepper, *Common RAPD pattern of Pseudomonas aeruginosa from patients and tap water in a medical intensive care unit*. International Journal of Hygiene and Environmental Health, 2006. **209**(4): p. 325-331.
264. Rogues, A.M., H. Boulestreau, A. Lashéras, A. Boyer, D. Gruson, C. Merle, Y. Castaing, C.M. Bébear, and J.P. Gachie, *Contribution of tap water to patient colonisation with Pseudomonas aeruginosa in a medical intensive care unit*. Journal of Hospital Infection, 2007. **67**(1): p. 72-78.
265. Robbie, D. and M. Noy, *P2.05 Evaluation of a Novel Method to Address Pseudomonas aeruginosa Contamination of Water Supply to Patient Showers*. Journal of Hospital Infection, 2006. **64**, **Supplement 1**(0): p. S12-S13.
266. Lacey, S. and S.V. Want, *Pseudomonas pickettii infections in a paediatric oncology unit*. Journal of Hospital Infection, 1991. **17**(1): p. 45-51.
267. Ferroni, A., L. Nguyen, B. Pron, G. Quesne, M.C. Brusset, and P. Berche, *Outbreak of nosocomial urinary tract infections due to Pseudomonas aeruginosa in a paediatric surgical unit associated with tap-water contamination*. Journal of Hospital Infection, 1998. **39**(4): p. 301-307.
268. Breathnach, A.S., M.D. Cubbon, R.N. Karunaharan, C.F. Pope, and T.D. Planche, *Multidrug-resistant Pseudomonas aeruginosa outbreaks in two hospitals: association with contaminated hospital waste-water systems*. Journal of Hospital Infection, 2012. **82**(1): p. 19-24.
269. Hamanaka, D., M. Onishi, T. Genkawa, F. Tanaka, and T. Uchino, *Effects of temperature and nutrient concentration on the structural characteristics and removal of vegetable-associated Pseudomonas biofilm*. Food Control, 2012. **24**(1-2): p. 165-170.
270. Peyton, B.M., *Effects of shear stress and substrate loading rate on Pseudomonas aeruginosa biofilm thickness and density*. Water Research, 1996. **30**(1): p. 29-36.

271. O'Donnell, M.J., C.M. Tuttlebee, F.R. Falkiner, and D.C. Coleman, *Bacterial contamination of dental chair units in a modern dental hospital caused by leakage from suction system hoses containing extensive biofilm*. Journal of Hospital Infection, 2005. **59**(4): p. 348-360.
272. Manuel, C.M., O.C. Nunes, and L.F. Melo, *Dynamics of drinking water biofilm in flow/non-flow conditions*. Water Research, 2007. **41**(3): p. 551-562.
273. Simões, M., L.C. Simões, and M.J. Vieira, *A review of current and emergent biofilm control strategies*. LWT - Food Science and Technology, 2010. **43**(4): p. 573-583.
274. O'Donnell, M.J., M. Boyle, J. Swan, R.J. Russell, and D.C. Coleman, *A centralised, automated dental hospital water quality and biofilm management system using neutral Ecasol™ maintains dental unit waterline output at better than potable quality: A 2-year longitudinal study*. Journal of Dentistry, 2009. **37**(10): p. 748-762.
275. Florjanič, M. and J. Kristl, *The control of biofilm formation by hydrodynamics of purified water in industrial distribution system*. International Journal of Pharmaceutics, 2011. **405**(1–2): p. 16-22.
276. Nwachuku, N. and C.P. Gerba, *Microbial risk assessment: don't forget the children*. Current Opinion in Microbiology, 2004. **7**(3): p. 206-209.
277. Buse, H.Y., M.E. Schoen, and N.J. Ashbolt, *Legionellae in engineered systems and use of quantitative microbial risk assessment to predict exposure*. Water Research, 2012. **46**(4): p. 921-933.
278. Enoch, D.A., A.J. Simpson, and C.C. Kibbler, *Predictive value of isolating Pseudomonas aeruginosa from aerobic and anaerobic blood culture bottles*. Journal of Medical Microbiology, 2004. **53**(11): p. 1151-1154.
279. Li, D., Y. Feng, L. Zhou, Z. Ye, J. Wang, Y. Ying, C. Ruan, R. Wang, and Y. Li, *Label-free capacitive immunosensor based on quartz crystal Au electrode for rapid and sensitive detection of Escherichia coli O157:H7*. Analytica Chimica Acta, 2011. **687**(1): p. 89-96.
280. Lepage, P. and B. Dan, *Chapter 115 - Infantile and childhood bacterial meningitis*, in *Handbook of Clinical Neurology*, M.L. Olivier Dulac and B.S. Harvey, Editors. 2013, Elsevier. p. 1115-1125.
281. Said, G. and C. Krarup, *Chapter 22 - Chronic inflammatory demyelinating polyneuropathy*, in *Handbook of Clinical Neurology*, S. Gérard and K. Christian, Editors. 2013, Elsevier. p. 403-413.
282. Preusser, M. and J.A. Hainfellner, *Chapter 11 - CSF and laboratory analysis (tumor markers)*, in *Handbook of Clinical Neurology*, F.B. Michael J. Aminoff and F.S. Dick, Editors. 2012, Elsevier. p. 143-148.
283. Chamberlain, M.C., *Chapter 22 - CSF Dissemination of Primary Brain Tumors*, in *Handbook of Brain Tumor Chemotherapy*, H.B. Newton, Editor. 2006, Academic Press: San Diego. p. 316-331.
284. Kelly, M.E., R. Dodd, and G.K. Steinberg, *Chapter 39 Subarachnoid hemorrhage*, in *Handbook of Clinical Neurology*, F. Marc, Editor. 2008, Elsevier. p. 791-808.
285. Hacin-Bey, L., T.C. Origitano, and J. Biller, *Chapter 15 - Subarachnoid Hemorrhage in Young Adults*, in *Stroke in Children and Young Adults (Second Edition)*, J. Biller, Editor. 2009, W.B. Saunders: Philadelphia. p. 289-314.
286. Stolze, H., J.P. Kuhtz-Buschbeck, H. Drücke, K. Jöhnk, C. Diercks, S. Palmié, H.M. Mehdorn, M. Illert, and G. Deuschl, *Gait analysis in idiopathic normal pressure hydrocephalus – which parameters respond to the CSF tap test?* Clinical Neurophysiology, 2000. **111**(9): p. 1678-1686.
287. Alfayate-Miguélez, S., L. Marín-Vives, L. Martínez-Lage-Azorín, S. García-Martínez, M.J. Almagro, and J.F. Martínez-Lage, *Normal ventricular-CSF may confound the diagnosis of tuberculous meningitis hydrocephalus*. Neurocirugía, 2011. **22**(2): p. 157-161.
288. Yuh, E.L. and W.P. Dillon, *Intracranial Hypotension and Intracranial Hypertension*. Neuroimaging Clinics of North America, 2010. **20**(4): p. 597-617.

-
289. Williams, G.M., B.A. Perler, J.F. Burdick, F.A. Osterman, Jr., S. Mitchell, D. Merine, B. Drenger, S.D. Parker, C. Beattie, and B.A. Reitz, *Angiographic localization of spinal cord blood supply and its relationship to postoperative paraplegia*. *J Vasc Surg*, 1991. **13**(1): p. 23-33; discussion 33-5.
290. Slack, S.M., *Appendix A - Properties of Biological Fluids*, in *Biomaterials Science (Third Edition)*, B.D. Ratner, et al., Editors. 2013, Academic Press. p. 1479-1482.
291. Lonnapan, A., V. Thomas, G. Bindu, **C. Rajasekaran**, and **K.T. Mathew**, *Analysis of Human Cerebro Spinal Fluid at the ISM Band of Frequencies*. *Journal of Electromagnetic Waves and Applications*, 2006. **20**(6): p. 773-779.
292. Blakey, R., O. Korostynska, A. Mason, and A. Al-Shamma'a, *Real-Time Microwave Based Sensing Method for Vegetable Oil Type Verification*. *Procedia Engineering*, 2012. **47**(0): p. 623-626.
293. Korostynska, O., R. Blakey, A. Mason, and A. Al-Shamma'a, *Novel Method for Vegetable Oil Type Verification Based on Real-Time Microwave Sensing*. *Sensors and Actuators A: Physical*, (0).
294. Jackson, D.R., *Overview of Microstrip Antennas*.
295. Wong, K.L., *Compact and Broadband Microstrip Antennas*. 2002: Wiley.
296. Shackelford, A.K., L. Kai-Fong, and K.M. Luk, *Design of small-size wide-bandwidth microstrip-patch antennas*. *Antennas and Propagation Magazine, IEEE*, 2003. **45**(1): p. 75-83.
297. Singh, P.K.G., *Microstrip Antennas Loaded with Shorting Post*. *Engineering*, 2009. **1**(1-54): p. 41-45.
298. Chii-Ruey, L., H. Tzu-Chen, C. Hsiu-Hsien, H. Jou-Hsiung, C. Jin-Sen, and L. Yuan-Chih. *A novel open slot monopole antenna with a coupling element for WiMAX 3.5 GHz applications*. in *Applications of Electromagnetism and Student Innovation Competition Awards (AEM2C), 2010 International Conference on*. 2010.
299. Tseng, C.-C., Y.-H. Chou, T.-W. Hsieh, M.-W. Wang, Y.-Y. Shu, and M.-D. Ger, *Interdigitated electrode fabricated by integration of ink-jet printing with electroless plating and its application in gas sensor*. *Colloids and Surfaces A: Physicochemical and Engineering Aspects*, 2012. **402**(0): p. 45-52.
300. Tsamis, E.D. and J.N. Avaritsiotis, *Design of planar capacitive type sensor for "water content" monitoring in a production line*. *Sensors and Actuators A: Physical*, 2005. **118**(2): p. 202-211.
301. Kitsara, M., D. Goustouridis, S. Chatzandroulis, M. Chatzichristidi, I. Raptis, T. Ganetsos, R. Igreja, and C.J. Dias, *Single chip interdigitated electrode capacitive chemical sensor arrays*. *Sensors and Actuators B: Chemical*, 2007. **127**(1): p. 186-192.
302. Kallempudi, S.S. and Y. Gurbuz, *A nanostructured-nickel based interdigitated capacitive transducer for biosensor applications*. *Sensors and Actuators B: Chemical*, 2011. **160**(1): p. 891-898.
303. Altenberend, U., F. Molina-Lopez, A. Oprea, D. Briand, N. Bârsan, N.F. De Rooij, and U. Weimar, *Towards fully printed capacitive gas sensors on flexible PET substrates based on Ag interdigitated transducers with increased stability*. *Sensors and Actuators B: Chemical*, (0).
304. Anschau, A., M.C.A. Xavier, S. Hernalsteens, and T.T. Franco, *Effect of feeding strategies on lipid production by *Lipomyces starkeyi**. *Bioresource Technology*, 2014. **157**(0): p. 214-222.
305. Minges, M.L. and A.I.H. Committee, *Electronic Materials Handbook: Packaging*. 1989: ASM International.
306. Hall, S.H. and H.L. Heck, *Advanced Signal Integrity for High-Speed Digital Designs*. 2011: Wiley.
307. Association, E., I.o. Electrical, and E. Engineers, *Electrical Overstress/Electrostatic Discharge Symposium Proceedings, 1999: Orlando, Florida September 28-30, 1999*. 1999: ESD Association.
308. Society, E.D.F.A., *Microelectronic Failure Analysis: Desk Reference : 2002 Supplement*. 2002: ASM International.
-

309. Wild, R., S. Patil, M. Popovi, M. Zappi, S. Dufreche, and R. Bajpai, *Lipids from Lipomyces starkeyi*. Food Technology and Biotechnology, 2010. **48 (3)**: p. 329 - 335.
310. Lin, J., H. Shen, H. Tan, X. Zhao, S. Wu, C. Hu, and Z.K. Zhao, *Lipid production by Lipomyces starkeyi cells in glucose solution without auxiliary nutrients*. Journal of Biotechnology, 2011. **152(4)**: p. 184-188.
311. Crossley, A., T.D. Heyes, and B.J.F. Hudson, *The effect of heat on pure triglycerides*. Journal of the American Oil Chemists Society, 1962. **39(1)**: p. 9-14.
312. Okpokwasili, G.C. and C.N. Molokwu, *Yeast and mould contaminants of vegetable oils*. Bioresource Technology, 1996. **57(3)**: p. 245-249.
313. Fadda, C., A. Del Caro, A.M. Sanguinetti, P.P. Urgeghe, V. Vacca, P.P. Arca, and A. Piga, *Changes during storage of quality parameters and in vitro antioxidant activity of extra virgin monovarietal oils obtained with two extraction technologies*. Food Chemistry, 2012. **134(3)**: p. 1542-1548.
314. Criado, M.N., M.J. Motilva, M. Goñi, and M.P. Romero, *Comparative study of the effect of the maturation process of the olive fruit on the chlorophyll and carotenoid fractions of drupes and virgin oils from Arbequina and Farga cultivars*. Food Chemistry, 2007. **100(2)**: p. 748-755.
315. Blakey, R., I. Nakouti, O. Korostynska, A. Mason, and A. Al-Shamma'a, *Real-Time Monitoring of Pseudomonas Aeruginosa Concentration Using a Novel Electromagnetic Sensors Microfluidic Cell Structure*. Biomedical Engineering, IEEE Transactions on, 2013. **60(12)**: p. 3291-3297.
316. Diallo, M.A., A. Shaw, J.H. Goh, S.R. Wylie, A. Mason, and A. Al-Shamma'a. *Electromagnetic sensor for leak detection and asset management for the water industry*. in *Sensing Technology (ICST), 2012 Sixth International Conference on*. 2012.
317. Goh, J.H., A. Mason, A.I. Al-Shamma'a, M. Field, M. Shackcloth, and P. Browning, *Non Invasive Microwave Sensor for the Detection of Lactic Acid in Cerebrospinal Fluid (CSF)*. Journal of Physics: Conference Series, 2011. **307(1)**: p. 012017.
318. Goh, J.H., A. Mason, A.I. Al-Shamma'a, S.R. Wylie, M. Field, and P. Browning. *Lactate detection using a microwave cavity sensor for biomedical applications*. in *Sensing Technology (ICST), 2011 Fifth International Conference on*. 2011.

Appendix 1. Publications resulting from the research

Journal publications

R. T. Blakey, A. Mason, C. E. Rolph, G. Bond, and A. I. Al-Shamma'a, "Lipid droplet detection by the cavity perturbation method", *Journal of Physics: Conference Series*, vol. 307, DOI:10.1088/1742-6596/307/1/012021, 2011.

R. Blakey, O. Korostynska, A. Mason, and A. Al-Shamma'a, "Real-Time Microwave Based Sensing Method for Vegetable Oil Type Verification", *Procedia Engineering*, vol. 47, pp. 623-626, DOI: 10.1016/j.proeng.2012.09.224, 2012.

R. T. Blakey, A. Mason, A. Al-Shamma'a, C. E. Rolph, and G. Bond, "Dielectric Characterisation of Lipid Droplet Suspensions Using the Small Perturbation Technique", in *Advancement in Sensing Technology*. vol. 1, S. C. Mukhopadhyay, K. P. Jayasundera, and A. Fuchs, Springer Berlin Heidelberg, pp. 81-91, DOI: 10.1007/978-3-642-32180-1_5, 2013.

R. T. Blakey, A. Mason, and A. I. Al-Shamma'a, "A Fluidic Cell Embedded Electromagnetic Wave Sensor for Online Indication of Neurological Impairment during Surgical Procedures", *Journal of Physics: Conference Series*, vol. 450, p. 012024, DOI: 10.1088/1742-6596/450/1/012024, 2013.

O. Korostynska, R. Blakey, A. Mason, and A. Al-Shamma'a, "Novel method for vegetable oil type verification based on real-time microwave sensing", *Sensors and Actuators A: Physical*, vol. 202, pp. 211-216, DOI: 10.1016/j.sna.2012.12.011, 2013.

R. Blakey, I. Nakouti, O. Korostynska, A. Mason, and A. Al-Shamma'a, "Real-Time Monitoring of Pseudomonas Aeruginosa Concentration Using a Novel Electromagnetic Sensors Microfluidic Cell Structure", *IEEE Transactions on Biomedical Engineering*, vol. 60, pp. 3291-3297, DOI: 10.1109/TBME.2013.2268277, 2013.

Conference Publications

R. T. Blakey, A. Mason, A. I. Al-Shamma'a, C. E. Rolph, and G. Bond, "Dielectric characteristics of lipid droplets suspended in YEPD media", Fifth International Conference on Sensing Technology, Palmerston North, New Zealand, 2011.

R. T. Blakey, A. Mason, C. E. Rolph, G. Bond, and A. I. Al-Shamma'a, "Lipid droplet detection Using NDT Microwave Spectroscopy," Ampere 2011, Toulouse, France, 2011.

R. T. Blakey, A. Mason, C. E. Rolph, G. Bond, and A. I. Al-Shamma'a, "Dielectric Characterisation of Triacylglycerol Lipid Droplets", Built Environment and Natural Environment (BEAN) 2011, Liverpool, UK, 2011.

R. Blakey, A. Mason, A. I. Al-Shamma'a, K. A. Rostron, C. E. Rolph, and G. Bond, "Utilisation of a Resonant Structure to Differentiate Lipomyces Yeast Cultures based upon Lipid Content", Sixth International Conference on Sensing Technology (ICST2012), Kolkata, India, 2012.

R. T. Blakey, A. Mason, A. I. Al-Shamma'a, C. E. Rolph, and G. Bond, "Dielectric Characteristics of Lipid Droplet Suspensions Using the Small Perturbation Technique", Proc. 46th Annual Microwave Power Symposium (IMPI 46), Las Vegas, USA, pp. 188-194, 2012.

R. T. Blakey, A. Mason, A. I. Al-Shamma'a, C. E. Rolph, and G. Bond, "Dielectric characterisation of lipid droplet suspensions using the small perturbation technique", Built Environment and Natural Environment (BEAN) 2012, Liverpool, UK, 2012.

R. Blakey, A. Mason, O. Korostynska and A. I. Al-Shamma'a, "Utilisation of an Embedded Resonant Structure to Differentiate Lipomyces Yeast Cultures based upon Lipid Content and Cell Concentration", Seventh International Conference on Sensing Technology (ICST2013), In-Press.

R. T. Blakey, A. Mason and A. I. Al-Shamma'a, "An Electromagnetic Coplanar Sensor Embedded in a Continuous Fluidic Monitoring System for Lipid Profiling of Yeast Cells", 8th Built Environment and Natural Environment (BEAN) Conference, pp. 15-16, 2013.

R. Blakey, A. Mason, and A. I. Al-Shamma'a, "Cell Counting Using a Low-Cost Microwave Sensor Technique", International Microwave Power Symposium (IMPI 47), pp. 84-88, ISBN: 9780956274748, 2013.

Appendix 2. Technical Appendix

1.1 LabVIEW control software

LabVIEW (National Instruments, USA) is data flow, graphic based system design software that can be used to control instruments, manipulate data and express results. It uses a dataflow programming tool called G. Execution of programs is governed by the structure of graphical block diagrams that represent a function or task interconnected to form a chain of data.

LabView was used to control the HP8720 ET VNA throughout the research using a laptop PC (Toshiba, Japan) installed with a VXI driver via GPIB-USB interface controller (NI GPIB-USB-HS, National Instruments, USA). Commands were sent through this interface using Virtual Instrument Software Architecture (VISA). In this way sequences of processes can be combined into a single program increasing efficiency and standardising measurement methodologies.

Using this type of interface allowed the VNA to be controlled using commands that are derived from the purpose of the function they control. For example, to set the start frequency at 500 MHz the command is "STAR 500 MHz". To set the marker at the centre of the frequency sweep the command "MARKCENT" would be used.

The first program created to control the VNA incorporated all of the functions the VNA can carry out into a single interface (Figure 0.1 and Figure 0.2).

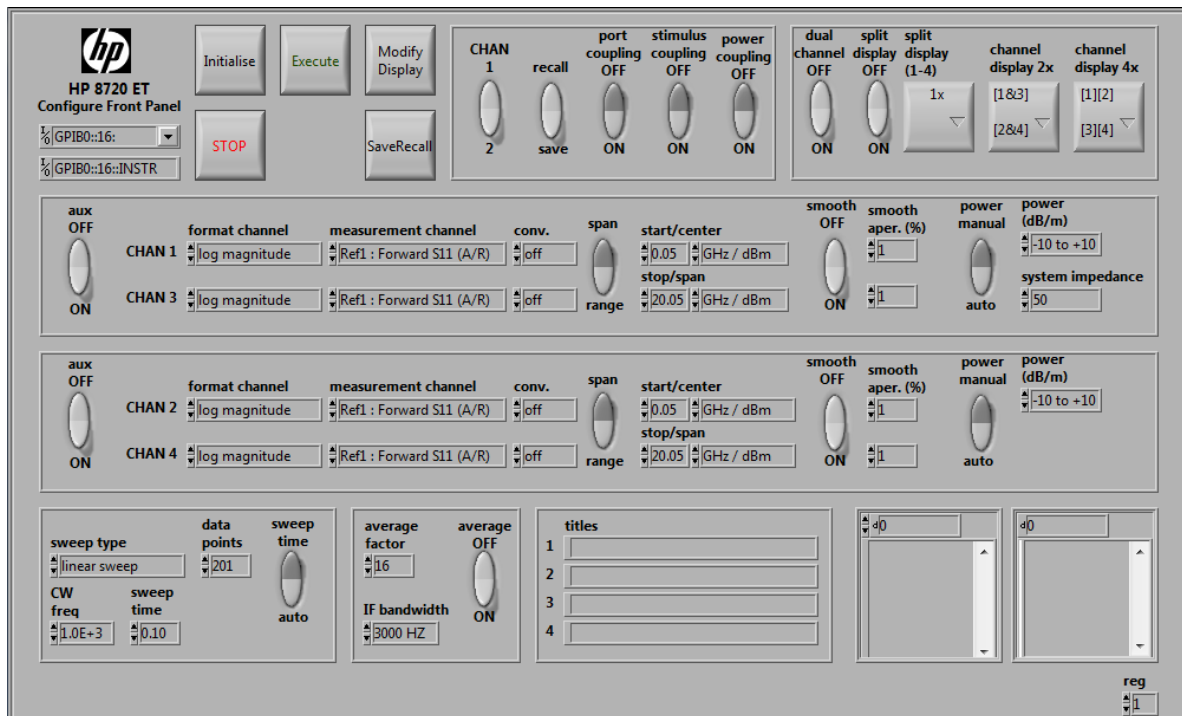


Figure 0.1. LabVIEW Interface for configuring the HP 8720 ET VNA.

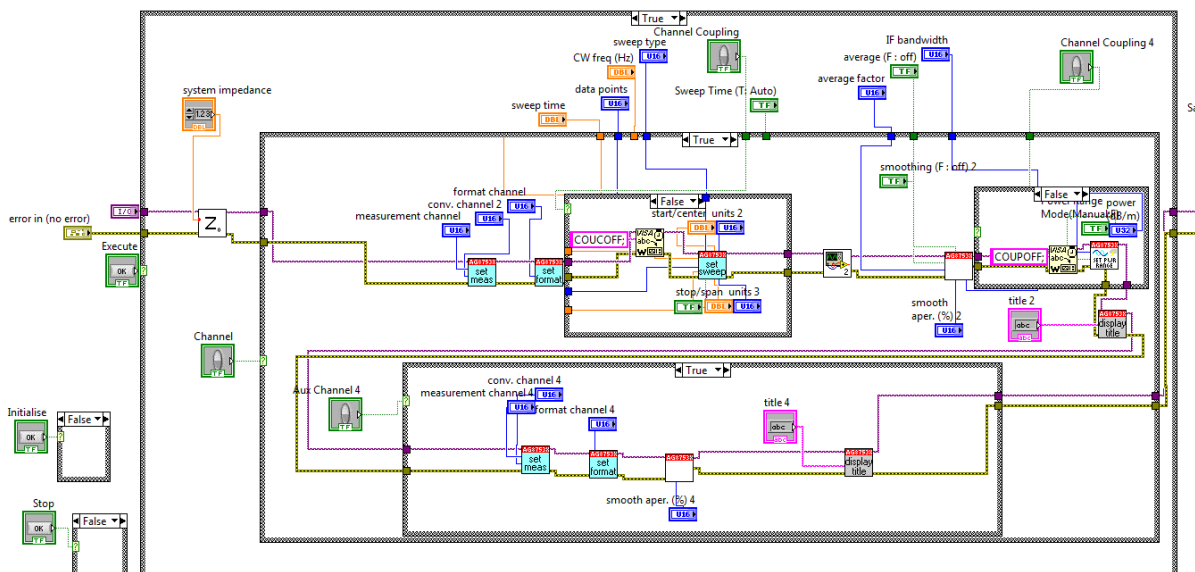


Figure 0.2. LabVIEW programming for above interface incorporating sub Vis.

With the basics of VISA programming established, a program was written that could conduct several frequency sweeps, storing the s-parameters for each sweep in a comma separated file (.csv) for initial data interpretation (Figure 0.3 and Figure 0.4). This program also gathered data on the centre frequency, bandwidth and quality factor of the peak or trough.

1.2 PCB routing methodology

After coplanar resonant structures were simulated and optimised a number of sensors were implemented as part of this research. When a sensor design was finalised after simulation, the micro strip patterns were input into specialised PCB design software, EAGLE PCB design software (CadSoft, Germany). The software provides an interface for designing the schematics of PCB based circuits.

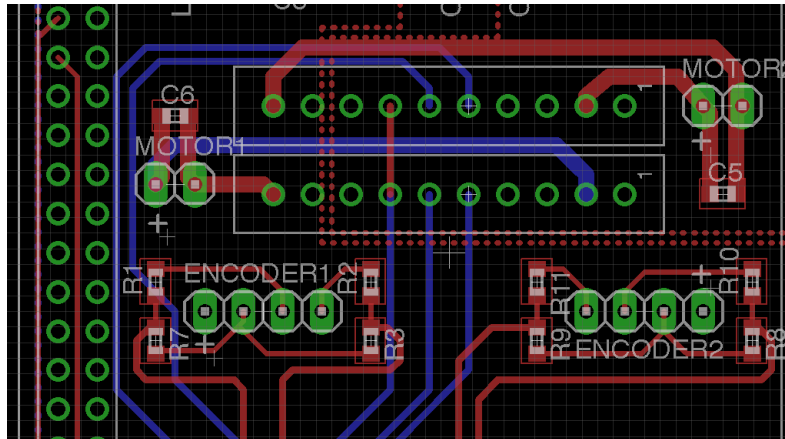


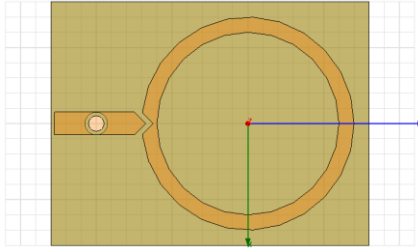
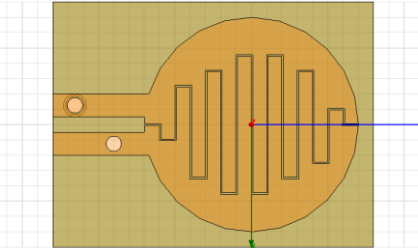
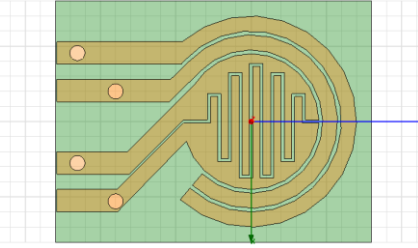
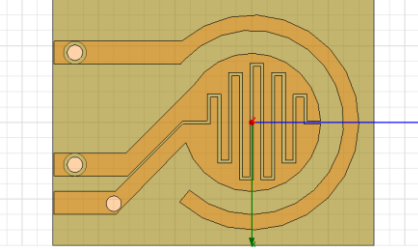
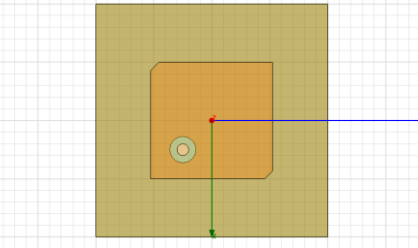
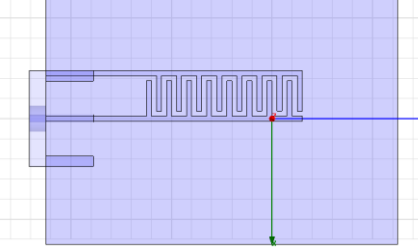
Figure 0.7. A typical PCB layout as seen in CadSoft EAGLE.

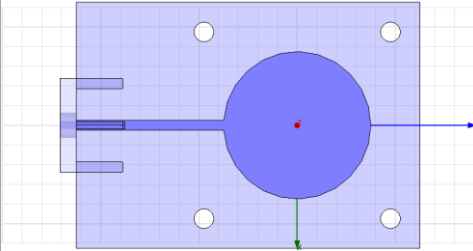
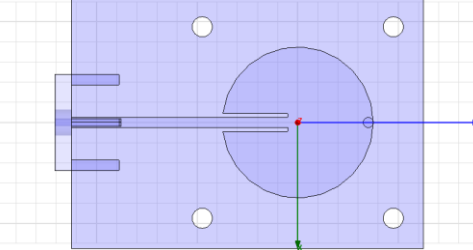
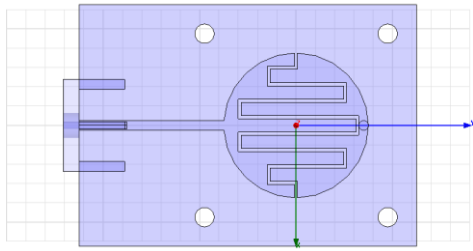
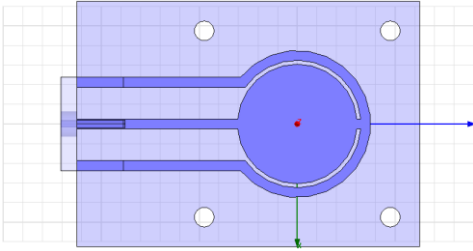
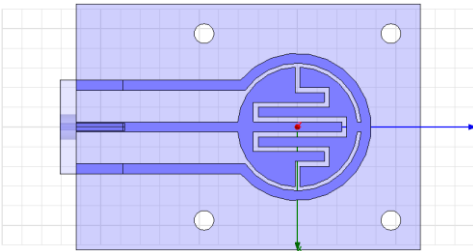
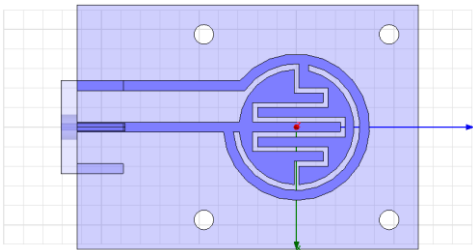
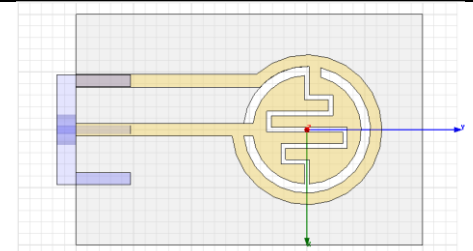
The sensor configuration was then converted into a vector based plotter file (.plt) by the software for interpretation by ABViewer (CadSoft, Germany) which is used to finalise the .plt file that will be used by the PCB router.

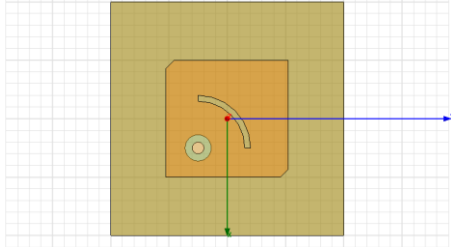
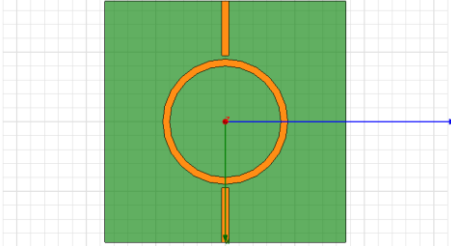
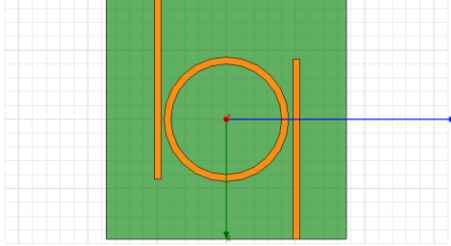
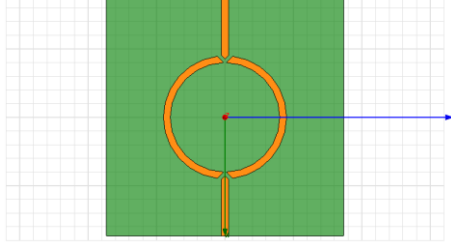
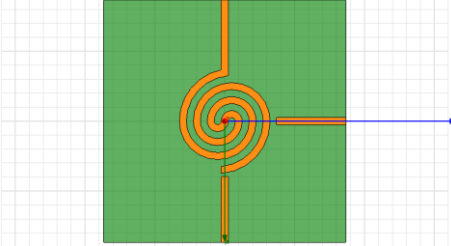
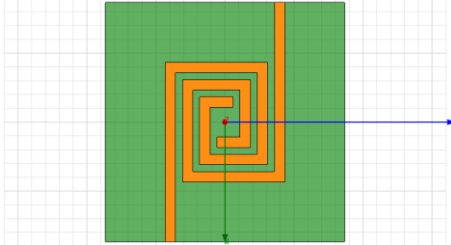
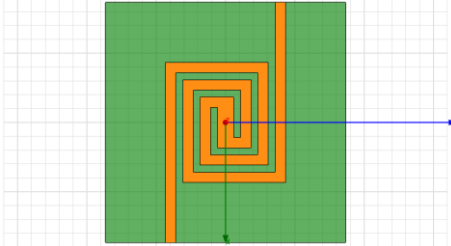
1.3 Statistical software

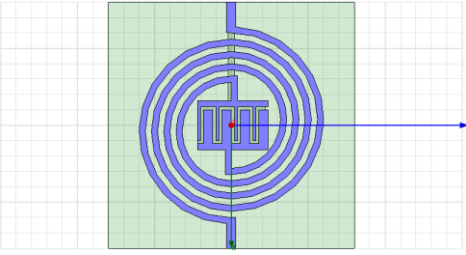
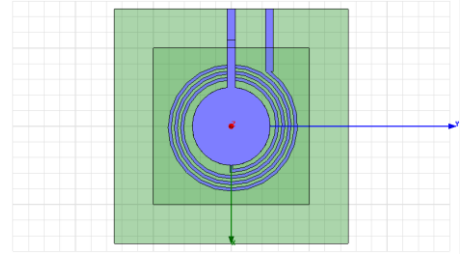
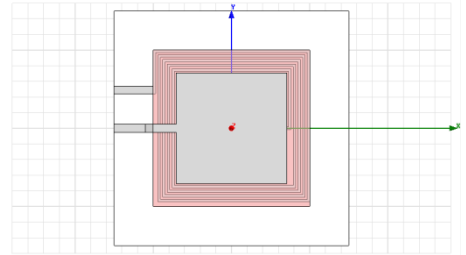
Data generated from simulations and experiments were primarily handled in Office Excel (Microsoft, USA). The statistical analysis program used for this research is OriginPro (OriginLab, USA). This software generates publication-quality graphs, performs data analysis, data interpretation and statistical analysis.

1.4 Sensors developed

Sensor	Schematic	Characteristics
B1.1	 A schematic diagram of a ring sensor on a green substrate. It features a circular ring with a small protrusion on the left side. A red dot is at the center of the ring, with a blue arrow pointing to the right and a green arrow pointing downwards.	Ring sensor 3.8 GHz
B3.0	 A schematic diagram of an interdigitated capacitive sensor on a green substrate. It features a circular area with several vertical interdigitated fingers. A red dot is at the center, with a blue arrow pointing to the right and a green arrow pointing downwards.	Interdigitated capacitive sensor 1.4 GHz
B4.0	 A schematic diagram of a two-port capacitive sensor with an inductive ring on a green substrate. It features a circular area with interdigitated fingers and an outer ring. Four ports are on the left. A red dot is at the center, with a blue arrow pointing to the right and a green arrow pointing downwards.	Two-port capacitive sensor with inductive ring 2.9 GHz
B4.1	 A schematic diagram of a two-port capacitive sensor with an inductive ring on a green substrate. It features a circular area with interdigitated fingers and an outer ring. Two ports are on the left. A red dot is at the center, with a blue arrow pointing to the right and a green arrow pointing downwards.	Two-port capacitive sensor with inductive ring 1.6 GHz
B10.0	 A schematic diagram of a rectangle patch antenna on a green substrate. It features a rectangular patch with a small circular hole on the left side. A red dot is at the center, with a blue arrow pointing to the right and a green arrow pointing downwards.	Rectangle patch antenna 6.5 GHz
OK-8	 A schematic diagram of an interdigitated capacitive sensor on a blue substrate. It features a horizontal interdigitated structure. A red dot is at the center, with a blue arrow pointing to the right and a green arrow pointing downwards.	Interdigitated capacitive sensor

RTB-1		5.15 GHz
RTB-2		1.9 GHz
RTB-3		2.45 GHz
RTB-4		2.65 GHz
RTB-5		0.9 GHz
RTB-FINAL		0.95 GHz
RTB-through		1.3 GHz

		<p>5.7 GHz</p>
		<p>4.0 GHz</p>
		<p>4.35 GHz</p>
		<p>3.8 GHz</p>
		<p>Unstable resonant peaks</p>
		<p>0.8 GHz</p>
		<p>0.55 GHz</p>

<p>LC-01</p>		<p>Unstable</p>
<p>LC-03</p>		<p>0.07 GHz</p>
<p>LC-04</p>		<p>0.02 GHz</p>